Atmospheric Monitoring for Ground-Based Cosmic Ray Detectors

Zur Erlangung des akademischen Grades eines

Doktors der Naturwissenschaften

von der Fakultät für Physik des
Karlsruher Instituts für Technologie (KIT)

genehmigte

Dissertation

von

Dipl.-Phys. C. Martin Will
aus Karlsruhe (Baden)

Tag der mündlichen Prüfung: 15. Juni 2012
Referent: Prof. Dr. Johannes Blümer, Karlsruher Institut für Technologie
Korreferent: Prof. Dr. Lawrence Wiencke, Colorado School of Mines, USA
Betreuer: Dr. Bianca Keilhauer, Karlsruher Institut für Technologie

4. Mai 2012

He was born in the summer of his 27th year
Comin' home to a place he'd never been before
He left yesterday behind him, you might say he was born again
You might say he found a key for every door

It's the Colorado Rocky Mountain High
I've seen it rainin' fire in the sky
The shadow from the starlight is softer than a lullaby
Rocky Mountain High

John Denver (1972)
Rocky Mountain High

Contents

Chapter 1

Introduction

It has been exactly 100 years since Victor Hess set out in several daring balloon flights and discovered cosmic rays, which later was rewarded with the Nobel Prize. Our measurement techniques and subsequently our understanding of the nature of these particles have improved significantly since these days, the energy spectrum and the nuclear composition are measured for large ranges of energy (see Chapter 2). Still, there are many open questions, most of them concerning the high-energetic end of the spectrum. At energies several decades higher than what is achievable at man-made accelerators, the cosmic rays are messengers that allow us to study some of the most extreme processes in the universe. Their sources remain unknown, but several possible candidates and acceleration scenarios are proposed. The mass composition of the cosmic rays at the highest energies seems to be the key information to be able to distinguish between them.

The Pierre Auger Observatory in Argentina, the largest cosmic ray detector in the world (see Chapter 3), is able to measure ultra high energy cosmic rays with large statistics and infer the mass composition. A hybrid detector, the Pierre Auger Observatory consists of a large area Surface Detector (SD) of more than 1600 water Cherenkov detectors and a Fluorescence Detector (FD). The FD, consisting of 27 telescopes at four sites, is used to perform measurements of the shower energy and the longitudinal development of extensive air showers, which is sensitive to the mass of the primary particle. The fluorescence technique uses the atmosphere as a giant calorimeter. Secondary particles of the shower excite nitrogen molecules that emit an isotropic light in the UV range upon de-excitation. Via the measurement of this fluorescence light, the deposited energy of the shower in the atmosphere can be calculated. Atmospheric parameters have to be known very well to correct for influences of the atmospheric state variables – e. g. temperature, pressure and humidity – on the shower development and detection. An extensive balloon program was started in 2002 to measure the state variables, but for even higher quality of air shower reconstruction, a more efficient treatment of the state variables needs to be developed and implemented. The attenuation of the light on its way to the FD due to scattering has to be monitored continuously. Rayleigh scattering on small molecules is very predictable, but scattering on larger aerosols needs to be measured hourly. The next step has been to investigate whether this scheme for atmospheric monitoring can be used of an even larger cosmic ray detector, collecting about one order of magnitude more particles.

The state variables of the atmosphere are stable over the course of one night

as well as across the large array of the Pierre Auger Observatory. But day-to-day variations and seasonal effects alter the development of air showers and introduce a systematic uncertainty if not taken into account properly (see Chapter 4). The height-dependent profiles of state variables above the array were measured with weather balloons. This system is implemented in a rapid atmospheric monitoring system, aimed at providing as close to real-time atmospheric measurements as possible for interesting air showers, e. g. high-energetic air showers (see Chapter 5). However, due to the unclear validity time of single balloon data, the measured conditions might not even be valid at the time of the event that triggered the launch. The balloon program, especially as part of this rapid monitoring program, places a large financial burden on the collaboration. A feasibility study was performed to investigate data from the Global Data Assimilation System (GDAS) for replacing the balloon data (see Chapter 6). GDAS data are based on model calculations from numerical weather prediction and real-time atmospheric measurements. They are available every three hours. An interface between this data and the reconstruction framework of the Pierre Auger Observatory was developed which is now the default source of atmospheric state variables.

Another important atmospheric correction in the reconstruction of air showers is due to the attenuation of the measured light on aerosols between the shower track and the detector. The aerosol concentration is highly variable over the course of a night, so hourly measurements are inevitable. A laser facility close to the center of the array is used as an atmospheric test beam. The side-scattered light from the beam is used to measure the transmission properties of the atmosphere. The facility is almost equidistant to three of the four FD sites, the fourth station is too far away for reliable measurements. In 2009, a second laser station was assembled, closer to this FD site. Within this thesis, the second facility was incorporated into the standard aerosol monitoring and analysis software was developed (see Chapter 7).

A future ground-based array to measure cosmic rays of primary energy larger than 10^{19} eV needs to be even larger than the Pierre Auger Observatory, resulting in larger distances between the individual FD sites. This increases the importance of the knowledge of atmospheric conditions, especially for the precision measurements needed to answer the remaining questions about cosmic ray sources and mass composition. For this reason, a potential site needs to be evaluated from an atmospheric standpoint and it needs to be shown that the current methods of monitoring work on even larger scales. To investigate this question, a Research and Development effort was started in south-east Colorado, a proposed site for a large scale cosmic ray observatory in the Northern Hemisphere. The setup consists of a laser facility similar to the laser stations at the Pierre Auger Observatory and a small fluorescence detector about 40 km away, the Atmospheric Monitoring Telescope (AMT). The large distance between the detector site and the operators necessitate stable automatic operations and the possibility to remotely steer the system. Within this work, the AMT was set up and tested, the automatization and remote control were implemented, and several months of data were recorded and analyzed (see Chapter 8). An interesting addition to the side-scatter measurements is the Raman Lidar, using the backscattered light from the same laser source to measure the optical properties of the atmosphere. The complementarity of both systems provides more insights into the measurements of aerosol scattering. Parallel to the measurements of the aerosol conditions, a mobile small-scale balloon measurement program was performed.

Chapter 2

Extensive Air Showers and Cosmic Rays

Many questions remain about the origin(s), composition, and energy spectrum of cosmic rays at particle energies above 10^{19} eV. Since the particle flux drops from more than $1000/\mathrm{m}^2/\mathrm{s}$ at 10^9 eV to $1/\mathrm{m}^2/\mathrm{yr}$ at 10^{15} eV and further to about $1/\mathrm{km}^2/100\,\mathrm{yrs}$ at 10^{20} eV [1], direct detection methods become impractical at about 10^{14} eV. Consequently, the instrumentation developed over the past decades observes the primary particle indirectly by measuring properties of the extensive air shower of particles that is initiated by the collision of the primary particle with molecules in the upper stratosphere. Driven by results by different experiments on energy scale and spectrum, particle origin and mass composition, the scale and complexity of cosmic ray detectors and the analysis of cosmic ray data has grown considerably.

Extensive Air Showers

The use of the atmosphere as a giant calorimeter is a well-established technique to measure the highest energy cosmic rays known to exist. At these energies, extensive air showers are the only way to study cosmic rays. In this section, the phenomenology, detection techniques and basic analyses of cosmic ray observables are described. Our current knowledge about those observables will be presented in the next section.

Phenomenology

When a cosmic ray particle enters Earth's atmosphere, several billions of secondary particles are produced in hadronic interactions with molecules of the air. This cascade of particles can generally be divided into three sub-showers, the electromagnetic, muonic and hadronic parts. If the primary particle is a hadron, the hadronic sub-shower feeds the other two cascades. In Fig. 2.1, the components of a hadron-induced cosmic ray air shower are shown. The primary particle interacts with air molecules, producing mostly pions and a few kaons in hadronic interactions. Neutral pions decay into two photons, feeding the electro-magnetic cascade. Charged pions interact further or decay primarily into muons and neutrinos. These neutrinos cannot be measured with air shower detectors, they remove "invisible energy" from the shower. The average life time of a muon is $2.197\,\mu\mathrm{s}$ [2], but most of them do not decay before reaching the ground due to Lorentz boost. Besides keeping the

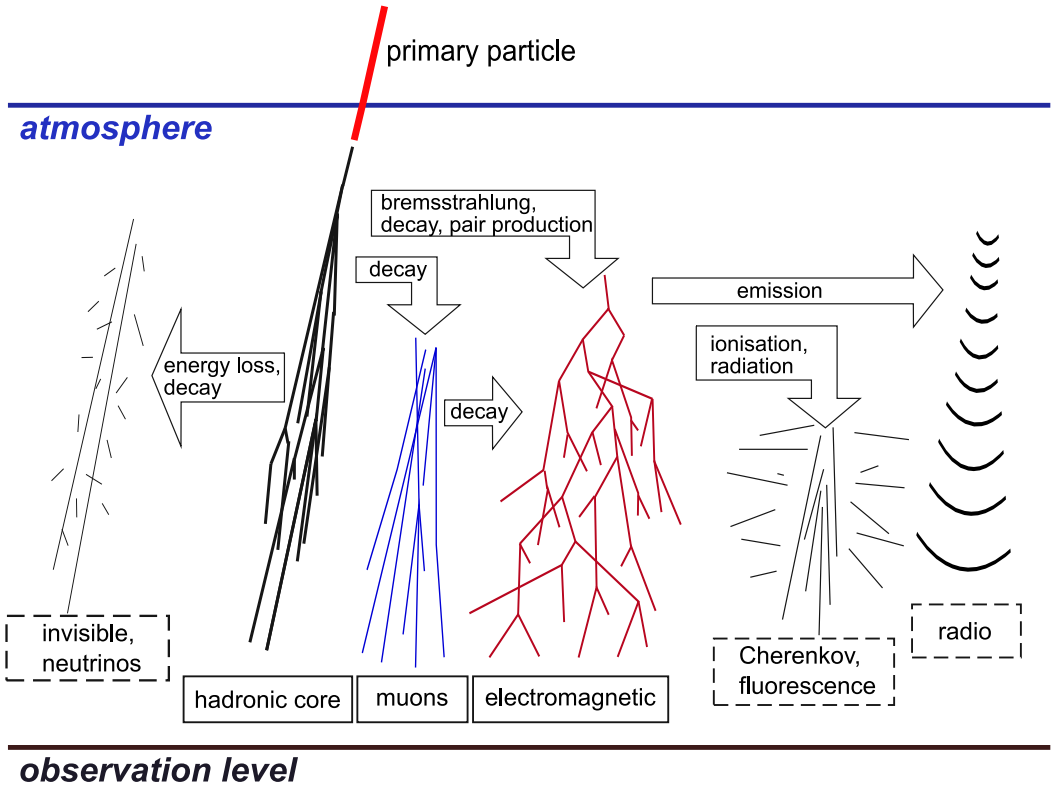

Figure 2.1: Components of an hadron-induced extensive air shower. Neutral pions produced in interactions of the primary with molecules of the atmosphere can interact with another air molecule or decay and feed the electro-magnetic component, charged pions decay into muons and neutrinos. The secondary electrons excite nitrogen molecules that emit fluorescence photons, the charge separation of electrons and positrons produces emissions in the radio frequency range. Some of the particles in the shower travel faster than the speed of light in air, producing Cherenkov photons. Taken from [3].

electro-magnetic cascade going, the secondary electrons excite nitrogen molecules that produce an isotropic emission of fluorescence photons. The particles of the air shower traveling faster than the speed of light in air produce forward-peaked Cherenkov light. Finally, charge separation in Earth's magnetic field and interactions in the plasma of the shower disk lead to radio wave emissions in the MHz and GHz regime.

To gain a comprehension of the phenomenology of hadronic air showers, first the electro-magnetic shower has to be understood. A simple model to describe a shower is the Heitler model [4], for simplicity vertical incidence is assumed. In Fig. 2.2, left panel, a schematic of the Heitler model is shown. The cascade is started by a particle with energy E_0 and is propagated mostly through two processes, bremsstrahlung of electrons and positrons and pair production by photons. This results in a doubling of the number of particles for every generation n, the number of particles per generation is 2^n. On average, the next interaction takes place after one radiation length of $X_0 \approx 37\,\mathrm{g\,cm^{-2}}$.

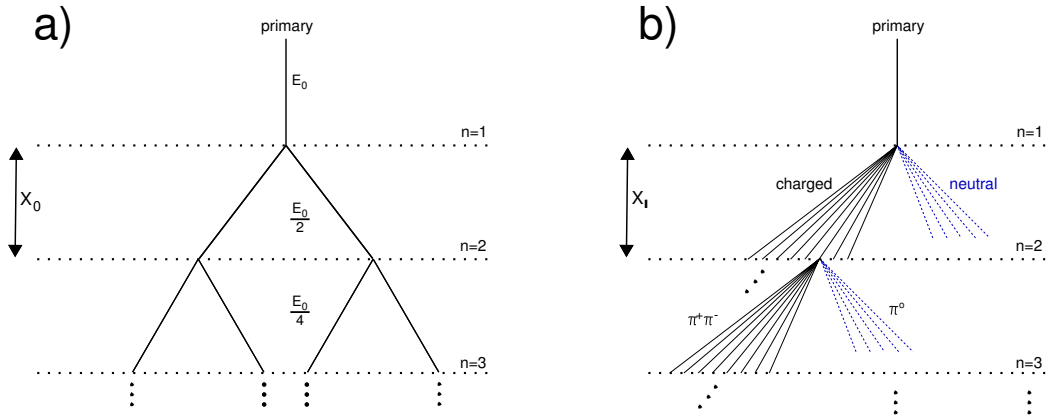

Figure 2.2: A schematization of the Heitler model [4] for electromagnetic showers (a) and the modified model for hadronic showers (b). Taken from [3].

The exponential rise in number is counteracted by radiative and ionization losses, resulting in the absorption of particles in the atmosphere through which they are lost to the cascade. If the mean energy of the electrons reaches a critical energy E_c of about 85 MeV, both processes have equal probability and the maximum of the shower is reached. Afterwards, energy losses predominate and the cascade dies out. The number of particles at this point N_max and the atmospheric depth of the shower maximum X_max are

$$\begin{aligned} N_\mathrm{max} &= \frac{E_0}{E_\mathrm{c}} \quad \text{and} \\ X_\mathrm{max} &= N_\mathrm{max} \cdot X_0 = \ln\left(\frac{E_0}{E_\mathrm{c}}\right) \cdot \frac{X_0}{\ln(2)}. \end{aligned} \tag{2.1}$$

The number of particles at the shower maximum is proportional to the primary energy.

It is possible to adapt this simple model to hadronic showers. While it is possible to produce muons and even hadrons in electro-magnetic cascades, their numbers are about one or two orders of magnitude smaller than those of hadron-induced showers [1]. In Fig. 2.2, right panel, a schematization of an hadronic shower is given. In every generation, two charged and one neutral pion are created. Neutral pions decay almost immediately into two photons and are lost to the hadronic cascade. Charged pions interact with another air molecule until the interaction cross section is smaller than the probability of a decay.

For a proton-induced shower, n_tot new particles are produced on average, each with an energy of E_0/n_tot. The depth of the shower maximum of the hadron-induced shower is approximately given by the maximum of the subsequent electromagnetic shower. However, the electromagnetic component starts to develop with an initial energy of E/n_tot after the first interaction of the primary particle with the atmosphere, which is given by the hadronic interaction length X_I,

$$X^\mathrm{p}_\mathrm{max}(E_0) \approx X_\mathrm{I} + X_0 \cdot \ln\left(\frac{E_0}{n_\mathrm{tot} E_\mathrm{c}}\right). \tag{2.2}$$

If the primary particle is a nucleus with mass A, $X_{\max}$ can be estimated by using a superposition model, treating the air shower as A fractional proton-induced showers with a lower primary energy E_0/A,

$$X^A_{\max}(E_0) \approx X^{\mathrm{p}}_{\max}(E_0/A) = X^{\mathrm{p}}_{\max}(E_0) - X_0 \cdot \ln A. \tag{2.3}$$

For the same primary energy, the position of shower maximum is higher in the atmosphere for heavier primaries. Because the iron shower develops higher in the atmosphere, the number of photons and electrons at ground level is reduced, compared to a proton shower. The initial energy of the fractional showers for iron primaries is lower, the produced pions decay into muons at a higher altitude. The number of muons is increased for the iron-induced shower. The higher number of sub-showers in an iron cascade also reduces statistical fluctuations when comparing two showers of identical primary.

Detection of Air Showers

For the measurement of air showers, many techniques and technologies have been developed over the years. In principle, two different approaches are used. One measures a snapshot of the secondary particles of the shower development at the ground. The other method is to observe parts of the shower development in the atmosphere. Both techniques have advantages and difficulties, which is why a hybrid concept combining several techniques in one observatory is favored.

Surface detectors sampling the shower particles at ground were the first detectors used to measure air showers. Simple Geiger-Müller counters were used by Pierre Auger for his pioneering work in 1938 [5]. More recent arrays were built using scintillation counters, e. g. Volcano Ranch [6], Yakutsk [7], KASCADE-Grande [8], AGASA [9] and Telescope Array [10], or using Cherenkov detectors, e. g. Haverah Park [11] and the Pierre Auger Observatory [12]. A large advantage of surface arrays is their theoretical duty cycle of 100%. The detectors are spaced out over a large area to measure the footprint of the particle cascade. The distance and the total area is designed for the targeted energy range of cosmic rays. Lower energy particles are more abundant but produce small footprints on the ground, so a dense but small array is needed. At the highest energies, the cascades are still spread out over large areas on the ground, but statistics are so low that huge areas need to be covered.

From the precise timing information of several triggered ground stations, the arrival direction and core of the shower can be reconstructed very accurately. Using comparisons with Monte Carlo simulations, energy estimators can be developed. The determination of the position of the shower maximum $X_{\max}$, which is related to the measurement of the mass of the primary, is rather difficult since it cannot be measured directly. One possibility to estimate the mass of the primary particle is to measure the electro-magnetic and the muonic component of the air shower separately, since the muon-poor showers are initiated by heavier elements and muon-rich showers by light primaries. This was done by both the KASCADE-Grande and the Yakutsk experiments. In recent studies, several other mass-sensitive observables have been identified.

A different method of observing the air shower is possible through the isotropic emission of nitrogen fluorescence. Nitrogen molecules of the air are excited by passing secondary particles of the shower and de-excite by emitting photons in the UV

range. The pioneer experiment to exploit this detection technique was Fly's Eye [13] and its successor HiRes [14]. Building on the success of both experiments, the Pierre Auger Observatory and the Telescope Array use fluorescence telescopes to supplement their surface detectors and create true hybrid observatories, capitalizing on the advantages of both techniques.

The major advantage of the fluorescence technique is the possibility to observe a large part of the air shower development from the side. From the gathered light, the number of particles and the deposited energy at a certain atmospheric depth can be calculated using the yield of fluorescence photons and the attenuation of the photons on the way between shower axis and detector. The inherent difficulties and methods to estimate these corrections for the attenuation are the subject of this thesis and will be discussed in more detail in the following chapters. The determination of energy, $X_{\max}$ and arrival direction as well as the hybrid methodology will be covered in Sec. 3.2.

Radio Emissions in the MHz and GHz Regime

Charged secondary particles of cosmic ray air showers, mostly electrons and positrons, are deflected by Earth's magnetic field. This charge separation produces geo-synchrotron emissions in the radio range. The strength of the signal is related to the energy of the air shower and since radio waves are marginally attenuated in the atmosphere, it is possible to measure the radio waves on the ground using radio antennas. A major drawback is the high radio noise background associated with populated areas. It was only possible to reliably use this method after progress in digital signal processing in the past couple of decades.

The proof of principle was shown by the LOPES experiment [15] and since then, several other installations have been taking data in coincidence with proven air shower detectors. It was demonstrated, that an autonomous detection of air showers using radio emissions is possible [16], and a large air shower array is being built in Argentina [17] to fully investigate this new technique and its potential use in future cosmic ray observatories.

Two mechanisms of microwave emissions from air showers are being investigated at the present time. The first mechanism is the isotropic emission of GHz radiation from the plasma of electro-magnetic particles in the air shower disk in the form of molecular bremsstrahlung radiation [18]. In a laboratory setting, this emission was seen as strong enough to be used to measure cosmic ray air showers above the background. Two more laboratory experiments at accelerator facilities, one at Fermilab [19] and one in Frascati [20], are being carried out, trying to validate this result. The second possible emission scenario is the extension of the geo-synchrotron effect, responsible for the MHz radio emissions, into the GHz regime. This would most likely restrict the detection of this emission to very special shower geometries. A combination of both mechanisms is also conceivable.

The CROME experiment [21], set up in Karlsruhe and colocated with the KASCADE-Grande detector, measured first microwave signals [22] in coincidence with air showers detected by KASCADE-Grande. Further investigations are underway. At the site of the Pierre Auger Observatory, two microwave detectors are already taking data and more are planned [23], see also Sec. 3.3.

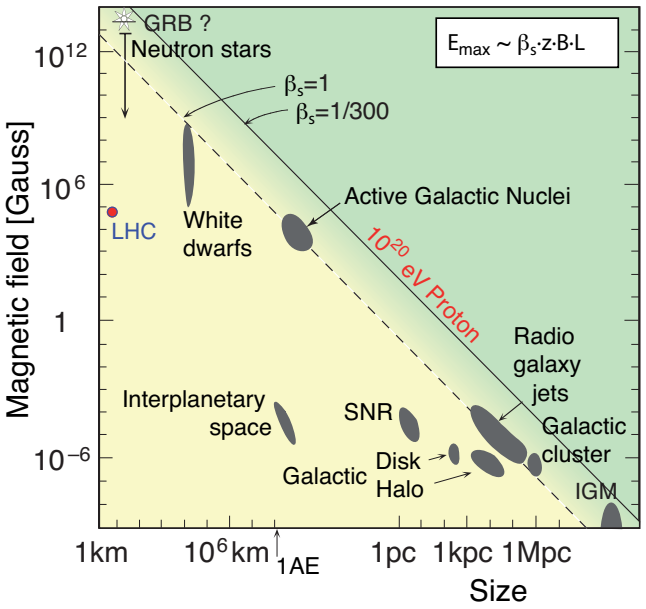

Figure 2.3: The Hillas plot of astrophysical sources that are possible accelerators for cosmic rays [1]. Shown is the magnetic field inside a source versus the relative size of the active region. The LHC at CERN is drawn in comparison.

Cosmic Rays

Where do cosmic rays come from? What is the energy spectrum of cosmic rays? What is their mass composition? These are just the fundamental questions that arose in the last 100 years, ever since Victor Hess discovered them in 1912 [24]. Later, it was discovered that these rays are not actually rays, but charged particles that are deflected by magnetic fields. Our understanding of cosmic rays grew substantially since then, and those questions could be answered for energies up to 10^{18} eV with balloon-borne, satellite and ground-based detectors. In the ultra-high energy regime above 10^{18} eV, the answers are very hard to come by. The rapidly decreasing flux requires giant ground arrays of several thousand square kilometers running for many years to collect enough data. In the following sections, the results of several decades of cosmic ray research are summarized and recent results from current cosmic ray detectors are presented.

Acceleration and Propagation

Before possible sources of cosmic rays can be hypothesized, theories of mechanisms that are capable of releasing particles at energies at which we observe them are needed. In general, two basic principles are possible, bottom-up processes accelerate particles from lower to higher energies, while in top-down scenarios super-heavy exotic particles decay, leaving the secondary particles with large kinetic energies. Theoretical candidates for such exotic particles are topological defects, dark matter and others [25].

Acceleration of cosmic rays is possible with the Fermi mechanism [26]. When a plasmas interacts with the surrounding medium, e. g. in the bow of a supernova

shock front or the regions around massive black holes, particles can be accelerated by the associated magnetic fields. The maximum energy up to which this mechanism is capable of accelerating particles depends on the size of the active region L, the strength of the magnetic field B and the velocity of the shock wave β_s. In Fig. 2.3, the Hillas plot [27] is shown, putting those two quantities in relation. A wide range of possibilities is found. For cosmic rays with energies up to 10^{17} eV, remnants of supernova explosions were identified as likely source [28]. Particles of energies below 10^{18} eV are confined to the galaxies by the galactic magnetic fields. Measurements of radioactive isotopes in cosmic rays [29] show that they traverse the galaxy for several million years before haphazardly colliding with the Earth.

At energies above 10^{18} eV, no known sources within our galaxy exist. The particles are only slightly deflected by galactic magnetic fields and cannot be confined inside our galaxy, they have to be of extragalactic origin. Using the Hillas plot (Fig. 2.3) again, only a few sources remain that are capable of accelerating these particles, most noticeable Active Galactic Nuclei (AGN), Gamma Ray Bursts (GRB) and radio lobes of FR II radio galaxies [30].

Compton scattering and synchrotron radiation are of minor importance to charged cosmic rays particles. The interaction with photons of the Cosmic Microwave Background radiation (CMB) on the other hand can lead to significant energy losses due to secondary particle production. At an energy of about 5×10^{19} eV, protons can interact with CMB photons to form a Δ^+ resonance, which in turn decays into a nucleon and a pion. The proton loses about 20% of its energy in this process [31, 32]. For ultra-high energy cosmic rays this process is repeated until the energy drops below the threshold energy of pion production. This suppression of high energy cosmic rays is called GZK effect. For heavier nuclei, photodisintegration is the predominant process of energy loss. Already at energies of 10^{17} eV, the CMB photon interacts with both heavy and light particles to produce electron-positron pairs. The energy loss due to this process is smaller than the energy loss associated with the GZK effect.

Energy Spectrum

The energy-dependent flux of cosmic rays is well-known over 11 decades in energy, starting a few hundred MeV where their source is the sun and the flux shows a modulation depending on the solar cycle. The flux above 10 GeV is shown in Fig. 2.4. At first glance, it looks like an almost featureless $E^{-\gamma}$ decline. But closer examination of the data reveals distinct changes in the spectral index indicating changing acceleration mechanisms and a varying composition of cosmic rays. At about 3–5×10^{15} eV, a steepening of the spectrum is visible, the so-called knee. It was shown that this feature is due to a significant decrease in the flux of lighter particles like protons and Helium nuclei [33]. A possible explanation is the limited capability of galactic accelerators to effectively confine lighter particles at these energies, they escape the acceleration region. Heavier elements like iron are easier confined by the magnetic fields of the accelerators due to their higher charge number. At a certain energy, however, also the heavier particles escape, causing a second steepening of the spectrum at 8×10^{16} [34].

At higher energies, the exponent γ of the energy spectrum increases for a small range in energy before going down again. In Fig. 2.5, two spectra are shown at

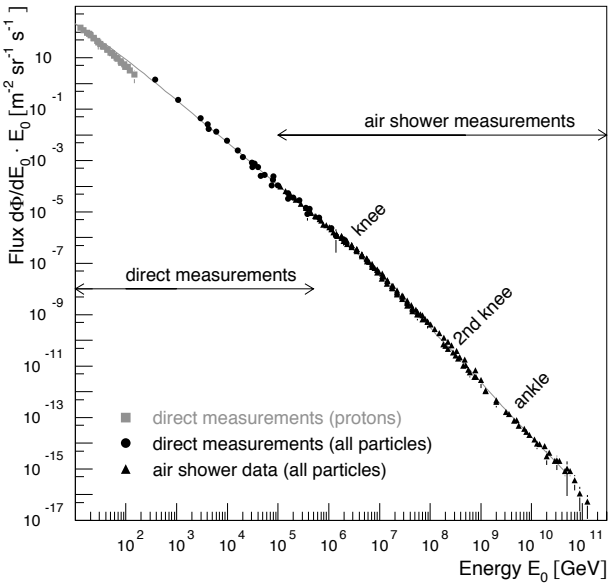

Figure 2.4: The energy spectrum of cosmic rays from 10 GeV up to about 100 EeV [1]. At low energies, the measurements are done by observing the primary particle in balloon-borne or satellite detectors. At energies above 10^{14} eV, also indirect measurements of ground-based detectors are possible, while at energies above 10^{15} eV only indirect measurements are feasible. Several features are visible, the knee at about 3–5 $\times 10^{15}$ eV, the second or iron knee at about 10^{17}, the ankle at about 4×10^{18} eV and finally a flux suppression at around 5×10^{19} eV. Details see text.

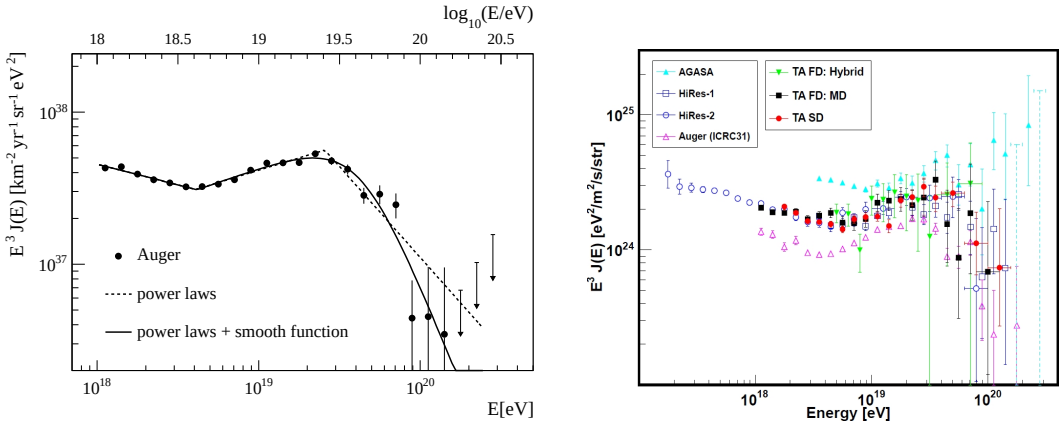

Figure 2.5: The energy spectrum of cosmic rays at the highest energies as measured by the Pierre Auger Observatory [35] (left panel) and the Telescope Array [36] (right panel). In both spectra, the ankle and the flux suppression at highest energies are visible. In the right panel, several additional spectra are superimposed, they agree within their systematic uncertainties (not pictured) given by the collaborations. Only the AGASA spectrum (blue triangles) does not include a flux suppression.

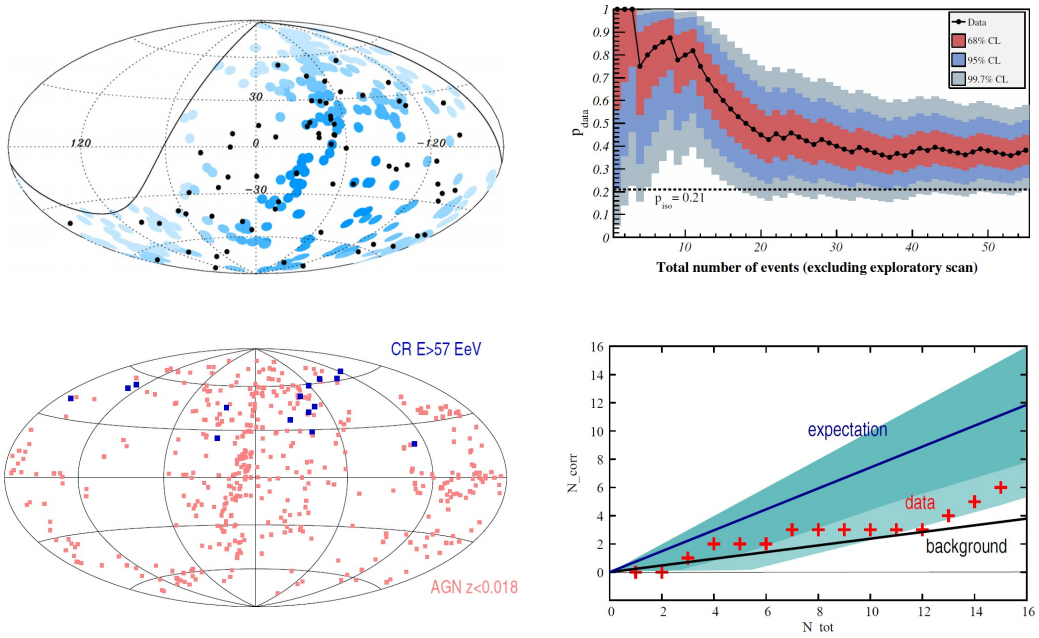

Figure 2.6: Maps of the arrival directions superimposed on maps of close-by Active Galactic Nuclei on the left and correlation studies on the right for data measured at the Pierre Auger Observatory [43] (top) and at the Telescope Array [44] (bottom).

the highest energies. In the left panel, the most recent combined spectrum of the Pierre Auger Observatory [35] can be seen. On the right, the latest spectrum of the Telescope Array [36] is depicted, other spectra are superimposed for comparison. They agree within the systematic uncertainties stated by the experiments. The first feature at lower energy is called ankle. It was determined using data of the Pierre Auger Observatory to be at about 4×10^{18} eV [37]. Two theories have been put forward, the first assumes a transition from galactic to extragalactic cosmic rays [38]. According to the second theory, the interaction of extragalactic cosmic rays with the CMB to form electron-positron pairs is responsible. The particles above a certain energy would lose energy and a dip in the spectrum below this threshold would form [39]. Above 4×10^{19} eV, a suppression is observed [40, 41], roughly at the energy predicted for the GZK effect. However, this decrease in the flux might also be caused by the maximum injection energy of the cosmic ray sources [42].

Arrival Directions

The sources of ultra-high energy cosmic rays are still one of the great mysteries of cosmic rays. On the one hand, these particles only suffer relatively small deflections in the galactic and intergalactic magnetic fields. Their reconstructed direction should roughly point back to their source. On the other hand, the GZK effect creates an energy-dependent horizon of about 200 Mpc for particles above the GZK threshold. Particles coming from farther distances would have lost their energies in interactions with the CMB. Therefore, it might be possible to measure anisotropies in the arrival directions of cosmic rays above 5×10^{19} eV or correlations of the directions with catalogs of known astronomical objects in the close-by universe.

The arrival directions of 69 events measured by the Pierre Auger Observatory

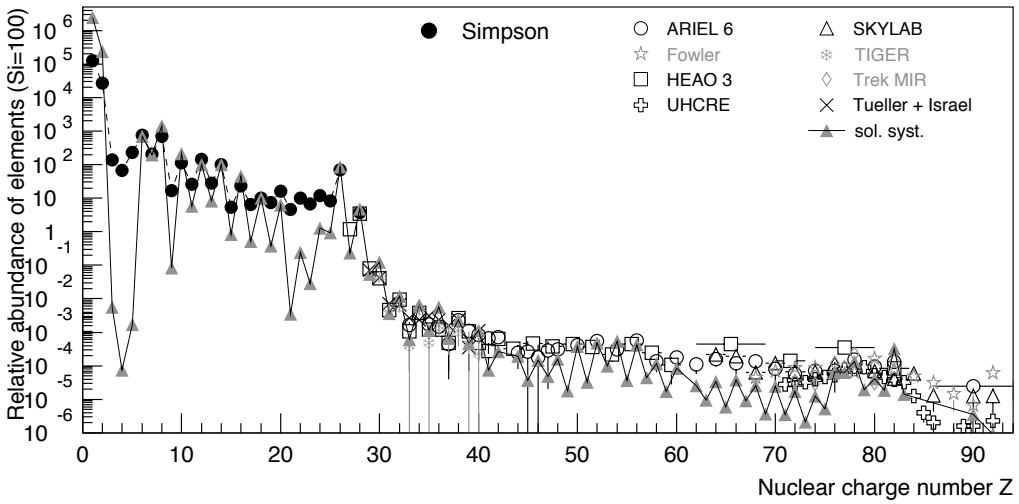

Figure 2.7: Abundance of elements in cosmic rays at energies of about 1 GeV/n [1]. The data are normalized to Silicon. Superimposed is the abundance of elements in the solar system (gray triangles).

above 5.5×10^{19} eV are shown in Fig. 2.6, top left panel. Also shown are locations of Active Galactic Nuclei (AGN) within 75 Mpc with a smearing of 3.1°, accounting for small deflections in magnetic fields [43]. Due to the GZK effect, particles at these energies or higher cannot reach us from distances larger than 200 Mpc, the correlation was found to be best in a range below 75 Mpc. The directions of the cosmic rays seem to correlate with the AGNs, and isotropy could be rejected with 99% confidence, see Fig. 2.6, top right panel.

A similar study was performed with the data of the Telescope Array in the Northern Hemisphere. In Fig. 2.6, bottom left panel, all 15 events with energies larger than 5.7×10^{19} eV are shown on a map of local AGNs. Using the same parameters as the study done for the Pierre Auger Observatory, a blind test was performed and the expectation value of the analysis of the Pierre Auger Observatory was not met [44], see Fig. 2.6, bottom right panel. However, since the statistics of only two years of data taking is rather low, both the level of anisotropy found in data of the Pierre Auger Observatory and complete isotropy are within the uncertainties.

More detailed studies of point sources have also been performed, especially of multiplets in the arrival directions that might be coming from the same source. The closest radio galaxy is Centaurus A with a distance of 4 Mpc. An excess of particles has been measured from 18° around its direction, rejecting the possibility of an isotropic distribution [43]. Additionally, large scale anisotropies have been studied [45] at energies above 2.5×10^{17} eV, but no evidence could be found.

Mass Composition

The abundance of elements within the cosmic rays have been studied quite precisely at lower energies where a direct measurement of the primary particle is possible. In Fig. 2.7, the distribution of elements at about 1 GeV per nucleon is shown as

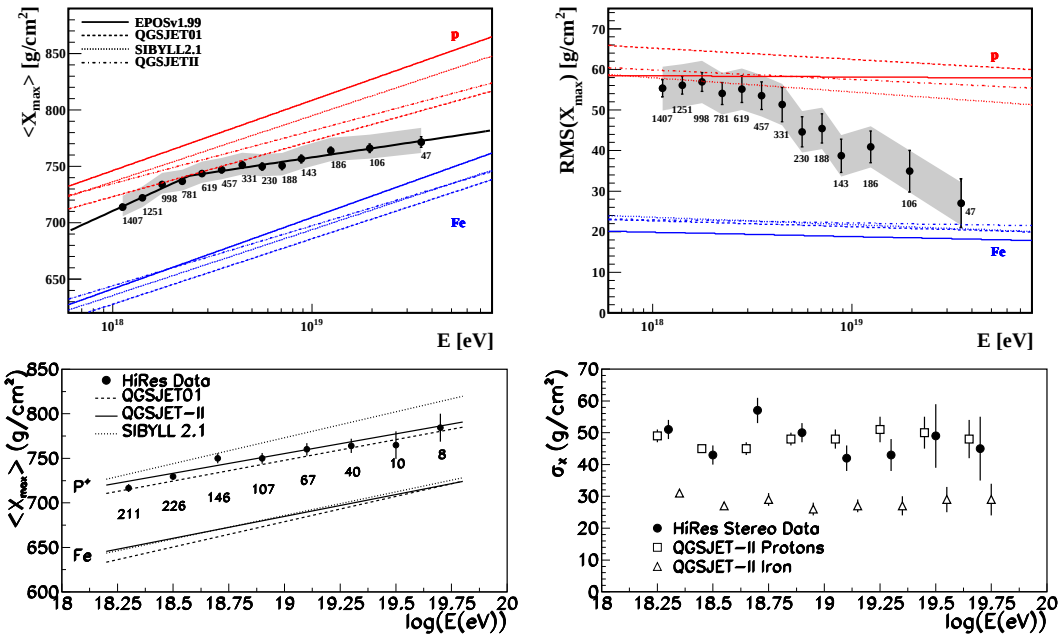

Figure 2.8: Measurement of $\langle X_{\max} \rangle$ and the RMS of the $X_{\max}$ distribution as measured by the Pierre Auger Observatory [46] (top) and the HiRes experiment [47] (bottom).

measured by several experiments [1]. Superimposed is the abundance of elements within the solar system. Both spectra agree quite well except for the regions below carbon ($Z = 6$) and below iron ($Z = 26$), where the abundance in cosmic rays is much larger than the regional occurrence would suggest. This can be attributed to spallation processes of the CNO group and the elements around iron in interactions with galactic matter.

The picture is less clear in the energy region around the knee. It is possible to reconstruct individual spectra for different elemental groups [33] and infer the mass composition from those results. At the highest energies, statistics and detection techniques are more limited, and individual spectra are not feasible. However, knowing the chemical composition is important to distinguish between several acceleration and propagation scenarios, as discussed above. It is possible to estimate an average composition at different energies from the measured shower development.

As was described in Sec. 2, the atmospheric depth of the shower maximum $X_{\max}$, measured in $\mathrm{g\,cm^{-2}}$, is sensitive to the mass of the primary particle. Due to the statistical nature of those processes, information about the mass cannot be gathered on a shower-to-shower basis, conclusions can only be drawn from averages of $X_{\max}$ of larger samples. For the same reason, the RMS of the $X_{\max}$ distribution is a good estimator of the mass of the cosmic ray particle.

In Fig. 2.8, $\langle X_{\max} \rangle$ and the RMS of $X_{\max}$ for several energies are shown. On the top, the results from the Pierre Auger Observatory [46], on the bottom the results from the HiRes experiment [47]. The data points have to be compared with simulations of air showers assuming pure elemental compositions. Such simulations are very dependent on the choice of hadronic interaction model and other factors. In Fig. 2.8, several models were used to create reference lines corresponding to pure

iron and pure proton expectations. The data from the Pierre Auger Observatory suggests a trend from lighter primaries at lower energies towards heavier elements at the highest energies, both in $\langle X_{\mathrm{max}} \rangle$ and the X_{max} RMS. However, the data from HiRes are compatible with a light composition at all energies. A preliminary result from the Telescope Array experiment [10] also favors a light composition, but the uncertainties also include the possibility of a mixed to heavy composition at highest energies. For a final answer, more data are needed and the hadronic interaction models have to be consolidated at higher energies.

Neutrino and Photon Flux

Several production scenarios of high-energetic neutrinos are associated with cosmic ray acceleration in the dense regions around massive black holes. Measuring these neutrinos in the cosmic ray flux would give evidence of cosmic ray sources, since the neutrinos would travel straight from their production. Other processes of neutrino production occur during cosmic ray propagation, e. g., the pions produced in interactions of protons with CMB photons decay into muons and neutrinos. So far, no high energy neutrinos have been found in the data of the Pierre Auger Observatory [48] or the Telescope Array [49], but very strict limits were set that can compete with the limits set by dedicated neutrino experiments.

Similar studies are done to look for photons in the data. High energy photons are expected from the interactions during propagation of ultra-high energy cosmic rays, but also from certain cosmic rays production scenarios. Again, only upper limits of the photon fraction in the cosmic ray flux could be set, both using data of the Pierre Auger Observatory [50] and of the Telescope Array experiment [49].

Chapter 3

The Pierre Auger Observatory and Beyond

The Pierre Auger Observatory is located in Argentina, close to the small town of Malargüe at the foothills of the Andes. To measure extensive air showers initiated by cosmic rays, the Observatory employs a multitude of different detectors and detection techniques. In its basic design, the Observatory consisted of two detectors, a large-aperture Surface Detector (SD) and a Fluorescence Detector (FD) at the periphery of the SD array. Since then, several extentions have been implemented. A large array to detect the radio emission of air showers, several detectors to measure microwave emission and underground muon detectors are among them. Additionally, the Observatory is an ideal place for interdisciplinary science. The properties of the atmosphere like the measurement of the state variables and aerosol properties are an important task of the monitoring of the Pierre Auger Observatory and will be covered in detail in the following chapters. Furthermore, the detectors and the infrastructure of the Observatory can be used to study solar physics, volcanoes and seismic activities in the Andes, as well as lightning.

3.1 The Surface Detector (SD)

The large-area SD array consists of approximately 1 650 individual stations [51, 52] on an area of 3 000 km^2. The detector stations are spaced 1.5 km apart on a triangular grid. Each detector is a 12 000 liter water Cherenkov tank equipped with three photomultiplier tubes. The secondary particles of air showers reaching the ground produce Cherenkov light when they travel through the water with a speed that exceeds the speed of light in the medium. This light is reflected from a lining inside the tank walls towards the PMTs on top of the tank.

Each station is calibrated internally by muons that traverse the tank vertically. The mean signal of such a muon defines the unit 1 VEM, vertical equivalent muon. If a signal at one station exceeds a certain threshold for a certain time, this detector sends its information to the Central Data Acquisition System (CDAS). If triggered stations in the direct neighborhood are found, the data by all close-by stations is read out by CDAS and stored at the Central Campus. A high-quality event, which is the basis requirement to be used in physics analyses of the Pierre Auger Observatory are based, is found if the station with the highest signal is surrounded by a hexagon

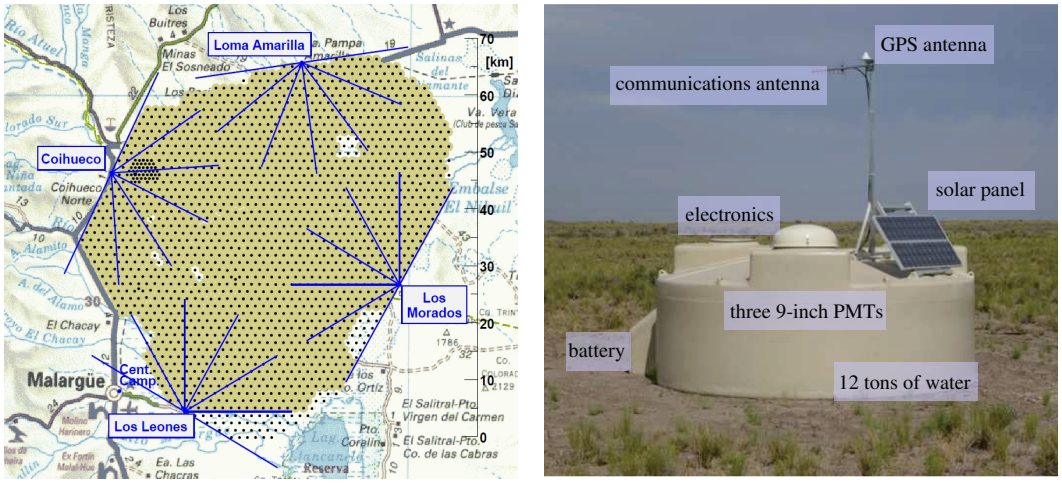

Figure 3.1: The Pierre Auger Observatory as of January 2012. Every black dot in the shaded yellow area represents an active Surface Detector (SD) station that is equipped with electronics and filled with water. The black dots outside the yellow are theoretical tank positions where for different reasons no tank was placed or a tank was removed and put somewhere else in the array. On the periphery of the SD array, the locations of the four FD sites are drawn. On the right, a closeup of an SD tank is pictured. The electronics are housed in the hemispherical cover on top, the solar panels and the batteries supply the power and the antenna transmits the data to the closest FD site, from where it is rerouted to the Central Campus.

of working stations that also triggered.

The SD has a duty cycle of almost 100%, measurement time is not limited by external factors but only by outages of single stations due to electronic failures or other damage. A drawback of the SD is that the energy of the primary particle cannot be determined accurately. The stations only sample the air shower at ground level, which highly depends on the development of the shower in the atmosphere. Using Monte Carlo simulations, the development and the resulting SD signal is modeled for a large set of air showers in order to find energy estimators from SD data. However, the Pierre Auger Observatory is a hybrid detector. Since the FD can measure the energy of the shower directly, see Sec. 3.2, the SD energy scale can be fixed using shower events that were recorded by the SD and the FD in unison [53], see Fig. 3.2. The full efficiency for vertical showers is reached at about $10^{18.5}$ eV.

The SD was supplemented with a hexagonal infill array of 23.5 km^2 where 49 additional tanks are placed halfway between two other tanks, reducing the distance between tanks to 750 m to enable the measurement of showers with lower energy down to about $10^{17.5}$ eV [54]. The infill is indicated in Fig. 3.1, close to the FD site Coihueco in the west. An even smaller infill array of 5.9 km^2 with a spacing of 433 m is planned, potentially lowering the efficiency threshold down to about 10^{17} eV.

3.2 The Fluorescence Detector (FD)

Four Fluorescence Detector (FD) stations measure the isotropically emitted fluorescence light from air showers at the periphery of the SD array [55], pictures of the

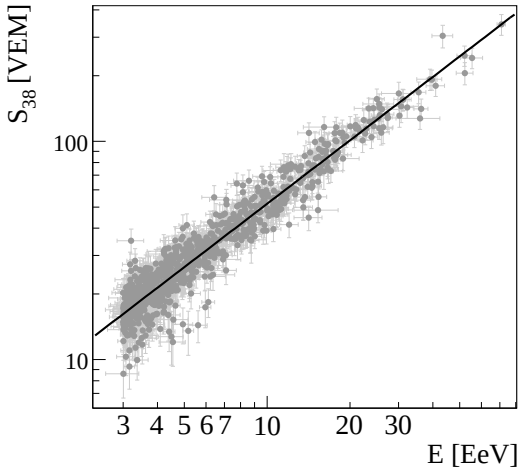

Figure 3.2: Calibration of SD energy scale using hybrid events measured with both the FD and SD [53].

Figure 3.3: The Fluorescence Detector (FD). On the left, the FD site at Coihueco with the more recent HEAT telescopes in the foreground and a LIDAR station in the background. The inside of a telescope is shown on the right. The light enters through the aperture at the left and is reflected off the mirror onto the PMT camera in the middle.

outside and inside of a telescope building can be seen in Fig. 3.3. The four sites are Los Leones (LL) in the south, Los Morados (LM) in the east, Loma Amarilla (LA) in the west and Coihueco (CO) in the west, see also on the map of the array in Fig 3.1. Each station is composed of six telescopes. The light enters the telescope through a 2.2 m diameter aperture which is equipped with a corrector ring to correct for spherical aberrations at the edge of the aperture. The photons are then reflected from a large segmented mirror onto a camera made up of 440 hexagonal PMTs, arranged in 20 rows by 22 columns. Each pixel of the PMT camera covers a field of view about $1.5^\circ \times 1.5^\circ$. The whole camera covers about $30^\circ \times 30^\circ$ and is arranged so that it covers a range of 2° to 32° in elevation. The six telescopes of every station combined cover 180° in azimuth.

In August 2009, three additional High Elevation Auger Telescopes (HEAT) started taking data [56]. They are mounted close to the Coihueco detector in individual containers that can be tilted upwards by 30°, see the left picture of Fig. 3.3. This enables HEAT to observe showers higher up in the atmosphere, therefore lowering the threshold energy. HEAT is a standard part of data taking and is used to measure low energy showers with good precision and, together with the data recorded at Coihueco as a virtual FD detector, can cover high energy showers up to 60° in elevation. This enables an unbiased measurement of the shower maximum to lower energies, making composition studies at those energies possible. HEAT overlooks the SD infill and a smaller infill called HEATlet (see Fig. 3.1, west of the infill) closer to the FD station to enable hybrid measurements at low energies.

The FD is only operated during nights with low illuminated moon fraction, otherwise the telescopes are overwhelmed by background light. Additionally, wind has to be moderate and no rain is required in order to operate the FD safely. These conditions can differ across the large array, so one site might not take data due to unsuitable conditions while the others operate normally. These restrictions limit the duty cycle of the FD to about 12% [57].

An important aspect of FD operations is the slow control. Since the stations are separated by tens of kilometers, it has to be possible to control everything from the Central Campus, with safeguards in place to make sure the connection is stable and, in emergency cases, take the necessary precautions to preserve the detectors. Under normal operational conditions, the slow control system is used to power up the camera, this includes the low and high voltage for the PMT power supply, opening the shutters and sending commands to the calibration systems. If the light background of a camera or a single pixel is too high or the weather changes so that FD operations are not possible anymore, the shutters are closed and a curtain can be dropped in front of the aperture in case the shutter fails.

The data acquisition for each camera is mounted in a crate with power supply and a cooling fan. It houses 20 First Level Trigger (FLT) boards, each connected to a analog board, and one Second Level Trigger (SLT) board. One FLT board with 22 channels is used per vertical column. The FLTs digitizes the signals from each PMT and checks all channels if their signal is above a certain threshold and marks the pixel as triggered if necessary. The digitization bin width of the FLTs for the standard telescopes (for HEAT) is 100 ns (50 ns), corresponding to 10 MHz (20 MHz). The SLT collects the trigger data from the FLTs, combines them to a single event and looks for patterns in the triggered pixels across the camera that resemble patterns produced by air showers, see Fig. 3.4, left panel. If a pattern is found, adjacent pixels to the trace are read out to make sure the shower is well contained in the recorded data. The information is then sent to a central computer for each FD site. On this computer, a software rejects obvious background events like lightning and electronic noise forming a third level trigger. This T3 is then sent to the Central Campus, where a readout of the quarter of the SD array in front of the FD site generating the T3 is initiated to make sure possible hybrid FD-SD events are recorded that would otherwise not have triggered the SD on their own, resulting in the loss of that data.

The reconstruction of the arrival direction using data from a single FD site is rather imprecise, since only the shower detector plane defined by the image of the shower on the camera can be reconstructed accurately. The position of the axis

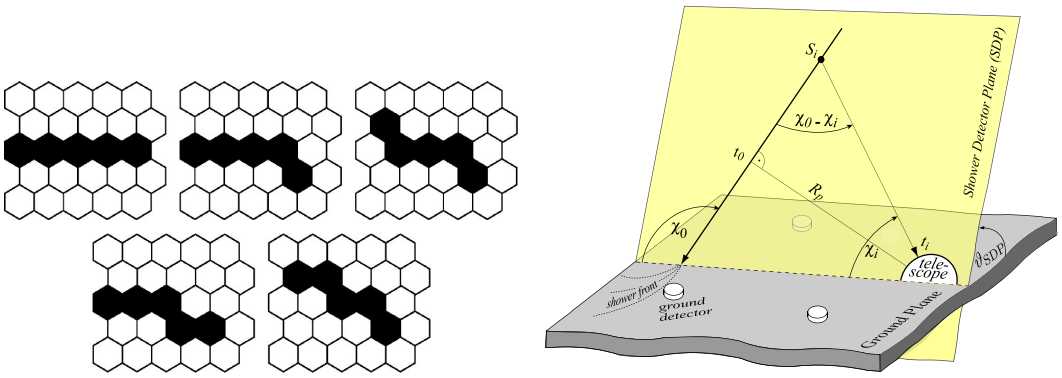

Figure 3.4: Left: Possible trigger patterns for the FD [12]. Right: Geometry reconstruction of hybrid events using timing and geometrical information from both SD and FD measurements.

within this plane has to be calculated from the viewing angles and detection times of single pixels. A reconstruction using information from two FD sites improves the accuracy. Using the information provided by the SD, a joint hybrid track reconstruction can be performed, see Fig. 3.4, right panel. Combining the shower detector plane of the FD with the very accurate detection of the shower core by the SD, it is possible to significantly improve the angular resolution of reconstructed hybrid events [58]. To make sure no SD data are discarded that might help in the hybrid reconstruction, the entire SD array close to a FD station that detected an air shower is queried for data. That way, single triggered SD stations are read out even though no surrounding stations triggered and no independent SD trigger was formed.

The flux of fluorescence photons reaching the FD telescope from the track of an air shower is proportional to the energy loss per unit slant depth X of traversed atmosphere, $\mathrm{d}E/\mathrm{d}X$ [59]. It is possible to make a calorimetric estimate of the energy of the primary cosmic ray particle by observing the number of photons and therefore the energy loss, after correcting for "missing" energy that is not recorded by the FD, mostly by neutrinos that do not deposit their energy in the atmosphere [60].

An example light profile recorded with the fluorescence telescopes is shown in Fig. 3.5. From the total light, direct and scattered Cherenkov light as well as multiple scattered light have to be subtracted in order to obtain the fluorescence light. To reconstruct the fluorescence light at the shower axis, the attenuation of the photons on their path to the FD by scattering and absorption has to be corrected for in order to estimate the energy of the shower correctly. For this reason, all ground-based cosmic ray observatories in the past had atmospheric monitoring programs of some kind. The Pierre Auger Observatory employs a unique and very extensive monitoring program which is the main scope of this work and will be described in much more detail later. Systematic uncertainties associated with the determination of the energy of the cosmic ray are mostly due to the uncertainties in the fluorescence yield (see Sec. 4.2). Additional uncertainties are due to the absolute detector calibration and its dependence on wavelength as well as uncertainties in the reconstruction procedure. A total systematic uncertainty of 22% is currently associated with the FD energy scale [37].

The determination of the position of shower maximum X_{max} is straightforward

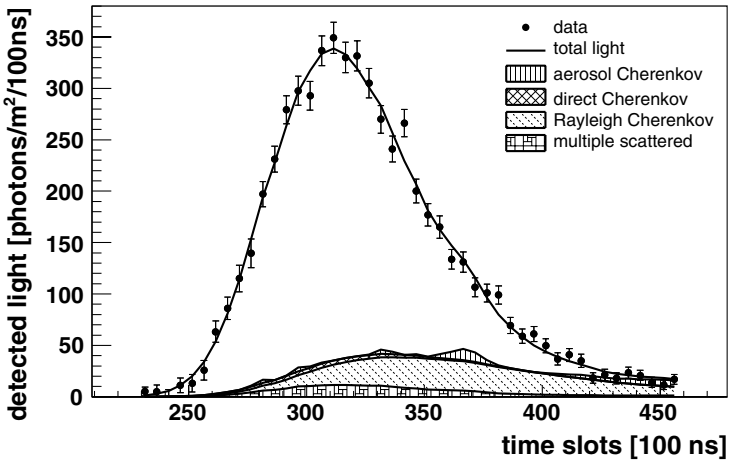

Figure 3.5: Reconstructed light profile measured by the FD [55]. Depending on the geometry, the total light consists mostly of fluorescence light. The remaining photons are Cherenkov light that reaches the telescope directly or either Mie or Rayleigh scattered. A small percentage is multiple scattered light that is scattered back into the field of view.

from the recorded light profile. Uncertainties are due to the choice of the atmospheric description in the conversion from measured height in meters to atmospheric depth in $\mathrm{g\,cm^{-2}}$. The calibration of the FD and the reconstruction procedure are also sources of systematic uncertainties. In total, the systematic uncertainty on the determination of $X_{\max}$ is $13\,\mathrm{g\,cm^{-2}}$ [61].

3.3 Extentions

The Auger Extensive Radio Array (AERA) measures the radio component of air showers in the 10–100 MHz range [17]. Currently, 21 radio stations are deployed close to the SD infill, since the energy range covered overlaps with that of the infill and the overlooking HEAT telescopes. In 2010, self-triggered pulses were measured for the first time. Until then, the trigger had to be provided by nearby SD tanks. In its final phase, AERA will cover about $20\,\mathrm{km^2}$ with 160 radio antennas.

Several approaches are used to measure microwave emissions from air showers in the GHz range [23]. Projects like AMBER (Air-shower Microwave Bremsstrahlung Experimental Radiometer) and MIDAS (Microwave Detection of Air Showers) use large diameter parabolic dishes to collect those signals, using triggers from the SD or HEAT to read out the electronics. A different approach is used by EASIER (Extensive Air Shower Identification using Electron Radiometer). Replacing one of the PMTs of a SD tank with an antenna and using the already existing SD infrastructure and communications, this method is very cost-effective and does not affect regular SD measurements. First measurements of signals in the microwave range were achieved by several of these projects, the results are as of yet inconclusive.

The aforementioned SD infill array, together with underground muon counters, is part of the Auger Muon and Infill for the Ground Array (AMIGA). The currently

deployed prototype array will consist of seven scintillation detectors, each with an area of $30\,\mathrm{m}^2$, buried at a depth of 2.3 m [54]. Each muon detector will be buried next to a SD tank with the possibility to trigger off the air shower signals from the SD station. A self-trigger mode is also implemented. With this enhancement, it will be possible to gain a better understanding of the muon content of air showers, which is coupled to the mass composition of the primary cosmic rays.

3.4 Interdisciplinary Science

The Pierre Auger Observatory is an ideal site for the detection of air showers, but in recent years its large potential for interdisciplinary science was exploited more and more. This includes the use of existing detectors for lightning and solar activity studies, but also the use of the Observatory's infrastructure to support dedicated measurement stations for other scientific fields. In April 2009, a special conference was held in Cambridge, United Kingdom, to bring together scientists working in those fields and collaborators of the Pierre Auger Observatory to facilitate a continued cooperation [62].

Lightning is a field of investigation that might also affect our understanding of cosmic rays and their interaction with the atmosphere. Several dedicated lightning sensors are deployed throughout the Observatory to study correlations between lightning and air showers measured with the SD array. The radio stations of AERA are also sensitive to lightning and changes in the electrical field and can be used in this study. It is thought that cosmic rays traversing the atmosphere can leave behind ionized trails and induce lightning, or facilitate the relativistic runaway breakdown in clouds.

Elves are another luminescent phenomenon that occur around 80–95 km above ground above thunderstorms. They appear as a flattened, expanding glow with a diameter up to 600 km that lasts typically less than one millisecond. The fluorescence detectors of the Pierre Auger Observatory are sensitive enough to pick up those events. They originate in thunderstorms below the horizon, several hundred kilometers away from the site [63], so the lightning does not affect the FD data taking.

The modulation of galactic cosmic rays because of variable solar activity [64] and other solar and galactic phenomena can be studied using the scaler mode of the SD detector. The scaler mode is a single particle technique, recording traces with a low threshold. This mode was implemented in 2005 to look for transient events like Gamma Ray Bursts [1] and solar flares that modify the flux of low-energy cosmic rays on a short time scale. After correction for atmospheric effects, long-time recordings of scaler data can be used to study the 22-year solar cycle and its modulation of cosmic rays. Another interesting field of study are Forbush decreases, rapid decrease in the observed galactic cosmic ray intensity following a coronal mass ejection. It occurs due to the magnetic field of the solar wind sweeping some of the galactic cosmic rays away from Earth. In 2005, such a decrease was measured and could be verified using neutron monitors in Chile [64].

The Andes mountains are a highly volcanic and seismically active region. The Pierre Auger Observatory with its infrastructure and power supply even in remote

[1] Gamma Ray Bursts can also be observed with the FRAM optical telescope [65]

parts of the array provides a unique platform for volcanologists and seismologists to study nearby volcanoes and frequent seismic activities. Seismic measurement stations are deployed at each FD site and the Balloon Launch Station, as well as several sites outside the Observatory, measuring several earthquakes from the Andes region and the nearby subduction zone. Another seismic array called MalaRRgue will consist of 80 stations in a engineering array, which will be partially colocated with the Pierre Auger Observatory. On of its main tasks is the monitoring of several volcanoes.

3.5 The Future of Ground-based Cosmic Ray Detectors

After 10 years of data taking and analysis, some questions about high energy cosmic rays could be answered with the data from the Pierre Auger Observatory, and several hints were uncovered to answer several more. It is clear, that the highest-energy cosmic rays have to come from outside our galaxy, and it seems there are sources in our "neighborhood". A flux suppression is measured that corresponds to a possible GZK effect. Analyses of the mass composition in data of the Pierre Auger Observatory suggest a change towards heavier elements at higher energies. On the other hand, preliminary data from the Telescope Array in the United States suggests a composition of lighter particles and arrival directions that are compatible with isotropy. However, both experiments are working on reducing their systematic uncertainties by improving their reconstructions and analyses, and with a longer run time both results will get more definitive.

In any case, more statistics is needed at the highest energies, which on ground can only be achieved by an even larger detector, in the order of $20\,000\,\mathrm{km}^2$. Recent results suggest detectors in the MHz and GHz regime are not suited for large-scale deployment. The hybrid concept of the Pierre Auger Observatory and Telescope Array is still the most favored. Using modern technologies to make the detector stations more efficient and cost-effective, a future ground array seems feasible.

While the detector technologies are one challenge, to effectively cover such a large area the spacing of the detectors needs to be optimized. In the case of fluorescence detectors, this means even larger baselines between individual stations, in the order of 80 km, extending the field of view of one stations to about 40 km. The measurement of air fluorescence across such distances requires a superior atmospheric monitoring.

Part of this work was the commissioning and operating of a research and development project to gather informations about the atmosphere at a potential site for a future large-scale ground array in Colorado, United States. Such a system can gauge the purity of the atmosphere and the possibility of observing fluorescence light from air showers across baselines in the order of 40 km. Combining the experience and analyses techniques gathered at the Pierre Auger Observatory with state-of-the-art atmospheric sensing technology and publicly available meteorological data, this project or something similar will also be needed if another site should be chosen.

Chapter 4

Atmosphere

For the measurement of cosmic rays with ground-based detectors, the atmosphere is used as a giant calorimeter. The development of the extensive air shower, the production of fluorescence and Cherenkov light, as well as the propagation of the light to the detectors are dependent on atmospheric parameters and conditions. The Pierre Auger Observatory employs a sophisticated atmospheric monitoring system to observe atmospheric state variables (see Chapter 5) and measure the aerosol content and cloud coverage above the Observatory (see Chapter 7). In this chapter, the atmospheric conditions relevant to air shower measurements and their influence on shower observables are detailed.

4.1 State Variables of the Atmosphere

The state of the atmosphere is characterized by several variables. Temperature, pressure and relative humidity are measured by most atmospheric probes like weather stations and weather balloons and are used to calculate other relevant quantities. For the measurement of air showers, not only surface values are needed, but height-dependent profiles of these parameters are of importance.

Earth's atmosphere can be separated in several layers, characterized by common lapse rates in temperature. The temperature T, measured in K, is a macroscopic, intensive state variable. It is a measure for the average energy in each degree of freedom of the particles in a system. The lowest layer, called Troposphere, extends to about 15–20 km above ground. It is heated primarily by heat transfer from the surface, resulting in a linear decrease of temperature with height. The Troposphere contains approximately 80% of the total mass of the atmosphere and almost all of its water vapor and aerosols. Part of the Troposphere is the planetary boundary layer which is directly above the surface. It extends to about 1 km and is usually well-mixed during day which can lead to temperature inversions and becomes more or less stably stratified during night. Above the Troposphere, the Stratosphere extends to about 50 km. The temperature lapse rate is negative in this layer, meaning the temperature increases again due to the absorption of UV radiation by ozone. The region where the lapse rate changes from positive to negative is called Tropopause and shows typically no change in temperature with height over several kilometers. Above the Stratosphere, the Mesosphere with a positive lapse rate extends to about 80 km. The lowest temperatures of about 190 K (−85°C) are found here. Rare

lightning events like Elves and Sprites are found in this layer. The next layer is the Thermosphere, where extremely high temperatures are reached due to the intense solar radiation and the very low particle density. This trend continues in the adjacent Exosphere, where particles of the atmosphere can be found up to several hundred kilometers above the surface. However, the Exosphere and large parts of the Thermosphere do not behave like a fluid anymore with frequent collisions and interactions between particles. For practical purposes, in air shower physics the top of the atmosphere is set to heights of about 100–120 km. The Exosphere, Thermosphere, and upper parts of the Mesosphere are ionized by solar radiation and are also called Ionosphere. It forms the inner edge of Earth's magnetosphere.

Most weather phenomena like clouds and precipitation are limited to the Troposphere and the lower part of the Stratosphere. The lowest 20 km is also where the bulk of the air shower development takes place and atmospheric variables influence it the most. Hence, the need for detailed knowledge of the profiles of atmospheric variables can be limited to about 25 km above ground. Differences between day and night are mostly noticeable in the boundary layer directly above the surface. At higher altitudes, seasonal effects are larger than diurnal fluctuations. This will be discussed in more detail in Sec. 6.1.

Pressure p is defined as the force exerted against a surface per unit area. The SI unit for pressure is the Pascal (Pa), equal to one Newton per square meter or $\mathrm{kg\,m^{-1}\,s^{-2}}$. In atmospheric sciences, the unit hPa is more commonly used, since it corresponds to 1 mbar. The pressure at sea level is roughly 1 bar, or 1000 hPa. In the atmosphere, the force is generated by the gravitational force acting on the mass of the air column above a certain area of the Earth or other surface in the atmosphere, hence

$$p(h, \Phi) = \frac{F(h)}{A} = \frac{m(h) \cdot g(h, \Phi)}{A}, \tag{4.1}$$

$m(h)$ being the mass of the air column above a unit area A, decreasing with height, $g(h, \Phi)$ is the local acceleration due to gravity in its dependence on altitude h and geographical latitude Φ [66],

$$\begin{aligned} g(h, \Phi) = g_0(\Phi) \quad &- \quad (3.085462 \cdot 10^{-4} + 2.27 \cdot 10^{-7} \cdot \cos(2\Phi)) \cdot h \\ &+ \quad (7.254 \cdot 10^{-11} + 1.0 \cdot 10^{-13} \cdot \cos(2\Phi)) \cdot h^2 \\ &- \quad (1.517 \cdot 10^{-17} + 6 \cdot 10^{-20} \cdot \cos(2\Phi)) \cdot h^3, \end{aligned} \tag{4.2}$$

measured in $\mathrm{cm\,s^{-2}}$. $g_0(\Phi)$ is the acceleration at sea level with dependence on latitude,

$$g_0(\Phi) = 980.6160 \cdot (1 - 0.0026373 \cdot \cos(2\Phi) + 0.0000059 \cdot \cos^2(2\Phi)).$$

Due to the flattening of the Earth, g increases from the equator towards the poles, it decreases with altitude. The column exerting the gravitational force also decreases with height, therefore, the pressure decreases with altitude. This behavior can be adequately described by the barometric height formula. If the atmospheric conditions at height h_0 are known, the pressure at height h_1 is given by

$$p(h_1) = p(h_0) \left(1 - \frac{L \cdot (h_1 - h_0)}{T(h_0)}\right)^{\frac{Mg}{RL}}, \tag{4.3}$$

where L is the temperature lapse rate in $\mathrm{K\,m^{-1}}$, R is the universal gas constant for air and M the molar mass of air in $\mathrm{kg\,mol^{-1}}$.

For the study of air showers, water vapor is a very important constituent of air. The absolute amount of water in the atmosphere can be characterized in several ways, e. g. as mass per volume, measured in $\mathrm{kg\,m^{-3}}$ analogous to the air density. A more convenient variable – since pressure is usually the measured quantity in meteorological instruments, density is derived – is the partial pressure of water in the air, the water vapor pressure e. If the water content in air reaches a critical level, water droplets form around condensation nuclei. This saturation value depends on the temperature of the air. Over-saturated atmospheres are possible, but only under very clear conditions. In Earth's atmosphere, aerosols act as condensation nuclei and clouds form when saturation is reached, preventing further increase of water vapor. The maximum partial pressure of water vapor at a given temperature, the saturation vapor pressure E in hPa can be approximated by the empirical Magnus formula [67],

$$E(\vartheta) = 6.1070 \cdot \exp\left(\frac{17.15 \cdot \vartheta}{234.9 + \vartheta}\right), \quad \vartheta \geq 0°\mathrm{C}, \tag{4.4}$$

$$E(\vartheta) = 6.1064 \cdot \exp\left(\frac{21.88 \cdot \vartheta}{265.5 + \vartheta}\right), \quad \vartheta < 0°\mathrm{C}, \tag{4.5}$$

where ϑ is the temperature in °C. The relative amount of water u in % is the fraction of water vapor pressure of the saturation pressure. It is the measured quantity in radiosondes and weather stations, they use capacitive humidity sensors with dielectric polymers that absorb or release water proportional to the relative humidity. The drawback of the relative humidity is its strong variablity with temperature. The water vapor pressure in hPa is calculated using the relative humidity,

$$e(\vartheta, u) = E(\vartheta) \cdot \frac{u}{100\%}. \tag{4.6}$$

The air density is usually not measured by atmospheric probes. It can be calculated in $\mathrm{kg\,m^{-3}}$,

$$\rho(p, T) = \frac{p \cdot M_{\mathrm{air}}}{R \cdot T}, \tag{4.7}$$

where p is the pressure in Pa, T is the temperature in Kelvin, M_{air} is the molar mass of air in kg $\mathrm{mol^{-1}}$ and R is the universal gas constant. Moist air can be separated into three components to calculate its molar mass: dry air, water vapor and carbon dioxide. The molar mass of moist air is the sum of the molar masses of the components, weighted with the volume percentage of that component,

$$M_{\mathrm{air}} = M_{\mathrm{dry}} \cdot \varphi_{\mathrm{dry}} + M_{\mathrm{w}} \cdot \varphi_{\mathrm{w}} + M_{\mathrm{CO_2}} \cdot \varphi_{\mathrm{CO_2}}. \tag{4.8}$$

The molar masses for dry air, water vapor and CO_2 are 0.02897, 0.04401 and 0.01802 $\mathrm{kg\,mol^{-1}}$, respectively. The volume percentage of CO_2 is taken as 385 ppmv, the percentage of water φ_{w} is the partial pressure e of water vapor divided by the pressure p, and dry air makes up the rest, $\varphi_{\mathrm{dry}} = 1 - \varphi_{\mathrm{w}} - \varphi_{\mathrm{CO_2}}$.

Similar to particle physics, interactions and decays of particles in the atmosphere are described in dependence of the amount of matter traversed, the atmospheric depth X. At a certain height h_0, it is calculated by integrating the air density,

$$X_{\mathrm{slant}}(h_0) = \int_{h_0}^{\infty} \rho(h)\mathrm{d}h. \tag{4.9}$$

The atmospheric depth can be approximated using the pressure and the gravitational acceleration from Eq. (4.2). A volume of gas within the atmosphere is exposed to several forces: the gravitational force pulling it towards the center of the Earth, the resulting force from the pressure below pushing the volume upwards, and the pressure above pushing it down. The hydrostatic equilibrium is found when those forces compensates each other. The differential form of this balance is given by

$$\frac{\mathrm{d}p}{\mathrm{d}h} = -g(h) \cdot \rho_{\mathrm{air}}(h) = -g(h) \cdot \frac{p(h) \cdot M}{R \cdot T(h)}. \tag{4.10}$$

The solution of this differential equation, neglecting height dependences of g and T and inserting Eq. (4.9) is

$$\begin{aligned} p(h) &= p_0 \cdot \exp\left(-\frac{g(h) \cdot M}{R \cdot T(h)} \cdot h\right) \\ \Rightarrow \quad p(h_0) &\approx g \cdot \int_{h_0}^{\infty} \rho_{\mathrm{air}}(h)\mathrm{d}h \\ \Leftrightarrow \quad p(h_0) &= g \cdot X(h_0). \end{aligned} \tag{4.11}$$

Since every cosmic ray has a different direction and zenith angle θ when entering the atmosphere, the amount of matter traversed by an EAS is geometry-dependent. Inclined showers travel through much more matter and therefore develop at higher altitudes. To take this into account, the slant depth is used,

$$X_{\mathrm{slant}}(h_0) = \frac{1}{\cos\theta} \cdot X. \tag{4.12}$$

Eq. (4.12) assumes a flat Earth and atmosphere and is only useful up to zenith angles of $\theta \approx 70°$. For more inclined showers, a curved model of the atmosphere has to be used.

4.2 Impact of Atmospheric Parameters on the Emissions of Extensive Air Showers

Varying atmospheric conditions can alter the development and, in particular, the detection of extensive air showers. The observation of the longitudinal shower profiles by fluorescence telescopes is based on geometrical altitudes h. Thus, geometrical altitudes must be converted into atmospheric depth using Eq. (4.9) and Eq. (4.12).

The air fluorescence emission excited by the passage of an air shower depends on pressure, temperature, and humidity [59]. The de-excitation of excited nitrogen molecules mainly occurs in two ways, through emission of radiation or collision with another molecules of the atmosphere like nitrogen, oxygen, and water vapor. These quenching processes are pressure and temperature dependent as described by kinetic gas theory, and depend on the water vapor content in air. Furthermore, the temperature-dependence of the collisional cross sections for nitrogen-nitrogen and nitrogen-oxygen have to be accounted for. In reconstructions of air shower data from the Pierre Auger Observatory, the fluorescence yield with its dependence on atmospheric conditions is described using experimental results from the AIRFLY

experiment [68, 69],

$$Y_{\mathrm{air}}(\lambda, p, T) = Y_{\mathrm{air}}(337\,\mathrm{nm}, p_0, T_0) \cdot I_\lambda(p_0, T_0) \cdot \frac{1 + \frac{p_0}{p'_{\mathrm{air}}(\lambda, T_0)}}{1 + \frac{p}{p'_{\mathrm{air}}(\lambda, T_0)\sqrt{\frac{T}{T_0}}\frac{H_\lambda(T_0)}{H_\lambda(T)}}}. \tag{4.13}$$

The absolute calibration of the main fluorescence emission at 337 nm, $Y_{\mathrm{air}}(337\,\mathrm{nm}, p_0, T_0)$, is taken from Nagano et al. [70]. $I_\lambda(p_0, T_0)$ is the wavelength band intensity relative to this calibration value, p'_{air} is a reference pressure at which the collisional quenching and the radiative de-excitation are the same. This calculation can be modified to include the temperature-dependent cross sections and vapor quenching,

$$\frac{H_\lambda(T)}{H_\lambda(T_0)} = \left(\frac{T}{T_0}\right)^\alpha, \tag{4.14}$$

$$\frac{1}{p'_{\mathrm{air}}} \rightarrow \frac{1}{p'_{\mathrm{air}}}\left(1 - \frac{e}{p}\right) + \frac{1}{p'_{\mathrm{H_2O}}}\frac{e}{p}, \tag{4.15}$$

where $p'_{\mathrm{H_2O}}$ is the characteristic pressure for water vapor quenching, defined analogous to p'_{air}. The coefficient α can be either positive or negative, depending on the nature of the quenching partners and the type of interaction [59]. Most recent experimental data indicate a negative exponent α.

The dependence of the fluorescence yield on atmospheric conditions translates to an atmospheric dependence of the reconstructed cosmic ray energy and the depth of shower maximum. Even short-term variations of the atmosphere may introduce noticeable effects on these reconstructed parameters and increase the corresponding uncertainties.

Most of the secondary particles of extensive air showers travel faster than the speed of light in air. As a result, they induce the emission of Cherenkov light in a narrow, forward-beamed cone. Some of this light in the UV range may be – depending on the shower geometry relative to the FD telescope – detected together with the fluorescence light. To effectively take into account the fraction of Cherenkov photons from the total number of photons detected, the amount of Cherenkov light emitted by the air shower must be estimated. The Cherenkov yield depends on the refractive index n of the air, which itself depends on the wavelength of the emitted light as well as the temperature, pressure and humidity [71, 72]. Parameterized formulae for the refractive index of dry air, CO_2 and water vapor are used to calculate a total refractive index,

$$n_{\mathrm{tot}} - 1 = (n_{\mathrm{dry}} - 1) \cdot \frac{\rho_{\mathrm{dry}}}{\rho_{\mathrm{air}}} + (n_{\mathrm{CO_2}} - 1) \cdot \frac{\rho_{\mathrm{CO_2}}}{\rho_{\mathrm{air}}} + (n_{\mathrm{w}} - 1) \cdot \frac{\rho_{\mathrm{w}}}{\rho_{\mathrm{air}}}. \tag{4.16}$$

The refractive index of each component is weighted with its density, which can be calculated using the number density and the molar mass of the constituent. Finally, the effect of the decreasing number density with altitude is parameterized [73] as a function of pressure p and temperature ϑ,

$$n_{\mathrm{air}} - 1 = (n_{\mathrm{tot}} - 1) \cdot p \cdot \frac{1 + p \cdot (61.3 - \vartheta) \cdot 10^{-10}}{96095.4 \cdot (1 + 0.003661 \cdot \vartheta)}. \tag{4.17}$$

The effects due to depth-to-height conversion and Cherenkov light production on the reconstruction of extensive air showers can be taken sufficiently into account

by using a proper description of the atmospheric state, e. g., the local atmospheric monthly models derived from multi-year meteorological balloon radio soundings (see Sec. 5.2) or data from numerical weather models (see Sec. 6.1). They affect the reconstruction results of air shower data, mainly primary energy and position of shower maximum, only by marginally broadening the uncertainties without any significant systematic shifts.

4.3 Influence of the Atmosphere on the Detection of Extensive Air Showers

The number of fluorescence photons $\mathrm{d}N_{\mathrm{fl}}$ which are emitted from a layer of atmosphere with thickness $\mathrm{d}X$ and detected by a fluorescence detector can be written as

$$\frac{\mathrm{d}N_{\mathrm{fl}}}{\mathrm{d}X} = \frac{\mathrm{d}E_{\mathrm{dep}}^{\mathrm{tot}}}{\mathrm{d}X} \int Y_{\mathrm{air}}(\lambda, p, T, e) \cdot T_{\mathrm{atm}}(\lambda) \cdot \epsilon_{\mathrm{det}}(\lambda)\mathrm{d}\lambda. \tag{4.18}$$

$\mathrm{d}E_{\mathrm{dep}}^{\mathrm{tot}}/\mathrm{d}X$ is the total energy deposited in the atmospheric layer, the air fluorescence yield $Y_{\mathrm{air}}(\lambda, p, T, e)$ was discussed in the previous section (Sec. 4.2), $T_{\mathrm{atm}}(\lambda)$ is the transmission factor due to loss of photons between production and detection, and $\epsilon_{\mathrm{det}}(\lambda)$ is the efficiency of the detector.

The light produced from the air shower is predominantly scattered rather than absorbed in the atmosphere. In the following, the term "attenuation" is used to indicate photons that are scattered in such a way that they do not contribute to the light signal recorded at the detector. The transmission factor $T_{\mathrm{atm}}(\lambda)$ from Eq. (4.18) can be separated in a molecular transmission coefficient $T_{\mathrm{mol}}(\lambda, s)$ due to Rayleigh scattering and an aerosol scattering component $T_{\mathrm{aer}}(\lambda, s)$, both indicating the fraction of light intensity that is not attenuated by scattering after a path length s.

An accurate measurement of the transmission factors during data acquisition is necessary for a reliable reconstruction of the shower and proper measurement of the physical properties of the primary cosmic ray. While the molecular transmission factor $T_{\mathrm{mol}}(\lambda, s)$ can be determined analytically using the vertical temperature, pressure and humidity profiles of the atmosphere, the aerosol transmission factor $T_{\mathrm{aer}}(\lambda, s)$ depends on the aerosol distribution and has no analytical solution.

The molecular transmission factor $T_{\mathrm{mol}}(\lambda, s)$ is a function of the total Rayleigh cross section (Eq. (4.21)) and of the density profile in the atmosphere,

$$T_{\mathrm{mol}}(\lambda, s) = \exp\left(-\int_0^s \sigma_{\mathrm{R}}(\lambda) N_{\mathrm{mol}}(s)\mathrm{d}s\right). \tag{4.19}$$

$N_{\mathrm{mol}}(s)$ is the atmospheric molecular density along the line of sight s, measured in molecules per m^{-3},

$$N_{\mathrm{mol}}(s) = \frac{N_{\mathrm{A}}}{R} \cdot \frac{p(h)}{T(h)}, \tag{4.20}$$

where N_{A} is Avogadro's number. $\sigma_{\mathrm{R}}(\lambda)$ is the wavelength-dependent Rayleigh scattering cross section [74],

$$\sigma_{\mathrm{R}}(\lambda, p, T, e) = \frac{24\pi^3}{\lambda^4 \cdot N_{\mathrm{mol}}^2} \cdot \left(\frac{n_{\mathrm{air}}^2 - 1}{n_{\mathrm{air}}^2 + 2}\right)^2 \cdot F_{\mathrm{air}}(\lambda, p, e). \tag{4.21}$$

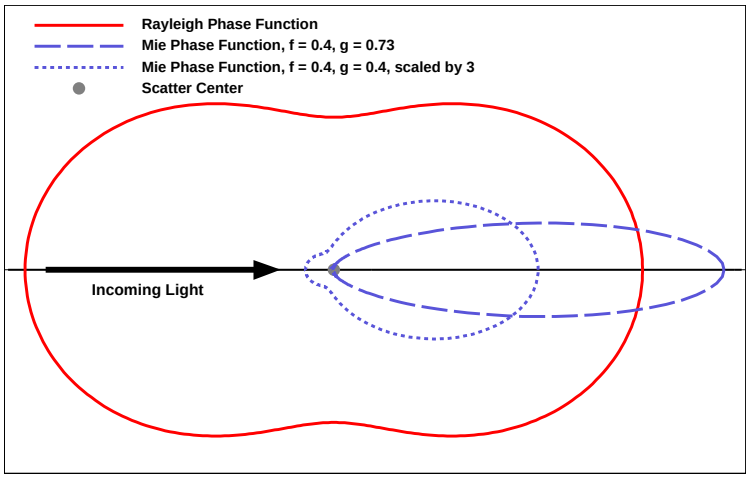

Figure 4.1: Scattering phase function for Rayleigh (red) and Mie scattering (blue).

where λ is the wavelength in m and F_{air} is the King factor that accounts for the anisotropy in the scattering introduced by non-spherical scatter centers, which depends slightly on pressure and humidity. The refractive index n_{air} depends on several atmospheric state variables, see Eqs. (4.16) and (4.17).

Aerosol scattering can be described by Mie scattering theory. Assuming a horizontally uniform aerosol distribution, $T_{\text{aer}}(\lambda, s)$ can be expressed as a function of the aerosol extinction coefficient $\alpha_{\text{aer}}(h)$ from the ground to a point at altitude h observed from the detector at an elevation angle ψ,

$$T_{\text{aer}}(\lambda, h) = \exp\left(-\frac{1}{\sin\psi}\int_0^h \alpha_{\text{aer}}(z)\,\mathrm{d}z\right) = \exp\left(-\frac{\tau_{\text{aer}}(h)}{\sin\psi}\right), \tag{4.22}$$

where $\tau_{\text{aer}}(h)$ is the vertical aerosol optical depth, i. e. the integral of the aerosol extinction $\alpha_{\text{aer}}(z)$ from the ground to a point at altitude h. For the Pierre Auger Observatory, hourly measurements of $\tau_{\text{aer}}(h)$ are performed at each FD site using the data collected from vertical laser beams from two dedicated laser facilities (see Sec. 7.2) to account for the highly variable aerosol content.

The amount of light scattered in a certain direction from the scatter center depends on the scattering angle for both Mie and Rayleigh scattering. For Rayleigh scattering, the intensity at a certain angle depends on the initial intensity of the beam, the Rayleigh cross section (Eq. (4.21)) and the phase function. In Rayleigh scattering theory, the phase function is proportional to $(1 + \cos^2\theta)$. To take into account the anisotropy of the scattering molecules, it can be extended using a parameterization in dependence on a small depolarization factor $\gamma \approx 1\%$ [75],

$$P_{\text{mol}}(\theta) = \frac{3}{16\pi}\,\frac{1}{1+2\gamma}\,[\,(1+3\gamma) + (1-\gamma)\cos^2\theta\,]. \tag{4.23}$$

The phase function is maximal in the extreme forward and backwards direction, it is half that value in the directions perpendicular to the trajectory of the incoming light, see Fig. 4.1.

The description of the aerosol phase function is more complex, since it has no analytical solution. It is strongly peaked in the forward direction with a small

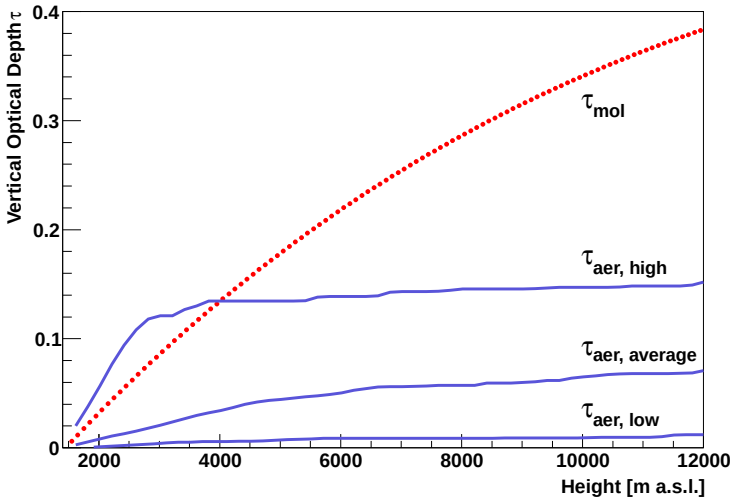

Figure 4.2: Calculated molecular optical depth profile at 355 nm (dots), shown together with measured aerosol optical depth profiles with high, average, and low concentration of aerosols.

backscattering component. A parameterization describing the general behavior can be used [76, 77],

$$P_{\text{aer}}(\theta) = \frac{1-g^2}{4\pi}\left(\frac{1}{(1+g^2-2g\cos\theta)^{3/2}} + f\,\frac{3\cos^2\theta-1}{2(1+g^2)^{3/2}}\right). \tag{4.24}$$

The parameter $g = \langle\cos\theta\rangle$ is a measure for the asymmetry of the scattering. The first term accounts for the forward scattering [78], the second term describes the peak in backward scattering observed in aerosol scattering, f is the relative strength between the two. Both f and g are characteristic for local aerosol concentrations. For the Pierre Auger Observatory, values of $f = 0.4$ and $g = 0.6$ describe the conditions on average, however, aerosol conditions are highly variable and average values are not applicable. Two parameterized phase functions are shown in blue in Fig. 4.1. In both cases, $f = 0.4$ is used. For $g = 0.73$, the strong forward scattering of aerosol scattering is seen, the backward peak is visible in the phase function with $g = 0.4$ (scaled by a factor of 3).

In Fig. 4.2, the molecular vertical optical depth profile $\tau_{\text{mol}}(h)$ for UV light at 355 nm is compared with measured aerosol profiles $\tau_{\text{aer}}(h)$ with high, average and low concentrations of aerosols in the air. For the calculation of the molecular optical depth profile, monthly averaged temperature, pressure, and humidity profiles for the site of the Observatory were used. The 12 resulting optical depth profiles were averaged, the fluctuations introduced by the varying atmospheric conditions throughout the year are very small, in the order of the size of the points in Fig 4.2. While the molecular optical depth is increasing with altitude and only affected by the decreasing number density of nitrogen and oxygen, the aerosol optical depth saturates between 4–8 km where the aerosol concentration becomes negligible. The molecular optical depth is consistently higher than the aerosol optical depth, except for high aerosol concentrations at low altitudes.

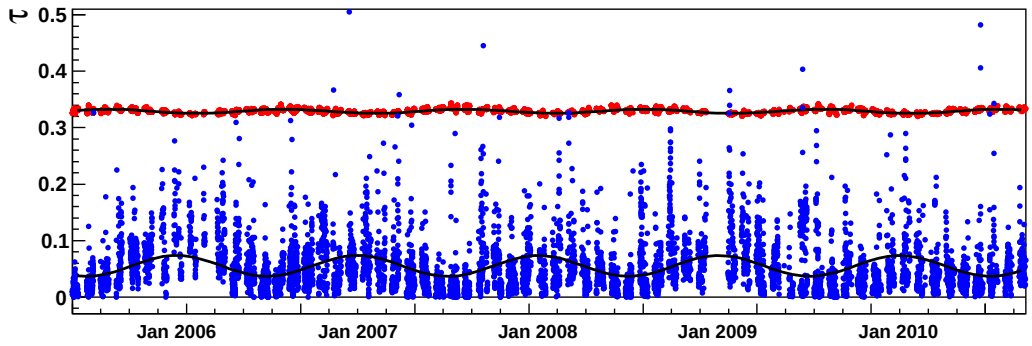

Figure 4.3: Molecular (red) and aerosol (blue) optical depth versus time at an altitude of 8 km. Sinusoids are overlaid to guide the eye.

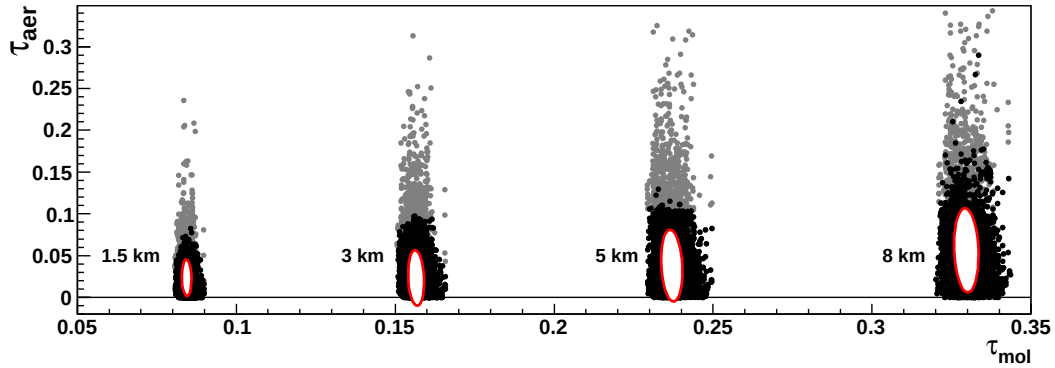

Figure 4.4: Correlation between molecular optical depth and aerosol optical depth for different heights, including correlation ellipses. Hours with $\tau_{\mathrm{aer}}(4.5\,km) > 0.1$ in gray.

In Fig. 4.3, it is again evident that the seasonal variations in molecular optical depth are negligible. Here, both the calculated molecular (red) and measured aerosol optical depth (black) are shown at an altitude of 8 km above ground. Every point corresponds to one hour. Sinusoids are fit and superimposed on both distributions, strictly to guide the eye and emphasize the seasonal effects. In the case of aerosol scattering, the fluctuations are very large, no parameterization is capable if describing the measured values adequately.

In Fig. 4.4, the correlation between molecular and aerosol optical depth are shown for altitudes of 1.5, 3, 5, and 8 km above ground. The plot covers the same time period as Fig. 4.3, again every dot corresponds to one hour. The distributions are very narrow in molecular optical depth and large fluctuations in aerosol optical depth are found. The correlation ellipses are slightly tilted counterclockwise, indicating a small but negligible anti-correlation between the optical depths. In most physics analyses for the Pierre Auger Observatory, only data measured during hours with $\tau_{\mathrm{aer}}(h) < 0.1$ at 4.5 km above ground are used, to discard data measured during times with large corrections due to high aerosol concentrations. This is the case in less than 5% of the time. Those hours with low aerosol contributions are drawn in black, rejected hours in gray.

Chapter 5

Monitoring of Atmospheric State Variables

In this chapter, measurement equipment, data sources, monitoring techniques, and analyses concerning the molecular part of the atmosphere are presented. In Fig. 5.1, instruments for measuring the atmospheric state variables are shown on a map of the Surface Detector (SD) of the Pierre Auger Observatory. The location and field of views of the stations of the Fluorescence Detector (FD), as well as the Central Laser Facility (CLF) in the center of the array are illustrated.

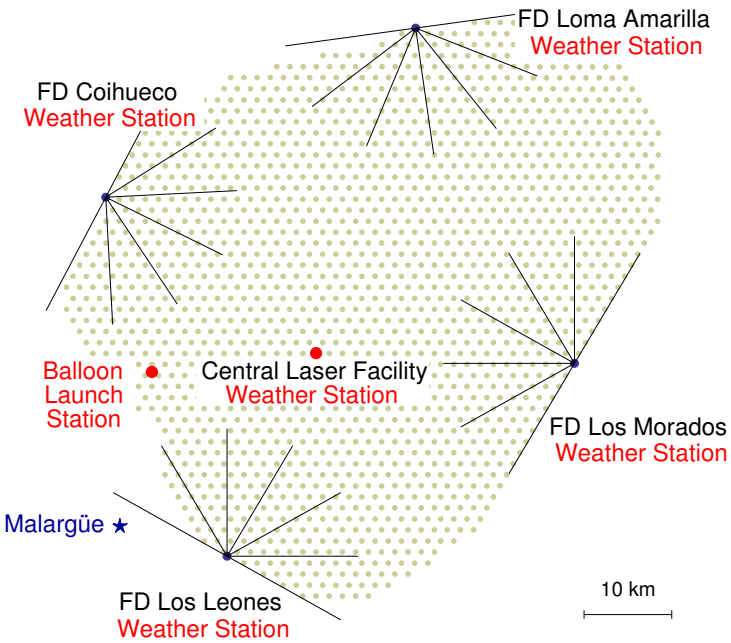

Figure 5.1: A map of the Pierre Auger Observatory with various atmospheric monitoring devices highlighted. This map only includes equipment that measures atmospheric state variables or other quantities related to the molecular atmosphere. Aerosol measurement instruments are depicted in Fig. 7.1. The Central Campus of the Pierre Auger Observatory is located in Malargüe. Map modified from [79].

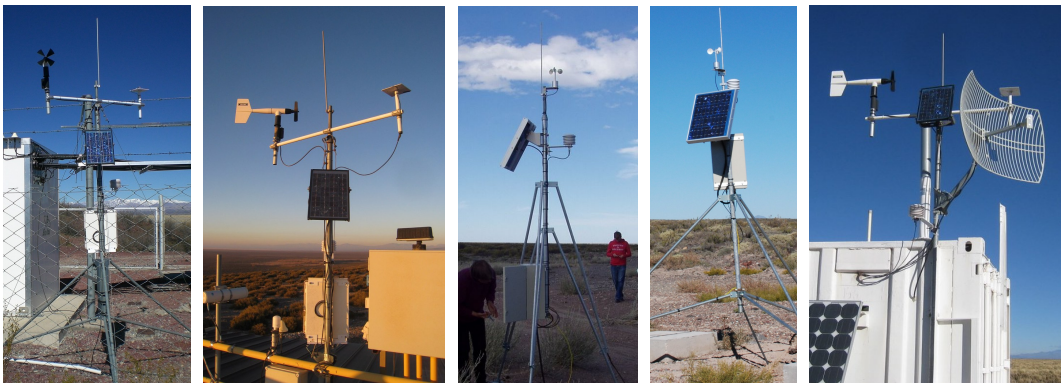

Figure 5.2: Weather stations at Los Leones, Coihueco, Loma Amarilla, Los Morados and the CLF (from left to right).

5.1 Weather Stations

Weather stations are used to monitor the atmospheric state variables at surface level on an almost continuous basis. At the Pierre Auger Observatory, five stations are operated. One at each FD site, and one in the approximate center of the array at the CLF. All stations are similar in their equipment, they contain temperature, pressure, humidity and wind sensors. They are powered by solar panels and communicate their data to the Central Campus via the communication facilities of their respective site, the FD station or the CLF.

In Fig. 5.2, the stations at Los Leones, Coihueco, Loma Amarilla, Los Morados and the CLF are shown. As can be seen from the pictures, the stations are not sheltered. A small radiative shielding protects the hygrometer and thermometer from direct sunlight. A big source of systematic uncertainty is the placement of the stations. For reasons like communication, mounting and protection from wildlife, some stations are placed in the wind shadow of infrastructure (FD building, communication tower), on top of large metal containers or above concrete surfaces. This can introduce a small seasonal bias and the wind measurements are not reliable.

Every five minutes, a set of measurements is recorded. The accuracy of the sensors for conditions typically found at the site of the Pierre Auger Observatory are about 1 hPa in pressure, 0.5 °C in temperature and 2% in relative humidity. Besides temporary failures in the data taking, Los Leones operates since January 2002 and together with the CLF station, an almost complete set of both stations with continuous data was recorded since June 2004. However, data from 2007, 2008 and large parts of 2009 of the Los Leones station had to be removed due to a faulty pressure sensor. The Coihueco station was taking data since 2006, but communication problems prevented the recording of the data. The latest station was commissioned at Loma Amarilla in September 2007. This station is very often affected by lightning strikes requiring repair, so periods of continuous data taking are rather short. Small gaps in the acquisition times are due to data logger failures. The data acquisition times of each station are visualized in Fig. 5.3.

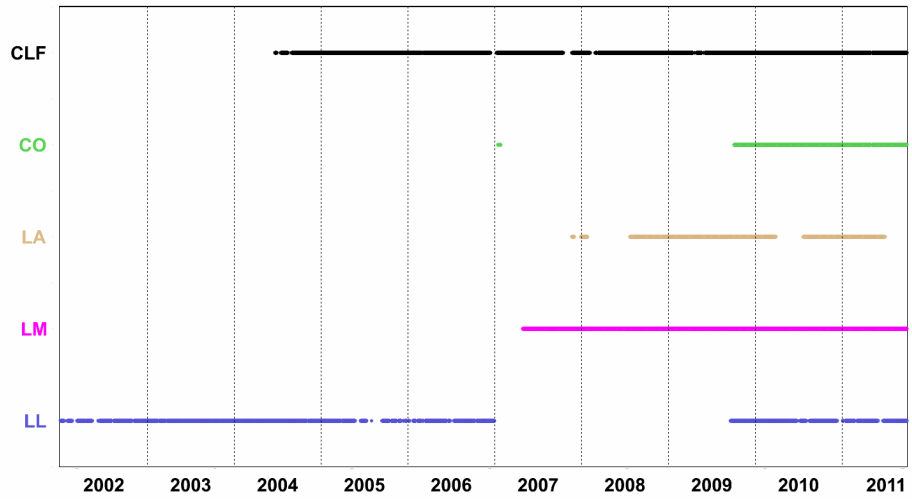

Figure 5.3: Data acquisition times for all weather stations. Large gaps are due to lightning strikes (LA) or faulty pressure sensors (LL). Small gaps are mostly due to problems with defective sensors or data loggers.

5.2 Balloon Measurements

Using helium-filled weather balloons to launch meteorological radiosondes is a well-established method to obtain vertical profiles of atmospheric state variables. The bulk of the development of extensive air showers takes place in the lowest 20 km. For measurements at the Pierre Auger Observatory, balloons are used that are filled with about 1 m^3 of helium and burst around 25 km. Radiosonde launches were performed in Argentina at the site of the Pierre Auger Observatory and in south-east Colorado as part of the atmospheric R&D. The only difference in equipment is the ground station. The Colorado station is mobile and can be used anywhere in the field, provided an adequate power supply, the station in Argentina is installed in a fixed assembled container from where almost all sondes are launched since July 2005.

5.2.1 Equipment and Procedure

The balloon program relies on atmospheric sensing equipment supplied by German manufacturer *GRAW* [80]. Besides the helium-filled balloon and the radiosonde, the probe is equipped with a parachute to slow down the payload decent after the balloon has burst. The data are sent to the ground continuously during the flight where it is received with an antenna and dedicated hardware that processes the data and GPS information and sends it to a computer, where the data are visualized and stored.

The path of the balloon in horizontal directions is entirely governed by the wind, the horizontal movement is determined by the buoyancy of the balloon, which depends on the amount of helium and the weight of the payload. Due to decreasing pressure, the balloon expands to several meters in diameter until it bursts. A picture of the entire assembly can be seen in Fig. 5.4, left. The sonde could in principle be

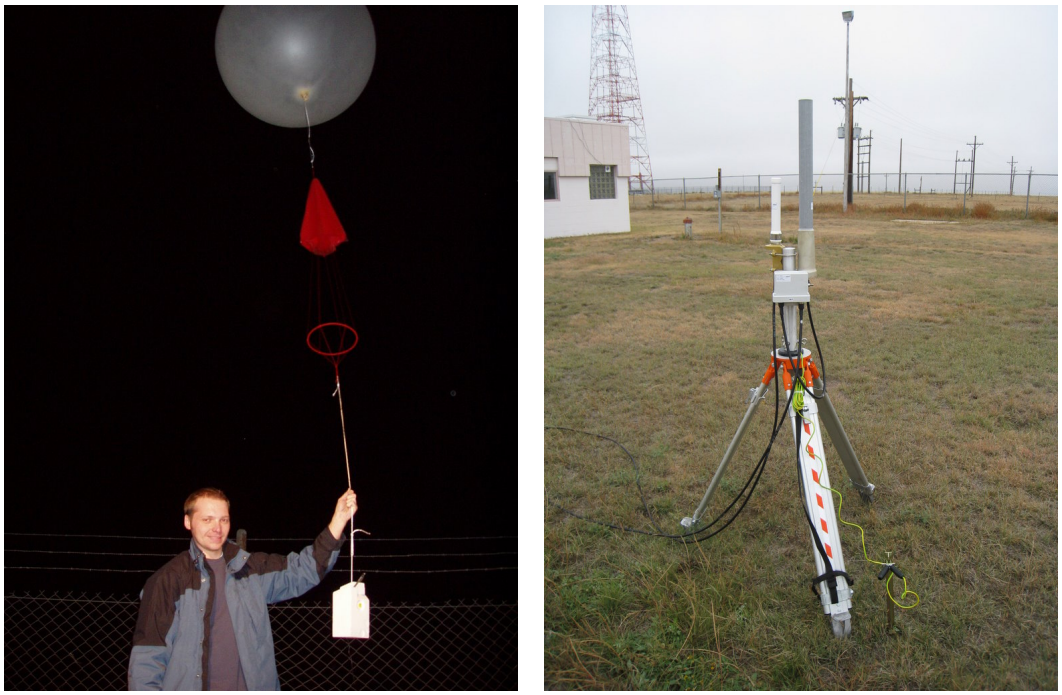

Figure 5.4: Left: A weather balloon with parachute (red, middle) and radiosonde (white, bottom). Right: Ground equipment used in Colorado. The GPS antenna is the smaller, white antenna on the left, the receiving antenna in gray on the right side of the tripod. The white box mounted below the antennas is a signal amplifier.

retrieved and reused after re-calibration by the manufacturer. Besides the shipping costs back to Germany, strong winds usually displace the sonde by several hundreds of kilometers in sometimes difficult to access terrain, so the recovery is highly impractical.

The ground station receives the radiosonde signals and provides local GPS information. All functions of the station are software-controlled by a standard PC using an interface card or connected to special hardware through a USB port. The radiosonde signal is received by a narrow-band Software Defined Receiver (SDR) at frequencies between 400 and 406 MHz using an omnidirectional antenna. A picture of the mobile ground station used in Colorado is shown in Fig. 5.4, right. The station in Argentina uses similar antennas, they are fixed on the container that houses the electronics and computer.

The *GRAW* radiosonde model DFM-06 is used for all radio soundings. It only weighs 90 g and is designed to provide reliable measurements up to an altitude of about 40 km, the maximal range of the data transmission is about 250 km. It is shielded in a polystyrene casing box for minimal mechanical protection and thermal insulation. The sondes are equipped with temperature and humidity sensors on an external sensor boom, an on-board 3D-GPS provides the altitude and information about wind speed and direction through the relative movement of the sonde. The batteries to power the electronics are inside the casing. A set of data is recorded every 3 seconds, corresponding to a height difference of about 10–20 m, and sent down to the ground station. The pressure is not measured directly, but calculated

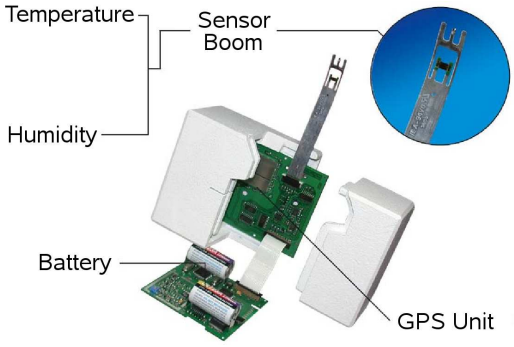

Figure 5.5: Radiosonde model DFM-06. The model actually used in Argentina and Colorado had a different casing. Picture modified from *http://www.graw.de*.

Table 5.1: Measurement ranges and uncertainties of the sensors in the radiosondes used for atmospheric soundings at the Pierre Auger Observatory and the Colorado R&D site.

Quantity	Accuracy
Pressure	$< 1\,\mathrm{hPa}$
Temperature	$< 0.2\,^{\circ}\mathrm{C}$
Relative Humidity	$< 5\%$
Wind Speed	$< 0.2\,\mathrm{m\,s^{-1}}$

using a ground value, the height information as well as the temperature and humidity profiles. Pictures of the sonde model can be found in Fig. 5.5, the accuracies of the sensors are listed in Tab. 5.1.

5.2.2 Measurements at the Pierre Auger Observatory

Since August 2002, meteorological radio soundings have been performed above the Pierre Auger Observatory to measure altitude-dependent profiles of atmospheric state variables. Regular measurements were done until December 2008 in order to collect data for all months. Starting in March 2009, the radio soundings became part of the rapid atmospheric monitoring system known as the Balloon-the-Shower program, see Sec. 5.3.

The average duration of a weather balloon ascent at the Pierre Auger Observatory was about 100 minutes. The validity time of this launch is the time in which the measured profile describes the actual conditions. The minimum time of validity is the duration of the launch. How long the data from a single launch is valid before and after the duration is unknown. A procedure was developed to find this period of time using weather stations [81]. They can be used to identify stable periods or rapidly changing conditions. Consequently, this method can only apply to conditions at the surface. A validity time period of 200 minutes on average is found, double the duration of an average launch. A new method to determine the validity of radiosonde data will be presented in Sec. 6.4.4.

Due to the questionable validity of the radiosonde data and sometimes large gaps between measurements, a complete coverage of the measured air shower data of the Pierre Auger Observatory is not possible. For this reason, average models of monthly conditions were constructed from 261 local radio soundings performed between August 2002 and December 2008 [79, 82]. These monthly models are vertical profiles of atmospheric temperature T, pressure p, water vapor pressure e, density ρ, and atmospheric depth X between 1.2 km and 30 km above sea level in steps of 200 m.

The uncertainties of the model atmospheres are rather large. For temperature,

the RMS at ground level ranges between 3.0 K during austral summer[2] to 6.0 K during austral winter; at 26 km, the RMS is 0.5 K during austral autumn and 5.0 K during austral spring. Atmospheric depth varies mainly between 4 km and 8 km. The RMS of atmospheric depth at ground ranges between 2.3 g cm^{-2} (austral summer) and 6.5 g cm^{-2} (austral winter); the largest RMS, at 8 km, is about 7.5 g cm^{-2}. Above 18 km, the depth uncertainties are below 1.5 g cm^{-2}. The vapor pressure RMS at ground is 1.5 hPa (austral summer) and 4.0 hPa (austral winter), but is well below 0.2 hPa above 7 km.

5.2.3 Measurements at the Colorado R&D Site

The two main sites of the R&D effort in south-east Colorado are the Atmospheric Monitoring Telescope (AMT) and the Distant Raman Laser Facility (DRLF). The main purpose and aerosol measurements performed at these sites will be described in detail in Chapter 8, the basic layout can be seen in Fig. 8.1. In this section, the radiosonde program that accompanied these measurements is described. The program had several goals. The obtained profiles can be compared to profiles from close-by sources or data from numerical weather prediction (presented in Sec. 6.2). Another important property of the atmosphere for ground-based air shower experiments is lateral homogeneity. Furthermore, the profiles can be used in the aerosol measurements performed at the site.

Performance of Radiosonde Measurements

At the Colorado R&D site, the mobile ground station GS-E by *GRAW* was chosen to allow for balloon launches from almost any place. Only a power outlet is needed (100 to 240 V AC) or a 12 V DC outlet of cars (directly or via an inverter). The radiosondes are the same model as the sondes used at the site of the Pierre Auger Observatory. The receiving and GPS antennas are mounted on a tripod with an amplifier and connected to a receiver using coax cables. The receiver is the central unit, it is used to initialize the radiosondes before the launch and acts as an interface between the antennas and the computer. No special interface card is needed, the connection is established using a USB port and software drivers. All the data processing is done on the user's computer with a dedicated software.

Before the launch, the radiosonde is initialized, the transmission frequency is set, GPS satellites are located, and the ground temperature and humidity are recorded. Since the DFM-06 does not contain a pressure sensor, the ground pressure has to be entered manually using a handheld barometer. The initialization can take place inside, so the information of the GPS antenna outside is relayed using a small repeater antenna connected to the receiver. Once the initialization is done, the sonde is set to internal battery operation and tied to the parachute and the helium filled balloon. Before the launch, it is important to let the sonde acclimatize for a few minutes, especially if the initialization took place inside a building.

For the launch of radiosondes, especially at night, it is important to know possible obstacles around the launch site to avoid crashes in high wind conditions. The AMT is situated next to a small office container, both are no higher than 3 m, and several

[2] To avoid confusion, seasons in the Southern Hemisphere will be referred to as "austral", while seasons in the Northern Hemisphere are called "boreal".

small trees. The DRLF is located in a one-story building, surrounded by a 2 m high chain link fence. The surrounding terrain is very flat, the only major obstacle is a close-by 117.7 m high communication tower operated by a telecommunications corporation (the tower can be seen in the background of Fig. 5.4, right panel).

26 balloons were launched at the DRLF building, two sondes were started at the AMT container. A list of all launches can be found in Tab. 5.2. Both the AMT and DRLF positions are at a similar longitude, parallel to the Rocky Mountains front range, at a similar altitude. To check lateral homogeneity, a launch at the same latitude but different longitude would be desirable. Such launches were attempted but were unsuccessful due to failure to initialize the radiosonde. This could have been a power problem, since those were the only times the ground station was powered by a 12 V outlet of a car.

Measurements and Implications

The prevailing wind direction in eastern Colorado is west. The balloon usually ascents a few kilometers when high winds that come over the Rocky Mountains take the sonde over the Kansas state border and further east until the balloon bursts at an altitude of around 18 to 29 km. Three balloons burst earlier, two reached altitudes of 16 979.4 and 14 944.2 m, probably due to varying helium amounts in the balloons or small defects in the balloon skin. One balloon only reached 2138.1 m, the parachute was accidentally attached backwards, however it is unclear how this would cause a premature burst. Two sondes interacted with surrounding structures. One sonde hit the DRLF building when a gust of wind caught the balloon immediately after the release. The data seems good but has a few dropouts. A second balloon was tangled up in the close-by communications tower for several seconds before it continued. The data are usable.

In Fig. 5.6, example balloon paths and height-dependent profiles of temperature, pressure (difference to US Standard Atmosphere), relative humidity and vapor pressure are shown for two launches from 3 June, 2010. The first balloon was launched from the AMT container, the other 4 hours later from the DRLF building. The starting positions are almost 40 km apart, however, the balloon paths and the profiles of the state variables suggest that the molecular atmospheric conditions are very stable over the course of a few hours within the area of the R&D site. This measurement was only performed once, so no definite conclusion can be drawn concerning lateral homogeneity. As mentioned before, both locations are roughly equidistant to the Rocky Mountain front range. The surface height decreases steadily away from the mountains with very similar terrain features, so a symmetry in atmospheric conditions along the north-south axis is to be expected. For this reason, a second pair of measurements was planned to take place at the AMT and at a second location several kilometers due west of the AMT. Unfortunately, this measurement was not possible due to a failure in the hardware, as described above.

In Fig. 5.7, three ascents with paths that are untypical are shown. The first one was caught in a very strong south-west wind that carried it in about 150 minutes over a distance of more than 180 km. The second balloon was driven by north-west wind, barely crossing into Kansas. During the third ascent, almost no wind was present. In almost 2 hours of flight, it reached an altitude of over 23 km but only covered a distance of less than 34 km, not reaching the Kansas border.

Table 5.2: Statistics of all 28 radiosonde launches at the Colorado R&D site. All dates and times in UTC, local time is UTC–7 in boreal winter and UTC–6 in boreal summer.

No.	Date	Start	Duration	Max. Altitude	Site	Weather Conditions	Notes
1	2009-10-14	18:00:05	7170 s	26460.1 m	DRLF	Cloud covered, light rain	
2	2009-10-15	04:12:34	8430 s	27515.4 m	DRLF	Foggy	
3	2009-11-12	04:51:27	6420 s	24178.9 m	DRLF	No clouds, windy	
4	2009-11-12	10:05:48	6120 s	21032.0 m	DRLF	No stars visible, almost no wind	Got stuck at communication tower
5	2009-12-19	03:57:39	7470 s	22900.3 m	DRLF	Very clear, little wind	
6	2009-12-19	09:29:25	6950 s	23558.3 m	DRLF	Very clear, little wind	
7	2010-01-23	04:08:51	8970 s	27925.4 m	DRLF	Clear sky, windy	Almost hit the tower
8	2010-01-23	10:43:32	6535 s	25917.0 m	DRLF	Clear sky, high humidity	NE direction
9	2010-03-05	04:07:30	430 s	2138.1 m	DRLF	Clear sky, windy	N direction, burst early
10	2010-03-05	05:26:00	7530 s	22680.7 m	DRLF	Clear sky, very windy	N direction, sonde hit building
11	2010-03-05	09:55:06	6810 s	23069.4 m	DRLF	Clear sky, windy	
12	2010-03-06	04:37:26	6720 s	23958.4 m	AMT	Clear sky, almost no wind	
13	2010-03-06	08:23:21	7170 s	22106.1 m	DRLF	Clear sky, little wind	
14	2010-04-13	03:19:55	7110 s	24265.2 m	DRLF	Clear sky, very windy	
15	2010-05-18	05:13:03	6870 s	16979.4 m	DRLF	Few clouds, little wind	Thunderstorms to the south
16	2010-05-18	09:07:01	6780 s	19725.0 m	DRLF	Few clouds, little wind	Thunderstorms to the south
17	2010-05-21	06:02:20	9090 s	28282.0 m	AMT	Clear sky, almost no wind	
18	2010-06-16	06:27:56	7440 s	18639.7 m	DRLF	Clear sky	
19	2010-07-15	03:52:40	7225 s	18435.3 m	DRLF		Performed by Michael Coco
20	2010-07-15	06:50:15	8090 s	18703.1 m	DRLF		Performed by Michael Coco
21	2010-08-05	03:34:25	8670 s	22615.9 m	DRLF		Performed by Michael Coco
22	2010-10-02	04:14:16	7410 s	14944.2 m	DRLF		
23	2010-10-07	05:13:43	7255 s	26735.0 m	DRLF		
24	2010-10-08	03:24:21	8580 s	27922.3 m	DRLF		
25	2010-10-15	06:24:12	7080 s	23345.8 m	DRLF		
26	2010-10-30	04:00:14	6085 s	19968.9 m	DRLF		
27	2011-05-04	05:52:58	6560 s	23725.5 m	DRLF		Performed by Michael Coco
28	2011-05-20	03:47:35	8970 s	24924.3 m	DRLF		Performed by Michael Coco

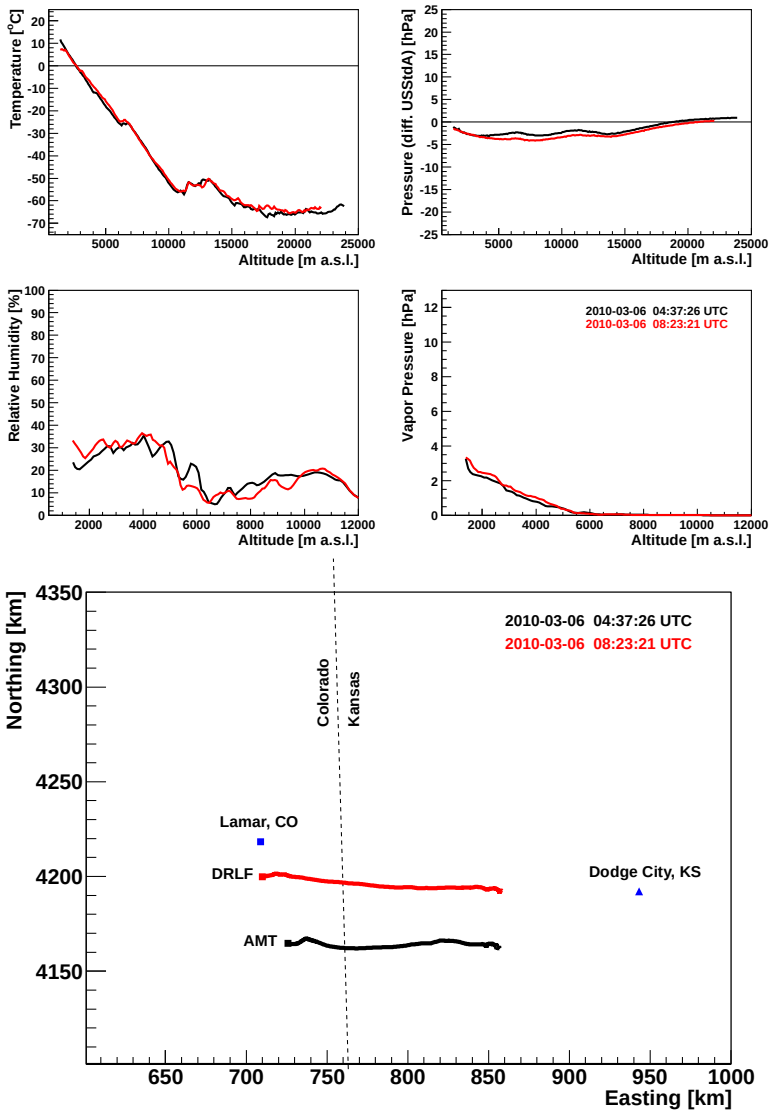

Figure 5.6: Profiles of temperature, pressure (difference to USStdA), relative humidity and vapor pressure versus height (top) and flight paths (bottom) of balloons launched at the R&D site. Data from two balloons launched from the DRLF and the AMT within 4 hours are shown.

With the radiosonde program, lateral homogeneity of the atmospheric conditions at the R&D site was investigated. Only one set of measurements was done, so a definite answer could not be found. Due to the large effort involved, a cheaper and easier source for atmospheric profiles to replace radiosonde launches was needed. Close-by airports launch sondes regularly, the data are compared to the measured data in the next section. Also, the data are compared to data from a numerical weather prediction in Sec. 6.2. Several balloons were launched in coincidence with aerosol measurements using the Raman LIDAR, described in more detail in Sec. 8.1.1.

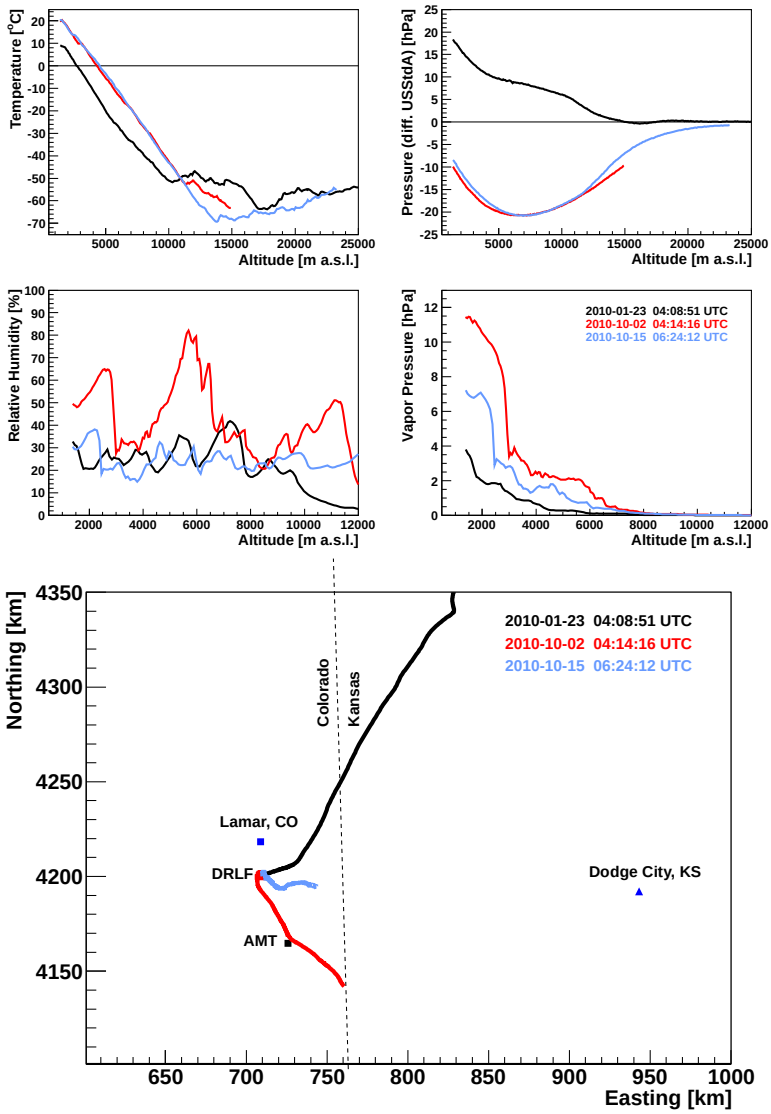

Figure 5.7: Profiles of temperature, pressure (difference to USStdA), relative humidity and vapor pressure versus height (top) and flight paths (bottom) of several balloon launches at the R&D site that deviate from the usual west-east flight path.

Comparison with Nearby Radio Soundings

The R&D site is in a remote area in south-east Colorado. Radio soundings are frequently performed at airports, usually twice per day. Only a few small towns are within several miles of the site, no major airports that provide radio soundings. In Fig. 5.8, a map with the positions of the four closest airports around the R&D site are shown that perform soundings and that are available through the website of the British Atmospheric Data Centre [83]. The four airports are in Dodge City, Kansas (distance to the DRLF of 233 km), Denver, Colorado (284 km), Amarillo, Texas (312 km), and Albuquerque, New Mexico (480 km). Complete data sets are available for the first 21 launches until August 2010, afterwards no data were available for the dates of the launches.

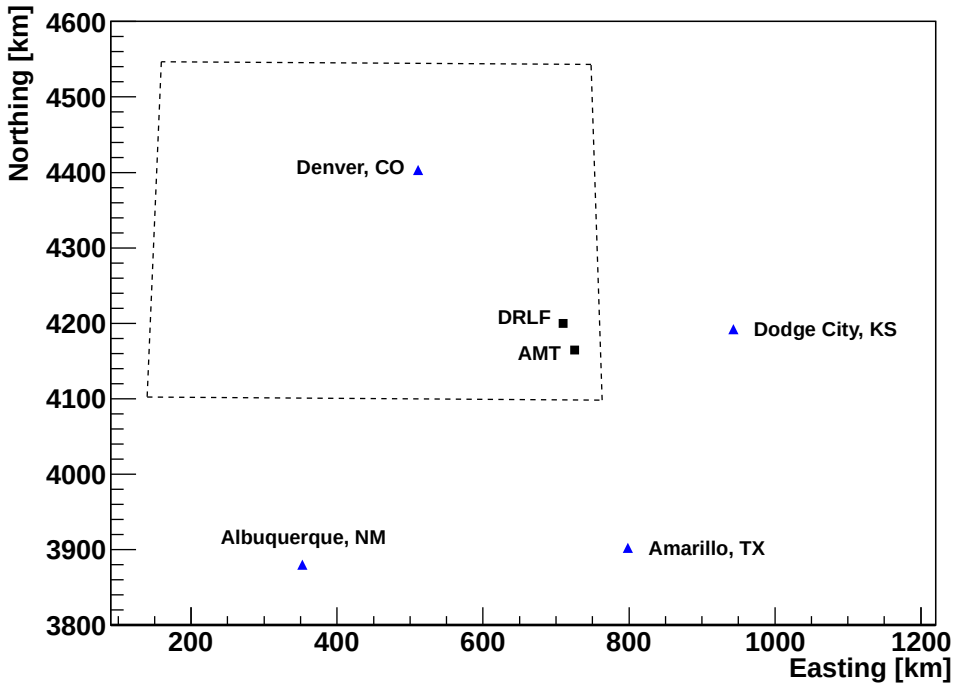

Figure 5.8: A map of airports that provide radio soundings close to the R&D site, indicated by the markers labeled DRLF and AMT. The Colorado state borders are shown for reference.

For the comparison of the R&D radiosonde data with airport radiosonde data, launches No. 9 (burst early) and 10 (dropouts in data due to collision of sonde) are excluded, leaving 19 profiles. The Denver airport performed four launches per day (9:00, 11:00, 14:00 and 23:00 UTC) until December 2009, afterwards two were performed at 11:00 and 23:00, as do the other three airports. All data from self-launched balloons are compared to data from all four airports from that time that is closest to the launch time of the R&D balloon. This is possible for all launches except No. 18, where no data from Dodge City are available.

In Fig. 5.9, the differences between the measured radiosonde data at the R&D site and data measured at the four close-by airports are shown. Dodge City is the closest, Amarillo is on a similar longitude as the DRLF site. Amarillo is also at a similar elevation of about 1100 m a.s.l., Albuquerque and Denver at 1600 m are about 400 m higher, and Dodge City at 760 m is about 400 m lower than the R&D site. As seen in the comparison between the DRLF and the AMT site, conditions on the same longitude show large similarities. In temperature, all airports except Denver show similar differences, in pressure Amarillo and Albuquerque to the south show smaller differences while Dodge City and especially Denver differ significantly. In water vapor pressure, Amarillo shows the largest difference, but again Denver does not show good agreement. The density measurements of three of of the airports agree quite well, with Dodge City at lower heights and Denver showing larger differences. Over all, data from Albuquerque is always amongst the best fitting profiles with no large deviations. Dodge City and Amarillo, expected to show the smallest

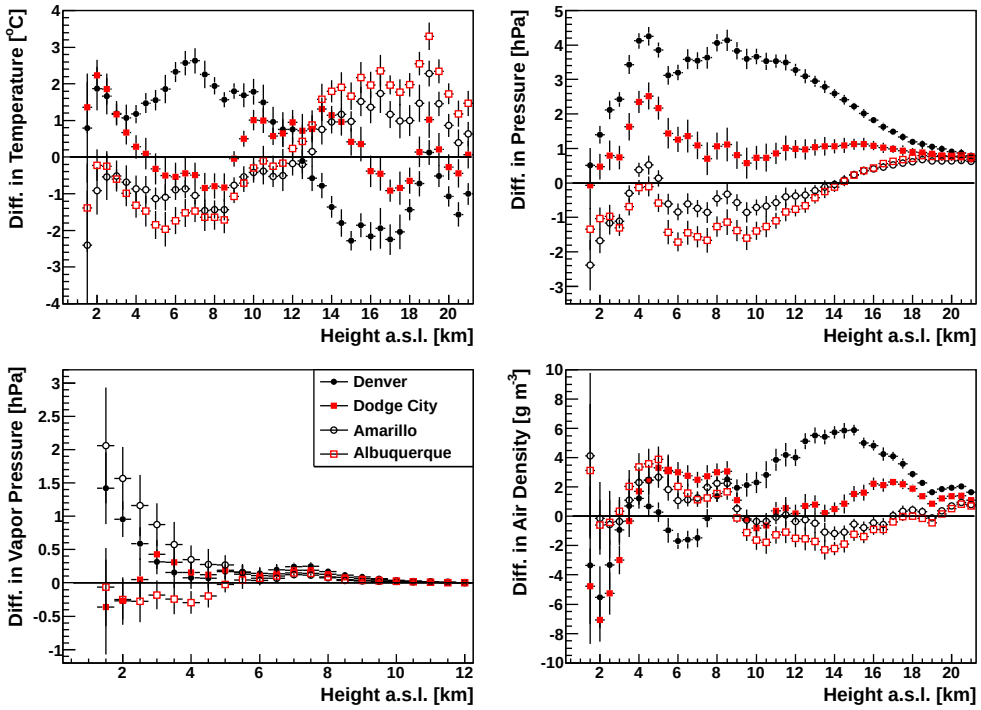

Figure 5.9: Difference in temperature, pressure, water vapor pressure and air density between radiosonde data measured at the R&D site and at four close-by airports.

differences, vary in several state variables especially closer to ground. The only definite answer that can be given is that data from Denver airport is rather unsuited to describe the data measured at the R&D site, which probably can be attributed to the close-by Rocky Mountains. Although Albuquerque is at a similar latitude and elevation as Denver, the Rocky Mountains are not as high in New Mexico and do not influence the local weather conditions as much.

Airport data are available for free online, and comparisons with the measured data show their potential as a description of local atmospheric conditions. However, the availability of the data is rather poor, very large amounts of data is missing or will only be made available several months later. Another drawback of the data is the resolution of the data of about 1–2 km in altitude and only 12 hours in time, making the airport data a rather bad choice as a description of the atmosphere for the R&D project or any future air shower detector. In Sec. 6.2, the R&D radiosonde data are compared to data from numerical weather prediction models with a much better spatial and temporal resolution and much better availability.

Severe Weather Conditions

Clouds and lightning are weather phenomena that can impede the measurement of air showers. Clouds obstruct or scatter fluorescence light and can cause higher background light for fluorescence detectors, while the high electric fields associated with thunderstorms can interfere with surface detectors. A lightning strike can even damage equipment. In some regions, severe weather phenomena like tornados and massive thunderstorms are known to occur frequently. For a future ground-based

observatory and the necessary R&D efforts, it is important to assess the risk for equipment and personnel due to severe weather.

Colorado is frequented by small to medium size tornados between the months of May and August. However, tornados outside the typical season as well as very strong tornados have been seen in the past. Tornados are usually formed in Super Cells, huge cloud complexes also associated with heavy lightnings and hail. While lightning and hail should not pose a significant threat to the equipment, tornados are known to destroy or severely damage houses and other infrastructure. While the high winds in and around a tornado account for a lot of the damage, some of the destructive power of a tornado stems from debris picked up and accelerated by the funnel.

Using a complete list of tornados in Colorado [84], the potential risk to a large area detector configuration similar to the Pierre Auger Observatory can be estimated. The track length and width of the tornado is provided. The strength of a tornado is measured on the Fujita scale, depending on the amount of damage done, ranging from F0 to F5. An F0 tornado is associated only with light damage comparable to strong winds. For this study, only tornados above F0 are considered significant. In Fig. 5.10, tornado tracks in Colorado between 1999 and 2010 are shown. F0 tornados are drawn in black, significant tornados in red. The Colorado state border is indicated by the dashed line, the blue rectangle are the borders of a potential 20 000 km^2 air shower array. The tornado-free area between $-108°$ and $-105°$ longitude are the Rocky Mountains. The area of Colorado that is interesting for a ground-based cosmic ray observatory in the east is where the most tornados are found.

90 out of a total of 375 tornados (24%) fall within the potential array, including 11 out of 58 (19%) significant tornados. Using the width and length to estimate the affected area, 55.7 km^2 of Colorado were hit by a tornado in the time period studied, and 21.7 km^2 inside the array. Compared to the area of the detector of 20 000 km^2 this affects about 0.11% of the array in this 11 year period. Even considering the high costs of an FD building for example, this is negligible. However, different sites, especially in Northern America, can exhibit an increased number of very significant tornado activity, making this kind of risk assessment necessary.

5.3 Rapid Atmospheric Monitoring

The use of monthly atmospheric models for the site of the Pierre Auger Observatory to estimate state variables and molecular scattering rather than measured radiosonde data introduces an uncertainty into the estimated production and transmission of fluorescence light for air shower measurements. This contributes to the systematic uncertainties in the reconstructed energy and position of shower maximum. The total effect is small compared to other uncertainties, but it depends on the shower energy. Between $10^{17.7}$ eV and 10^{20} eV, the monthly profiles contribute 1.5–3% to the energy resolution, increasing with energy, and 7.2–8.4 $\mathrm{g\,cm}^{-2}$ to the X_{max} resolution of the hybrid reconstruction [85, 86]. These numbers are characteristic of a large sample of showers, but the uncertainty in the reconstruction of individual showers can be larger, especially at higher energies. Therefore, a minimization of uncertainties introduced by atmospheric profiles in the reconstruction of such events is desirable.

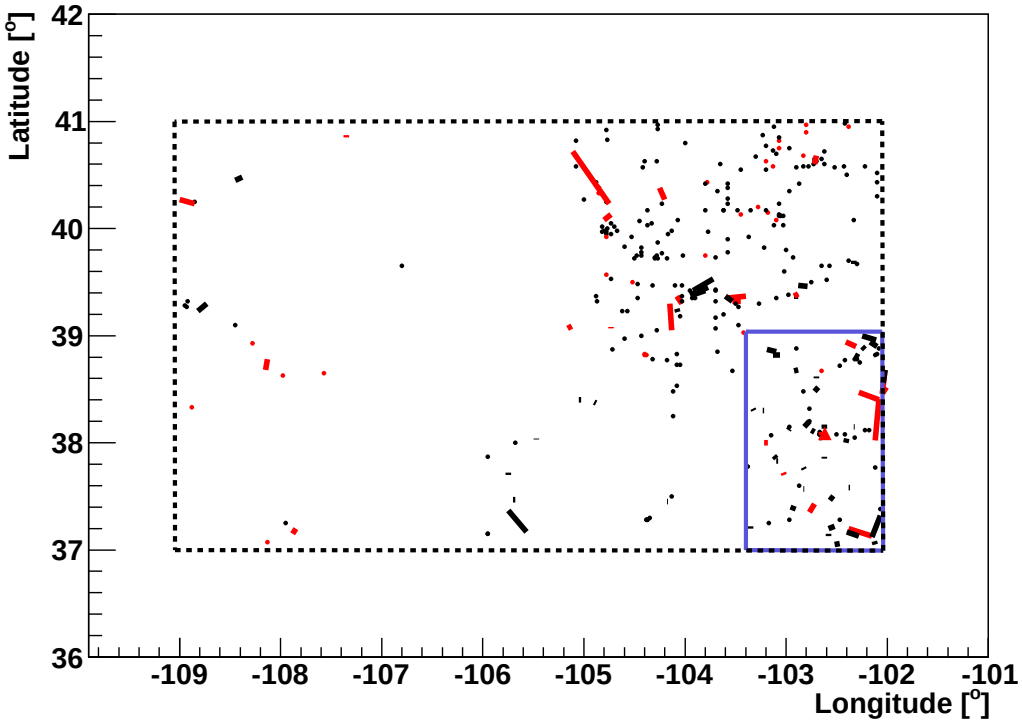

Figure 5.10: A map of tornados tracks in Colorado between 1999 and 2010. F0 tornados tracks are drawn in black, significant tornado tracks in red. Shown with a dashed black line are the Colorado state borders and with blue the area of a potential 20 000 km^2 air shower array.

To investigate the possibility of improving the resolution of the reconstruction for the highest energy showers, the Rapid Atmospheric Monitoring program was conceived [87] in 2009. Three atmospheric subsystems took part in this program, the LIDAR system, the FRAM telescope (for both see Sec. 7.1) and the radiosonde system (see Sec. 5.2.2). While the LIDAR program Shoot-the-Shower and the FRAM measurements are still ongoing, the radiosonde program Balloon-the-Shower (BtS) was operated between March 2009 and December 2010. Its purpose was to perform an atmospheric sounding within about three hours of the detection of a high quality, high energy event. When such events were identified in the results of the online reconstruction, a text message was sent to an on-site technician who then launched a weather balloon.

Until 2009, the measured air shower data were transferred from the Central Campus in Malargüe to several computer clusters off site, among them our local cluster in Karlsruhe. The processing and reconstruction took place several days later. For a rapid monitoring system, information about the showers need to be known after only a few minutes. For this reason, an online reconstruction was set up to run on a dedicated computer in the Central Campus and process the data in situ. During FD data acquisition, an automated process collects event data from the FD and SD. An online event builder merges the two shower data

streams. A hybrid reconstruction, based on a version of the *Offline*[3] reconstruction software [88] used at the Pierre Auger Observatory modified for online running reconstructs the data. All the detector and calibration data that are available at the time of reconstruction are used. Large-particle scattering by aerosols cannot be estimated online using real-time atmospheric monitoring data, so instead an average parametric model of aerosol scattering in Malargüe is used. Rayleigh scattering by molecules are calculated using the most recent version of the averaged monthly models (see Sec. 5.2.2). A final program broadcasts 80 geometry, quality, and energy parameters from each reconstructed shower to the computers running the analysis software that performs cuts for the three subsystems. Typical time delays between measurement and broadcast are in the order of 2 to 8 minutes and the performance of the online reconstruction is checked constantly and performs well compared to offline reconstructions [87]. Discrepancies between the online and offline events are mainly caused by the lack of true aerosol corrections in the online data and, to a minor extent, the use of several month old FD calibration data.

5.3.1 The Balloon-the-Shower Program (BtS)

BtS replaced regularly scheduled meteorological radio soundings at the Observatory in March 2009. The focus of the program was hybrid events with high-quality longitudinal profiles and high energies. FD events are used to calibrate the SD energy scale, high energy events are rare and an important lever arm of this calibration. Other analyses focusing on high-energetic showers are anisotropy and mass composition studies.

The atmospheric profiles from the BtS program represent an independent data set that can be compared to the Malargüe monthly models (MMM). The mean difference of each BtS profile to its corresponding MMM profile is plotted in Fig. 5.11. The width of the variations is in agreement with the uncertainties of the monthly models described in Sec. 5.2.2.

After the automatic BtS trigger, a technician was required to drive to the Balloon Launch Station and prepare the weather balloons. This logistical difficulty meant that in the best case, the radiosonde flights would occur a few hours after the detection of a cosmic ray event. Such delays were not expected to affect the validity of the radiosonde data, since fluctuations in the atmospheric profiles are much larger between nights than within a single night [89]. Nevertheless, to maximize the validity of the radiosonde data from BtS, it was decided that the delay in the balloon launch should be no longer than three hours after the detection of an air shower.

Quality Cuts

To trigger a BtS launch, showers from the online reconstruction were required to pass quality cuts based on the analyses of the SD energy spectrum and the hybrid mass composition [61, 37]. The cuts are listed in Tab. 5.3 and were designed to minimize the uncertainty in shower energy and position of shower maximum $X_{\max}$.

[3] From now on, the term "*Offline*" will be used if the software framework is meant, "offline" will be used if a reconstruction or analysis is performed several days to months after data taking using all available atmospheric and calibration data, as opposed to "online" reconstructions happening a few minutes after the event is recorded, using only calibration data that is available at this moment. All reconstructions, online and offline, are done using versions the *Offline* framework.

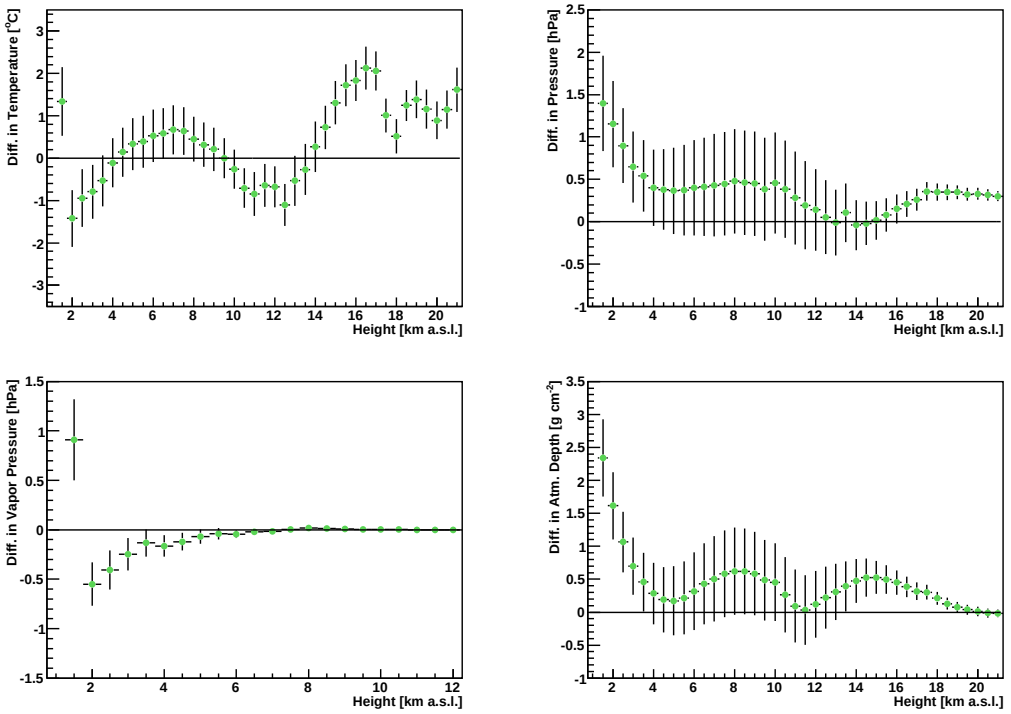

Figure 5.11: Mean difference between atmospheric profiles measured within the BtS program for temperature, pressure, water vapor pressure and atmospheric depth. Each measured profile is plotted in difference to the according monthly model.

The online reconstruction shows systematic uncertainties compared to the offline reconstruction, as discussed above. For this reason, the BtS criteria were made moderately stricter than those used in [61, 37].

Cuts (1) and (2) select showers in which the reconstructed energy and $X_{\max}$ are reliably estimated. Cut (3) removes showers in which $X_{\max}$ is less than $20\,\mathrm{g\,cm^{-2}}$ from either the minimum or maximum observed depth of the shower track. This reduces the possibility that $X_{\max}$ is mis-identified and also improves the reconstructed $\mathrm{d}E/\mathrm{d}X$ profile. Cut (4) is a standard geometry cut that ensures the surface station with the largest signal (i. e., the one used in the hybrid reconstruction) is close to the shower core. Cuts (5) and (6) are indicators of the quality of a Gaisser-Hillas parametric fit to the longitudinal shower profile. Cut (5) is effective at removing showers obscured by clouds and other atmospheric non-uniformities, since the profiles of such showers do not look like a Gaisser-Hillas curve. Cut (6), a χ^2 difference between a linear fit and a Gaisser-Hillas fit to the longitudinal profile, removes faint, low-energy showers from the trigger sample. The selection efficiencies of the cuts are included in Table 5.3.

The relative efficiencies of the cuts are shown as a function of energy for hybrid events recorded between January 2006 and January 2009 in Fig. 5.12. There are too many high-quality events that pass the BtS criteria to launch a balloon for every single event. Before the start of BtS, about 50 balloons per year were launched after a predetermined schedule. This number was a compromise between costs for equipment and man hours and the desire for as much data as possible during different

Table 5.3: A list of quality cuts for the BtS program. Selection efficiencies were calculated using hybrid data recorded from 2006 to 2009. Note that the percentage in each row is given with respect to the previous cut. In the last line, all remaining events which were below the energy threshold are listed.

Quality Cut		Rejected Events
(1) Energy uncertainty	$\sigma_{\mathrm{E}}/E < 0.2$	47.5%
(2) X_{max} uncertainty	$\sigma_{X_{\mathrm{max}}} < 40\,\mathrm{g\,cm^{-2}}$	59.5%
(3) Field of view	X_{max} well observed	8.8%
(4) Distance to SD with highest signal	$d_{\mathrm{axis}} < 1500\,\mathrm{m}$	0.5%
(5) Quality of Gaisser-Hillas (GH) fit	$\chi^2_{\mathrm{GH}}/n_{\mathrm{dof}} < 2.5$	5.3%
(6) Comp. of GH with linear fit	$\chi^2_{\mathrm{lin}} - \chi^2_{\mathrm{GH}} > 4$	36.8%
Energy threshold	$E_0 > 19.95\,\mathrm{EeV}$	99.3%

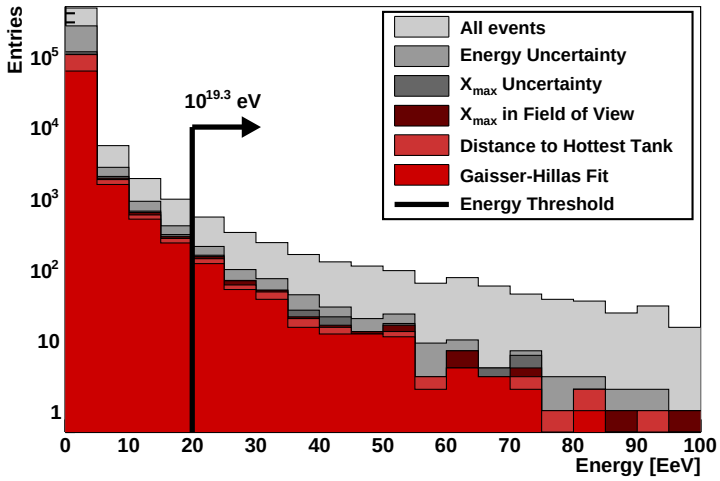

Figure 5.12: Candidate event distribution for BtS estimated by using hybrid events collected between 2006 and 2009. The effect of the quality cuts and the energy threshold is shown. Note that the two profile fit cuts (5) and (6) were combined.

times of the day in all seasons. BtS triggers will only happen at night, during FD data taking hours. This translates to a target launch rate of between 3 and 7 launches per FD measurement period, which lasts about 2.5 weeks around new moon phases. This range is rather imprecise, since the number of expected launches depends on the season. More triggers from high energy showers are expected in austral winter since the nights are longer and the atmosphere is much cleaner. Also, in different years, the number of events that would survive the quality criteria fluctuates. To reach the desired number of soundings per year, it was necessary to further reduce the size of the event sample with a cut on the reconstructed shower energy. The energy threshold, determined from the tuning sample of showers between 2006 and

2009, was

$$\log_{10}\left(\frac{E_{\min}}{\text{eV}}\right) = 19.3 \quad \Leftrightarrow \quad E_{\min} = 19.95 \text{ EeV}. \tag{5.1}$$

It was chosen a little too high deliberately, to make sure not too many events were cut and to allow for the possibility of tightening the cut in the future or introduce a seasonal cut, rather than lose events due to a cut that was set too strict. It turned out the threshold was set well and no later adjustments were necessary.

Text Message Trigger

After a shower passed the automatic BtS trigger, a short message containing the date and time of the event was sent to the mobile phone of an on-site technician. If the message was received in time, the technician would drive to the Balloon Launch Station and proceed with the atmospheric sounding within three hours of the event. Several tests were performed to ensure the reliability of the Argentinian cell phone network. At predetermined times, messages were sent to colleagues in Malargüe using several different cell phone providers. It was found that, especially at night when the BtS triggers are expected, the network was very stable and the text message trigger could be used without expecting too many lost triggers. Parallel to the messages to the technician, the triggers were also sent via email to Karlsruhe. In fact, both messaging systems relied on the outgoing mail server in Malargüe, which proved to be less reliable than the cell phone network. Only one or two messages were delayed after they were sent out because the technician was outside network coverage, while several triggers got stuck before even being sent by the mail server.

Between March 2009 and December 2010, 100 text messages were sent to the technician. From these 100 triggers, 52 balloons were launched successfully. Some messages were received while a radiosonde was already in flight, due to the tendency of high-quality, high energy observations to cluster during very clear, cloudless nights. Therefore, 62 BtS triggers were covered by the 52 flights. The remaining triggers, about one-third of the total, were lost due to technical issues such as a hardware failure at the Balloon Launch Station in August 2009 (11 events), problems in the communication network (mostly the outgoing mail server of the Central Campus) that delayed the text message more than three hours, or other failures in the radiosonde flights like premature bursts or data loss.

The BtS statistics between March 2009 and December 2010 is shown in Fig. 5.13. The chart shows events reconstructed using an offline reconstruction and not the online reconstruction. The same BtS quality criteria were applied to the offline sample. As mentioned before, the two event samples differ because of systematic uncertainties in the online reconstruction, which cannot use real-time calibration constants and atmospheric corrections. The offline sample using the correct FD calibration and measured aerosol profiles is used here as a reference. Scanning through the offline data, a set of showers that should have triggered a balloon launch are found and then compared to the set of showers after which a launch actually occurred.

During the period of BtS operations, 88 events reconstructed offline passed the BtS cuts. Of these, 59 were also identified online, meaning that out of 100 events in the online trigger 41 do not survive the BtS cuts after offline reconstruction. Of the 41 events missing from the offline sample, some did not satisfy the BtS cuts, while

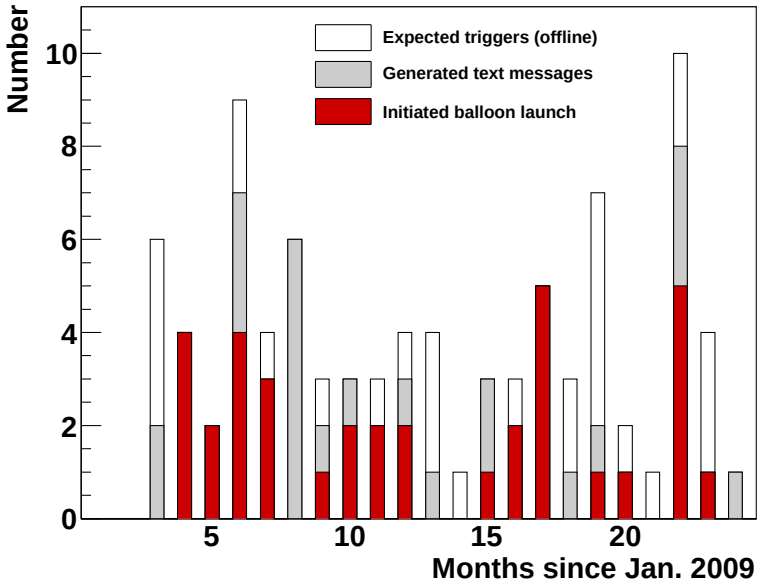

Figure 5.13: Expected BtS triggers between March 2009 and December 2010 determined in an offline reconstruction using BtS cuts (Table 5.3). Also shown in gray is the number of generated text messages for those expected events. Shown in red is the number of events that were covered by a balloon launch. No visible white bar means every interesting event was caught by the script. No visible gray bar means there was a launch for every text message.

others fell below $10^{19.3}$ eV. Finally, of the 59 common events, 35 were covered by a weather balloon launch. If the energy cut is relaxed slightly to $10^{19.2}$ eV, 51 offline events are covered by a balloon launch. While the statistics are below expectations for the BtS trigger, they do serve to demonstrate the importance of high time-resolution atmospheric corrections for choosing high-quality showers in the offline reconstruction.

In Fig. 5.14, the online reconstructed shower cores that should have triggered a BtS launch are shown. Showers that were detected by a telescope of Los Leones (33 events) are drawn in blue filles squares, showers measured in Los Morados (29 events) in open red circles, Loma Amarilla (36 events) in black open squares and Coihueco (59 events) in green triangles. The reason for the higher number of events seen in Coihueco might be due to the site's higher altitude. Coihueco is located about 200 m above the other sites, enabling the telescopes to observe more of the shower development. This increases the chance of including the shower maximum in the field of view and passing this quality criterion. More data points can also have an effect on the goodness of the profile fit and the uncertainties of the reconstructed shower parameters. Events are seen everywhere in the array, close to the eyes and far away, with no significant holes in the distribution. Events that were seen at two sites mostly occur at the overlap of the field of views in the middle between the two sites, events seen by more than two sites are located close to the center of the array, since enough light has to reach all participating telescopes. There were 33

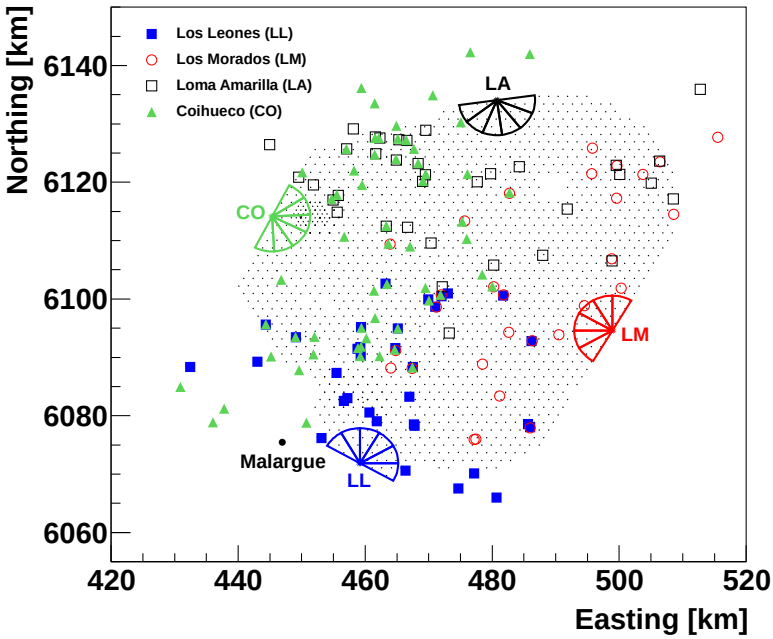

Figure 5.14: Online reconstructed shower cores for all showers that passed the BtS quality criteria, separated for the different FD sites. Some showers were observed by more than one telescope.

events measured at two sites, two events at three sites and one event was detected and passed the quality cuts at all four sites, resulting in a total of 117 events with 157 individual profiles. The higher number of 117 events compared to the 100 text messages sent can be explained by aforementioned problems or significant delays with the sending of the text message to the technician. A notable amount of showers was reconstructed outside the SD array, even though BtS cut (4) should restrict the distance between reconstructed shower core and the SD station with the highest signal. Due to an error in the data broadcast from the online reconstruction, this distance between the core and the station was set to zero, circumventing cut (4).

5.3.2 Air Shower Reconstruction Using BtS Data

To study the effect of the BtS data on the reconstruction of air shower profiles, 62 hybrid events covered by 52 BtS launches are reconstructed. This event sample contains 90 individual fluorescence profiles which pass all quality cuts after accounting for events observed in stereo with multiple telescopes. Also, the reconstruction using BtS data is compared to those using MMM and GDAS model profiles. In all cases, not only for the effects of the atmospheric profiles on light scattering are accounted for, but also for the effects of temperature, pressure, and humidity on fluorescence light production [59, 90]. For the fluorescence light calculation, experimental data from the AIRFLY experiment [68] and conference contributions [69] from the AIRFLY collaboration were used.

The shower observables of main interest are the reconstructed cosmic ray ener-

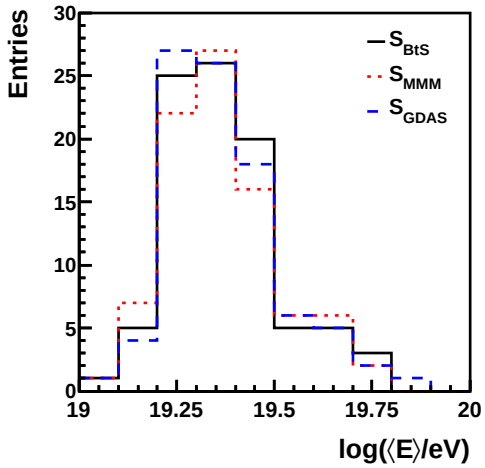

Figure 5.15: Energy distribution of all reconstructed FD profiles of the 62 high energy events which passed the BtS quality cuts during the online analysis and for which a radio sounding has been performed. The black, solid line represents the energy distribution of FD profiles reconstructed with actual atmospheric conditions as measured during the dedicated weather balloon ascents, S_{BtS}. The red, dotted line displays S_{MMM} and the blue, dashed line shows S_{GDAS}. Note that the S_{MMM} sample includes three events less than the others, details see text.

gies E and depths of shower maximum X_{max} of the air shower profiles. The energy distribution of the reconstructed profiles is provided in Fig. 5.15. 90 profiles represented by the solid line are reconstructed using the atmospheric profiles gathered within the BtS program, S_{BtS}. 87 reconstructions applying the monthly atmospheric conditions as described by MMM, S_{MMM}, are displayed with a dotted red line. The third set of 90 reconstructed air showers, S_{GDAS}, is plotted as a dashed blue line and was obtained using model atmospheres from GDAS. All three sets contain the same 87 profiles, reconstructed in with a different atmospheric description. Three events are missing in S_{MMM} set, they could not be reconstructed due to their geometry. The shower is measured in altitude while the reconstruction relies on the conversion to atmospheric depth, which in turn depends on the atmospheric description. It is possible that small changes in this conversion affect the reconstruction if the shower in this way, especially for showers with high energies very close to the detector. The distributions are similar and have no obvious systematic differences. Note that some events have spilled below the energy threshold of $10^{19.3}$ eV because of the systematic energy shift between the online and offline reconstructions. The mean energy of all three event samples is $10^{19.4}$ eV.

In Fig. 5.16, the distributions of the energy difference $\Delta E/\langle E\rangle$ between the S_{BtS} and S_{MMM} events (solid line) and the S_{BtS} and S_{GDAS} events (dotted line) are plotted. $\langle E\rangle$ is the average of the energies reconstructed with each pair of atmospheric profiles used in the two comparisons. For the first comparison, the mean difference in the reconstructed energy is 0.3% and the width of the distribution is 2.3%, with the most extreme difference of about 6%. For the second comparison, the mean difference in the reconstructed energy is -0.3% with an RMS of 1.2%. The improvement reflects the better time resolution of the GDAS profiles with respect to the monthly models,

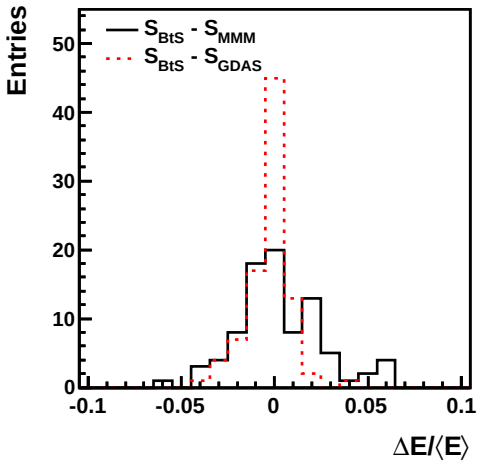

Figure 5.16: Energy difference between events selected by the BtS program. The air showers are reconstructed with three different atmospheric descriptions, details see text.

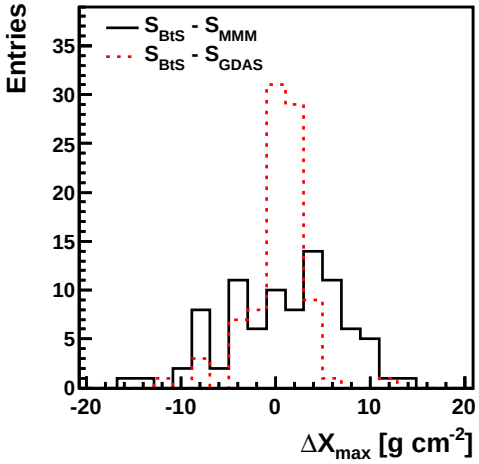

Figure 5.17: Difference of the position of shower maximum $X_{\max}$ between events selected by the BtS program. The air showers are reconstructed with three different atmospheric descriptions, details see text.

and indicates that the GDAS data provide a quite reasonable description of local conditions.

The distributions of the difference $\Delta X_{\max}$ between the reconstructions are shown in Fig. 5.17, where the S_{BtS}-S_{MMM} comparison is plotted as a solid line and the S_{BtS}-S_{GDAS} comparison is drawn with a dotted line. The mean of the S_{BtS}-S_{MMM} distribution is $0.9\,\mathrm{g\,cm^{-2}}$ with an RMS of $6.0\,\mathrm{g\,cm^{-2}}$, with individual differences as large as $16\,\mathrm{g\,cm^{-2}}$. The S_{BtS} and S_{GDAS} reconstructions appear to be more compatible, as before, with a mean of $0.4\,\mathrm{g\,cm^{-2}}$ and a width of $3.1\,\mathrm{g\,cm^{-2}}$.

Study of Systematics

Systematic effects in the reconstructed events due to the use of BtS measurements are investigated. The differences in the reconstructed energy and depth of shower maximum $X_{\max}$ after using the BtS, MMM, and GDAS data in the reconstruction are examined. The energy dependence of the distributions of $\Delta E/\langle E\rangle$ and $\Delta X_{\max}$ are shown in Fig. 5.18. The S_{BtS}-S_{MMM} comparisons are plotted with black points, while the S_{BtS}-S_{GDAS} comparisons are plotted with red squares. No significant energy dependence is observed.

Seasonal effects have been investigated by plotting the energy and $X_{\max}$ differences according to the calendar month (Fig. 5.19). While the primary energy does not show any signs of seasonal dependence, there appears to be some systematic decrease in $X_{\max}$ during the austral winter when using the MMM profiles instead of the BtS profiles in the reconstruction. The shift might be a real effect due to differences in the water vapor content of the monthly models and the real-time BtS data. However, the statistics are small and so it is possible that the shift is a chance effect. For June and July, we obtained 7 and 9 profiles, respectively, but for August, there is only one entry.

The third systematic dependence of interest is on vertical $X_{\max}$ (see Fig. 5.20), which can be interpreted as a projection of the inclined shower track to the vertical. This observable corrects for the different inclination angles of air showers and a clear relationship to the layering of the atmosphere is established. For both E and $X_{\max}$, no dependence is obvious. Note that the vertical $X_{\max}$ bin between 750 and $800\,\mathrm{g\,cm^{-2}}$ only contains one event, since only one air shower profile has been detected with such a deep $X_{\max}$ after applying all quality cuts of the BtS program. This particular shower entered the atmosphere with a reconstruction zenith angle θ of about 12°.

Additional searches for any dependence of $\Delta E/\langle E\rangle$ and $\Delta X_{\max}$ on the distance of the core position from FD telescope and zenith angle were performed, but the dependence of $\Delta E/\langle E\rangle$ and $\Delta X_{\max}$ on these parameters is negligible in all cases.

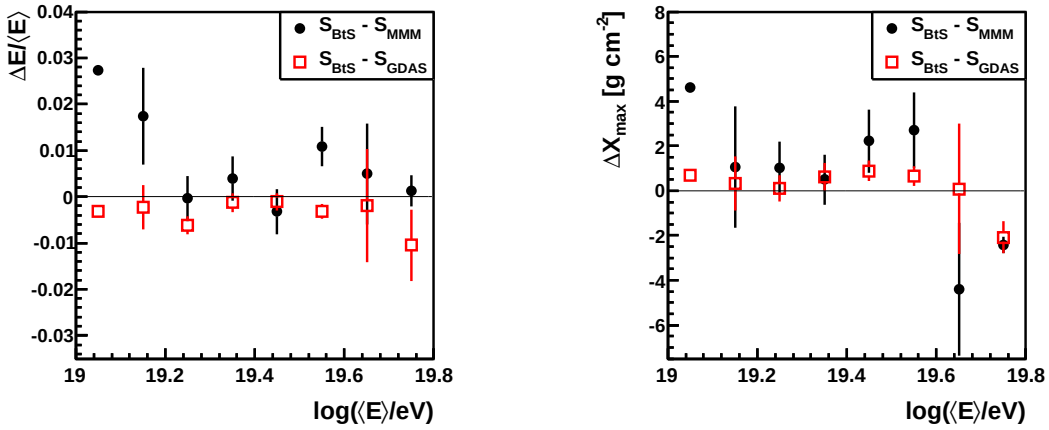

Figure 5.18: Differences in reconstructed energy (left) and $X_{\max}$ (right) vs. energy.

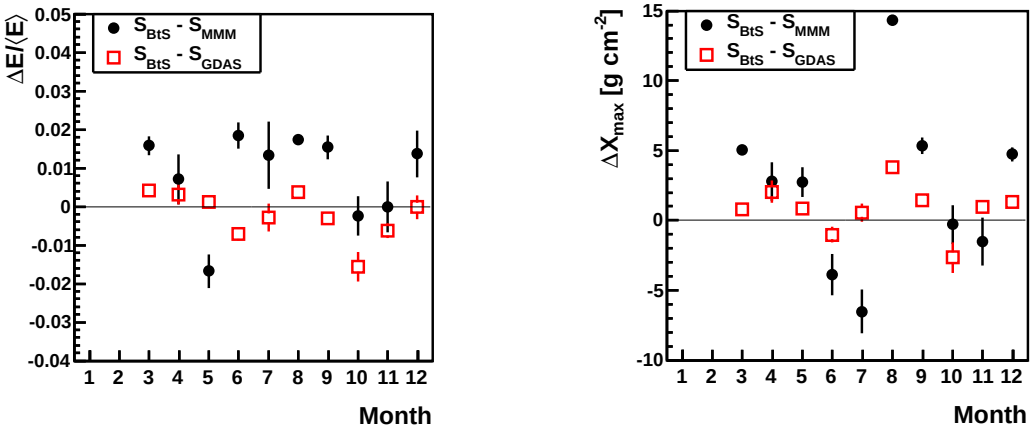

Figure 5.19: Reconstruction results in dependence on the month of year. Left: Difference in E. Right: Difference in $X_{\max}$. There were no balloon launches in January or February.

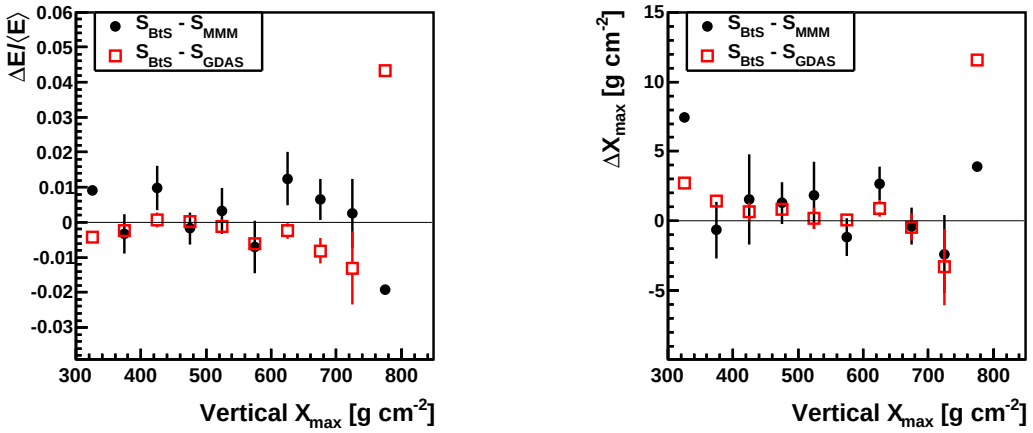

Figure 5.20: Reconstruction results in dependence on vertical $X_{\max}$. Left: Difference in E. Right: Difference in $X_{\max}$.

Chapter 6

Atmospheric Models from Numerical Weather Prediction for Air Shower Reconstruction [4]

In 1922, Lewis Fry Richardson proposed the possibility of numerical weather prediction [92]. However, without computers to perform the large number of complex calculations, his first attempts failed. J. Charney, R. Fjørtoft and J. von Neumann were the first to successful perform a numerical weather prediction using the ENIAC computer in November 1950 [93]. It took 33 days to complete. In the 1960s, computer power had advanced enough to produce forecasts in less than 24 hours, making numerical weather prediction practical.

In 1960, TIROS-1 became the first successful weather satellite. Since then, local measurements could be supplemented by these data to get the atmospheric conditions of the entire Earth. Several thousand weather stations all over the world perform synoptic observations, surface weather measurements made at periodic times (usually every 3 hours) of temperature, pressure, humidity, cloud cover, cloud height as well as wind speed and direction. Additional measurements are provided by radiosonde measurements at airports and other facilities.

Data assimilation is the adjustment of the development within a model to the real behavior of the atmosphere as found in meteorological observations [94]. The atmospheric models describe the atmospheric state at a given time and position. Three steps are needed to perform a full data assimilation:

1. Collect data from meteorological measuring instruments placed all over the world. These instruments include weather stations on land, ships, and airplanes as well as radiosondes and weather satellites.

2. Use a short-term forecast from a previous iteration of the numerical weather prediction together with the measurements to describe the current situation. This additional information is needed because the available observations alone are not sufficient, the forecast adds more information to the system. The models use non-linear differential equations based on thermodynamics and fluid dynamics.

[4] Parts of this chapter were previously published in [81, 91]

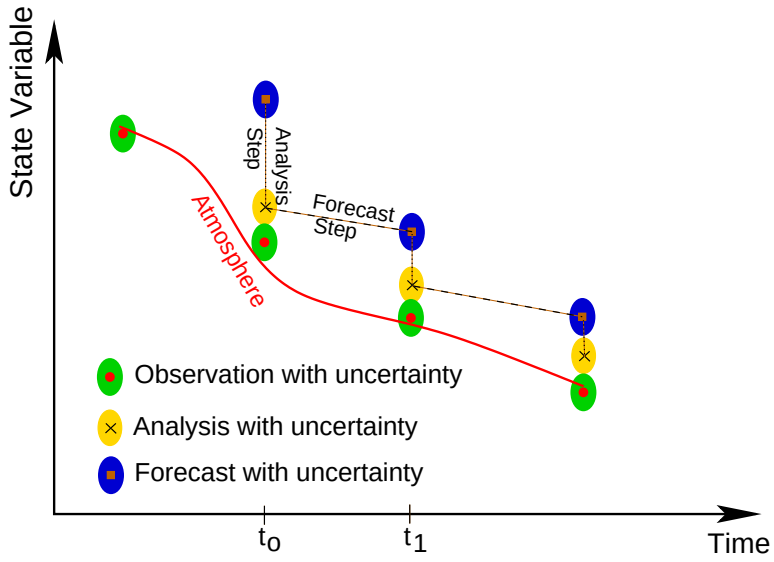

Figure 6.1: Schematic of the data assimilation process. Figure adopted in a modified form from [95].

3. Adjust the model output to the measured atmospheric state. The resulting 3-dimensional image of the atmosphere is called *analysis*.

A schematic showing the principle of data assimilation is given in Fig. 6.1. At a given time t_0, the observations provide the value of a state variable. A model forecast for this variable from a previous iteration exists for the same time. The analysis step combines observation and forecast to describe the current state better than the forecast. This analysis is the initial point for the weather prediction model to create the forecast for a later time t_1.

6.1 Global Data Assimilation System (GDAS)

The Global Data Assimilation System [96] is an atmospheric model developed at NOAA's[5] National Centers for Environmental Prediction (NCEP). It provides an analysis four times a day (0, 6, 12, and 18 UTC) and a 3-, 6- and 9-hourly forecast. The numerical weather prediction model used in the GDAS is the Global Forecast System (GFS).

3-hourly data are available at 23 constant pressure levels – from 1000 hPa (roughly sea level) to 20 hPa ($\approx$ 26 km) – on a global 1°-spaced latitude-longitude grid (180° by 360°). Each data set is complemented by data for the surface level. The data are stored in weekly files and made available online [96]. In Tab. 6.1, the level indices corresponding to each data level are listed. For reference, the altitude from the US Standard Atmosphere 1976 (USStdA) [97] is also given in the table. The actual height of the pressure level is stored in the data file. GDAS data are available starting January 2005. There are two periods without data in the sets.

[5]National Oceanic and Atmospheric Administration

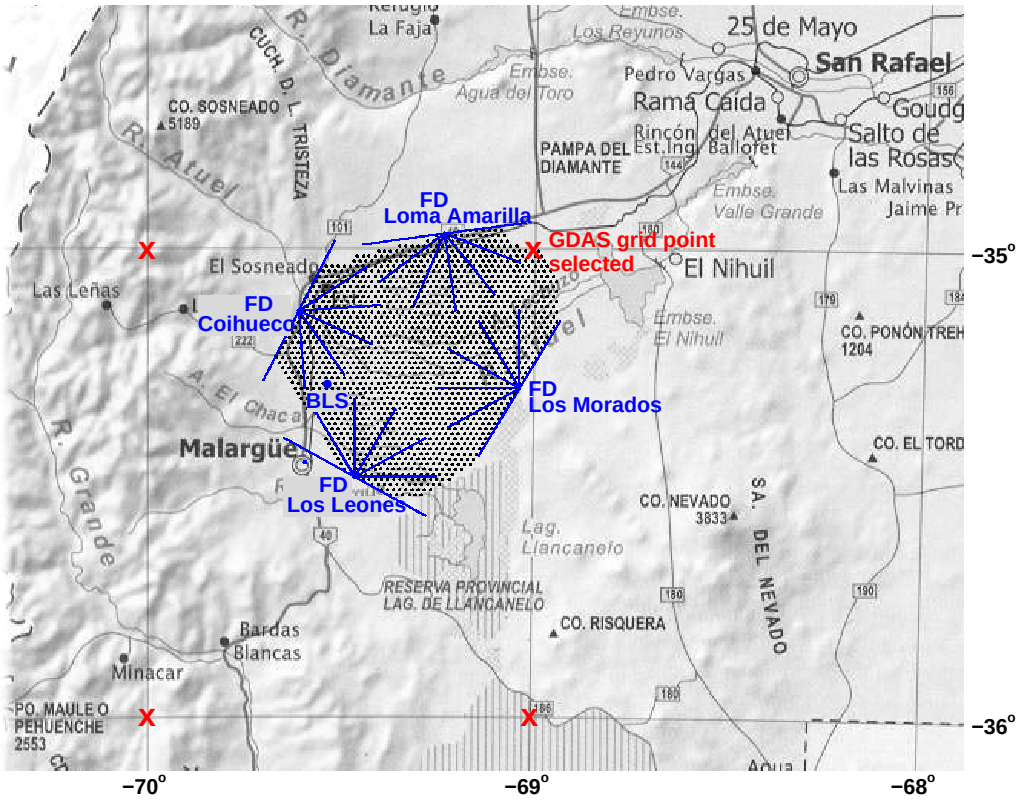

Figure 6.2: Map of the region around the array of the Pierre Auger Observatory with geographical latitudes and longitudes marked at the boundary of the figure. The positions of the surface and fluorescence detectors are superimposed. The available GDAS grid points for that area are marked as red crosses. The coordinates of Malargüe are −35.48° (south) and −69.58° (west), the coordinates of the selected GDAS grid point are −35° (south) and −69° (west).

The first two weeks of May 2005 and weeks 3 and 4 of November 2005 are missing. Other than that, the record is complete up to the present time (end of April 2012).

Because of the lateral homogeneity of the atmospheric variables across the site of the Pierre Auger Observatory [79], only one location point is needed to describe the atmospheric conditions. In Fig. 6.2, the available GDAS grid points are marked as red crosses on a map together with a map of the surface and fluorescence detectors of the Pierre Auger Observatory. The grid point at 35° south and 69° west was chosen, at the north-eastern edge of the surface detector array. The two points to the west of the array are in the foothills of the Andes mountains and therefore not suitable. The point to the south-east of the array is quite far away and with a surface height of 1685 m a.s.l., it is also too high. Nevertheless, the profiles at this point are very similar to those at the chosen point, on average differing by less than 1 K in temperature, less than 1 hPa in pressure and less than 0.3 hPa in water vapor pressure at all altitudes, confirming the homogeneity, see Fig. 6.3.

The height at which the surface data are given changes over the years for the selected grid point. The reasons for these changes are regular improvements of the

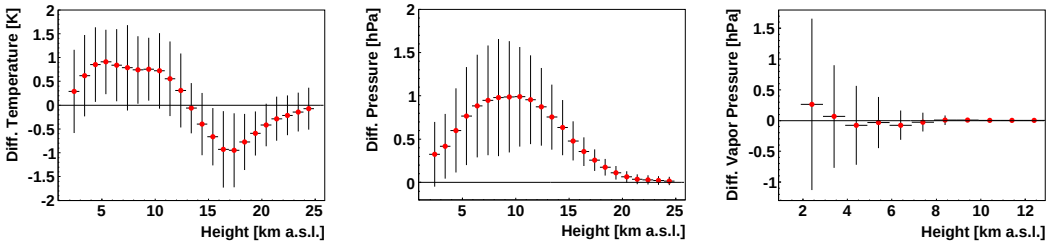

Figure 6.3: Difference in temperature, pressure and water vapor pressure for the chosen GDAS grid point and the point 1° south for 2009. The uncertainties are not normalized to the number of entries.

Table 6.1: Vertical levels of pressure surfaces. For reference, the USStdA height is listed in this table, the actual height for each pressure level is given in each data file. Pressure level 0 contains the surface values.

Level	Pressure [hPa]	Height [km]	Level	Pressure [hPa]	Height [km]
23	20	26.4	11	600	4.2
22	50	20.6	10	650	3.6
21	100	16.2	9	700	3.0
20	150	13.6	8	750	2.5
19	200	11.8	7	800	1.9
18	250	10.4	6	850	1.5
17	300	9.2	5	900	1.0
16	350	8.2	4	925	0.8
15	400	7.2	3	950	0.5
14	450	6.3	2	975	0.3
13	500	5.6	1	1000	0.1
12	550	4.9	0	surface	

models and calculations used to produce the GDAS profiles, or resolution changes in the meteorological model [98]. Starting in January 2005, the surface altitude is 1831.29 m above sea level. On May 31, 2005, the surface height changes to 1403.38 m, and on August 22, 2006 it goes down further to 1328.68 m and stays within a few centimeters of this value until July 27, 2010, when it changes to 1404.65 m. In Fig. 6.4, the surface height provided by the GDAS data sets is shown between January 2005 and December 2011. For reference, the altitudes of the lowest SD tank of the Pierre Auger Observatory (1331.05 m) and the highest and lowest FD sites (Coihueco at 1712.3 m and Los Leones 1416.2 m a.s.l.) are also shown. These changes can occur again in the future, so the surface height of the data has to be monitored for undesired changes [99].

For air shower analysis, only data above ground level in Malargüe are interesting. Therefore, only data from the surface and from pressure levels 6 and above was used. The data from beginning of January to the end of May 2005 have a surface height of around 1800 m. This is even above the height of the highest FD building at

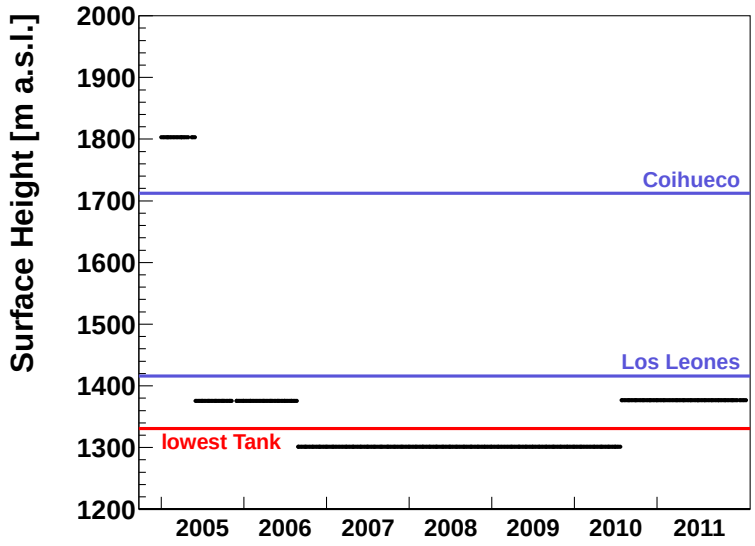

Figure 6.4: The surface height of the GDAS data between January 2005 and December 2011. For reference, the red line marks the height of the lowest tank in the array, and the blue lines represent the height of the FD buildings at Los Leones and Coihueco.

Coihueco. No extrapolation down to the actual ground level of around 1300 m was attempted and these data were discarded. Therefore, the first usable set of data is from June 1, 2005 at 0:00 UTC.

For air shower analyses, several types of information are stored in databases such as the one describing the state variables of the atmosphere. It contains values for temperature, pressure, relative humidity, air density, and atmospheric depth at several altitude levels. The first three quantities and the altitude are directly available in the GDAS data. Air density and atmospheric depth must be calculated. The surface data contain ground height, pressure at the ground, and relative humidity 2 m above ground. Two temperature values are given, one at the surface and one 2 m above ground. The latter was used since it is needed together with the relative humidity, which is also given 2 m above ground, to calculate water vapor pressure.

In the GDAS data, the altitude is given in geopotential meters with respect to a geoid (mean sea level). In the *Offline* air shower analysis framework of the Pierre Auger Observatory, geometric heights with respect to the WGS-84 ellipsoid are used. To move from geoid to ellipsoid, a constant value of 26 m that arises from the geographic location of the Pierre Auger Observatory must be added to the height values of the model. The second step is to convert from geopotential height h to geometric altitude z (both measured in m),

$$z(h,\phi) = (1 + 0.002644 \cdot \cos(2\phi)) \cdot h + (1 + 0.0089 \cdot \cos(2\phi)) \cdot \frac{h^2}{6245000}, \qquad (6.1)$$

where ϕ is the geodetic latitude [100].

Since the GDAS data only go up to around 25 to 30 km, the atmospheric depth at the top of the data profile has to be approximated using the pressure and the

gravitational acceleration from Eq. (4.2), $X = p/g$. From that height, the density is then numerically integrated down to ground level, see Eq. (4.9). The integration is done by interpolating the density every 200 m and using the trapezoidal rule to approximate the integral.

For the simulation and reconstruction of air showers, the description of the atmospheric parameters should ideally range from ground level to the top of the atmosphere. GDAS provides data between about 1400 and 30 000 m. All profiles are extended up to 100 000 m – the approximate boundary to outer space – using the US Standard Atmosphere 1976 [97] which describes the conditions above 30 000 m reasonably well. Below 1400 m, pressure, atmospheric depth, density, and water vapor pressure are exponentially extrapolated down to 1000 m based on the lowest two data points. The temperature profile is extrapolated linearly. Both extensions are outside the field of view of all FD stations.

6.2 GDAS vs. Local Measurements

To validate the quality of the GDAS data and to verify its applicability for air shower reconstructions at the Pierre Auger Observatory, GDAS data are compared with local measurements – atmospheric soundings with weather balloons and ground-based weather stations. The Malargüe Monthly Models (MMM) are also shown in some comparisons as a reference since they were the standard profiles used in reconstructions until recently.

GDAS vs. Soundings with Weather Balloons

Local atmospheric soundings have been performed above the array of the Observatory since 2002, but not on a regular basis. In the beginning, several week-long campaigns of launches were performed. Then, a pre-determined schedule was used to coordinate launches during and between dark periods with FD data taking and finally, with the BtS program, soundings are triggered by particularly high energy events during FD data taking only (see Sec. 5.3). Most of the balloons were launched from the Balloon Launching Station (BLS, see Fig. 6.2). To provide a set of atmospheric data for every measured air shower, the soundings were averaged to form monthly mean profiles. The current version of these Malargüe Monthly Models (MMM) were compiled in early 2009. The models on average describe the atmosphere reasonably well, but show considerable fluctuations when compared to the actual sounding data [79]. The uncertainties of the profile for each variable are given by the standard error of the variation within each month together with the absolute uncertainties of the sensors measuring the corresponding quantity. For atmospheric depth profiles, a piecewise fitting procedure is performed to ensure a reliable application of these parameterizations to air shower simulation programs. An additional uncertainty is included which covers the quality of the fitting procedure.

In Fig. 6.5, the GDAS model data are compared with the measured radiosonde data between 2005 and 2008. The comparison between the radiosonde data and the monthly models is also shown. The monthly mean profiles are averaged from the sounding data until end of 2008, thus, they fit local sounding data of this period very well, see red squares in Fig. 6.5. The error bars denote the RMS of the differences at each height. The wave-like shape in the difference graph for the atmospheric depth

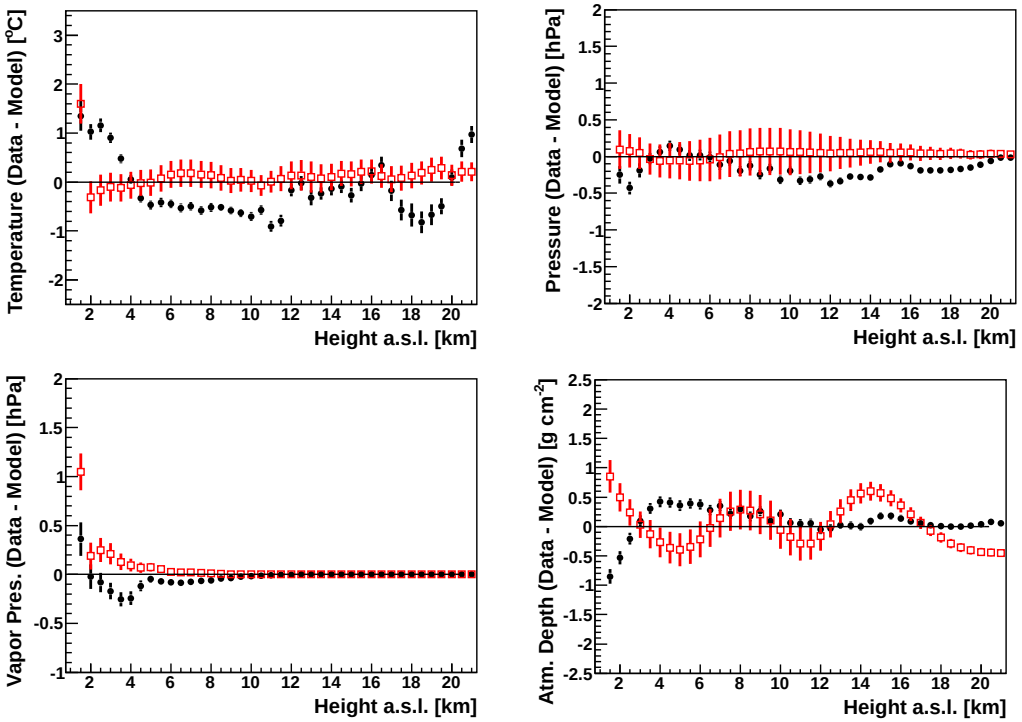

Figure 6.5: Difference of measured radiosonde data and GDAS models (black dots) and monthly mean profiles (red squares) versus height for all sounding data between 2005 and 2008.

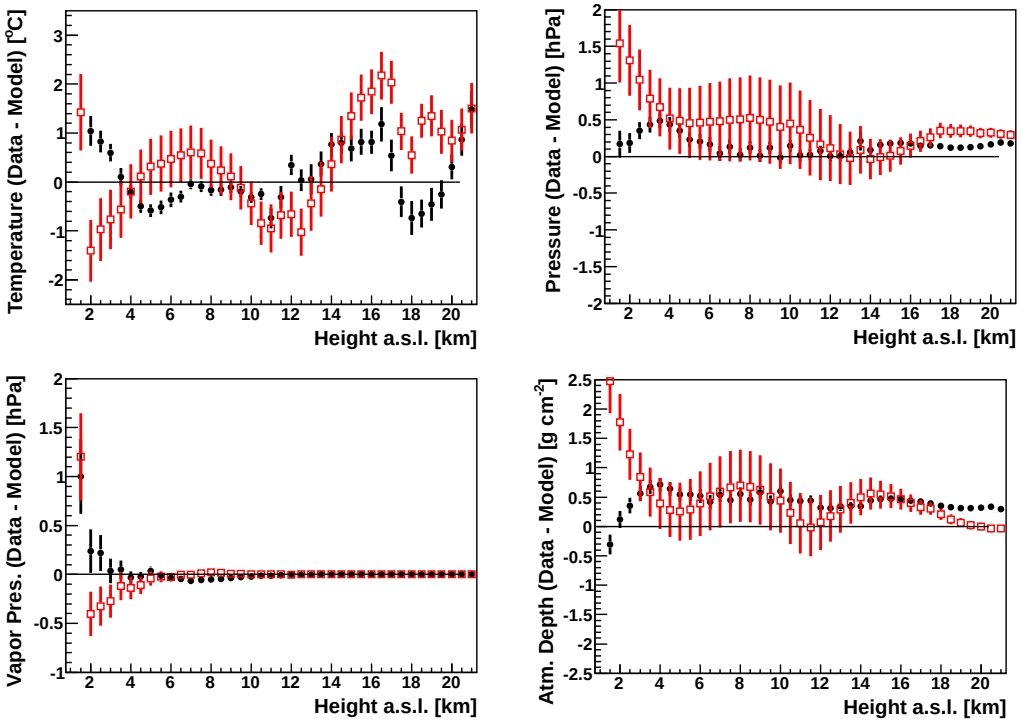

Figure 6.6: Difference of measured radiosonde data and GDAS models (black dots) and monthly mean profiles (red squares) versus height for all radiosondes performed in 2009 and 2010.

X is driven by the piecewise parameterization of X in the MMM. Above around 5 km, the GDAS data deviate only marginally from the measured data (black dots in Fig. 6.5). Closer to the ground, slightly larger differences become apparent. The measured temperature is consistently higher than the model temperature. However, this might be caused by two problems acting in the same direction. For our local radio soundings, the temperature sensor might be quite often not properly acclimatized to outside conditions but is affected by the inside temperature of the Balloon Launching Station. It takes some minutes to overcome this effect during which time the weather balloon is already launched. When compiling the MMM, only temperature data at 1600 m a.s.l. and above were taken from the radio soundings. To extrapolate to lower altitudes, a fit to these sounding data combined with data from local weather stations at 1401 m, 1420 m, 1423 m, 1483 m, and 1719 m was performed. However, data from the weather stations might be influenced by the direct surface conditions beneath, since they are not standardized meteorological stations. It is also possible that the GDAS model does not adequately describe the heated surface of the elevated plain of the Pampa Amarilla and tends to assume free-atmosphere conditions. The pressure data of both models are in good agreement. The water vapor pressure fits almost perfectly, although the model values close to ground are both too low compared to measured data which can be traced back to the difficult handling of humidity in general. In particular, the pressure differences propagate into the atmospheric depth where deviations from the measured data on the same scale as for the monthly mean profiles are seen.

In the comparison displayed in Fig. 6.6, only radiosonde data from 2009 and 2010 are used in order to illustrate the strength of the GDAS model data. The MMM are completely independent of this set of radio soundings. The most obvious changes compared with Fig. 6.5 are the worse descriptions of actual radio soundings with monthly mean profiles. Even though the uncertainties become larger, the MMM do not describe the conditions measured during the years 2009 and 2010 very well. In contrast, the GDAS data can represent the local conditions much better and the intrinsic uncertainty is consistently small.

In the following, the non-perfect agreement between GDAS data and local sounding data below approximate 5 km a.s.l. is investigated in more detail. This effect close to ground could be caused by the nearby Andes and their influence on the climate above the array. GDAS was developed for global atmospheric predictions and therefore could be inadequate for very local atmospheric conditions. Under normal circumstances, the wind carries weather balloons launched at the Pampa Amarilla north-east or east with a horizontal displacement of about 100 to 150 km for ascents up to about 20 km a.s.l. In some cases however, the balloon just ascends with only a small horizontal drift in any direction, whereas the opposite extreme cases are horizontal displacements of more than 200 km. For this study, 25 short and localized ascents and 18 launches with very long balloon paths were selected manually. The differences between GDAS data and the measured data for both groups are shown in Fig. 6.7. The pressure data from GDAS do not describe these extreme conditions at the Pierre Auger Observatory as well as those seen under normal circumstances. For extremely short soundings, the local measurements reveal a high pressure area close to ground. This typically quite local effect is not reproduced by GDAS but for higher altitudes, the model data fit very well again. High pressure zones often indicate a stable atmospheric layering, so conditions change only on long-term

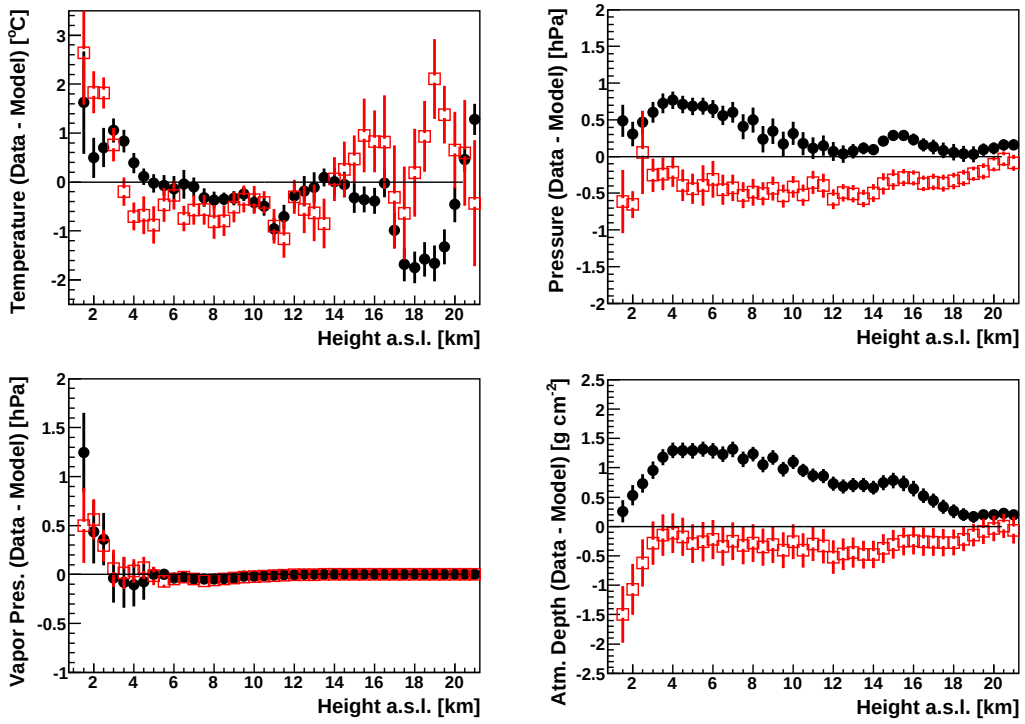

Figure 6.7: Difference of measured radiosonde data and GDAS models for short (black dots) and long ascents (red squares) versus height.

scales. This could cause the good description of temperature profiles by GDAS. For the other extreme case, the launches with very long balloon paths, the local pressure data indicate a low pressure area, accompanied by significant winds. The conditions are dominated by turbulences, indicated by short-term and small-scale temperature variations. Thus, the GDAS model data do not fit the local measurements well. Overall, it is rather difficult to say if the topology of the Andes is the source of uncertainty or if it is also an effect of quite extreme weather conditions which might be induced by the structure of the Andes in the vicinity of the Pampa Amarilla. Moreover, both groups of investigated ascents are extremes and do not describe the usual conditions. Less than 20% of the ascents launched at the Pierre Auger Observatory fall into either category.

Finally, possible inconsistencies between local measurements and GDAS data close to the surface are investigated by using weather station data. While radiosondes may suffer from measurement uncertainties near the ground, the weather stations are specifically designed to continuously measure the ground values.

GDAS vs. Ground Weather Stations

Five weather stations continuously monitor atmospheric values close to the ground, at about 2 to 4 m above surface level. Four are located at the FD stations, and one was set up near the center of the array at the Central Laser Facility (CLF). To make sure that the GDAS data describe the conditions at the ground reasonably well, the values provided by the GDAS data set are compared to all available weather station

Table 6.2: Mean and variance values for the histograms shown in Fig. 6.8. Values for the pressure were not corrected for the height difference of the stations, but they are consistent with those differences. Applying the USStdA, the pressure difference due to the different altitudes of the weather stations are −2.0 hPa (LL), −8.6 hPa (LA), −2.3 hPa (LM), and −32.8 hPa (CO).

	Mean			RMS		
	ΔT [K]	Δp [hPa]	Δe [hPa]	ΔT [K]	Δp [hPa]	Δe [hPa]
$x_{\mathrm{WS}} - x_{\mathrm{GDAS}}$						
CLF	1.3	0.4	−0.2	3.9	1.2	2.1
LA	−0.3	0.2	−0.7	3.9	1.1	2.3
$x_{\mathrm{WS}} - x_{\mathrm{CLF}}$						
LL	1.3	−1.3	0.0	2.6	0.4	0.9
LM	1.3	−1.6	0.6	3.3	0.4	0.9
LA	1.3	−8.0	0.5	2.8	0.5	1.0
CO	0.5	−34.2	−0.6	4.1	1.1	1.0

data. The GDAS data are interpolated for the height of the weather station.

In the histograms on the left of Fig. 6.8, the differences between measured weather station data and GDAS model data are shown for the weather stations close to the CLF and FD Loma Amarilla. All data measured in 2010 were used. Temperature, pressure, and water vapor pressure agree very well. Details of the histograms are listed in Tab. 6.2.

On the right side of Fig. 6.8, the differences of the data of the individual weather stations are shown. The CLF weather station is close to the middle of the array and was chosen as a reference. Values for the pressure were not corrected for the height difference of the stations, but they are consistent with the expected pressure differences due to the differences in height of the stations. The mean and width of the LA-CLF distribution is very similar to the distributions on the left for the GDAS data. These two histograms are expected to be similar because of the vicinity of the selected GDAS grid point and the FD building Loma Amarilla. Overall, the differences between the GDAS data and the weather station data are of the same order as the difference in data of two different weather stations. Only the difficult predictability of water vapor in the atmosphere close to ground can be seen again.

In Fig. 6.9, the differences in temperature for the weather station at Los Morados are analyzed in more detail. At the top left, all data measured every 5 minutes are compared with GDAS data. Additionally, only station data every three hours at which new GDAS data are available are shown, scaled by a factor of 36. Both distributions show identical means of 0.1 K, as well as similar RMS values of 2.7 K and 2.6 K for all data and for the 3-hourly data, respectively. The atmospheric parameters at the Observatory are very stable during 3-hour periods. At the top right, the data are split into day and night. Night is defined as the UTC hours between 0 and 10. Therefore, with 14 compared to 10 hours of data, the daytime distribution contains more data. For Los Morados, both distributions are close to

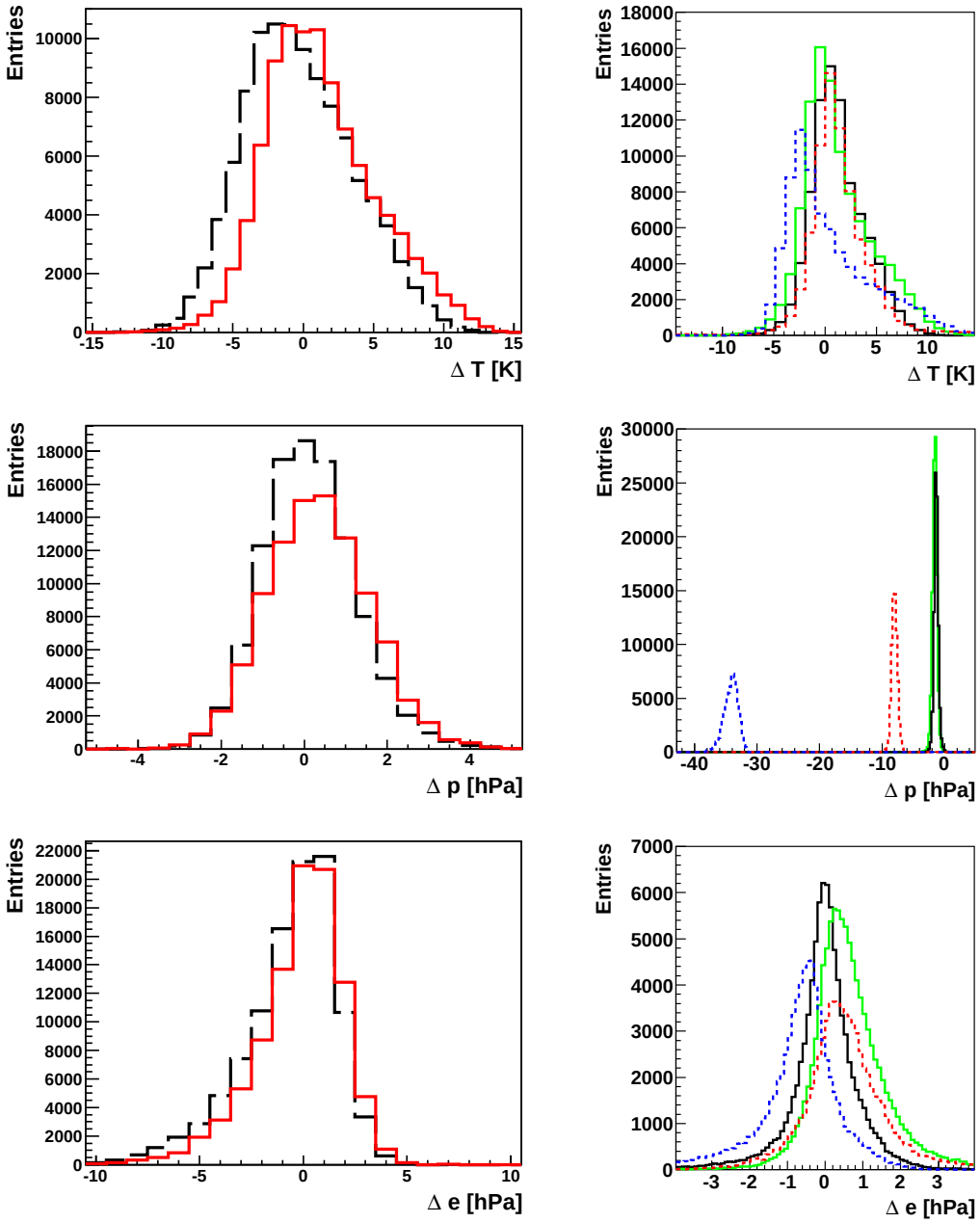

Figure 6.8: Difference of measured weather station data and GDAS models for all data from 2010. The mean and variance values for all histograms shown can be found in Tab. 6.2. On the left, the differences GDAS model minus measured data in temperature T, pressure p, and water vapor pressure e are shown for the weather station at the CLF (solid red line) and the station at FD Loma Amarilla (dashed black line). On the right, the differences between the data of the individual stations are shown. The solid black line represents the difference between data measured with the Los Leones (LL) weather station and the data from the CLF weather station. The solid green line corresponds to Los Morados (LM) minus CLF, the dashed red line is for Loma Amarilla (LA) minus CLF and the dotted blue line indicates Coihueco (CO) data minus CLF data.

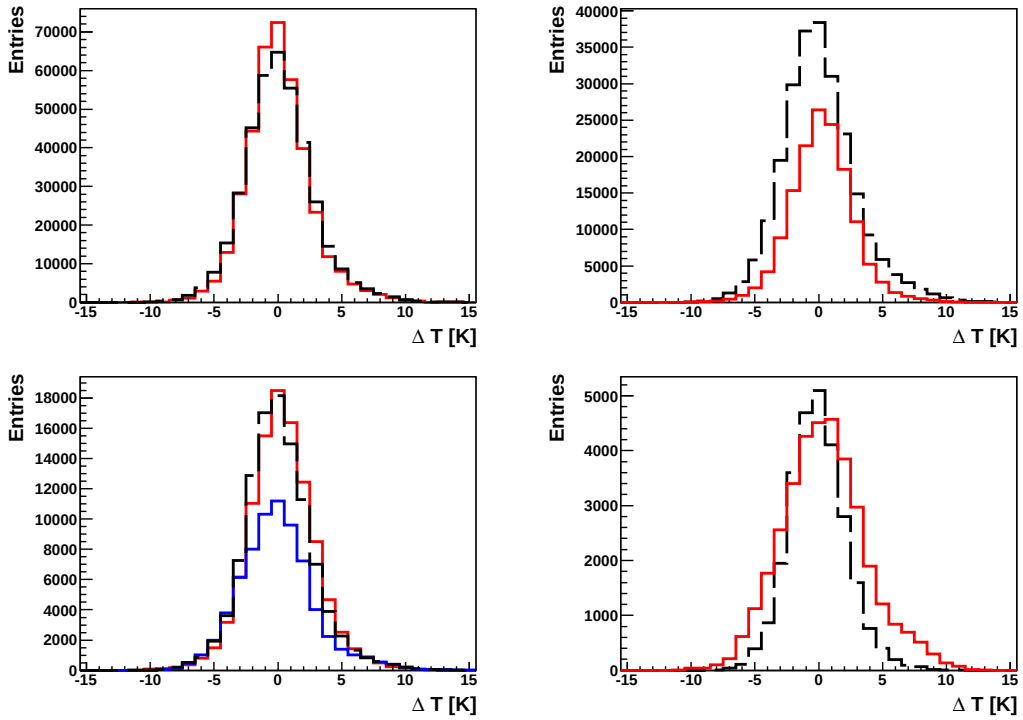

Figure 6.9: The difference of GDAS minus weather station data in temperature is shown for the weather station at Los Morados. At the top left, the difference of all data measured every 5 minutes (dashed black) is compared to the difference only of data measured every three hours when new GDAS data are available (solid red, scaled by 36). At the top right, all data are split into daytime (dashed black) and nighttime (solid red) measurements. At the bottom left panel, all data are separated by years (2007 in solid blue, 2008 in solid red, 2010 in dashed black). At the bottom right, data are split into austral summer and winter, represented by one month each (January in dashed black, July in solid red).

each other, with a mean of 0.0 K and RMS of 2.9 K during the day and a mean of 0.2 K and RMS of 2.4 K at night. A small difference at night is noticeable, with the GDAS data giving higher temperatures than the weather station. The distributions for different years (bottom left) and different seasons (bottom right), represented by one month of austral summer and one from winter, show no distinct features or differences. Similar studies for pressure and water vapor pressure mostly yield similar results. Nevertheless, two deviations from this general pattern are discussed in the following.

In the left panel of Fig. 6.10, the temperature distributions for the station at Loma Amarilla are shown, split into daytime (solid red) and nighttime (dashed black) measurements. A clear separation of the two distributions is found. The mean of the distributions is -1.6 K for daytime and 1.6 K for nighttime, resulting in a difference of 3.2 K. This difference might be due to the local environment in which the weather station is placed. While some stations are far away from the FD buildings, others had to be mounted closer to or on top of other facilities. Thus, a standardized meteorological measurement can not be guaranteed.

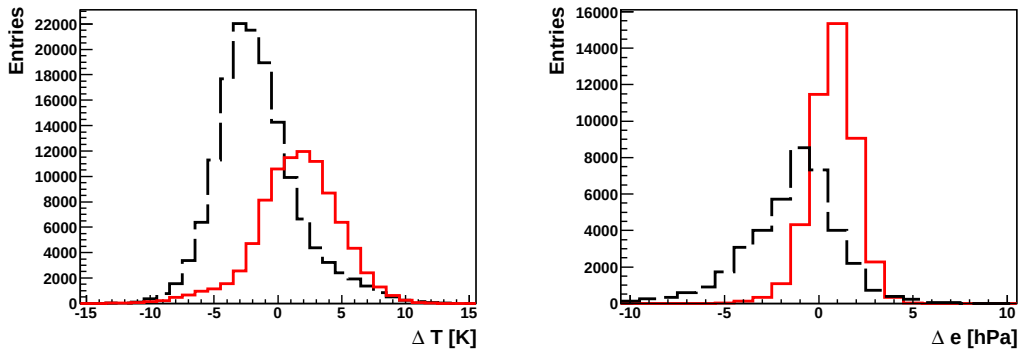

Figure 6.10: The difference of GDAS minus weather station data in temperature is shown in the left panel for the station at Loma Amarilla, separated by time of day (nighttime in dashed black, daytime in solid red). In the right histogram, the difference in water vapor pressure for the station at the CLF is shown separated by seasons (austral summer in dashed black, winter in solid red).

On the right of Fig. 6.10, the water vapor pressure for different seasons measured at the weather station at the CLF is shown. Clear differences are apparent. In austral winter (July), the water vapor pressure is very low, and the measurements agree better with GDAS data, the mean of the distribution is 0.8 hPa with an RMS of 1.2 hPa. In austral summer (January), the deviations are largest, where the mean difference drops to -1.4 hPa, and the RMS doubles to 2.4 hPa. This indicates that the GDAS description of humidity is not perfect, underestimating the humidity in summer. However, the water vapor pressure calculation strongly depends on the temperature, so differences in temperature due to local effects of the surroundings of the station also affect this comparison.

A comparison of wind profiles from GDAS data and measured wind from radiosondes was done for a study of air mass trajectories and aerosol origins above the Pierre Auger Observatory [101]. The agreement was found to be very good.

Apart from the differences that were seen between radiosonde data and GDAS data near the surface in the previous section, the comparison of GDAS data with weather station data shows a very good agreement. The GDAS data describe the conditions at the Pierre Auger Observatory very well. Because of its highly reliable availability and high frequency of data sets, GDAS data are a suitable replacement for local radio soundings and also for the local monthly models.

GDAS vs. Radio Soundings at the Colorado R&D Site

In addition to the measurements in Argentina, similar radiosonde launches were performed in south-east Colorado, see Sec. 5.2.3. 28 weather balloons were launched between September 2009 and May 2011 using identical radiosondes and equipment. The comparisons with the GDAS data for this location show differences of the same order as for the location of the Pierre Auger Observatory, see Fig. 6.11. A temperature difference of less than 1.5°C in temperature, 0.6 hPa in pressure and vapor pressure, and 0.5 g cm^{-2} in atmospheric depth is seen at all altitudes. Compared to the differences found in Argentina, cf. Fig 6.6, the difference in temperature is

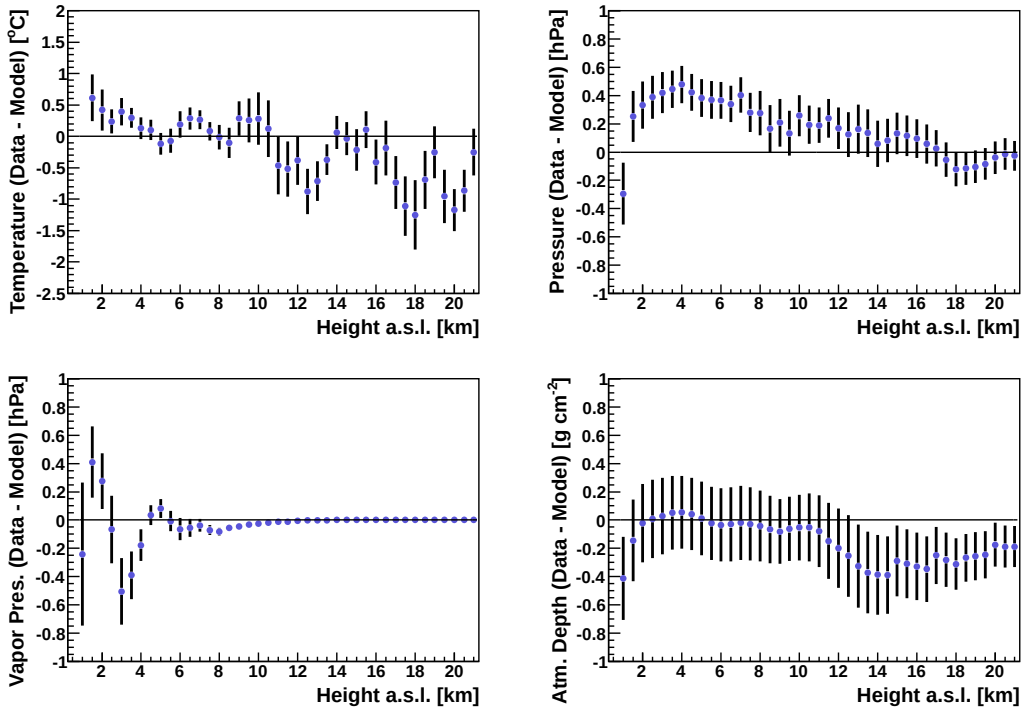

Figure 6.11: Difference of measured radiosonde data and GDAS models in temperature, pressure, vapor pressure and atmospheric depth for balloons launched at the Colorado R&D site.

slightly smaller in the lower part of the atmosphere and a little larger above 16 km. The pressure difference is about the same. In vapor pressure, the differences found in Argentina are smaller, in atmospheric depth the differences in Colorado are much smaller. It should be noted that the balloon launches in Colorado do not cover every season with similar statistics, possibly introducing a seasonal bias. Still, it is remarkable that the differences in Argentina are of the same order or sometimes even better than the differences in Colorado, because most of the global atmospheric models, in particular those developed in Europe and North America, typically describe the conditions at the northern hemisphere much better. This is due to the fact that atmospheric measurements in South America and in general at the southern hemisphere are sparse and accurate modeling of the atmosphere is predicated on real data.

Comparisons of GDAS data and radio soundings at further locations like airports have been done and similar or smaller differences have been found. However, the radio soundings from south-east Colorado are independent data while other available data are from radio sounding databases which are part of the global meteorological network used for the creation of GDAS.

6.3 Air Shower Reconstruction using GDAS data

To study the effects caused by using the GDAS data, all air shower data collected at the Pierre Auger Observatory between June 1, 2005 and end of 2010 are used in

a reconstruction analysis using the *Offline* software framework of the Pierre Auger Observatory [88]. The change of atmosphere description will mainly affect the reconstruction of the fluorescence data, c.f. Sec. 4.2. It is known that varying atmospheric conditions alter the fluorescence light production and transmission [79]. The transmittance of the actual atmosphere is regularly measured during FD shifts and made available for air shower reconstructions via databases. The light production has to be calculated analytically during the reconstruction procedure. Its strong atmosphere-dependence as described in Sec. 4.2 is applied in the air shower reconstruction analysis.

Data Reconstruction

The following analysis is based on three sets of reconstructions. The first set, FY, is the until recently standard reconstruction of the Pierre Auger Observatory. The fluorescence yield is calculated with its atmosphere-dependence as described in [102], along with the monthly mean profiles (MMM) obtained for the site of the Pierre Auger Observatory. For the second set, $\mathsf{FY}_{\mathrm{mod}}$, all currently known atmospheric effects in the fluorescence calculation are taken into account. Together with the standard atmosphere-dependence, the temperature-dependent collisional cross sections and humidity quenching are included ([59] and references therein). Parameterizations for these two effects are taken from AIRFLY [68] and later conference contributions by the AIRFLY collaboration. Again, the MMM are used. The third set, $\mathsf{FY}_{\mathrm{mod}}^{\mathrm{GDAS}}$, also explores the efficiency of the full atmosphere-dependent fluorescence description, but here the atmospheric MMM are exchanged with the new 3-hourly GDAS data.

Comparing the reconstruction sets with each other, the variation of the reconstructed primary energy E of air showers and the position of shower maximum X_{max} can be determined, see Fig. 6.12. In the two upper figures, the binned difference of E and X_{max} is displayed, and the dependences on energy and month of these differences are shown in the figures in the middle and bottom, respectively.

Using GDAS data for the reconstruction instead of MMM affects the reconstructed primary energy only slightly. The mean of the difference $\mathsf{FY}_{\mathrm{mod}}^{\mathrm{GDAS}}$ minus $\mathsf{FY}_{\mathrm{mod}}$ is 0.4% with an RMS of 1.4% (Fig. 6.12, top left, solid black line). For the reconstructed X_{max}, only a small shift of $-1.1\,\mathrm{g\,cm^{-2}}$ is found with an RMS of $6.0\,\mathrm{g\,cm^{-2}}$ (Fig. 6.12, top right, solid black line). However, comparing the full atmosphere-dependent reconstruction $\mathsf{FY}_{\mathrm{mod}}^{\mathrm{GDAS}}$ with the unmodified reconstruction FY, a clear shift in E can be seen. An increase in E by 5.2% (RMS 1.5%) and a decrease of X_{max} by $-1.9\,\mathrm{g\,cm^{-2}}$ (RMS $6.3\,\mathrm{g\,cm^{-2}}$) is found. These modified fluorescence settings are now used in the reconstruction of the Pierre Auger Observatory, in conjunction with other improvements to the procedure, see [53].

The difference in reconstructed E vs. mean E (Fig. 6.12, middle left) reveals a small energy dependence, increasing towards higher energies. The description of atmospheric conditions close to the ground is very difficult in monthly mean profiles since the fluctuations in temperature and humidity are larger in the lower levels of the atmosphere (below 4 km) than in the upper layers. Consequently, a more precise description of actual atmospheric conditions with GDAS will alter the energy reconstruction compared with MMM-based reconstructions for air showers that penetrate deeply into the atmosphere, usually high energy events. The full atmosphere-

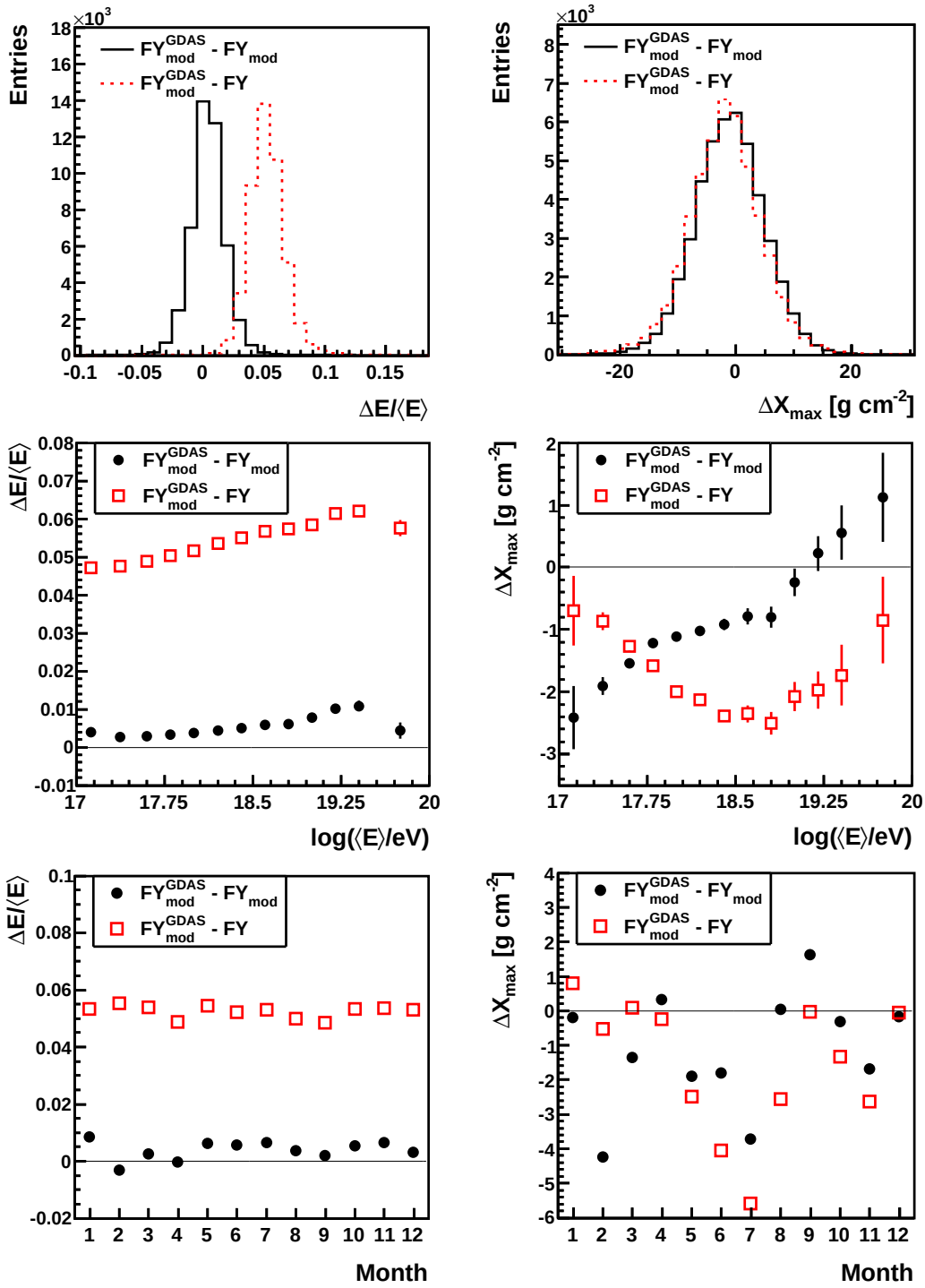

Figure 6.12: Difference of reconstructed E (left) and $X_{\max}$ (right). Top row: binned differences. Middle row: differences as a function of energy. Bottom row: differences as a function of month. Black solid line or filled dots for $\mathsf{FY}_{\mathrm{mod}}^{\mathrm{GDAS}}$ minus $\mathsf{FY}_{\mathrm{mod}}$, and red dashed line or open squares for $\mathsf{FY}_{\mathrm{mod}}^{\mathrm{GDAS}}$ minus FY.

dependent fluorescence calculation alters the light yield for conditions with very low temperatures, corresponding to higher altitudes. The energy dependence of the $X_{\max}$ differences is a combined effect of slightly changed humidity conditions close to ground and temperature conditions higher up in the atmosphere together with the full atmosphere-dependent fluorescence calculation (Fig. 6.12, middle right).

The difference in energy is quite uniform throughout the year, see Fig. 6.12, bottom left. For switching on GDAS instead of MMM (black dots), it is confirmed that GDAS describes the conditions at the Pierre Auger Observatory very well, as good as the MMM. Switching on the full atmosphere-dependent fluorescence calculation does not show a monthly dependence because the overall integral of the longitudinal light profiles is hardly changed, see e.g. [103]. Only the modification of the shape of the longitudinal light profile causes a small monthly dependence of $X_{\max}$ (Fig. 6.12, bottom right).

In the following, some systematics caused by the particular shower geometry are studied. In the first set of figures (Fig. 6.13, top row), the difference in E and $X_{\max}$ vs. zenith angle θ of the shower is displayed. The energy variation is quite uniform around the mean value up to about 60°. Only more inclined showers show a stronger shift of reconstructed energy for the modified fluorescence yield calculation. Concerning the position of shower maximum, a dependence on zenith angle can be seen above 30°.

Shown in the bottom row of Fig. 6.13, the E and $X_{\max}$ dependence on geometrical height of shower maximum gives a more pronounced view of the atmospheric conditions in combination with the atmosphere-dependent fluorescence description. Showers reaching their maximum at an average altitude between 3 and 7 km show the mean E difference as expected from Fig. 6.12, top left. Showers with very shallow or very deep $X_{\max}$ are reconstructed with a 7–8% higher primary energy compared with that using the standard fluorescence calculation. The reconstructed $X_{\max}$ follows the expectations according to the study shown in [103].

Impact on Shower Reconstruction Uncertainties

To study the effect that the GDAS data have on the uncertainties of air shower reconstructions, air showers induced by protons and iron nuclei are simulated using the CONEX shower generator [104] with the QGSJETII hadronic interaction model [105] for shower energies between $10^{17.5}$ eV and 10^{20} eV. The fluorescence light is generated including temperature-dependent collisional cross sections and vapor quenching. The time stamps of the air shower events correspond to the times of 109 radio soundings between August 2002 and December 2008 so that actual atmospheric profiles can be used in the simulation. All 109 launches were performed at night during cloud-free conditions. After the atmospheric transmission, the detector optics and electronics are simulated. The resulting data are then reconstructed using the radiosonde data, as well as the GDAS data.

A basic set of quality cuts is applied. The shower maximum has to be in the observed part of the track, and the uncertainty in reconstructed energy and $X_{\max}$ must be below 20% and 40 g cm^{-2}, respectively. Also, the Gaisser-Hillas profile fit has to have a given quality, $\chi^2/\mathrm{Ndf} < 2$, and the fraction of Cherenkov light from the shower observed by the telescopes must be less than 50%. After applying all cuts, the values of energy and $X_{\max}$ from the reconstructions with different

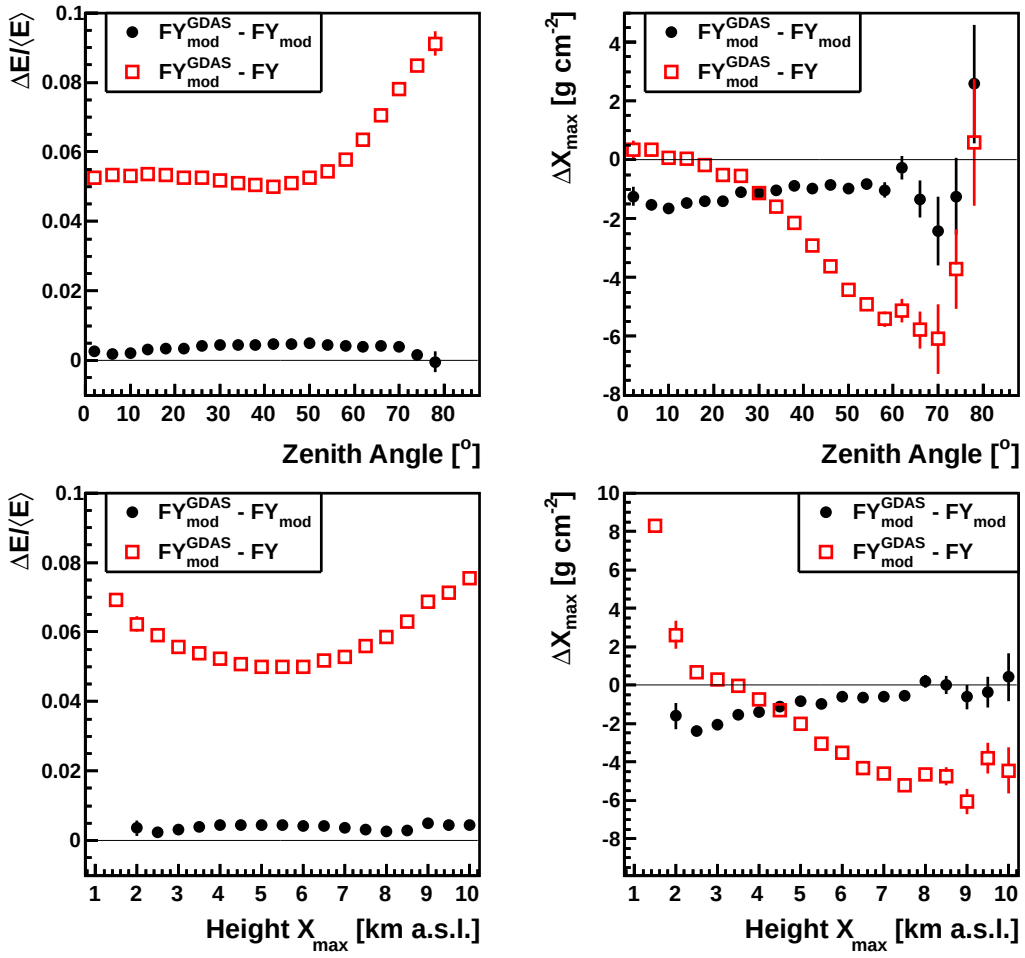

Figure 6.13: Energy difference (left) and $X_{\max}$ difference (right) vs. zenith angle θ of EAS (top) and vs. geometrical height of shower maximum (bottom). Black filled dots are for $\mathsf{FY}^{\mathrm{GDAS}}_{\mathrm{mod}}$ minus $\mathsf{FY}_{\mathrm{mod}}$, and red open squares for $\mathsf{FY}^{\mathrm{GDAS}}_{\mathrm{mod}}$ minus FY.

atmospheric description are compared. The differences in these reconstructions yield the uncertainties that are introduced by the use of the GDAS data instead of the actual atmospheric profile.

The same study has been performed to determine the uncertainties from the MMM [85]. There, the systematic error is less than 1% in energy and less than $2\,\mathrm{g\,cm^{-2}}$ in $X_{\max}$. In the energy range from $10^{17.5}\,\mathrm{eV}$ to $10^{20}\,\mathrm{eV}$, random energy-dependent reconstruction uncertainties of $\pm 1\%$ and $\pm 5\,\mathrm{g\,cm^{-2}}$ for low energies up to $\pm 2\%$ and $\pm 7\,\mathrm{g\,cm^{-2}}$ for high energies were found. In the course of our new study, the same uncertainties due to the MMM are computed again. The main difference between the current analysis and the previous one is the implementation of the temperature-dependent collisional cross sections and the humidity quenching in the calculation of the fluorescence yield.

In Fig. 6.14, both results of the new study are shown, the uncertainties due to MMM and those due to GDAS. A deviation from zero indicates a systematic error, and the error bars denote the RMS spread of all simulated events and are a measure of the reconstruction uncertainty due to this atmospheric parameterization.

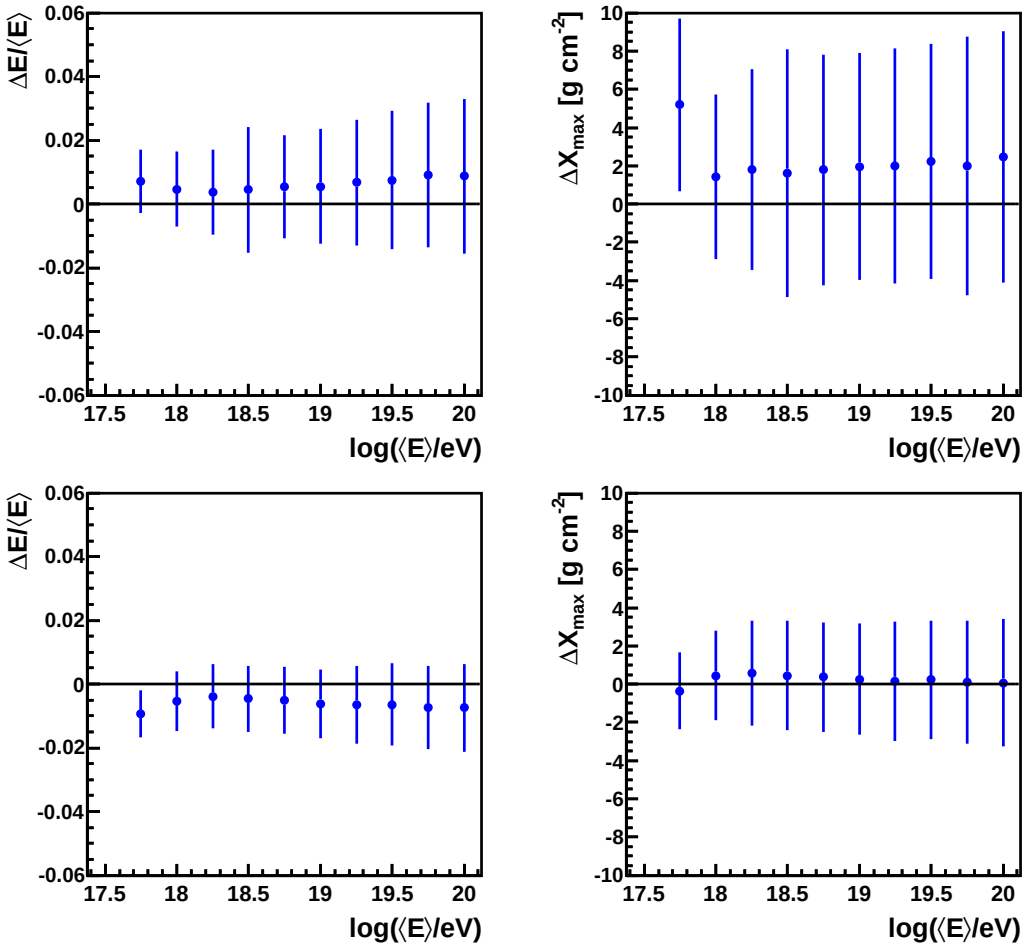

Figure 6.14: Energy difference (left) and $X_{\max}$ difference (right) vs. reconstructed FD energy for simulated showers. The influences of the monthly models (top) and of GDAS data (bottom) are shown. Error bars denote the RMS spread.

In the top panels, the influence of the MMM compared to the measured atmospheric parameters from radiosondes is shown. The results for the systematic shifts are in agreement with the previous study [85], with only the systematic shift for $X_{\max}$ in the lowest energy bin being higher. The RMS spread in energy is $\pm 0.9\%$ for low energies and up to $\pm 2.4\%$ for high energies. In $X_{\max}$, the RMS is between $\pm 4\,\mathrm{g\,cm^{-2}}$ for low energies and $\pm 6.5\,\mathrm{g\,cm^{-2}}$ for high energies.

The influence on the reconstruction due to GDAS data is shown in the bottom part of Fig. 6.14. The systematic shifts in energy are of the same order, below 1%, but of opposite sign. The shifts in $X_{\max}$ are much smaller than for the MMM, less than $0.5\,\mathrm{g\,cm^{-2}}$. The RMS spread is also considerably smaller, $\pm 0.9\%$ and $\pm 2\,\mathrm{g\,cm^{-2}}$ for low energies, and $\pm 1.3\%$ and $\pm 3.5\,\mathrm{g\,cm^{-2}}$ for high energies. The energy uncertainty at low energies is comparable to the uncertainty introduced by the MMM, but at high energies the uncertainty is reduced by almost 50%. For $X_{\max}$, the uncertainties in all energy bins are reduced by a factor of two.

This study of the reconstruction uncertainties further demonstrates the advantages of GDAS data over the monthly mean profiles.

6.4 Monthly Models and Parameterizations from GDAS data

The air shower simulation package CORSIKA [106] uses parameterizations of atmospheric depth to simulate particle interaction in the atmosphere. The parameterization is done in four layers between mean sea level and 100 km. A fifth layer is added for technical reasons. In this layer between 100 km and 112.8 km, the atmospheric depth is decreasing linearly to $0.0\,\mathrm{g\,cm^{-2}}$. Apart from the parameterizations of the US Standard Atmosphere 1976 [97] and some other local atmospheres, five seasonal parameterizations (two austral winter profiles) for Malargüe conditions are available which were compiled in 2003 and are based on 37 balloon launches from 2002 and 2003 [107].

GDAS data are available for the whole globe with a temporal resolution of 3 hours. For the site of the Pierre Auger Observatory, close to the city of Malargüe, the grid point at 35° south and 69° west is chosen. At this position, reasonable data are available starting in June 2005. To avoid the over-representation of certain months in these new GDAS monthly models, all GDAS data were used until May 2011. There is a gap of two weeks in November 2005, but it is small enough not to affect the average. In total, 17 416 single profiles, around 1 450 per month, were used.

GDAS provides profiles for temperature T, pressure p, and relative humidity u up to a height of about 26 km. Using this information, the water vapor pressure e and the air density ρ are calculated. The atmospheric depth X is calculated by integrating the density from the highest point of the GDAS profile down to the ground. The starting value for this integration is estimated at the highest available point using the pressure and gravitational acceleration.

In Fig. 6.15, altitude-dependent profiles of T, p, u, e, ρ and X are shown for every month between June 2005 and May 2011. A clear seasonal effect can be seen in all four observables, but the same months from different years show very similar behavior. The six individual profiles for each year were averaged to monthly profiles, see Fig. 6.16. The two most extreme conditions are found in February, the average is shown in red, and July, in blue. The influence of using only GDAS data of hours during daytime or nighttime was investigated. A difference is only noticeable up to a few kilometers above ground and was within the statistical uncertainties introduced by the averaging, see Fig 6.17. Thus, all data are used for the procedure and no explicite nighttime atmospheric profiles are produced.

6.4.1 Parameterizing the Atmospheric Depth

To simulate air showers using realistic atmospheres, parameterized atmospheric depth profiles can be implemented in CORSIKA. The atmosphere between sea level and 100 km is divided into four layers with variable borders. A fifth layer is added in order to decrease the atmospheric depth linearly to zero. Since GDAS only provides values up to a height of around 26 km, the profiles are extended using adjusted pressure profiles of the US Standard Atmosphere 1976 [97], USStdA in the following. The USStdA fits the Argentine atmosphere rather poorly in the lowest 20 km, but agrees quite well for higher altitudes, as can be seen from the differences in pressure and atmospheric depth in Fig. 6.16. In the lowest four layers $i = 1 \ldots 4$, the depth

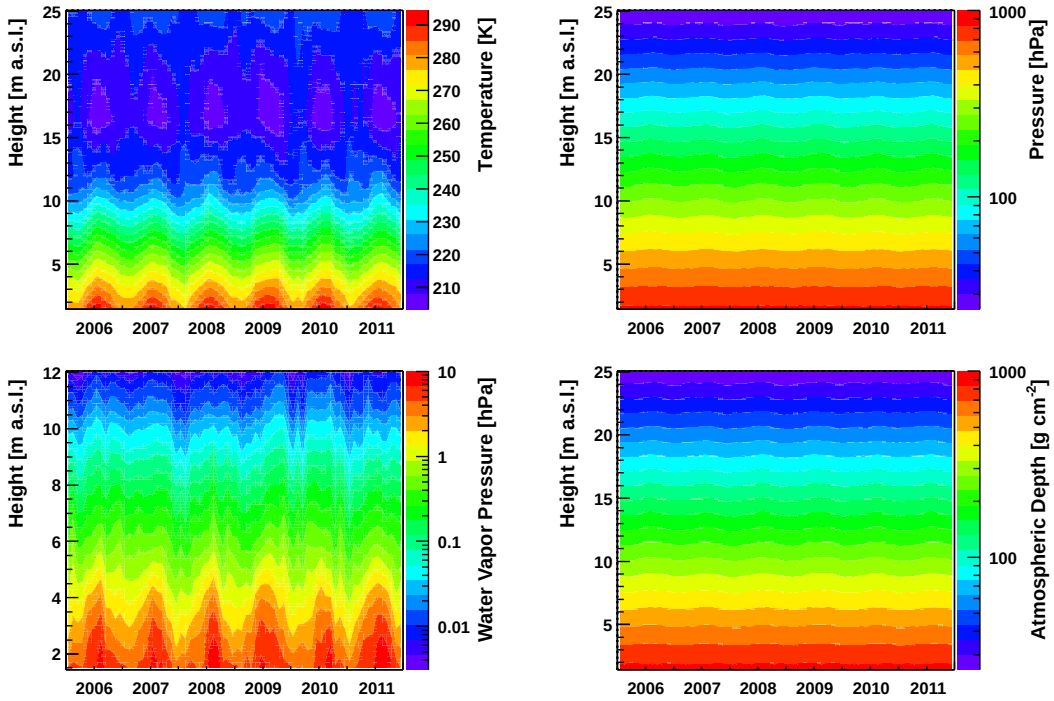

Figure 6.15: Monthly average profiles between June 2005 and May 2011. The dates mark the start of that year.

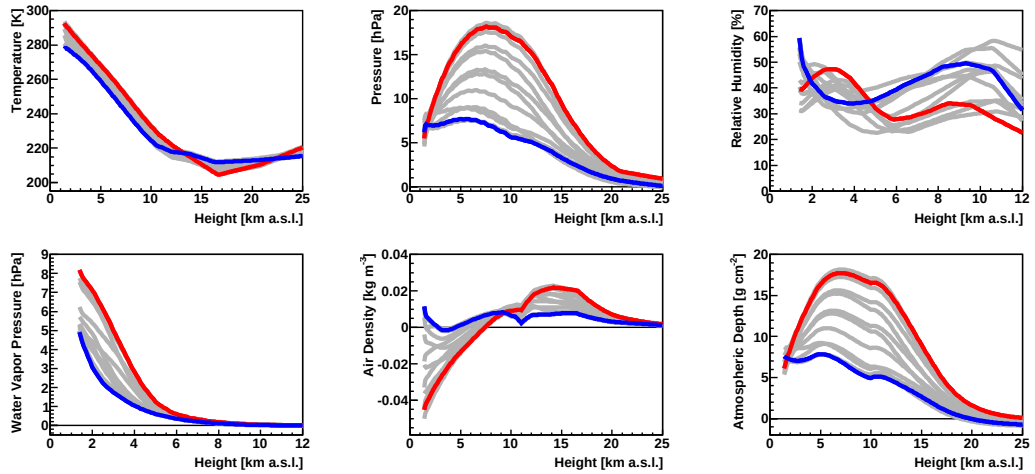

Figure 6.16: Monthly averages for temperature, pressure, relative humidity, water vapor pressure, air density and atmospheric depth. Pressure, density and depth are shown relative to the US Standard Atmosphere [97]. The kinks in the differences are due to the different layers in the USStdA. February is drawn in red, July in blue. Please note, that the relative humidity and the water vapor pressure are only plotted up to 12 km because of its negligible contribution at higher altitudes.

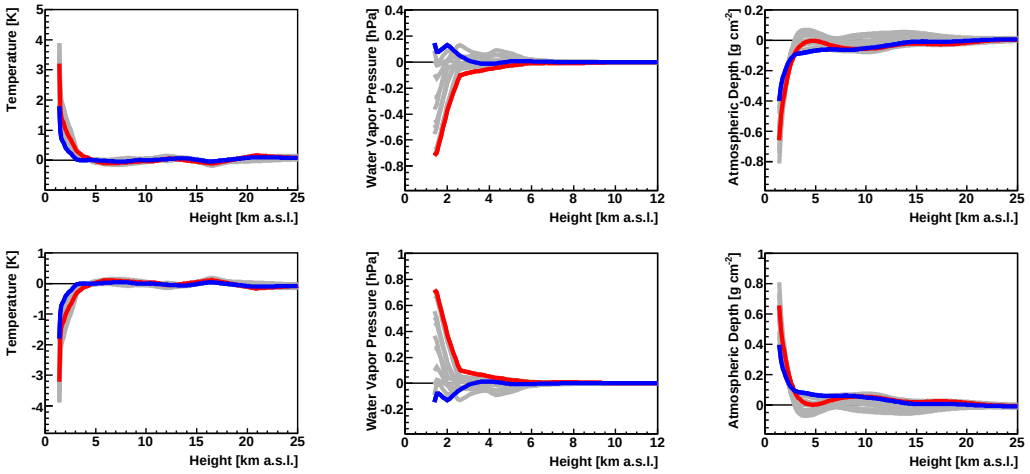

Figure 6.17: Differences between average models shown in Fig. 6.16 and averages using only daytime (top) and nighttime (bottom) GDAS data for temperature (left), water vapor pressure (middle) and atmospheric depth (right). February in red, July in blue.

is parameterized using

$$X(h) = a_i + b_i e^{-h/c_i}, \tag{6.2}$$

h is in cm. In a sophisticated fit procedure, the three times four parameters as well as the layer borders are determined for every month taking into account some boundary conditions for the functions and their derivatives. The fifth layer is adapted from the parameterization of the USStdA,

$$X(h) = a_5 - b_5 \frac{h}{c_5}, \tag{6.3}$$

with $a_5 = 0.01128$ g cm^{-2}, $b_5 = 1$ g cm^{-2}, and $c_5 = 10^9$ cm. The resulting profiles for atmospheric depth are shown in Fig. 6.18. In the left panel, the differences to the USStdA[6] are drawn, the residuals of the fits to the averaged profiles are shown in the right panel. For comparison, the same plots are shown for the MMM in Fig. 6.19. The residuals of the GDAS models are very similar for every month and are much smaller compared to the MMM residuals due to the much higher statistics of the used profiles.

6.4.2 Making the Models Self-Consistent

After the fit procedure, the atmospheric depth profile is not perfectly consistent with the other state variables due to small differences between the averaged and the parameterized depth profile, see Fig. 6.18 right. To make all profiles describing the atmospheric state variables consistent with each other, the atmospheric depth parameterizations are differentiated to get a consistent air density profile,

$$\rho(h) = -\frac{\mathrm{d}}{\mathrm{d}h} X(h). \tag{6.4}$$

[6] a parameterization from 2003 is used, which is also available with the CORSIKA package [107]

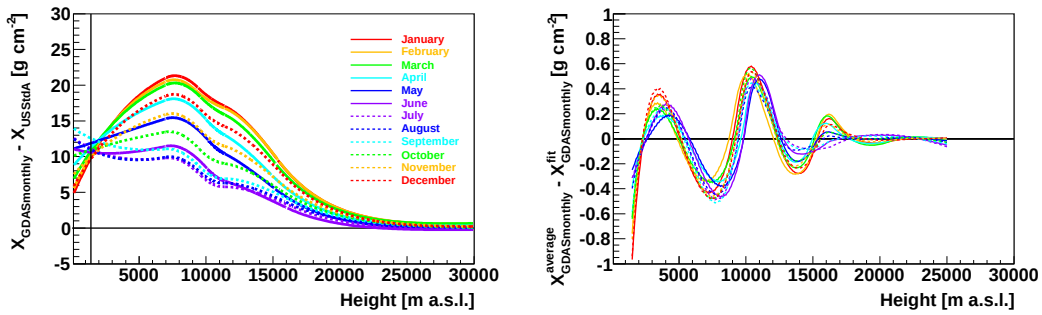

Figure 6.18: Left: Monthly profiles from GDAS for atmospheric depth in difference to the USStdA. Right: Difference of the parameterized monthly depth profiles vs. the averaged monthly depth profiles from the GDAS data.

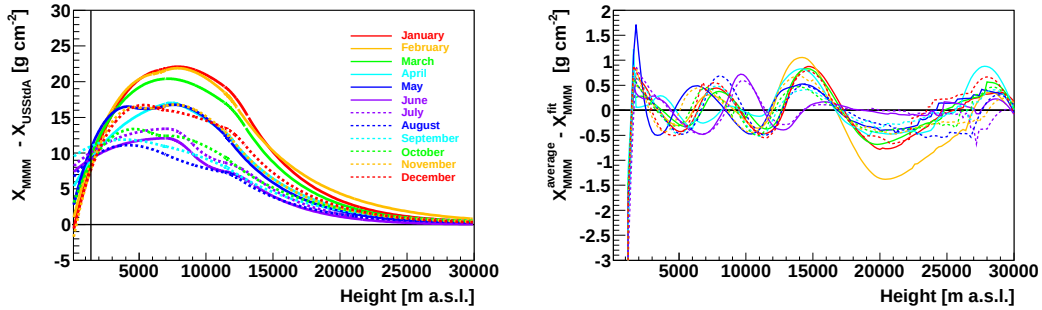

Figure 6.19: Left: Monthly profiles from the MMM for atmospheric depth in difference to the USStdA. Right: Difference of the parameterized MMM depth profiles vs. the averaged depth profiles from local radiosonde data measured between mid-2002 and end of 2008.

Using the averaged pressure p and water vapor pressure e with the ideal gas law, a new temperature profile is derived,

$$T(h) = \frac{p \cdot M_{\mathrm{mol}}(e,p)}{R \cdot \rho(h)}, \tag{6.5}$$

where R is the universal gas constant and M_{mol} is the molar mass of moist air. This procedure is chosen because from a measurement point of view, pressure data have a higher accuracy than temperature data. The differences of averaged minus derived observable for the density and temperature profiles are shown in Fig. 6.20, left and middle panel. For better convenience, the differences are shown in absolute values in the upper row of Fig. 6.20 and in relative values in the bottom row. Technically, this temperature profile is not perfectly consistent with the other profiles since the water vapor pressure used to calculate the molar mass of moist air in Eq. 6.5 is the original averaged profile. A derived vapor pressure profile is recalculated later using this derived temperature profile. However, the difference in temperature introduced by using the averaged water vapor profile instead of the derived profile is less than 0.1%. This small value was added to the uncertainty of the temperature profile rather than come up with a more complicated algorithm.

Since the relative humidity is the actual measured quantity, the original averaged

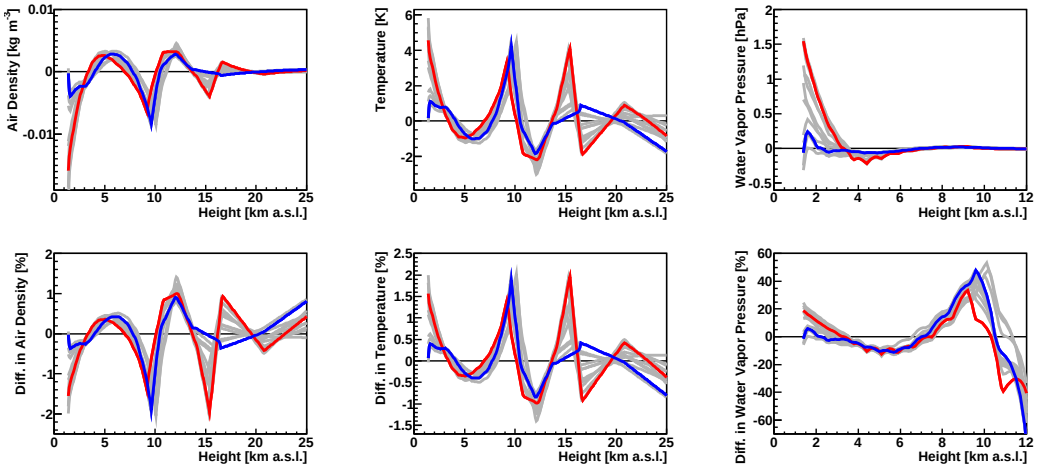

Figure 6.20: Differences between derived and averaged density (left), temperature (middle) and water vapor pressure (right). Top row: absolute values; Bottom row: relative values. February in red, July in blue.

profile was kept and the water vapor pressure recalculated. This also eliminates the possibility of producing derived relative humidity profiles with nearly saturated or even over-saturated values, meaning $u > 100\%$. Using the derived temperature and the averaged relative humidity, the water vapor pressure is calculated,

$$e = \frac{u}{100\%} \cdot 6.1070 \cdot \exp\left(\frac{17.15 \cdot \vartheta}{234.9 + \vartheta}\right), \quad \vartheta \geq 0°\mathrm{C}, \tag{6.6}$$

$$e = \frac{u}{100\%} \cdot 6.1064 \cdot \exp\left(\frac{21.88 \cdot \vartheta}{265.5 + \vartheta}\right), \quad \vartheta < 0°\mathrm{C}, \tag{6.7}$$

where u is the relative humidity in % and ϑ is the temperature in °C. The differences of the derived to the averaged profiles are displayed in Fig. 6.20, right panel. At altitudes around 9 km, a large difference is found. However, humidity is almost negligible at this altitude, the absolute difference not significant.

This step of making the profiles self-consistent was not done for the MMM, since it would have introduced large differences of up to 10 K for the temperature profile. For the GDAS models, the difference is around 2–4 K, which is of the order of the statistical uncertainties introduced by the averaging process.

6.4.3 The Final Models

For pressure and relative humidity, the statistical error from the averaging was used as uncertainty, for the other profiles this error was added in quadrature with the difference of the derived with the averaged profile. In Fig. 6.21, the final T, p, u, e, ρ and X profiles are shown. The final p and u profiles are identical to the averaged profiles shown in Fig. 6.16.

In CORSIKA, only parameterized profiles of atmospheric depth are used for air shower simulations. The parameters and borders of the 12 parameterizations of the GDAS monthly models that are available with CORSIKA now are detailed in Tables A.1–A.12 in Appendix A.

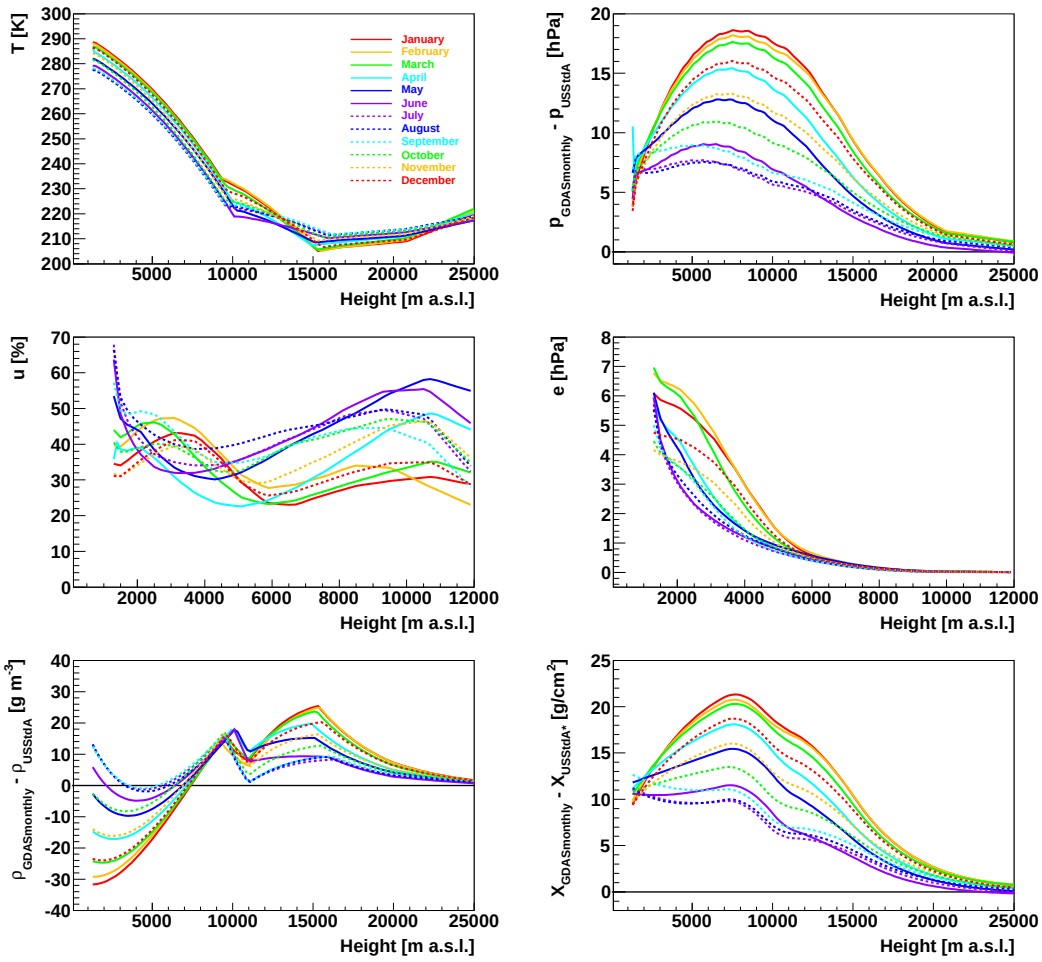

Figure 6.21: Monthly averages after fit and self-consistency procedures for temperature, pressure, relative humidity, water vapor pressure, air density and atmospheric depth (from top left to bottom right). Pressure, density and atmospheric depth are shown in difference to the US Standard Atmosphere.

6.4.4 Determination of Validity Periods of Radiosonde Data

The procedure to find the validity period of a balloon launch using weather stations to determine stable and unstable weather conditions was described briefly in Sec. 5.2.2. The classification of those conditions can only apply to the surface. Using the GDAS profiles described in this chapter, a second method was developed which is sensitive to changing conditions at all heights of the radiosonde profile.

The conditions at the ground may appear to be stable or unstable, while the upper parts of the profile might show a different behavior. Through comparison of the radiosonde profile with the GDAS data before and after the time of the launch, the validity period can be estimated. While this method is sensitive to changes in the entire profile, the time resolution of 3 hours is significantly worse than the 5 minute intervals in which the weather station data are available.

227 balloons were launched between June 2005 and December 2010, the period

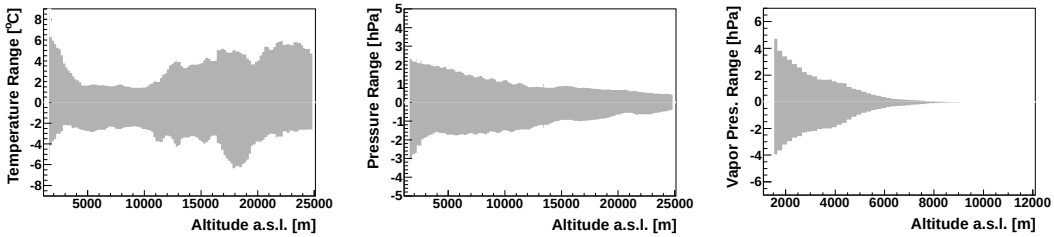

Figure 6.22: Allowed ranges for the difference between radiosonde profile and GDAS data. The bands were obtained by averaging over all radiosonde-GDAS differences, allowing for a difference of two standard deviations.

during which GDAS data for the site of the Pierre Auger Observatory are available. The average difference of the temperature, pressure and water vapor pressure data from these radiosondes minus the GDAS profile closest in time to the majority of the balloon ascent was binned in 200 m steps. This defines the allowed range for the difference of radiosonde to GDAS data. Two criteria were set for each of the three state variables that indicate if a GDAS profile is compatible with a given radiosonde profile. If the difference in T, p or e leaves the valid range for more than 5 consecutive bins, corresponding to 1 km, or if more than 25 bins in total are outside the range, the GDAS profile is invalid. Since the water vapor pressure is negligible above 10 km, the number of total bins that are allowed outside the range was reduced to 15. Applying these criteria to the differences between the radiosonde data and the closest GDAS profile, the differences that were used to define the ranges, close to 90% of the GDAS profiles would be invalid. The ranges are small compared to differences of GDAS data to ground values (see Fig. 6.8), so even though almost all the profiles show fluctuations outside the defined ranges, the differences are well within the desired ranges for fluorescence data analyses. Rather than relaxing the cuts on the differences, it would seem counterproductive to let the difference leave the range for more than 1 km, the 2-σ range of the averaged differences was used, they are shown in Fig. 6.22. The new allowed ranges are now of the same order than the differences found with weather station data while for 91 of 227 launches, the closest GDAS profile is not valid for the radiosonde data.

For every launch, first the closest GDAS profile is checked for validity. Then, the GDAS profiles before and afterwards are scanned until a profile is found that is not valid anymore according to the criteria defined above. If no GDAS profile is valid, the duration of the launch remains the validity time. If the closest GDAS profile is valid, the validity is at least 3 hours, plus whatever part of the duration of the launch exceeds the validity of the GDAS profile on either end. An additional 3 hour period is added for every valid GDAS profile before or after the launch. Using this method, the new validity time is found for every launch. The results are shown in Fig. 6.23. The new average duration of validity of a balloon launch is 7.72 hours with an RMS of 8.75 hours. The majority of profiles is valid less than 3 hours, these are 91 profiles where no GDAS profile is valid. 21 profiles are extended to 3 hours where only the closest GDAS profile is valid. The three largest periods of validity are 42, 48 and 72 hours. This is possible during an inversion, where the temperature lapse rate up to a certain height is inverted and higher layers are warmer than the air

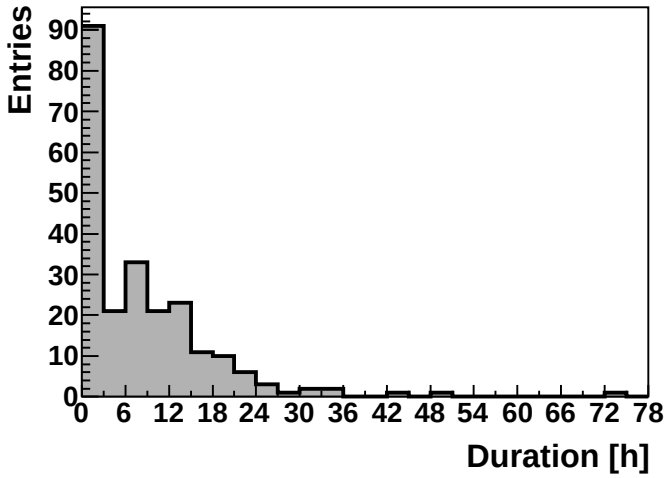

Figure 6.23: New periods of validity after scanning procedure using GDAS profiles. The mean is 7.72 hours with an RMS of 8.75 hours.

below. The cooler air at the bottom has a lower density and therefore mixing with higher layers is reduced to a minimum. In combination with the Andes mountains acting as a barrier, this basically traps the air masses above the Observatory with very little change in atmospheric conditions.

100 events from the online reconstruction would have triggered a balloon launch (see Sec. 5.3), 52 balloons were launched successfully. An additional 10 events would have triggered a launch while a balloon was already in the air. However, only 5 events are within the validity period of a launch if only the duration of the launch is considered. With the GDAS profile method to extend the validity, 40 BtS events are now covered. One event is even covered twice, the launch on April 28, 2009 that was extended to 72 hours covers an event on the previous night which is also covered by the respective balloon launch on April 27. This launch which was extended 21 hours after the launch, missing the BtS event on April 28 by only 2 hours. In Fig. 6.24, the differences between the two profiles are shown. The large differences in the first height bin are explained by the time of day the balloons were launched, one was launched during the night and one in the early morning with temperatures already rising. The differences are within the tolerances set for the difference between launches and GDAS profiles. This supports the assumption of extremely stable conditions during these few days.

With two thirds of the events covered, this method is more effective than the method using weather station data, but still not effective enough so that radiosonde launches could be used for routine air shower reconstructions. Up to now, using GDAS profiles is the best way to implement profiles of atmospheric state variables in air shower reconstructions.

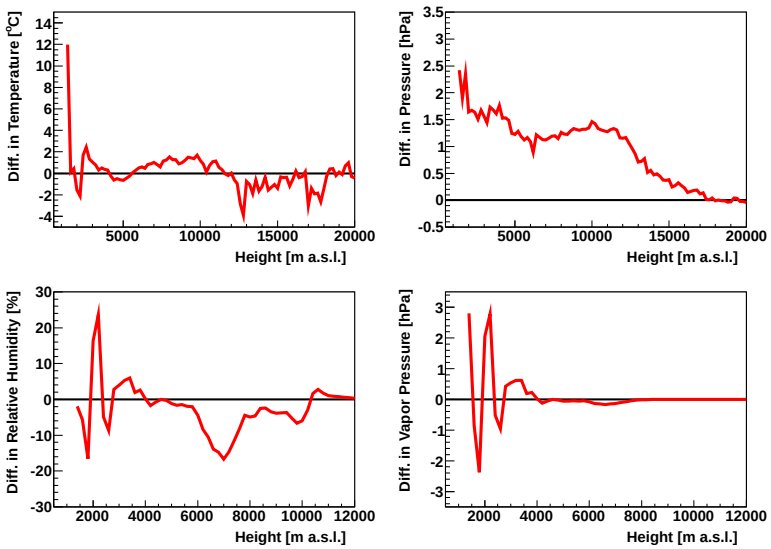

Figure 6.24: Difference in temperature, pressure, relative humidity and water vapor pressure for the two launches performed on April 27 and 28, 2009.

Chapter 7

Aerosol Measurements

Aerosols in the atmosphere are fine solid particles or liquid droplets suspended in the air. Mineral dust from the Andean desert region, where the Pierre Auger Observatory is located, make up a large part of the aerosol concentration at the site of the Observatory [108]. Biomass burning is another contributor at certain times of the year. The area is only populated sparsely, so pollution is not a significant factor. Other sources of aerosols are soil particles and salt from surrounding salt lakes and also the Pacific ocean. These results are confirmed by analyzing the backward trajectories of air masses above the site [101]. While water vapor is a gas, water droplets that form clouds can be classified as aerosols, the droplets share several physical characteristics with dust and smoke particles.

All these particles and droplets are on the order of or larger than the wavelength of the UV light emitted by air showers and detected with the FD telescopes. Therefore, Mie theory has to be applied to evaluate the scattering on aerosols. It is not possible to solve this problem analytically, so different approaches have been found to measure all needed quantities to describe the attenuation of light by aerosols and to apply the corrections in the shower reconstruction. For the measurement of air showers, the microscopic parameters of aerosols like the size and shape in the atmosphere above the Pierre Auger Observatory are not monitored. Only the bulk properties of the aerosol attenuation are measured.

Clouds obstruct the UV light of air showers. The variation in optical depth across a single cloud and between different clouds is so large that no corrections can be applied to data measured under overcast conditions. Since cloud conditions can change on very short timescales, it is important to detect clouds above the array and measure their base height, thickness and the cloud cover.

Several different systems can be used to estimate aerosol and cloud properties and the optical depth. At the Pierre Auger Observatory, these include dedicated laser stations, LIDARs, infrared cloud cameras, aerosol sampler, monitors of the phase function and robotic optical telescopes [79]. Similar detectors and measurements are performed at other current cosmic ray observatories, e. g. the use of LIDARs and a central laser station at the Telescope Array [109, 110], and have been in the past, e. g. at the HiRes experiment [111].

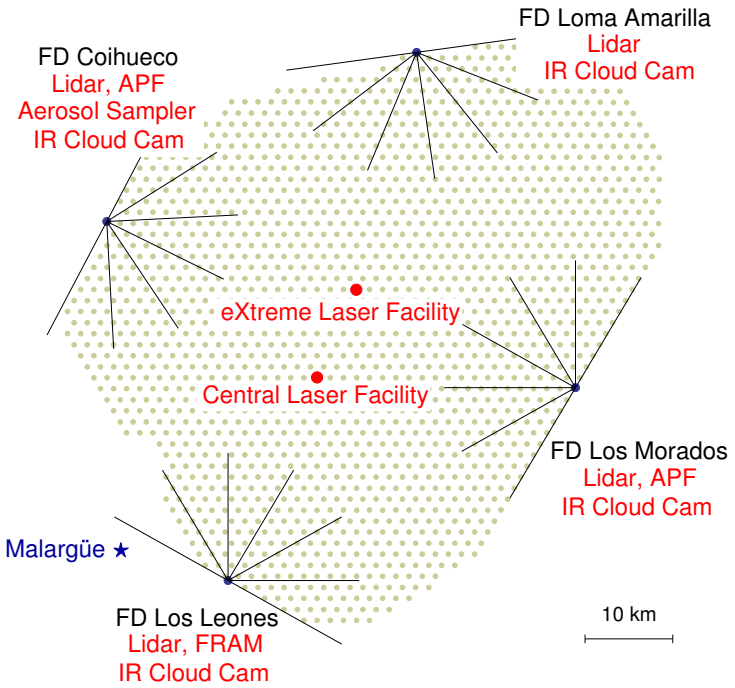

Figure 7.1: A map of the Pierre Auger Observatory with various atmospheric monitoring devices highlighted. This map only includes equipment that measures aerosols or quantities related to aerosols, e. g. optical depths and clouds. Measurement instruments for the molecular part of the atmosphere are depicted in Fig. 5.1. Map modified from [79].

7.1 Measurements of Aerosols at the Pierre Auger Observatory

A map showing the locations of the instruments used to measure aerosol properties at the Pierre Auger Observatory can be found in Fig. 7.1. At all four FD sites, LIDARs use the backscattered light from a laser beam to measure aerosol and cloud properties [112]. The laser is a diode-pumped solid state laser with a wavelength of 351 nm. The light from the laser is attenuated by aerosol and Rayleigh scattering on its way from the LIDAR, scatters back towards the receiver on air molecules or aerosols, and is again attenuated on its return path. The reflection on aerosols depends strongly on their concentration and shape. While the Rayleigh scattering on air molecules can be calculated analytically (see Sec. 4.3), the determination of both the backscatter coefficient and the aerosol transmission from a single return signal is the inherent problem of LIDAR measurements. They are not possible without certain assumptions about the predominant aerosol shape and horizontal uniformity, which is given with sufficient accuracy in the vicinity of the FD sites of the Pierre Auger Observatory [79]. One way to simplify the calculation is to scan over a part of the sky to eliminate some ambiguities. Still, a reliable analysis of these data is very complex and a different method is used to infer aerosol scattering parameters, see Sec. 7.3.

The LIDARs are a valuable tool to detect clouds. Clouds are very obvious in the

LIDAR return since they reflect almost all of the light back to the ground and it is possible to measure the distance between the cloud and the LIDAR from the time delay of the light return. Unfortunately, the LIDAR operation interferes with regular FD measurements since the wavelength of the LIDAR beam is in the detectable range of the FD telescopes. Therefore, infrared cloud cameras were installed at all FD sites [113]. Since those measurements are passive, they can collect data in the FD field of view of the FD all the time. Together with the LIDAR measurements that are performed in the field of view a few times at night while the FD telescopes are vetoed, the cloud coverage of each pixel can be determined.

Another important property of aerosol scattering is the phase function detailing the amount of scattered light as a function of the scattering angle (cf. Fig.4.1). One way of measuring this function as parameterized in Eq. (4.24) is the Aerosol Phase Function monitor (APF) [114]. At two FD sites, a horizontal UV beam from a collimated Xenon flash lamp is shot across all six telescopes. Attenuation is negligible since the laser is so close to the telescopes and a fit using the parameterization yields the needed two parameters. This method of extracting the aerosol phase function is effective between 30° and 150°, however, aerosol scattering is strongly peaked in the forward direction and the small angles needed to fully parameterize the phase function cannot be measured with the APF monitors. Therefore, a new method to extract the phase function was developed [115] based on laser shots from the central laser stations but is not yet implemented.

Two more instruments measure aerosol properties. The (F/Ph)otometric Robotic Atmospheric Monitor (FRAM) [116] is an optical telescope that records CCD images of the night sky. By comparing the observed magnitude of stars with the expected magnitude, the integrated attenuation of the atmosphere can be estimated. Finally, an aerosol sampler measures the chemical composition of aerosols [108] found at the Observatory. The instrument filters large particles from the air that can be later analyzed using an electron microscope. Since it takes a long time to accumulate large enough quantities, only long-time measurements can be taken and only at the surface. For air shower measurements the composition at higher altitudes is of interest and campaigns to measure this are planned for the future.

7.2 Laser Facilities for Atmospheric Test Beams

Two laser stations close to the middle of the array provide atmospheric test beams for the FD telescopes. The amount of photons received at the telescope from a 5 mJ laser beam corresponds to an air shower of 10^{20} eV. Besides calibrating the FD detectors, both laser facilities are used to measure atmospheric attenuation. The Central Laser Facility (CLF) [117] is located roughly equidistant from Los Leones (26.0 km), Los Morados (29.6 km) and Coihueco (30.3 km). The distance to Loma Amarilla is larger (40 km) and it is therefore only possible to measure well during very clear nights, as is the case for air showers with an energy of 10^{20} eV. The eXtreme Laser Facility (XLF) is located to the north of the CLF and is at about the same distant from Los Morados (27.6 km), Loma Amarilla (28.8 km) and Coihueco (29.6 km), while it is farther away from Los Leones (37.3 km). Both stations are solar-powered and operated remotely.

Figure 7.2: Pictures of the Central Laser Facility (left) and the eXtreme Laser Facility (right).

7.2.1 Hardware and Operations

The CLF and XLF laser systems are described elsewhere [117, 118], in this section only the features relevant to this work are provided. In Fig. 7.2, pictures of the CLF and XLF are shown. Both lasers use frequency tripled Nd:YAG lasers to produce a beam with a wavelength of 355 nm near the middle of the main part of the nitrogen fluorescence spectrum. The beam can be directed into the sky vertically by a mirror without any moving parts. The beam direction is maintained within 0.04°. Since the Nd:YAG laser emits linearly polarized light, depolarizers are used to make sure the observations of the side-scattered light by the FD is not biased. The polarization was measured using a polarizing beam splitter cube which splits the laser beam into two orthogonally polarized components. By rotating the cube, the intensity of one polarization direction can be measured as a function of angle. The results can be visualized as a polarization ellipse. The deviation between major and minor axis of the ellipse was determined to be less than 3%. The nominal energy per pulse is 7 mJ and the pulse width is 7 ns. The laser is triggered relative to a GPS clock to match each laser shot to the recorded data of the FD. Nightly operations are automated and are initiated remotely.

The CLF and XLF fire 50 vertical shots every 15 minutes during the FD data acquisition. Specific GPS timing is used to distinguish laser from shower events. The CLF fires either 250 ms or 500 ms after the full GPS second, the XLF fires at 350 ms and 700 ms. If a trigger at those offsets is detected by the FD data acquisition system, the data are directed into a special laser file so laser tracks don't contaminate the regular air shower data. Only very few actual air shower events are diverted into the laser files. The direction, time, and energy calibration probe reading of each laser pulse is recorded at the laser stations and can later be matched to the corresponding laser event.

An upgrade [119] to the CLF is planned for 2012. This upgrade will include an automated robotic calibration system as used at the XLF and the addition of a backscatter Raman LIDAR receiver, for details see also Sec. 8.6.

7.2.2 Calibration

The CLF uses two pickup probes for relative calibration [118]. A photodiode and a pyroelectric detector pick up a fraction of the energy that is split from the vertical beam at two points of the beam path. Pyroelectric probes are crystals that produce a voltage pulse proportional to the absorbed energy generated when heated by the absorption of the laser beam.

An absolute calibration of the laser energy was performed once or twice per year until end of 2010 and in monthly campaigns since then. A radiometer is mounted in the vertical beam and records the sky energy, which is then compared to the pick-off probe readings, see Fig. 7.3. The data were provided by colleagues from the Colorado School of Mines, United States [120]. The ratio of the sky energy and the reading is used as a calibration constant, see Fig. 7.4. The last mirror that directs the beam skyward is located after the pyroelectric probe. Since this mirror is oriented in a 45° angle to the horizontal, it can easily accumulate dust which is always present even though the optical table is sealed as thoroughly as possible. This diminishes the output light of the CLF but is not recorded in the relative calibration log. In early 2010, the optics were cleaned and an absolute calibration was done before and after. An increase in calibration constant of 27% can be seen after the cleaning.

Over time, the sky energy decreases while the pick-off probe does not record this. For this reason, a time-dependent calibration constant was introduced. To make a fit to the constants, the points from before 2010 were shifted upwards to account for the cleaning. This was done for both the photodiode and the pyroelectric probe. The time-dependent calibration constants for the pyroelectric probe are

$$E_{\text{sky}} = -0.783 \cdot \Delta t + 6.560, \quad \text{for 2008 and 2009,} \tag{7.1}$$
$$E_{\text{sky}} = -0.783 \cdot \Delta t + 8.511, \quad \text{for 2010 and 2011,} \tag{7.2}$$

for the photodiode, the function is

$$E_{\text{sky}} = -0.565 \cdot \Delta t + 5.425, \quad \text{for 2008 and 2009,} \tag{7.3}$$
$$E_{\text{sky}} = -0.565 \cdot \Delta t + 7.019, \quad \text{for 2010 and 2011,} \tag{7.4}$$

where Δt is the date, calculated as

$$\Delta t = (year - 2011) + ((day - 1) + (month - 1) \cdot 30.4)/365. \tag{7.5}$$

In Fig. 7.5, the normalized calibration constants for both pick-off probes are shown. The constants are divided by the fit values to correct for the time-dependent shift. The pyroelectric probe shows small fluctuations of about 1.2%, the photodiode has larger fluctuations of 2.2%. For this reason, the reading of the pyroelectric probe is used whenever it is possible.

The main difference between the CLF and XLF calibration system is the use of an automated robotic beam calibration system that can be moved in the vertical beam. It is usually operated at least twice per night, at the beginning and the end of the run, to absolutely calibrate the XLF. A polarization analyzer can also be moved in the path of the laser. An additional pyroelectric probe picks off part of each laser beam for a relative calibration [118].

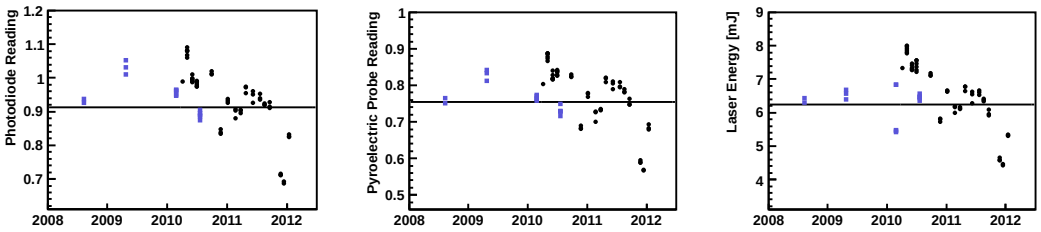

Figure 7.3: Relative calibration values of the photodiode (left), the pyroelectric probe (middle) and the measured energy (right). Black dots are monthly measurements since 2010, blue squares are annual or occasional calibrations.

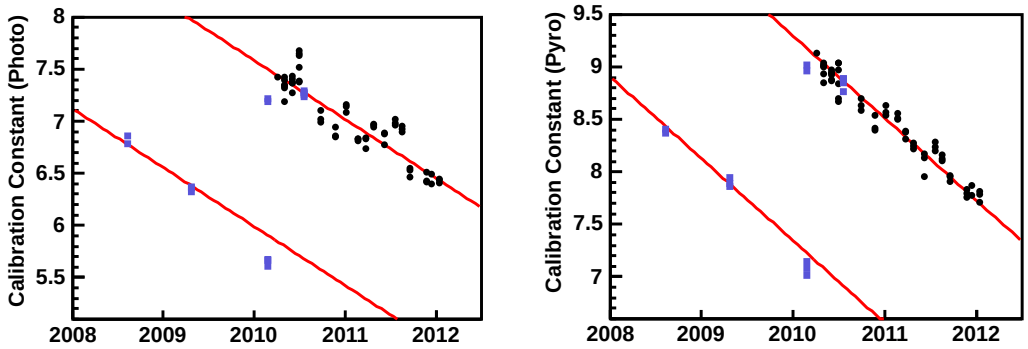

Figure 7.4: Calibration constants: ratio of measured energy and photodiode value (left) and pyroelectric probe (right). The first three sets of points were shifted upwards by 27% and a combined fit was performed. Details see text.

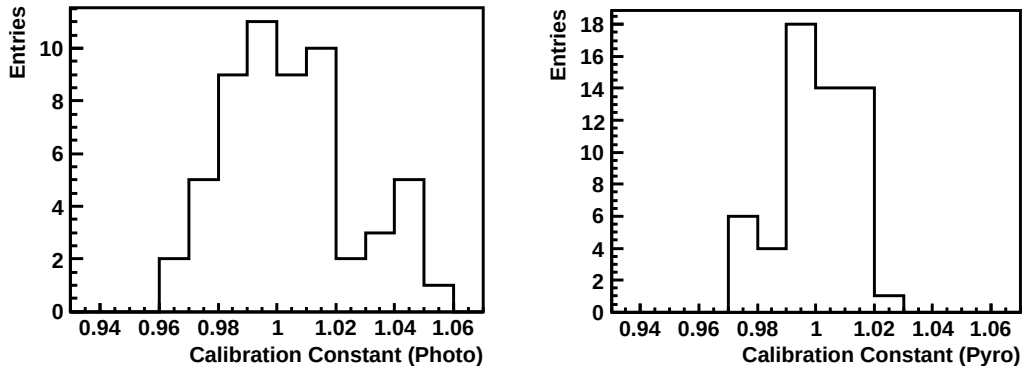

Figure 7.5: Calibration constants normalized to the time-dependent fit for the photodiode (left) and pyroelectric probe (right).

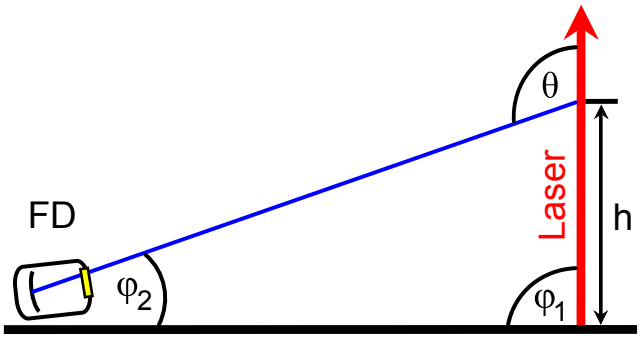

Figure 7.6: Scheme of the laser-FD geometry. The light is scattered out of the laser beam at a height h at an angle θ and received at the FD site under an angle φ_2. For vertical shots, the angle φ_1 is 90°.

7.3 Side-Scatter Method to Measure the Aerosol Optical Depth

The light scattered out of the CLF laser beam is recorded by the FD (see Fig. 7.6 for the laser-FD geometry layout). As mentioned above, the inherent problem in analyzing scattering returns is the ambiguity in extracting both the aerosol attenuation and scatter coefficient from a single light return. To circumvent this problem, the scattering angles of light from the beam observed by the FD are in the range of 90° to 120°. The differential scattering cross section of aerosol scattering is minimal in this range, the scattering of light is dominated by well-known molecular scattering processes, see also Sec. 4.3 and Fig. 4.1 therein. The distance between the laser beam and the detector is more than the aerosol horizontal attenuation length, the distance where the light transmission due to aerosol scattering has dropped to 1/e. Therefore, the measured light signal is dominated by the attenuation of the beam on its path between the scatter point and the detector. Even for aerosol particles smaller than the wavelength of the laser beam, for which the scattering phase function in the direction of the detector increases, the attenuation would dominate. The effect of small aerosols on the attenuation would be included in the measurements.

Laser light is attenuated in the same way as fluorescence light as it propagates towards the FD. Therefore, the analysis of the amount of CLF light that reaches the FD can be used to infer the attenuation due to aerosols. The amount of light scattered out of a 7 mJ laser beam by the atmosphere is roughly equivalent to the amount of UV fluorescence light produced by an air shower of 5×10^{19} eV [121]. Besides determining the optical properties of the atmosphere, the identification of clouds is a fundamental task in the analysis of CLF laser shots. Clouds can have a significant impact on shower reconstruction.

The light recorded by the PMT camera of the FD is summed up for every triggered pixel in the column where the laser track is expected and one adjacent column to each side to. Every hour, 200 laser shots are fired and recorded as a function of time which can be converted to height. More details about this conversion and the construction of hourly light profiles are given in Sec. 7.4. In Fig. 7.7, examples of various hourly profiles affected by different atmospheric conditions are shown.

Shown in panel (a) is a profile measured in a night in which the aerosol attenuation is negligible. Shown in (b), (c) and (d) are profiles measured while the aerosol attenuation was low, average and high, respectively. As conditions become hazier, the integral photon count decreases. The number of photons at 3.5 km above the ground compared to the clear night (a) is reduced by 17% (b), 31% (c) and 43% (d). The two bottom profiles (e) and (f) represent cloudy conditions. Clouds appear in CLF light profiles as peaks or holes depending on their position. A cloud positioned between the CLF and the FD can block the transmission of light in its travel from the emission point towards the fluorescence telescopes, appearing as a hole in the profile (e). The cloud could be positioned anywhere between the CLF and the FD site, therefore its altitude cannot be determined unambiguously. A cloud directly above the CLF appears as a peak in the profile, since multiple scattering in the illuminated cloud enhances the amount of light scattered towards the FD (f). In this case, it is possible to directly derive the altitude of the cloud from the peak in the photon profile since the laser-detector geometry is known.

Two independent analyses have been developed to provide hourly aerosol characterization in the FD field of view using CLF laser shots from the fixed-direction vertical configuration. To minimize fluctuations, both analyses make use of average light flux profiles normalized to a fixed reference laser energy. The *Data Normalized Analysis* is based on the comparison of measured data profiles with a reference night profile in which the light attenuation is dominated by molecular scattering. The *Laser Simulation Analysis* [122], run by colleagues from Napoli, Italy, is based on the comparison of measured light flux profiles to simulations generated in various atmospheres in which the aerosol attenuation is described by a parametric model.

The profiles (both measured and simulated) are affected by unavoidable systematics related to the FD and laser calibrations and to the simulation. Using measurements recorded on extremely clear nights where molecular Rayleigh scattering dominates, CLF observations can be properly normalized without the need for absolute photometric calibrations of the FD or laser. In such *reference clear nights*, the attenuation due to aerosols is minimal compared to the uncertainty of total attenuation, the scattering is dominated by the molecular part. In such a clear night, the measured light profiles are larger than profiles affected by aerosol attenuation indicating maximum photon transmission. Those profiles have shapes that are compatible with a profile simulated under atmospheric conditions in which only molecular scattering of the light is used [122].

As a check to verify that the chosen nights are reference clear nights is to analyze the measurement of the aerosol phase function (APF) (cf. Sec. 4.3 and Eq. (4.24)) for that night, measured by the APF monitor [114]. The molecular part of the phase function $P_{\mathrm{mol}}(\theta)$ can be calculated analytically from altitude-dependent profiles of temperature, pressure and humidity. After subtraction of the molecular phase function, the aerosol phase function remains. In a reference night, the total phase function is dominated by the molecular part with almost no contribution from aerosols. Since the APF light source only fires approximately horizontally, this method to find the reference nights is insensitive to clouds, so it can only be used as a verification of reference nights that were found using the procedure described in this section. After verification, the reference night is assumed to be valid for the complete CLF epoch. In Fig. 7.7, panel (a), an averaged light profile of a reference night is shown.

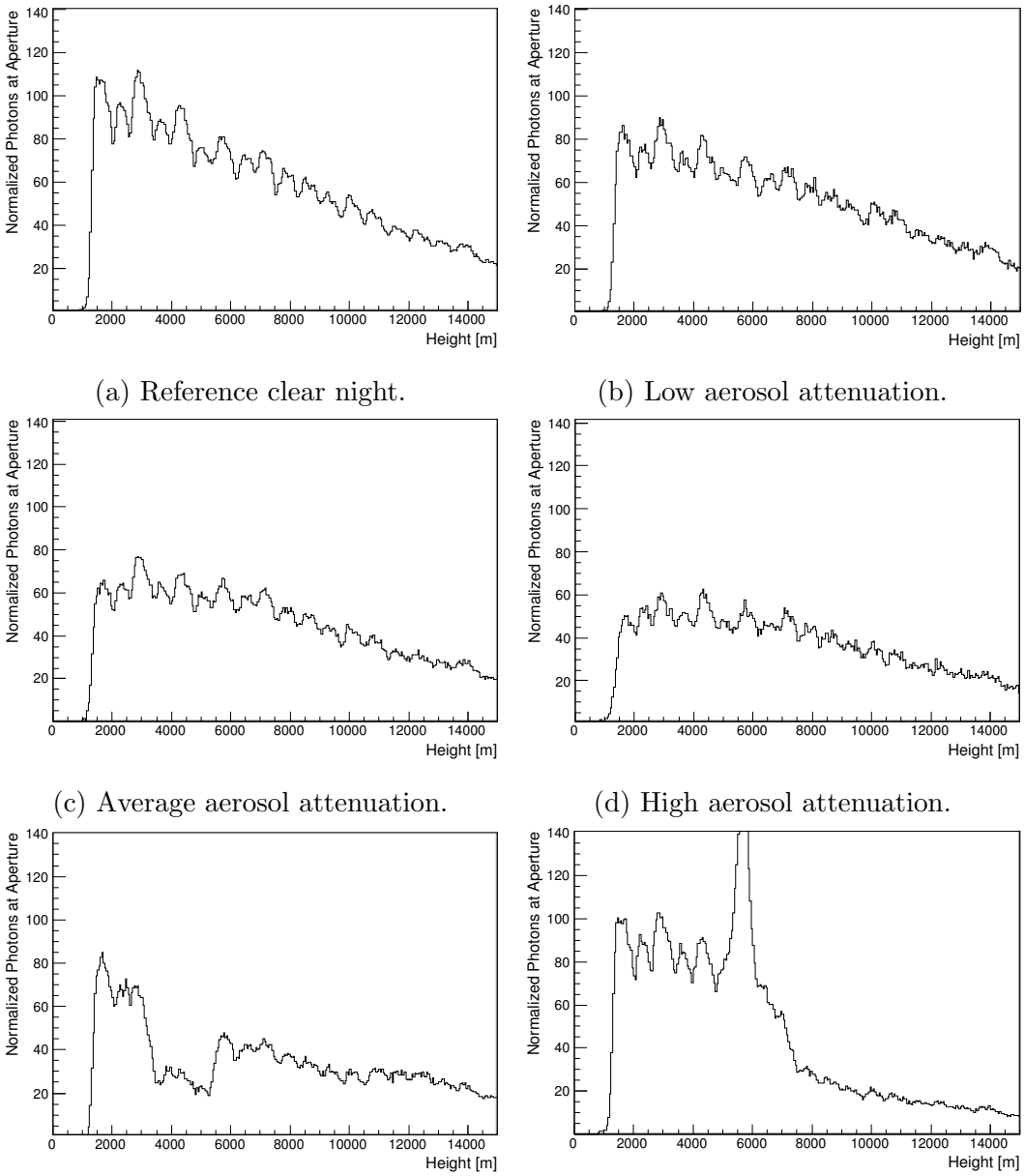

(a) Reference clear night.

(b) Low aerosol attenuation.

(c) Average aerosol attenuation.

(d) High aerosol attenuation.

(e) Cloud between FD and laser.

(f) Laser passing through cloud.

Figure 7.7: Examples of average light profiles of 200 laser shots measured with the FD at Coihueco under various atmospheric conditions. The height is given above the FD, the number of photons at the aperture of the FD was normalized to a laser energy of 1 mJ. Shown are a reference clear night (a); Low (b), average (c) and high aerosol attenuation (d); Cloud between FD and laser (e); Laser passing through cloud (f).

7.4 Data Normalized Analysis of Side-scatter Data

In the Data Normalized Analysis, measured data profiles are compared with the reference night in that epoch, as described in the previous section. This method was used to find aerosol corrections since 2004, the beginning of operations of the CLF. In this section, the method will be described and changes and improvements done within this work are detailed.

7.4.1 Description of Method

Using the timing of the event, the time bins of the FD data are converted to height at the laser track using the positions of the FD and CLF. The number of photons is scaled to the number of photons of a 1 mJ laser beam. An average profile is built for every 15 minute data taking period from a set of 50 vertical laser shots.

Clouds are then marked by examining the photon transmission of the quarter hour profiles and comparing them to the clear profile bin by bin. A ratio of the quarter hour transmission to the reference night transmission of less than 10% indicates a hole in the profile that is caused by a cloud between the laser beam and the FD. A ratio larger than 1.3 indicates that the laser beam passed through a cloud directly above the CLF, causing a spike in the profile. In both cases, the minimum cloud height is set to the height corresponding to the anomaly. Only bins corresponding to heights lower than this cloud height are used for the optical depth analysis. If there are no such discontinuities, the minimum cloud height is set to the height corresponding to the top of the FD camera field of view.

A preliminary full hour profile of the normalized light at the aperture is made by averaging all the available quarter hour profiles. One or more quarter hour profiles can be missing due to the start or stop of FD data taking, heavy fog, or technical problems at the CLF. During the laser event is recorded, random pixels of the camera of the FD telescope can trigger. However, their timing is not compatible with the triggered pixels of the laser beam and it is possible to identify them. After rejecting the random pixels, a new full hour profile is calculated. To eliminate anomalies and outliers in single bins of the profile that can cause problems in the optical depth analysis, the quarter hour profiles are subjected to a smoothing procedure by comparing the current profile to the preliminary full hour profile. After multiple iterations of this procedure, the final full hour profile is constructed.

Using the laser-FD viewing geometry shown in Fig. 7.6, and assuming that the atmosphere is horizontally uniform between the laser site and the detector, it can be shown [111] that the vertical aerosol optical depth is

$$\tau_{\mathrm{aer}}(h) = -\frac{\sin\varphi_1 \sin\varphi_2}{\sin\varphi_1 + \sin\varphi_2}\left(\ln\left(\frac{N_{\mathrm{obs}}(h)}{N_{\mathrm{mol}}(h)}\right) - \ln\left(1 + \frac{f_{\mathrm{aer}}(\pi-\theta)}{f_{\mathrm{mol}}(\pi-\theta)}\right)\right), \qquad (7.6)$$

where $N_{\mathrm{mol}}(h)$ is the number of photons from the reference profile as a function of height and $N_{\mathrm{obs}}(h)$ is the number of photons from the observed hourly profile as a function of height. $f_{\mathrm{aer}}(\theta)$ and $f_{\mathrm{mol}}(\theta)$ are the fractions of photons scattered by aerosols and molecules, respectively. These fractions depend on the aerosol and molecular phase functions and the density of scattering centers. In most cases, $f_{\mathrm{aer}}(\theta)$ is small compared to $f_{\mathrm{mol}}(\theta)$ and the second term in Eq. (7.6) can be neglected

at first order. Therefore, for vertical laser shots ($\varphi_1 = \pi/2$), Eq. (7.6) is reduced to

$$\tau_{\text{aer}}(h) = \frac{\ln N_{\text{mol}}(h) - \ln N_{\text{obs}}(h)}{1 + \csc \varphi_2}. \tag{7.7}$$

With these simplifications, the CLF optical depth measurements depend only on the elevation angle of each laser track segment and the number of photons from the observed track and the reference profile. The aerosol optical depth may be calculated directly from Eq. (7.7). The curvature of the Earth is on the order of 50 m over a distance of 30 km, this can be included in the calculations by adjusting the altitude of the laser station relative the the altitude of the FD site and a small correction to ($\varphi_1 = \pi/2$).

τ_{aer} is calculated for each bin in the hourly profile. This calculation provides a first guess of the measured optical depth τ_{meas}, assuming that aerosol scattering from the beam does not contribute to the track profile. While this is true for regions of the atmosphere with low aerosol content, τ_{meas} is only an approximation of the true τ_{aer} if aerosols are present. To overcome this, the τ_{meas} is differentiated to obtain an estimate of the aerosol extinction α_{aer}. For every 50 m height bin, τ_{meas} above that height is fit with two functions, one exponential, the other linear. Whichever function has the lower χ^2 is selected and the derivative value as a function of height is set as α_{aer} for that height bin. The next interval is processed using the same procedure until all of τ_{meas} has been fit and differentiated to create α_{aer}.

All negative values of α_{aer} are set to zero as these are unphysical. The remaining values of α_{aer} are numerically integrated to get the fit optical depth τ_{fit}. Since the fits used to determine α_{aer} are not perfect, it fluctuates in regions with low aerosol content. These fluctuations cause large differences between τ_{fit} and τ_{meas}. To make τ_{fit} better agree with τ_{meas}, α_{aer} is scaled through a renormalization process and fit again. The final values from the renormalized α_{aer} and τ_{fit} are filled in a database and can be used for corrections in light transmission during air shower reconstruction. The area of the Pierre Auger Observatory is divided into four zones, one for each FD site, and the τ_{aer} profile measured in each zone is used for showers detected in that area. This way, local aerosol conditions are incorporated in the reconstruction.

In Fig. 7.8, laser profiles and τ_{aer} for an average and a cloudy are shown night with the laser passing through a cloud. The black traces in the left panels represent the hourly profiles, the red traces represent the reference nights. In the right panels, the τ_{meas} profile and its uncertainties are shown in black as a function of height, τ_{fit} is overlaid in red. In the cloudy night, a large amount of light is scattered by a cloud starting from a height of approximately 7 km above ground height. In the bottom right panel, the minimum height at which a cloud was detected is indicated by a vertical dashed blue line and the maximum height of valid aerosol characterization is indicated by a vertical red dashed line.

Systematic uncertainties are due to uncertainty in the relative calibration of the FD (σ_{cal}), the relative calibration of the laser (σ_{las}), and the relative uncertainty in determination of the reference profile (σ_{ref}). These uncertainties are propagated for both the hourly profile ($\sigma_{\text{syst,hour}}$) and the clear profile ($\sigma_{\text{syst,clear}}$). The propagated systematic uncertainty depends strongly on height. The transmission of light decreases with the viewing angle from the FD to the laser, cf. Eq. (4.22), therefore the sensitivity of the amount of light detected depends less on the aerosol concentration with increasing height. This dependence on the viewing angle must be taken into

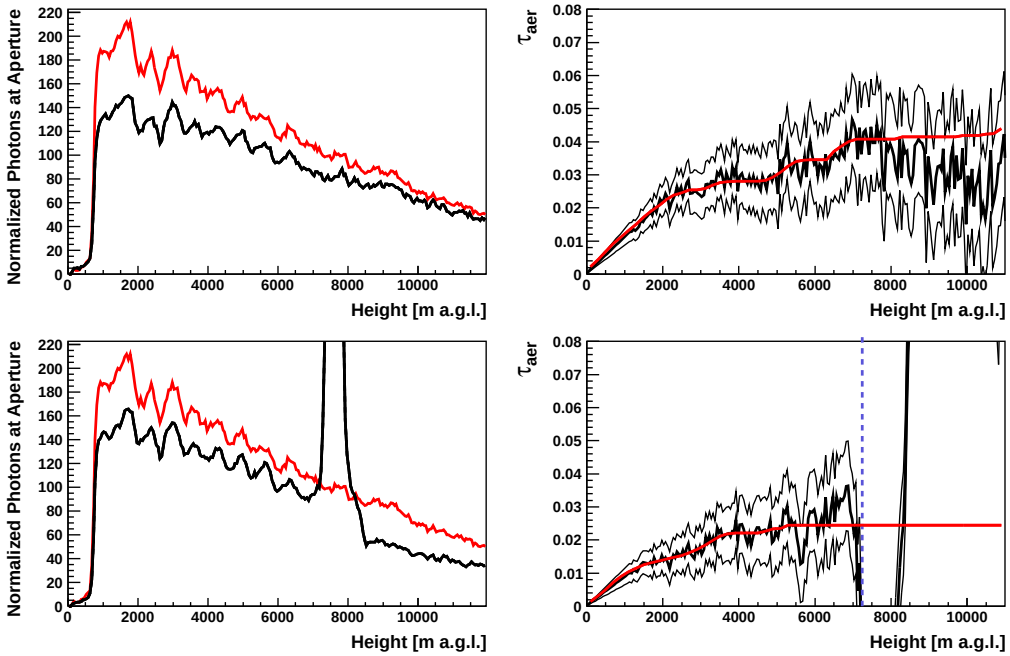

Figure 7.8: Examples of light profiles and vertical aerosol optical depth τ_{aer} measured with the FD at Los Morados during an average night (top) and with the laser passing through a cloud (bottom). The height is given above ground level, the light profile was normalized to a laser shot of 1 mJ. The black traces in the left panels represent the hourly profiles, the red traces the reference clear nights. In the right panel, the measured τ_{aer} profile is shown in black, the fit is shown in red. The thin black lines represent the uncertainties. In the bottom right panel, the minimum cloud height is indicated by the vertical blue line.

account. The final systematic uncertainty on τ_{meas} is calculated by adding $\sigma_{\text{syst,hour}}$ and $\sigma_{\text{syst,clear}}$ in quadrature, along with the height correction,

$$\sigma_{\text{syst}} = \frac{1}{1+\csc\varphi_2}\sqrt{(\sigma_{\text{syst,hour}})^2+(\sigma_{\text{syst,clear}})^2}. \tag{7.8}$$

Three separate profiles are then generated corresponding to the values of τ_{meas} and $\tau_{\text{meas}} \pm \sigma_{\text{syst}}$.

The statistical uncertainty σ_{stat} is due to fluctuations in the quarter hour profiles and are considered by dividing the RMS by the mean of all quarter hour profiles at each height. These statistical uncertainties are assigned to each bin of the $\tau_{\text{meas}} \pm \sigma_{\text{syst}}$ profiles. These two profiles are then subjected to the same slope fit procedure, renormalization and integration as τ_{meas} to obtain the final upper and lower bounds on τ_{fit}.

7.4.2 Upgrade of Method

In the course of this work, the data normalized method was upgraded. Some of the changes were related to the processing speed of the program. The program was migrated to a different system to allow for parallel grid processing of the data, substantially decreasing the time it takes to analyze data. Scripts for the comfortable

use of this new feature were written. Also, the program was further integrated into the analysis framework of the Pierre Auger Observatory to use some of the tools that are provided by the framework and the user has more possibilities to change important parameters of the analysis.

In the upgraded program, the possibility was added to analyze data from the second laser facility, the XLF. The data of the XLF are stored in the same laser data files as the CLF data. Data from both lasers can be analyzed either separately or at the same time to avoid processing the same file twice. The two laser sources are distinguished by their timing, vertical CLF shots are fired 250 µs, vertical XLF shots 350 µs after the full GPS second. The position of the XLF and the geometry relative to the FD sites was calculated using data from a GPS site survey in 2007 and implemented in the program. The nightly calibrations of the XLF system were processed by colleagues from the Colorado School of Mines [120]. Results from the new XLF analysis will be shown in Sec. 7.5.

Another upgrade of the analysis was the better conversion of time information measured with the camera of the FD telescope to actual height. The raw data of the FD combines the timing information of the measured photons of one pixel with the field of view of that pixel. Using the laser-FD geometry, these data are converted to the normalized number of photons versus the height above the laser facility. This was done in the old code by calculating the height for each 50 µs time bin and filling a height histogram with this information. The bin width of the histogram is 50 m, however, the length of the laser track corresponding to a single time bin increases with height. Close to the horizon, a shorter laser track is included in one time bin than higher up in the field of view of the telescope. For example, at a distance of 30 km, the pixel with a field of view closest to the horizon records a laser track of 787 m, corresponding to 2.63 µs. The pixel detecting light from the highest elevation angles records 1064 m of laser track, corresponding to 3.55 µs. This discrepancy introduces two effects. The converted height profile of the light profile is underestimated in the lower part of the atmosphere and overestimated in the upper part. This is less of a problem, since the τ_{aer} profile is calculated by comparing with a reference night, which is also affected by these effects. The ratio, and therefore the τ_{aer} profile, is unaffected. The second effect can modify the τ_{aer} profile. Due to small fluctuations of about 50 ns in both the recorded times of each PMT and the timing of the CLF GPS clock, the time-to-height conversion is not identical for every laser shot. This can lead to larger fluctuations in the light profile due to binning effects, which may not be consistent in the reference night and add fluctuations in the τ_{aer} profile.

An example of a light profile using the old algorithm is shown as the black profile in Fig. 7.9. The profile is corrected by normalizing the bins. To find a scaling factor for each bin, every hour the number of entries in every height bin for the approximately 200 laser shots in this period is recorded. The height bin width agrees with the actual track of the laser within a 50 µs window around 5–6 km above ground level. The number of entries in this range is used to scale the rest of the height bins. The result of this normalization is also shown in Fig. 7.9, red profile. The correction for the under and overestimation of the profile is obvious, also the reduction of the fluctuations, especially in the beginning and the end of the profile, can be seen.

Finally, the determination of the minimum cloud height was corrected. With the

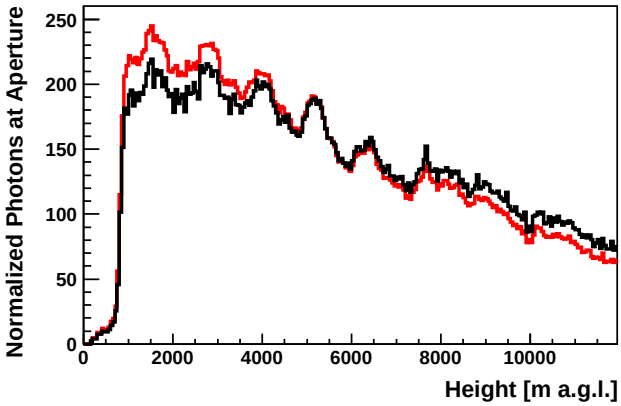

Figure 7.9: Example light profile measured at Los Leones in June, 2011. Shown in black is the result of the old time-to-height conversion, the normalized trace is shown in red. Both profiles overlap between 5–6 km a.g.l., a clear underestimation in the lower part and an overestimation in the upper part by the old code can be seen, as well as larger fluctuations in single bins.

old code, it was possible that the uncertainties close to a cloud were overestimated. The measured τ_{aer} profile would show large fluctuations due to the scattering in the cloud and the τ_{aer} fit would incorporate those fluctuations, resulting in large jumps. This was fixed by excluding the measured τ_{aer} profile above the detected cloud in the τ_{aer} fit. Also, the estimation of the cloud height is now made more conservatively to avoid spikes in the τ_{aer} profile. The overestimations of the old code were not propagated into the air shower analysis of the Pierre Auger Observatory, large fluctuations would be removed from the profile before they were used.

7.4.3 Database Update of 2011

The τ_{aer} data is filled in a database that is used in the air shower reconstruction of the Pierre Auger Observatory. This update of the database is usually done shortly after the calibration data of the FD telescopes are processed and published within the collaboration. In recent years, this happened about once per year. For the period between October 2010 and September 2011, new reference nights had to be identified in order to produce new aerosol correction constants for the database. Reference night profiles are found by both CLF data analysis groups independently. The Napoli group compares measured profiles to simulated average profiles of 50 CLF shots in a purely molecular atmosphere. The comparison is most sensitive to the shape of the measured profile. If it deviates too much from the simulation, it is either not a pure reference night or the profile modified by some other effect. For the Data Normalized method, a search algorithm compares all measured profiles to a reference profile. This reference profile can be any measured profile, e. g. a preliminary reference night candidate from a precious iteration of the algorithm or a reference night from an earlier epoch. Comparing this preliminary reference to all measured profiles, about 100 nights with the highest number of photons at the FD aperture are selected and narrowed down by visual examination. Special attention

Table 7.1: A list of the reference nights used for the analysis of the CLF data. For each FD site, the validity and date are listed. Hours in UTC.

Validity	Los Leones	Los Morados	Coihueco
Feb. 10, 2010 – Sep. 30, 2010	Jun. 15, 7–9	Jun. 15, 7–9	Jun. 15, 7–9
Oct. 1, 2010 – Sep. 29, 2011	Aug. 3, 5–7	Aug. 3, 5–7	Jun. 8, 4–6

has to be given to profiles affected by clouds that usually show the largest amount of photons due to multiple scattering in the cloud. The latter method is only sensitive to the number of photons, rather than the shape of the profile. Comparing the two sets of nights from each method, reference nights for this period were selected for each FD site. The choice was confirmed by data from the Aerosol Phase Function monitor, which measured a scatter phase function compatible with pure Rayleigh scattering in those nights. In Tab. 7.1, the reference nights for this period and the one before in 2010 are listed.

In Fig. 7.10, the comparison of the τ_{aer} profiles determined with the Laser Simulation (LS) and the Data Normalized method (DN) are shown for the time period of October 2010 until September 2011. The data are compared at altitudes of 1.5, 3 and 4.5 km above ground level for the FD sites Los Leones, Los Morados and Coihueco (from top to bottom). A fit to the data is shown as a red line. The resulting τ_{aer} profiles of both analyses agree very well.

7.5 XLF Analysis and Comparisons

With the upgraded side-scatter analysis, it is possible to reconstruct XLF events. Data from the XLF laser are available since 2010. Both XLF and CLF data can only be used if calibration constants for the FD are available, which is currently September 2011. To produce τ_{aer} profiles, the procedure described above for the CLF is used. The profiles with the maximum photon number were inspected by eye to make sure no irregular shapes or small spikes due to clouds are present. Reference nights were selected for the FD sites Los Morados, Loma Amarilla and Coihueco. Los Leones is not used with the XLF for now since the distance is too large, the track measured the the camera is not sufficiently bright to produce reliable τ_{aer} data. For the same reason, data from Loma Amarilla are not used the CLF analysis. Unfortunately, the laser simulation analysis was only available for 2010 for Los Morados and Coihueco, were the reference night selections could be confirmed [123]. For Loma Amarilla and for all sites in 2011, no independent confirmation of the reference nights is available. The selected reference nights are listed in Tab. 7.2. Compared to the reference nights of the CLF (cf. Tab. 7.1), only August 3, 2011 is a common night for Los Morados, Loma Amarilla and Los Leones. Usually, the final choice of a reference night is not unambiguous. If more than one candidate night is found, just a small difference in shape or photon count can make the difference. As mentioned in the description of the data normalized method, this choice of the reference night is reflected in the systematic uncertainties of the τ_{aer} profiles.

In Appendix B, the τ_{aer} profiles of all FD sites for both laser stations for 2010

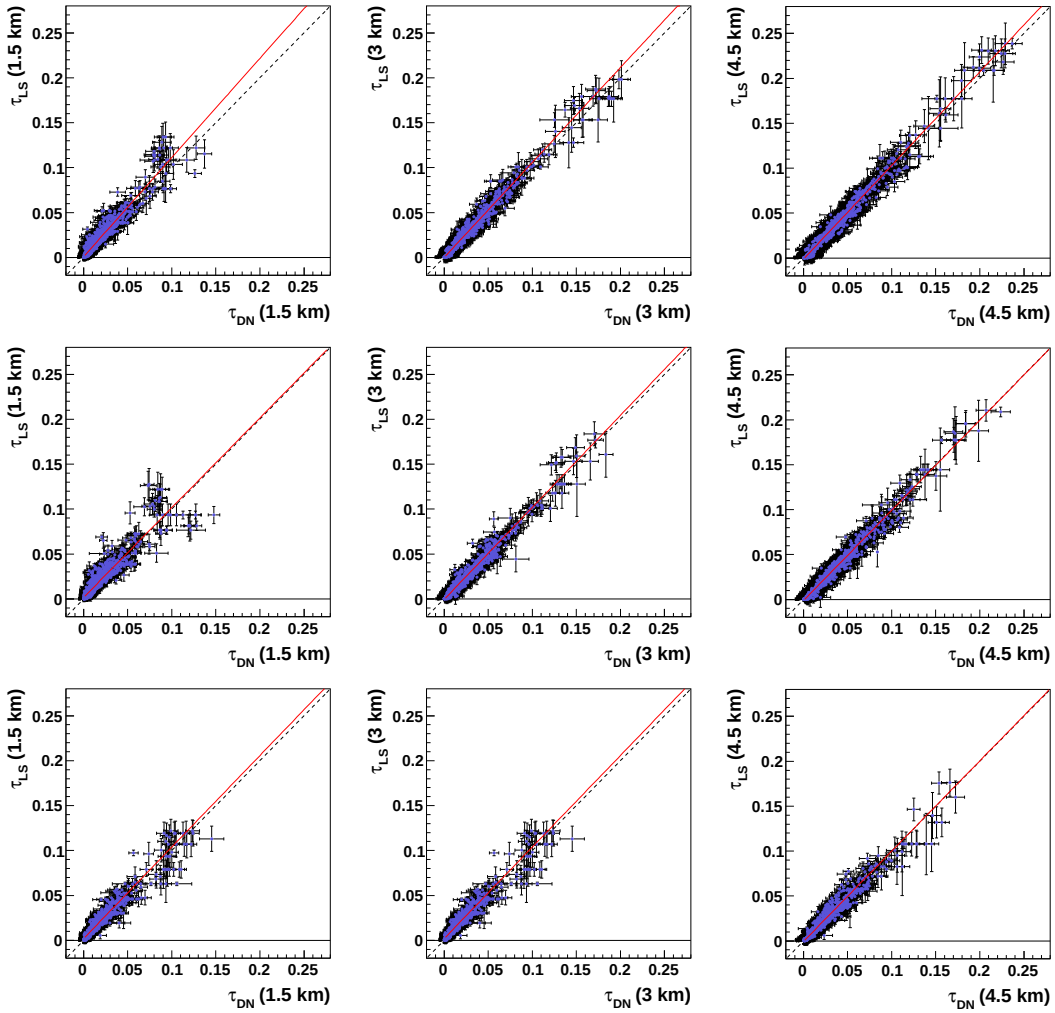

Figure 7.10: Comparison of τ_{aer} profiles calculated using the Data Normalized (x-axis) and the Laser Simulation method (y-axis) at 1.5, 3 and 4.5 km above ground (from left to right) for the FD sites Los Leones, Los Morados and Coihueco (from top to bottom). The black dashed line is the diagonal, a fit to the points is shown in red.

and 2011 are compared. Across a large array like the Pierre Auger Observatory, horizontal uniformity cannot be generally assumed for τ_{aer}, fluctuations between different sites are expected. Also, the altitude of the sites is different, Coihueco is about 200 m higher than the other sites, on a ridge overlooking the Pampa. It is expected, that the τ_{aer} measurements from Coihueco are lower than from the rest of the sites, since the light has to travel through less of the optically thick boundary layer close to ground. Still, local fluctuations can significantly alter this picture.

When comparing the results measured using the CLF with the XLF results, both data from Los Morados and Coihueco agree well for 2010 and 2011. In 2010, a systematic difference of about 0.005 is observed between XLF and CLF τ_{aer} (cf. Fig. B.1). This is a result of choosing the reference night. If a reference night is chosen that is not entirely free of aerosols, the resulting τ_{aer} measurements are sys-

Table 7.2: A list of the reference clear nights used for the analysis of the XLF data. For each FD site, the validity and date are listed. Hours in UTC.

Validity	Los Morados	Loma Amarilla	Coihueco
Jan. 1 – Dec. 31, 2010	Jun. 6, 4–6	Jun. 6, 5–6	Jul. 10, 5–7
Jan. 1 – Sep. 29, 2011	Aug. 3, 5–7	Aug. 3, 5–7	Jul. 23, 2–4

tematically too high. However, this effect is included in the systematic uncertainty estimation. In both comparisons of data measured at the Coihueco site (cf. Figs. B.3 and B.4), larger differences can be seen at increasing heights. A possible explanation is the missing confirmation of the reference nights by the Laser Simulation analysis. In the search for the reference night, only the light profiles with the highest integral light flux are found. The shape of a profile can be slightly higher in the lower part of the atmosphere due to extra scattering out of the laser beam or a small amount of aerosols in the air. This would result in the distortion of the τ_{aer} profiles only at certain altitudes.

Comparing the τ_{aer} results of different sites using the same laser source, larger spreads are apparent (cf. Figs. B.5–B.16). The absolute differences are compatible with zero, but variations of single measurements are larger than comparing measurements from the same site and different lasers. From the comparisons of the XLF and CLF measurements of the same FD site it can be concluded that the laser is not the source of these variances. Another possible source is the calibration of the FD telescopes, a much more likely explanation however is a difference in aerosol concentration at the different sites. The aerosol distribution is horizontally uniform only on smaller distances, not across the entire array. By far the largest differences in τ_{aer} of 0.01 are found in comparisons involving the 2011 profiles of Loma Amarilla as measured with the XLF. This is an effect of the reference night, but without independent confirmation it was not possible to identify a better reference night.

The measurements of τ_{aer} using both the CLF and XLF agree well and will provide a more complete set of aerosol information for all four FD sites in the future. With the possibility to cross-check the results of both laser stations, this will further improve the accuracy of the reconstruction of air showers at the Pierre Auger Observatory.

Chapter 8

Atmospheric Research and Development in Colorado

The understanding of the atmosphere is a critical aspect of ground-based cosmic ray observatories. Plans are being formulated to build even larger detectors, but budgetary restrains force larger baselines between fluorescence detectors, around 80–100 km, instead of the 50–70 km at the Pierre Auger Observatory. It is important to know if the side-scatter method used to evaluate aerosols can still be used over these distances. Another important aspect is the comparison with other techniques to measure aerosols like Raman LIDARs, currently established as the best practice in the atmospheric science community. A shared facility of both techniques can be used for future sites of ground-based cosmic ray detectors and will be implemented as an upgrade of the Pierre Auger Observatory [119]. Also, the atmospheric conditions at possible future locations for giant ground-based air shower arrays can be evaluated.

The Auger Atmospheric Research and Development Program (R&D) was carried out in south-eastern Colorado, see Fig. 8.1, the proposed site for a giant air shower array in the Northern Hemisphere. The two main sites were the Atmo-

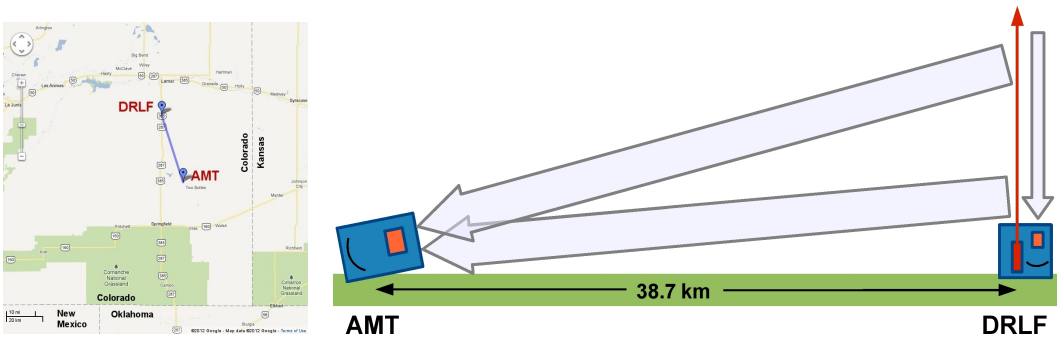

Figure 8.1: On the left, a map of south-east Colorado, courtesy of Google Maps. The DRLF is located about 15 km south of Lamar, the AMT was placed close to Two Buttes and about 25 km away from Springfield. The baseline between both sites is about 38.7 km. On the right, a sketch of the side-view of the R&D sites. The DRLF can produce two different laser beams, an unpolarized 4 Hz beam for side-scatter measurements with the AMT and a 100 Hz beam for backscatter Raman LIDAR operations.

spheric Monitoring Telescope (AMT)[7] and the Distant Raman and Laser Facility (DRLF)[8], formerly the Distant Laser Facility (DLF) during the engineering phase, prior to the installation of the Raman. The sites are located 38.7 km apart close to the city of Lamar and the township of Two Buttes. The effort was coordinated and remotely operated from the physics department of the Colorado School of Mines (CSM) in Golden, Colorado.

The AMT measures the side-scattered photons from a vertical laser beam sent from the DRLF, see right schematic in Fig. 8.1. A Raman Lidar at the DRLF site measures the back-scattered light from the same laser source. From both light returns, the aerosol content in the air above the laser facility and between laser and AMT can be independently estimated. In addition, the molecular atmosphere was measured as part of an atmospheric sounding program using weather balloons. This program was already described in detail in Sec. 5.2.3, data from this program was used in the Raman data analysis. All three parts are established methods to measure atmospheric parameters and have been used successfully at the site of the Pierre Auger Observatory in Argentina. This R&D testbed allows the testing of instrumentation for improvements to the Pierre Auger Observatory and other cosmic ray experiments.

Considerable work on the R&D program was conducted by eleven undergraduate students as part of the Senior Design Program of the Colorado School of Mines department of physics. This included initial planning, modification and installation of the AMT and the DLF in the engineering phase between 2008 and 2010, their help was also very important during the continued running and repairing of the equipment. The testing and installation of the Raman Lidar was done by a graduate student at the Colorado School of Mines and colleagues from the University of L'Aquila, Italy. The AMT DAQ and software were supplied by the Karlsruhe Institute of Technology. The calibration light source was provided by the Colorado State University, the weather stations were maintained by the Michigan Tech University.

As part of this work, I spent over one year in Colorado, where I set up and adapted the DAQ system and software, providing the data and software for subsequent data analysis which I helped the students do or did myself. I was in charge of creating the aerosol optical depth values and wrote the scripts to automatize the analysis steps. Two graduate students, Michael Coco and David Starbuck, and I created, automatized and fine tuned the nightly operations schedule and took shifts of overseeing operations. Both graduate students wrote their Master's theses on the R&D program. One focused on the AMT slow control, operations and data analysis [124], which was carried out in very close cooperation with this work. The other thesis [125] was written about the Raman Lidar measurements and data analysis.

A separate part of detector R&D is still being carried out around the same area in south-east Colorado [126]. Ten Cherenkov tanks of identical design as the tanks of the Surface Detector of the Pierre Auger Observatory are equipped with only one instead of three PMTs and have an additional insulation layer to prevent the water from freezing. Also, a new peer-to-peer communications network is tested between the tanks with several redundancies to prevent large-scale outages as they can happen in a centralized network as it is used at the Pierre Auger Observatory in Argentina. Both this group and the Atmospheric R&D shared personnel, equipment,

[7] Northing 4 164 624 m, Easting 725 811 m, Altitude 1268 m, UTM zone 13S.
[8] Northing 4 199 936 m, Easting 709 994 m, Altitude 1174 m, UTM zone 13S.

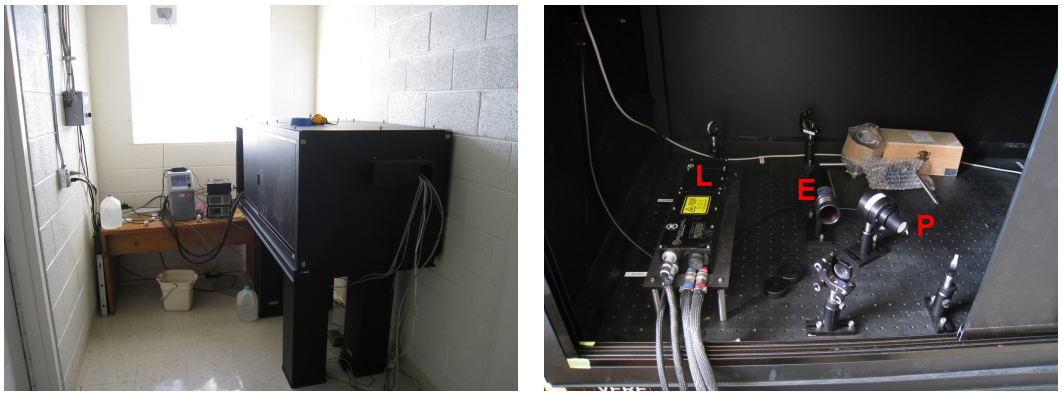

Figure 8.2: The Distant Laser Facility operated in the engineering phase until August 2010. In the left picture, the optical table and the flashlamp with the cooling system can be seen. On the wall on the left side are the circuits controlling the hatch on the roof. On the right picture, the optical components are shown. The laser (L) is directed through a beam expander (E). Afterwards, part of the light is picked off and sent to a pyroelectric probe (P). The rest of the light is diverted into the sky.

laboratory space and on-site facilities.

8.1 Laser Facility

An important part of the R&D is the laser facility that provides the beam for the AMT measurements. In the engineering phase until August 2010, the Distant Laser Facility (DLF) was operated with a flashlamp-pumped Nd:YAG laser, similar to the one used in the CLF (see Sec. 7.2). In Fig. 8.2, a picture of the setup and some of the optical components can be seen. The laser was calibrated by an external radiometer and used a pyroelectric pick-off probe for relative calibration of each laser pulse. The energy deviated less than 10% over the course of almost one year. To avoid a bias in the side-scattering of the photons out of the beam, a depolarizer had to be used. The polarization measurements were performed similar to the measurements at the CLF, described in Sec. 7.2.1. The deviation between major and minor axis of the polarization ellipse was determined to be less than 3.1%, the beam is sufficiently depolarized.

The DLF was used in the engineering phase of AMT operations as a test beam. Viewing from the AMT, the DLF is below the horizon, the alignment was verified with the observation of the DLF laser. We were also able to check the synchronization of the GPS clocks at both sites and the proper configuration of the AMT system to receive external triggers and record a laser beam. While it would be possible to produce aerosol optical depth values in principle, the AMT underwent several changes in hardware and was not calibrated properly. It was decided to only analyze aerosols after the installation of the Raman Lidar in August 2010.

The DRLF uses a diode-pumped laser, not unlike the XLF (see Sec. 7.2). A picture of the setup inside the DRLF and the optical bench can be found in Fig. 8.3. No water-cooling is needed, making the whole system more stable. The laser setup

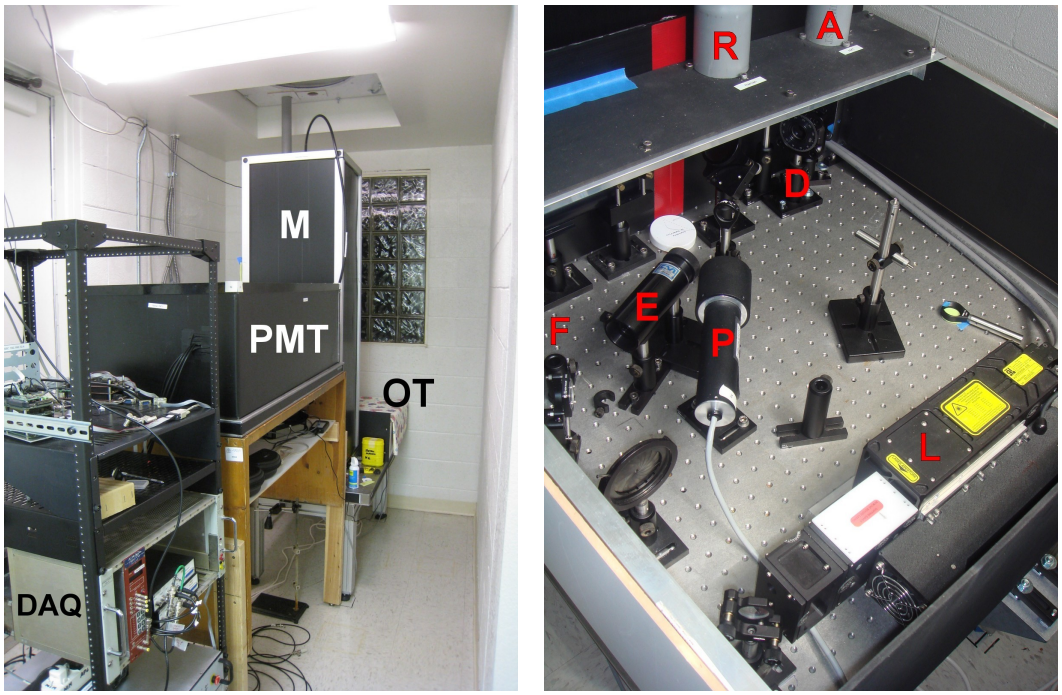

Figure 8.3: The Distant Raman Laser Facility was in operation until June 2011. On the left, the components of the LIDAR can be seen. In the back is the optical table (OT) with the laser and optics. The tall box (M) contains the mirror. One beam pipe can be seen going through the window protecting the mirror from outside conditions. The hole for the second beam pipe is also visible. The light guide on top of the tall box leads into the PMT box, where the return signal is split in separate beams of different wavelengths and is counted by a PMT. In the foreground, the trigger and DAQ electronics box (DAQ) can be seen. On the right, a picture of the optical table is shown. The laser is directed to a flipper mirror (F). If the Raman mode is selected, the flipper mirror is not in the laser path and the beam is directed by a mirror (outside the picture) through a beam expander and upwards through the left beam pipe (R). In the AMT mode, the flipper directs the laser through a different expander (E). Part of the light is sent into a pyroelectric probe (P), the rest of the beam leaves the building through the right beam pipe (A).

needs to perform two main tasks, provide a test beam for the side-scatter measurements like the DLF did, and enable the Raman LIDAR measurements. The requirements for both beams are quite different. For the side-scatter measurements, an unpolarized beam with no more than 4 Hz is needed, so the directionality of the scattering is not biased and the AMT DAQ is not overwhelmed with too many triggers per seconds and the PMTs have time to recover. The Raman measurements suffer from very small cross sections of the backscattering (see Sec. 8.1.1), so a laser with a high repetition rate of about 100 Hz over about 10 minutes at a time are needed to accumulate sufficient photon statistics.

The DRLF laser was run for almost nine months non-stop every night. There were some minor problems, but in general it performed extremely well. The sequence of operation will be described in more detail in Sec. 8.4.1, suffice it to say the

workload for the laser was very demanding.

8.1.1 Raman Lidar

The basic principle of a Lidar was described briefly in Sec. 7.2. The light from a laser beam is scattered in the atmosphere and the return signal contains information about the backscatter coefficient and the transmission of the atmosphere. The attenuation due to the molecular part of the atmosphere can be calculated using data from radiosonde measurements (see Sec. 5.2.3) or global models like GDAS (see Sec. 6.2), leaving only the aerosol scattering parameters open. The inherent problem of extracting both the backscatter coefficient and the optical depth due to aerosols from one return is the most challenging part of Lidar data analysis. The Raman Lidar solves this problem by using not only elastically scattered light, but also light that is returned after inelastic scattering on nitrogen and water molecules. This inelastic scattering results in a characteristic shift in wavelength of the return light. The wavelength of the elastic channel is 355 nm, identical to the wavelength of the laser. The nitrogen and water channels have wavelengths of 386.7 and 407.5 nm, respectively. Using filters, the combined return signal can be separated and collected in separate PMTs. The inelastic part of the signal is only affected by the aerosol concentration by means of transmission, the backscattering cross sections are known and the signal strength only depends on the concentration of nitrogen and water molecules. Using the nitrogen Raman channel, the aerosol transmission can be estimated and from the elastic return, the backscatter coefficient can be calculated. The theory is simple enough and the data analysis does not suffer from the inherent ambiguities of the elastic Lidar. Still, the Raman analysis is very challenging, problems arise in the signal treatment close to the laser facility, where the overlap of the laser beam and the field of view of the Raman Lidar receiver needs to be accounted for [125].

Since the Raman cross sections in the UV range are about four orders of magnitude smaller than the elastic backscattering probability [125], the laser has to be run with high frequency for several minutes to acquire enough signal. At the DRLF, the laser is set to 100 Hz in Raman mode and is fired for 12 minutes, three times per hour, resulting in 36 minutes of data taking. The Raman Lidar uses a 50 cm mirror that was pointed vertically and positioned under a UV-transmitting quartz glass window to protect it from outside conditions. The return signal is transmitted to the three receiving PMTs with a liquid light guide, the data acquisition is done using 250 MHz fast photon counting modules [119]. Prior to its shipping and installation in 2010, the Lidar was deployed in L'Aquila, Italy, and checked against the local Lidar that is part of the European Lidar network EARLINET [127].

8.1.2 Slow Control System

The slow control system of the DRLF can be operated manually and, more importantly, automatically for nightly operations. In Fig 8.4, all components and their connections are visualized. The central entity of the slow control is the Boss computer. It is a single board computer (SBC) with an attached GPSy2 board which is connected to a GPS antenna on the roof of the building. The Boss distributes preset commands from a command file to its subordinates at predetermined times. A second SBC actually controls the hatch in the roof after receiving commands from the

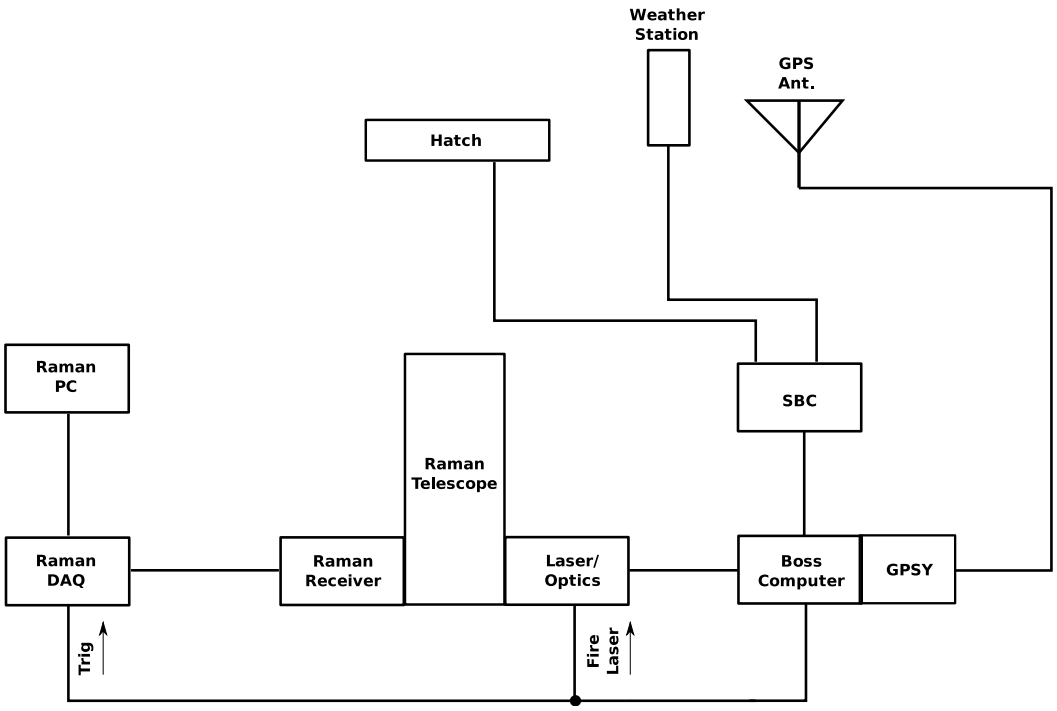

Figure 8.4: A schematic of the DRLF slow control system.

Boss. Two daemon programs run on this SBC, a hatch and a weather daemon. The weather daemon reads out the weather station periodically. If the wind is above a certain threshold or rain is detected, the daemon closes the hatch automatically. The daemon also prevents the hatch from opening during unsafe operational conditions.

The laser optics can be switched between AMT and Raman mode by the Boss. The GPSy2 board sends out the pulses to fire the laser. If the Raman mode is active, a signal is also sent to the Raman DAQ to start recording data from the Raman receiver. A dedicated Raman PC is set up for data storage and manual access.

The power supply of the Boss, SBC and hatch electronics are secured by UPS (Uninterruptable Power Supply), in case of main power failure the UPS makes sure enough power is available to close the hatch and shut everything down properly. All systems are also connected to RPCs, remote controlled power supplies that can switch the power on or off and are controlled via the network by the Boss or manually.

8.2 The Atmospheric Monitoring Telescope

In principle, the AMT is a fully functioning cosmic ray detector, see Fig. 8.5. Its optics and functionality is almost identical to the fluorescence telescopes used in cosmic ray experiments like HiRes, Telescope Array or the Pierre Auger Observatory. The light enters the AMT at its aperture as a parallel beam of photons. Using a large spherical mirror, see middle picture in Fig. 8.6, photons coming from the same direction in the field of view of the AMT are reflected onto a single spot on a photomultiplier camera, left picture in Fig. 8.6. The AMT was designed to measure cosmic rays in a self-triggered mode. For the R&D work, the AMT was reconfigured

Figure 8.5: On the left, a picture of the AMT and the support container. The telescope includes the mirror and the camera, weather sensors and a calibration system. The container is equipped with internet access and houses the data acquisition electronics, the single-board computers to steer the operations and a personal computer as gateway and for manual access. The power and data connections between both are underground. The old door design with two outward swinging doors can be seen. The new rolling door design is shown on the right.

to capture laser tracks from a distant vertical laser with well-known geometry. This is done using an external trigger from GPS clocks. The AMT is mounted on four concrete support pillars, the two in front are raised for the desired field of view. The optical axis, defined as the direction of the sky that is imaged on the center of the camera, was adjusted to 8.72° in elevation and 16° in azimuth using a theodolite. The alignment relative to the laser facility was done using a hill as a landmark that could be seen from both sites, since there is no direct line of sight between the sites. Correcting for the difference in altitude and the curvature of the Earth, the laser of the DRLF can be seen from the AMT between 1.31 and 10.54 km above ground at the DRLF, corresponding to 2.48 and 11.71 km above sea level.

The AMT was commissioned in January 2010, when the telescope was put in its place, the support container with the data acquisition electronics, internet access and computers was placed next to it, see Fig. 8.5. Both are connected by underground cables transmitting the commands to the telescope electronics and slow control in the one direction and the measured data in the other. In the support container, a personal computer acts as the internet gateway to the outside. Two single board computers are used to steer the automated data taking, calibration and the slow control (see Sec. 8.2.3).

Upon installation, the AMT was equipped with two doors that were hinged at the sides and were swung open by two motors. This system was unstable as it was susceptible to wind and the motors did not meet expectations. A new design using a roll-up door was installed in July 2010. Unfortunately, while the new doors were installed, a short circuit was created that severely damaged the DAQ electronics. All

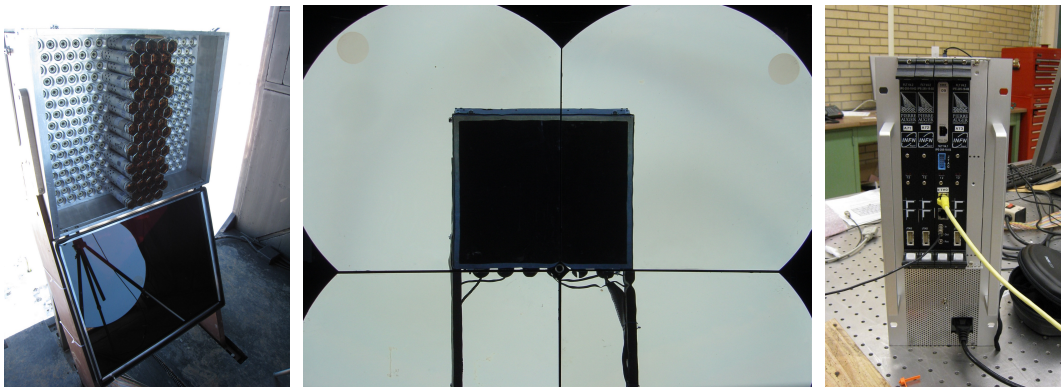

Figure 8.6: On the left, the camera of the AMT. The UV bandpass filter is lowered to allow inspection and manipulation of the PMTs. It can be seen in its upright position in the reflection in the mirror in the picture in the center. The mirror is divided into four segments. There is a small hole in the middle where the calibration light source is mounted (not yet in this picture). On the right, a picture of the data acquisition electronics in their mini-crate is shown. One central board with ethernet connection and three subsidiary boards are mounted. Also connected to the main board is the external trigger cable to initiate the data readout via the cables connected in the back.

three FLT boards sustained major damage, the SLT board had small burn marks from the damaged FLT next to it. All boards were sent back to Karlsruhe for inspection and repair. The SLT was not damaged and still functioning, the firmware was upgraded to the newest version. All three FLTs were beyond repair and had to be replaced.

Regular measurements started on October 8, 2010. In total, 320 hours of data were recorded with the AMT over nine dark periods. The decommissioning of the Distant Raman Laser Facility in July 2011 entailed the termination of AMT measurements.

8.2.1 Camera

The camera of the AMT has been previously used to measure cosmic rays as part of the HiRes experiment. It can be populated with up to 256 PMTs (16×16), a UV bandpass filter is attached to the camera to reduce background light. Since the laser track is vertical, the AMT camera is not fully equipped. Three adjacent vertical columns of 16 PMTs each are sufficient, see left picture in Fig. 8.7. Each PMT has a field of view of 1° in azimuth and elevation in this configuration, see right schematic in Fig. 8.7, resulting in a combined field of view for the camera of about 3–3.5° in azimuth and about 14° in elevation. These 48 PMTs were selected to have the best matched gain values. The PMTs have pre-amp assemblies attached and are plugged into the backplane of the camera. Through the backplane, the PMTs are supplied with ±5 V for the pre-amp electronics, as well as the high voltage needed to amplify the signal. The high voltage of up to 1200 V can be switched on or off and adjusted either manually or automatically. The PMT signal is read out at the backplane using DB-25 connectors with 8 channels per connector, two connectors are needed

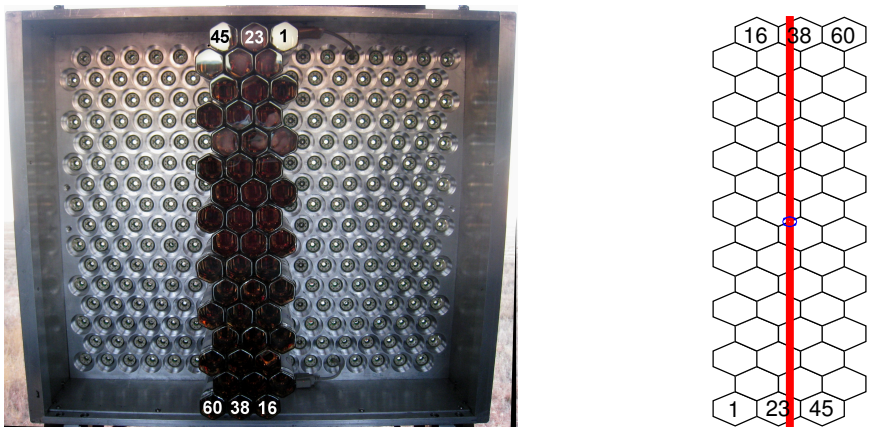

Figure 8.7: The pixel numbering of the AMT. The camera view is shown on the left. The pixels at the top of the camera observe the part of the sky closest to the horizon. On the right, the sky view is shown with the theoretical laser path. The blue dot marks the center of the camera in the optical axis.

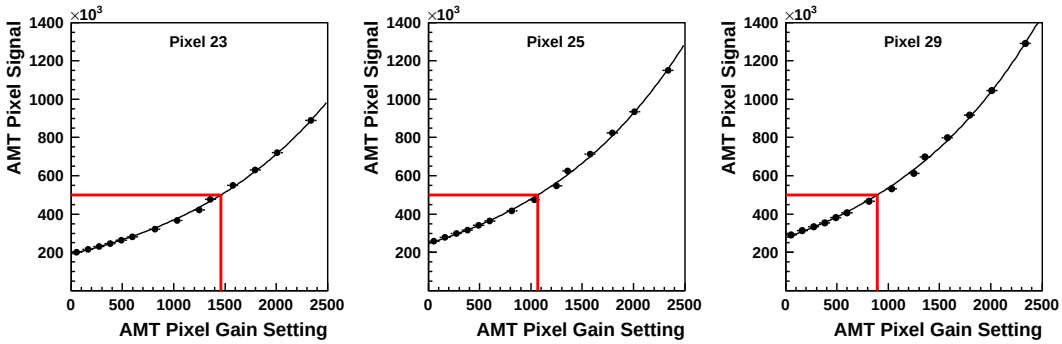

Figure 8.8: The response of three pixels to 400 LED pulses at different gain settings. A reference response of 500 000 was chosen to fix the gain setting for each pixel.

per 16 PMT column. The gain sorting and the design of the power supply system were done by undergraduate students at CSM.

The PMTs are the same type used at the Pierre Auger Observatory and are sensitive in a region from around 300 to 650 nm, the quantum efficiency is highest in the UV region and reaches a maximum of 30% around 375 nm. In front of the camera, a UV bandpass filter is used to suppress background photons. Contrary to the telescopes at the Pierre Auger Observatory, where the filter is mounted in front of the aperture, the size of the aperture is only limited by the size of the mirror with this design. However, the AMT is completely open to the environment during operations, small debris, dust and even wildlife could compromise the telescope. The filter transmits light with wavelengths above 300 nm and transmits less than 10% of the light above around 420 nm with a maximum transmission of 80% at around 360 nm [128].

The amplification of the photo electrons produced in the PMTs by the incoming light, the PMT gain, differs slightly between PMTs. The data acquisition system (see Sec. 8.2.2) that is used to read out the voltage signals of the PMTs can be

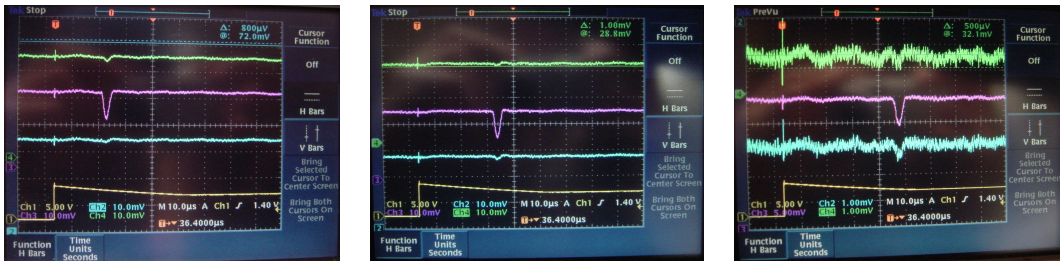

Figure 8.9: First signal seen at the AMT from a DLF laser shot, read out directly from the PMTs. From left to right the signals seen in row 3, row 8 and row 14 are shown for all three pixels of each row. The middle pixel receives the most light as expected with some contribution in the off-center pixels.

configured to account for this effect. The incoming signals are boosted or reduced according to a fixed electronic gain value for every PMT that is set in the front-end electronics of the PMT readout system. To obtain this electronic gain, an isotropic UV light source (see Sec. 8.3.2) is used to illuminate the whole camera uniformly. While the intensity of the light source was kept constant, the electronic gain of the individual PMT readouts was changed continuously. For each setting, 400 LED pulses were sent. The correlation between electronic gain setting and signal height was used to determine a gain for every PMT that results in a signal of the same amplitude, see Fig. 8.8. The electronic gain to response function is almost linear in the beginning and increases exponentially for higher electronic gain settings. The standard gain setting before the flat-fielding was 1000 for all pixels. The reference response of a signal of 500 000 was chosen so that the electronic gain is around 1000 for all pixels and the response does not change drastically for most pixels. Also, this value is not too far into the exponential rise of the function.

This process of flat-fielding is important to make sure differences in PMT signal in actual measurements of scattered light from the distant laser are due variations in the light intensity and not differences in PMT performance.

8.2.2 Data Acquisition

The voltages picked off at the PMTs need to be recorded for later analysis. In Fig. 8.9, the raw signals from the first light of the DLF laser seen at the AMT are shown. Pictured are the oscilloscope readouts of rows 3, 8 and 14 (for the numbering see Fig. 8.7). The laser light is expected to be seen in the middle column, a clear pulse is visible in all rows. Some light spilled into the adjacent pixels, this is due to the geometry of the camera. The laser beam is always to the right or the left of the center pixel, depending on the row, see right panel of Fig. 8.7. For higher rows, a shift of the pulse in time due to the longer light path from higher elevations is observed.

To acquire the data and save them for data analysis, the same front-end electronics are used that record data at the HEAT telescopes at the Pierre Auger Observatory, see Sec. 3.2. It is an updated version of the electronics used at the other four FD telescopes. It also records 100 µs of data, but with a sampling frequency of 20 instead of 10 MHz, resulting in 2000 data bins with a bin width of 50 ns instead of 1000 bins of 100 ns. The readout program is a modified version of the run control

program used for the FD telescopes of the Pierre Auger Observatory. The PMT voltage signals are converted to form traces of single laser shots that are then stored in a special file format for subsequent data analysis. The DAQ for the AMT is mounted in a mini-crate with power supply and a cooling fan, see Fig. 8.6. Similar to the electronics of the FD telescopes of the Pierre Auger Observatory, it also houses one Second Level Trigger (SLT) board, but only three instead of 20 First Level Trigger (FLT) boards. The AMT is only used to measure a narrow laser beam, so only three columns of PMTs are read out. The usual pattern recognition of the SLT is bypassed, the DAQ is triggered externally, either by a GPS module synchronized to a second GPS module that triggers the laser or, in case of LED calibration shots, by a trigger signal from the LED computer. Every trigger prompts the SLT to read out the FLTs and store the event.

One FLT board with 22 channels is used per 16 pixel vertical column. Cable converters were fabricated that map the two 8 channel DB-25 connectors per column at the AMT camera to the 22 channel inputs at the DAQ mini-crate. The pixel numbering of the AMT shown in Fig. 8.7 is a direct result of this. Since 22 channels are read out, but only 16 PMTs are connected, the first column has PMT numbers 1 to 16, column 2 includes pixels 23 to 38 and column 3 comprises of PMTs 46 to 60. Since the data visualization and data analysis is done with modified versions of the *Offline* air shower analysis framework of the Pierre Auger Observatory, this numbering scheme was not changed, simple sanity checks in the code prevent the use of non-existing pixels in the analysis.

To match the recorded traces to the fired laser shots, every event gets timestamped by the DAQ. The time is synchronized through the internet once every night using a Network Time Protocol (NTP) server. To keep the time aligned during the run, a one pulse per second signal (1 PPS) is required. In the beginning of operations, I modified one of our GPSy boxes that was used to provide trigger signals for the laser systems to reroute the 1 PPS signal to an output that was not used. During later operations in coincidence with the Raman LIDAR, this signal is delivered by a GPSy2 board of one of the control single board computers, see Sec. 8.2.3.

8.2.3 Slow Control System

The operations at the AMT are controlled by several Single Board Computers (SBC). In Fig. 8.10, the different components and their main functions are shown. All the computers are connected via an internal network. Inside the AMT, two SBCs are responsible for the slow control systems and the LED calibration system. The LED SBC can fire the LED at different pulse lengths and widths, delivers an external trigger pulse for every shot that can be used to trigger the data acquisition, and records voltage traces for every LED shot for later comparison to the measured pulse.

The AMT SBC controls and monitors the door, the power to the camera, the high voltage of the PMTs and the weather station. The weather station provides a set of temperature, pressure, wind, and precipitation every 5 seconds. A safety daemon on the AMT SBC checks if the values for wind and rain are within the safety margins. The SBC shuts the door and powers down the high voltage if wind of more than $7\,\mathrm{m\,s^{-1}}$ or rain is measured. The safety daemon also prevents the opening of

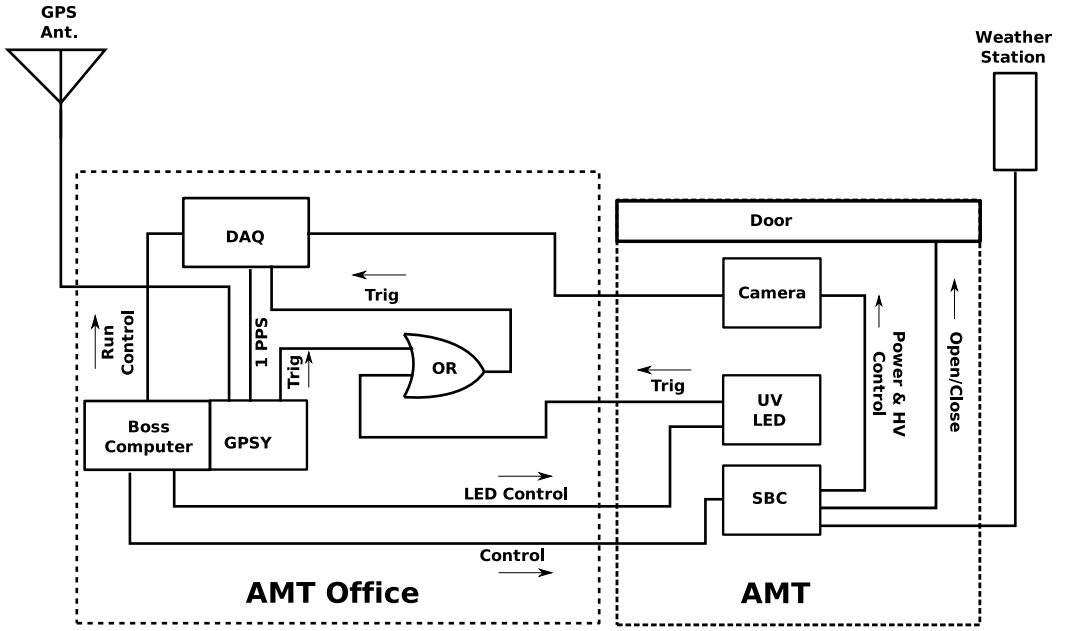

Figure 8.10: A schematic of the AMT slow control system.

the door during the day, it can only be opened between the hours of 2 and 10 UTC.

In the office container next to the AMT, the Boss SBC controls the nightly operations. From there, commands can be sent to both the AMT and the LED SBC. A daemon on the Boss is responsible for the automatization of the AMT measurements. It reads a set of commands from a text file and follows them during the night. The Boss SBC includes a GPSy2 board that is connected to a GPS antenna on the office container. The data acquisition can be triggered by this GPS signal of the Boss SBC in coincidence with DRLF laser shots.

The power supply of the Boss, the DAQ and all electronics inside the AMT are secured by UPS, similar to the systems at the DRLF. In case of main power failure, enough power is available to close the AMT door shut everything down securely. All systems are also connected to remote power control units that can switch the power on or off and are control via the network by the Boss or manually.

8.3 Calibration and Monitoring

8.3.1 Weather Stations

As part of the monitoring system, the environmental conditions are measured at the AMT and the DRLF. Important factors are wind and rain. If either exceed a threshold value, the door of the AMT closes or cannot be opened until the conditions are safe for operations. For this reason, identical weather stations are installed at the DRLF and the AMT site, see middle and right picture in Fig 8.11. For both stations, the *Weather Transmitter WXT520* by Finnish manufacturer *Vaisala* [129] is used. Besides capacitive sensors for temperature, pressure and humidity, an ultrasound sensor measures the wind speed and direction and an acoustic sensor measures the

Figure 8.11: On the left, the calibration LED that is used between runs for a relative calibration of the AMT pixels. In the middle, the weather station at the AMT can be seen, below the station is a cloud monitor and the GPS antenna. On the right, the DRLF weather station is shown.

rain. The software readout of both stations was supplied by the Michigan Tech University. The wind and rain data are read out every 5 seconds to determine safe operational conditions, the averages of both quantities along with all other available data are written to a file every 5 minutes. However, it was found that the readout program of the stations does not store negative temperature values. About 182 hours of 5642 measured hours, about 3.2% of the data are affected by this bug. During regular operations, only wind and rain data are needed, so the absence of reliable temperature data does not impede data taking.

In Fig. 8.12, the data from both stations are compared with each other and with the GDAS data for the Colorado location, see also Sec. 6.2. The DRLF station recorded data from December 2009 until June 2011, but was defective from December 2010 until April 2011, a total of about 1800 hours of data are available. The AMT station is running since December 2009 until the present time (April 2012) with a longer interruption in December 2010, more than 4000 hours of data can be used for comparison. The histograms in Fig. 8.12 are normalized for better visualization. The difference in temperature between the DRLF and the AMT station (black dashed line) is 0.66°C with an RMS of 7.6°C, the difference between GDAS and DRLF is 0.55°C with an RMS of 5.2°C, the difference between GDAS and AMT is 0.68°C with an RMS of 5.0°C. It has to be noted that no negative temperatures are included in this comparison due to an error in the readout program. Since only differences are evaluated, this should not change the comparisons significantly. The means agree quite well, the spread is rather large, even for a distance of almost 40 km. One reason for this can be the placement of the AMT station directly on top of a metal container which could cause a residual heating effect. The mean differences in vapor pressure are -0.28, 0.16 and 0.44 hPa with RMS of 3.8, 2.4 and 2.1 hPa, respectively. Since the relative humidity is the quantity measured by the weather stations, the vapor pressure is calculated using the temperature and the differences in temperature translate into the differences in vapor pressure. For the wind speed, the differences are 0.18, 0.19 and 0.50 $\mathrm{m\,s^{-1}}$ with an RMS of 4.1, 3.2 and 2.7 $\mathrm{m\,s^{-1}}$. Both weather stations agree quite well with each other and the GDAS data. In pressure,

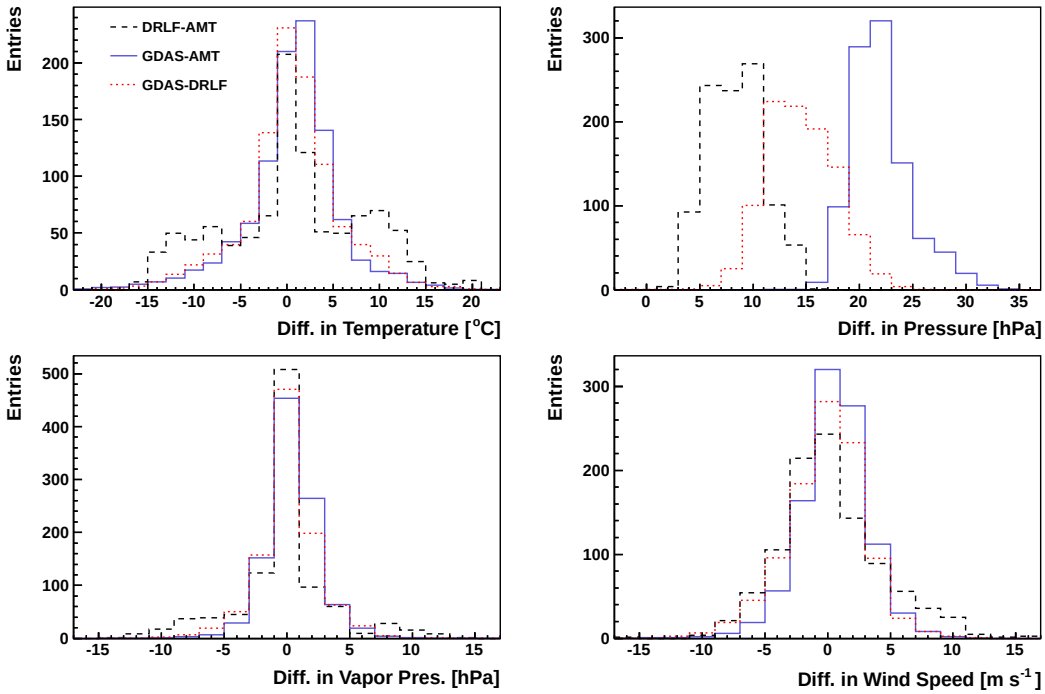

Figure 8.12: Difference in temperature, pressure, vapor pressure and wind speed for data from the weather stations at the AMT and the DRLF and the GDAS surface data. All histograms are normalized to correct for the different number of entries. The difference of DRLF and AMT (black dashed) is rather broad in temperature, differences GDAS-AMT (blue solid line) and GDAS-DRLF (red dotted) are well within expected differences across 40 km. Pressure data are not corrected for difference in altitude.

the differences are 8.3, 14.5 and 22 hPa with an RMS of 2.6, 3.3 and 2.8 hPa. The pressure values are not corrected for the different altitudes of the stations and the GDAS grid point. The GDAS grid point is about 110 m higher than the DRLF and about 220 m higher than the AMT, resulting in an expected pressure difference of 11 and 22 hPa, respectively. While the difference between GDAS and AMT is within expectations, the differences involving the DRLF station do not agree with the expected difference, which is most likely due to a faulty pressure sensor in the DRLF weather station.

The weather stations are important for the safe operations of the AMT and the DRLF, the comparison between both shows a rather good homogeneity across the baseline of the experiment, although the statistics are rather limited. At both sites, the GDAS data agree well with the weather station measurements.

8.3.2 Relative Calibration System

An hourly, relative calibration of the AMT is done with a UV light source mounted in front of the camera. In the engineering phase, several designs were used to do preliminary calibrations and test the PMT camera. For the calibration during nightly operations, it was decided to use a proven design used for the calibration of

the FD telescopes of the Pierre Auger Observatory. It was provided by collaborators from the Colorado State University. In the final design, the UV LED was mounted in the center of the mirror, pointing along the optical axis, see Fig. 8.11, left picture. Inside this calibration light source, a temperature-controlled UV LED produces short light pulses at 375 nm. The LED was calibrated in the lab relative to calibrated photodiodes by NIST[9]. It is of the same type used to calibrate the fluorescence detectors at the Pierre Auger Observatory [55]. Several layers of diffuser material are used to make the light almost isotropic when it reaches the camera. These pulses can be used to keep track of changes in the PMT response. The LED is fired 120 times at a frequency of 4 Hz, one minute before and after the laser shots from the DRLF, providing two sets of calibration data for each set of laser shots.

The current going through the LED is measured. Comparing the input signal with the output generated by the PMTs as measured by the data acquisition system, a relative calibration constant can be computed to correct the PMT signal. Before calculating this constant, the PMT response has to be corrected for two geometrical effects. The UV LED can be considered as a point source, the camera body with the PMTs is flat, resulting in a smaller signal for PMTs further away from the camera center. The flat camera body also causes a lowered effective area A_{eff} of the outer PMTs. Accounting for both effects reduces the observed light intensity of the LED to

$$I_{\text{obs}}(\theta) = I_0 \cdot \frac{A_{\text{eff}}}{4\pi r'^2} = I_0 \cdot \frac{A_{\text{PMT}} \cdot \cos^3\theta}{4\pi r^2}, \tag{8.1}$$

where r is the distance between the LED and the center of the camera, r' is the distance to a pixel offset from the center vertically by an angle θ.

The currents of the LED are averaged for every calibration set of 120 shots at 4 Hz, lasting 30 seconds in total. The calibration is run before and after each set of 200 laser shots. This redundancy is due to a technical problem with one of the trigger signals of the Boss SBC, causing the failure of a set of calibration shots. In this case, there should be another calibration constant from the second set of LED pulses. If neither calibration happened, the closest in time from a different set of laser shots is used, usually about 15 minutes before or after. The actual calibration constant is calculated for each AMT pixel by dividing the averaged voltage of the LED by the averaged PMT signal for every calibration set. This value is then normalized to the calibration constant of one of the first nights of data taking on November 3, 2010 to get calibration constants around unity.

In Fig. 8.13, top panel, the calibration constants for Pixel 23, the pixel in the central column with a field of view closest to the horizon, are shown for the entire data taking period. The average calibration constant is 1.04 with a standard deviation of 0.09, the calibration of this pixel is very constant. Also shown in Fig. 8.13, bottom panel, is the temperature as measured with the AMT weather station (black dots). Since the available data have several gaps when the station was not functioning or the temperature was below zero, the GDAS data are used to supplement the data (red line). When comparing the calibration constant with the temperature, it is obvious that unusually high calibration constants correlate with particularly low temperatures. This is most likely due to the calibration LED, in principle it is temperature controlled, but it seems not to function well below a temperature of -8°C. For this reason, data recorded under such conditions was discarded, the bad

[9]National Institute of Standards and Technology

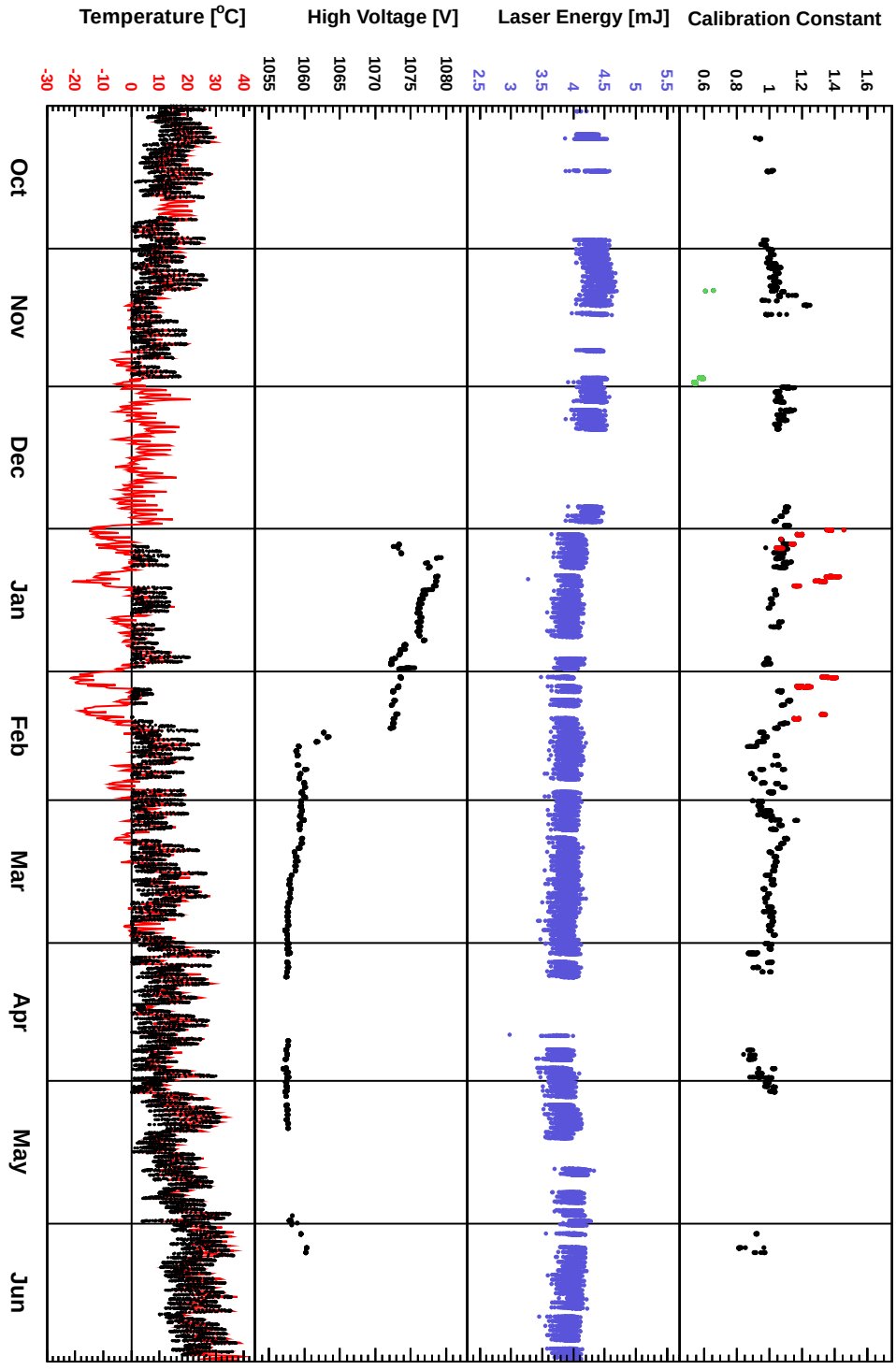

Figure 8.13: Calibration and monitoring data for the AMT and the DRLF. In the top panel, the calibration constant for pixel 23 is shown. In the second and third panel, the laser energy and the readout from the high voltage monitor can be seen. On the bottom, the temperature of the weather station at the AMT is shown, together with GDAS data in red. For more details see text.

Table 8.1: A list of bad periods identified for the AMT. The two reasons for bad periods are wrong gain settings in the front-end electronics and a temperature below −8°C.

Start Second	End Second	UTC Period	Reason
973401534	973406635	2010-11-10 05:18 – 2010-11-10 06:43	Gain
973412934	973415034	2010-11-10 08:28 – 2010-11-10 09:03	Gain
975034734	975207545	2010-11-29 02:58 – 2010-12-01 02:58	Gain
977821214	977940014	2010-12-31 09:00 – 2011-01-01 18:00	Temp.
977961614	978026414	2011-01-02 00:00 – 2011-01-02 18:00	Temp.
978048014	978069614	2011-01-03 00:00 – 2011-01-03 06:00	Temp.
978156014	978188414	2011-01-04 06:00 – 2011-01-04 15:00	Temp.
978231614	978242414	2011-01-05 03:00 – 2011-01-05 06:00	Temp.
978696014	978728414	2011-01-10 12:00 – 2011-01-10 21:00	Temp.
978739214	978804014	2011-01-11 00:00 – 2011-01-11 18:00	Temp.
978825614	978901214	2011-01-12 00:00 – 2011-01-12 21:00	Temp.
978912014	978955214	2011-01-13 00:00 – 2011-01-13 12:00	Temp.
980553614	980802014	2011-02-01 00:00 – 2011-02-03 21:00	Temp.
980812814	980866814	2011-02-04 00:00 – 2011-02-04 15:00	Temp.
981212414	981396014	2011-02-08 15:00 – 2011-02-10 18:00	Temp.
981417614	981471614	2011-02-11 00:00 – 2011-02-11 15:00	Temp.

calibration constants are marked in red in Fig. 8.13. In early and late November, different gain settings from before the flat-fielding were loaded accidentally, those calibration constants are plotted in green. Periods of low temperatures and wrong gain settings are discarded as bad periods, they are listed in Tab. 8.1.

8.3.3 Monitoring

For the data analysis of the DRLF laser shots, the laser energy for every event has to be known, so that the AMT response can be normalized to the laser energy. An absolute calibration of the DRLF laser was done in periodic intervals every few months by comparing the measured sky energy of the laser with the readout of the pick-off probe. In Fig. 8.13, second panel, the laser energy calculated from the pick-off probe is shown for the entire data taking period. The energy is very stable, with a mean of 4.02 mJ and an RMS of 0.20 mJ, fluctuating less than 5% over almost 9 months.

In January 2010, a high voltage monitor was installed at the AMT. In the third panel of Fig. 8.13, the HV data are shown. A sharp drop is observed on February 14, 2011. No clear reason could be identified for this jump, the system had to be restarted on this date, but this was also done on several other occasions. Before this date, the HV was 1075 V on average with an RMS of 2 V, afterwards the mean was 1058 V with an RMS of 1 V. The drop in HV was 1.6%, but the voltage appeared to be more stable after February 2011. A change in high voltage varies the response of the PMTs to the scattered light from the DRLF laser, but it also changes the response of the PMTs to the calibration LED, so the difference in HV should not

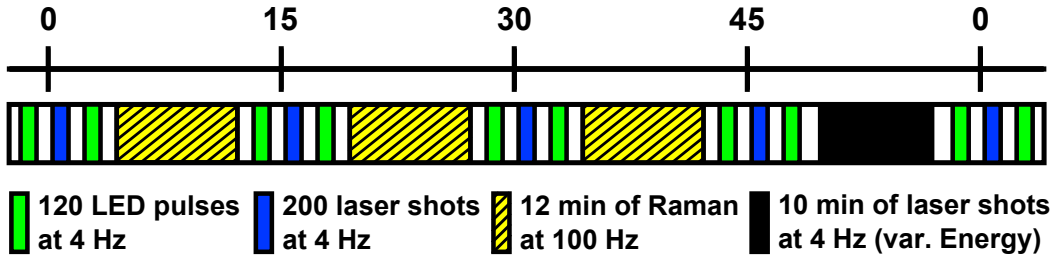

Figure 8.14: Scheme of the sequence of operations for one hour during combined data taking. 200 laser shots for the AMT are produced every 15 minutes starting at minute 1 of every hour. 120 LED calibration pulses are done before and after every laser set. In the first three quarter hour breaks, the Raman Lidar collects data for about 8 minutes. In the fourth quarter hour space, the laser is fired in AMT mode at different energies.

affect the measurement after calibration.

8.4 Data Taking

The Raman Lidar system and AMT can be operated manually by a shifter or automatically using a list of commands. To perform automated procedures, an operator starts scripts which control operations of the systems at the beginning of the night. Each system will power on, collect data, and power down at the correct times. If necessary, the operator can stop the automatic procedures and control the AMT or DRLF manually.

8.4.1 Sequence of Operations

The Raman Lidar system and AMT have independent procedures which run in parallel, a scheme of the hourly sequence is shown in Fig. 8.14. The procedures are synchronized by GPS. Each night, the Raman Lidar system operations start at 2:15 UTC and shut down at 11:00 UTC. Starting at 3:00 UTC, 200 vertical shots for the AMT measurements are fired into the sky on minutes 1, 16, 31 and 46 of each hour. The laser fires at 4 Hz, at 100, 350, 600, and 850 ms after the full second. The data acquisition of the AMT is triggered accordingly by the GPS on-board the Boss computer, corrected for the time the light takes to reach the AMT, around 130 µs. In the Raman mode, the laser fires at 100 Hz. Backscattered photons from these laser shots are measured by the Raman system, which collects data for eight minutes during the first three intervals between sets of AMT laser shots. Between minutes 47 and 57, vertical laser shots at lower energies are shot into the sky to check the linearity of the AMT camera.

The moon causes an intolerable level of interference for AMT data collection. Therefore, the hours of AMT operation are dictated by the moon phase. For each night, the hours in which the moonlight background is low are calculated and an AMT command list is produced to perform operations during these hours. During the hours of operation, 120 LED shots are fired before and after each set of AMT laser shots. The LED sends its own trigger to the DAQ each time it fires.

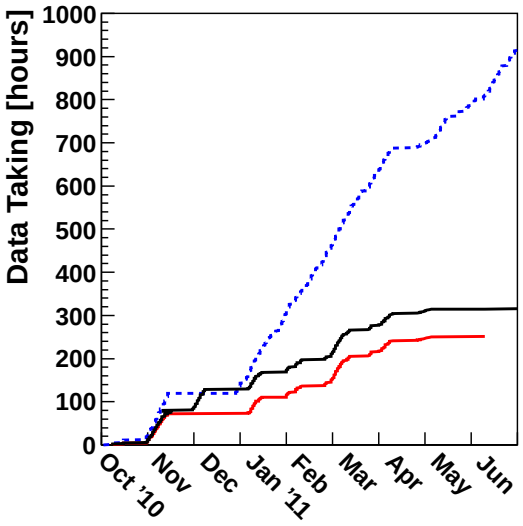

Figure 8.15: Cumulative number of operational hours of the Raman LIDAR (blue dashed) and the AMT (black). Hours where both systems acquired data are drawn in red.

8.4.2 Collected Data

Since each system is capable of performing its startup, data collection and shutdown procedures without an on-site shifter, these systems can be operated and monitored remotely. Operations began on October 8, 2010, the systems have been monitored from Golden, Colorado (approximately 500 km from the site), from Karlsruhe, Germany, from L'Aquila, Italy and once from Malargüe, Argentina. The Raman system can operate every night, moonlight does not hinder the operations. The longer period without data taking in November 2010 was due to a failure of the Raman DAQ. The AMT can only operate in nights with low illuminated moon fraction, so about 1.5 weeks before and after new moon. Regular operations were disturbed by broken components like the weather station or the high voltage power supply. Towards the end of measurements in June 2010, the operation of the AMT became more and more difficult, in May 2011 data from two hours and in June 2011 only one hour is available. It was decided to stop operations of the AMT one month earlier, the Raman was scheduled to be transported back to Golden in July. In total, 320 hours of data were collected by the AMT, 937 hours by the Raman alone and 251 hours of combined data are available, see Fig. 8.15. Rejecting the bad periods as listed in Tab. 8.1, 292 AMT and 233 combined hours remain.

Raman Data

The raw Raman data of τ_{aer} and the backscatter coefficient β_{aer} were processed and provided by colleagues from L'Aquila [130]. Both estimates were done using climatological molecular atmospheres. These are monthly averages based on daily radio soundings performed at the Denver Stapleton Airport in Colorado, accounting for the difference in altitude between Lamar and Denver. GDAS data were not used. For this particular analysis, only a rough Rayleigh scattering calculation was done

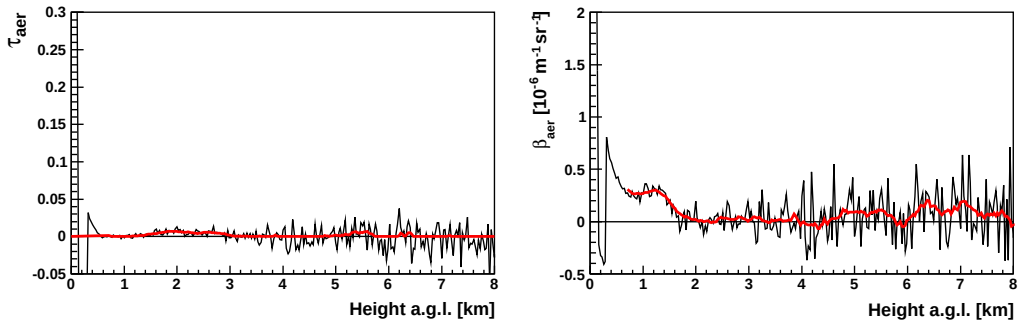

(a) January 7, 2011, 6–7 UTC: Very clear conditions.

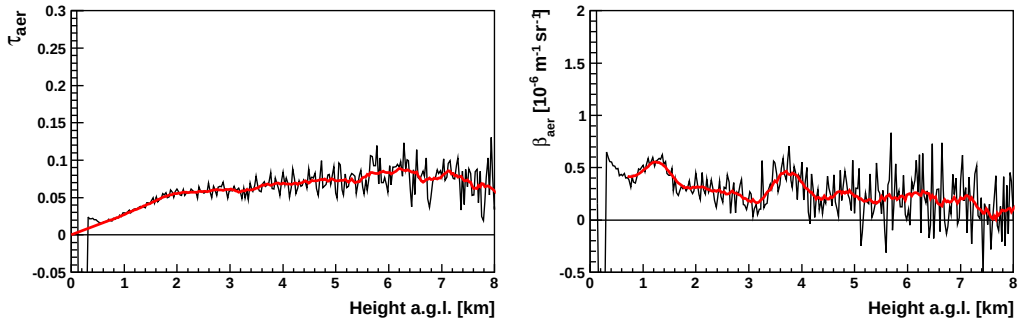

(b) April 5, 2011, 4–5 UTC: Average conditions.

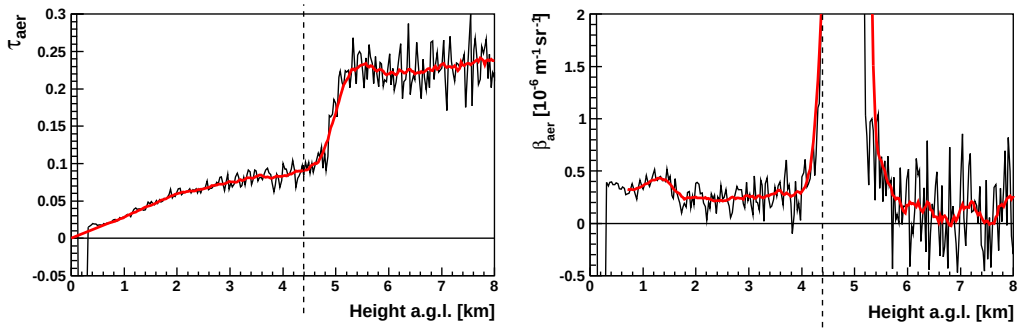

(c) May 11, 2011, 3–4 UTC: Cloud above the Raman around 4400 m a.g.l.

Figure 8.16: The raw data from the Raman analysis shown in black, the results after smoothing in red. On the left, the vertical aerosol optical depth τ_{aer}, on the right, the aerosol backscatter coefficient β_{aer}. From top to bottom, the Raman data measured during extremely clear (a), average (b) and cloudy conditions (c) are shown.

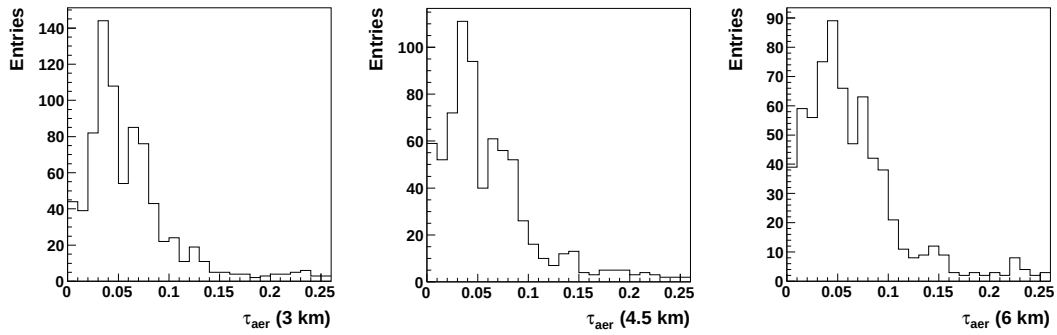

Figure 8.17: Mean τ_{aer} as measured by the Raman LIDAR at 3, 4.5 and 6 km a.g.l.

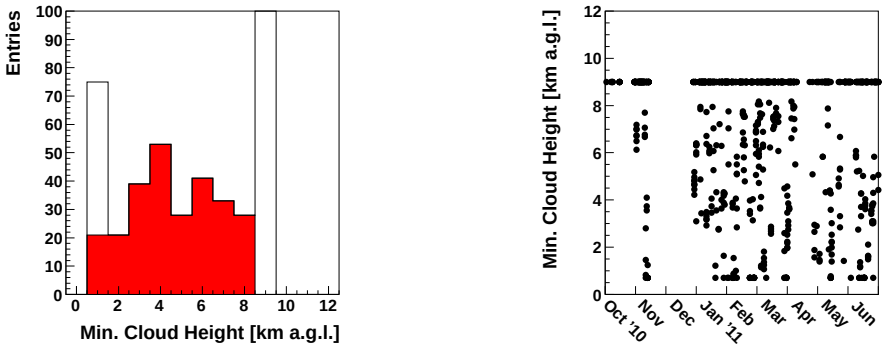

Figure 8.18: The minimum cloud height as determined from Raman data. On the left, actual clouds are included in the red histogram, cloud-free profiles populate the white bin at 9 km. At 2 km, profiles where the cloud height is set at the start of the profile are also excluded from the red histogram. The last bin contains 612 entries. On the right, the cloud height is shown versus time.

and there were no attempts to refine the LIDAR signal treatment, e. g. no optical overlap function and no analog or photon counting detection were used. Applying an overlap function is very challenging and work is in progress to implement this in the analysis. In the region close to the laser facility where the overlap of the laser beam and the Raman receiver are not given, the data is not used. Both τ_{aer} and β_{aer} profiles are valid in a range between about 0.5 km and 5–6 km above ground level. Data was collected during clear and cloudy periods. In total, from 937 hours of data taking, 930 reconstructed hourly profiles are available.

The data were smoothed using a central moving average. In Fig. 8.16, the raw data are drawn in black, the smoothed data in red. Three profiles of Raman data are shown measured during very clear (a) and average (b) conditions. In the bottom panel (c), the laser was reflected by a cloud, as can be seen in the backscatter data. A crude cloud height determination was introduced, if β_{aer} rises above $2 \times 10^{-6}\,\mathrm{m}^{-1}\,\mathrm{sr}^{-1}$, the minimum cloud height is set, visualized in the bottom panel of Fig. 8.16 by a black dashed line. The τ_{aer} distributions are shown in Fig. 8.17. The mean at 3 km a.g.l. is 0.061 with an RMS of 0.046, at 4.5 km the mean is 0.060 with an RMS of 0.046, and at 6 km, the mean is 0.064 with an RMS of 0.048.

In Fig. 8.18, the minimum cloud height determined from the Raman data is shown. On the left, the distribution of actual cloud heights is drawn in red, the remaining entries are either at the top of the range until which the data were analyzed or at the very beginning of the profile. The average cloud height of actual clouds is 4.7 km a.g.l.

AMT Data

Every hour during AMT operations, four sets of 200 laser shots are fired by the DRLF laser. A set is fired every 15 minutes, resulting in 800 shots per hour. The signal of every pixel is corrected by the calibration constant from the LED calibration system, then the traces of all pixels are summed and an hourly average is formed. In Fig. 8.19, top left panel, traces from several PMTs of a single laser shot on January 7, 2011 at 6:01:06 UTC are shown. In the top right panel, the sum of the traces of all pixels between the hours of 6 and 7 UTC after normalization of the height bins (see Sec. 7.4.2 for more details). In the bottom panels, the hourly average trace is split into center column pixels in the left panel and off-center pixels drawn in red and black in the right panel. The background was removed manually for the plot. The fine structure of the average trace is given by the PMT structure of the camera, some light is lost in the gaps between the pixels. The procedure to obtain the vertical aerosol optical depth profile is the same as was described in Sec. 7.4 with some modifications which will be described in the following.

The custom pixel calibration of the AMT and the rejection of bad periods had to be accounted for in the side-scatter analysis program, as well as the electronics with the higher sampling rate. The latter was a simple task of adjusting the bin numbers and widths of the histograms within the program code. The major difference to the analysis done for the data from the Pierre Auger Observatory are the pointing directions of the flat camera with less PMTs per column. The horizontal displacement of two pixels is 1° in field of view within one row, the vertical difference within one column is $\sqrt{3}/2$ or 0.866°.

The next step was identifying a reference clear night to calculate the aerosol optical depth. All available profiles were checked for the highest photon number at the aperture. Of all data, two hours within one night were identified, the chosen reference profiles were measured on January 7, 2011 between the hours of 6 and 8 UTC. The profile of hour 6 is shown in Fig. 8.19. This choice was verified by the Raman LIDAR data of this night which also shows a negligible aerosol contribution, see top panel in Fig. 8.16. Two hours are sufficient for defining a reference night, the number of shots in this time is 1600.

With the modified data normalized method and reference night in place, the vertical aerosol and cloud information could be extracted from the measured data. In Fig. 8.20, light profiles and aerosol optical depth profiles for four different conditions are shown. In the left panels, the averaged hourly light profile is shown together with the reference clear night. On the right side, the measured τ_{aer} profiles are shown as a thick black line with their uncertainties as thin lines. In red, the fit τ_{aer} profiles are superimposed, the minimum cloud height is indicated with a blue dashed line. From top to bottom, hazy[10] (a) and clear conditions (b), as well as

[10]The measurement of the example hazy profile was done before the safety daemon on the AMT was configured to prevent the door from opening after 10 UTC, see Sec. 8.2.3

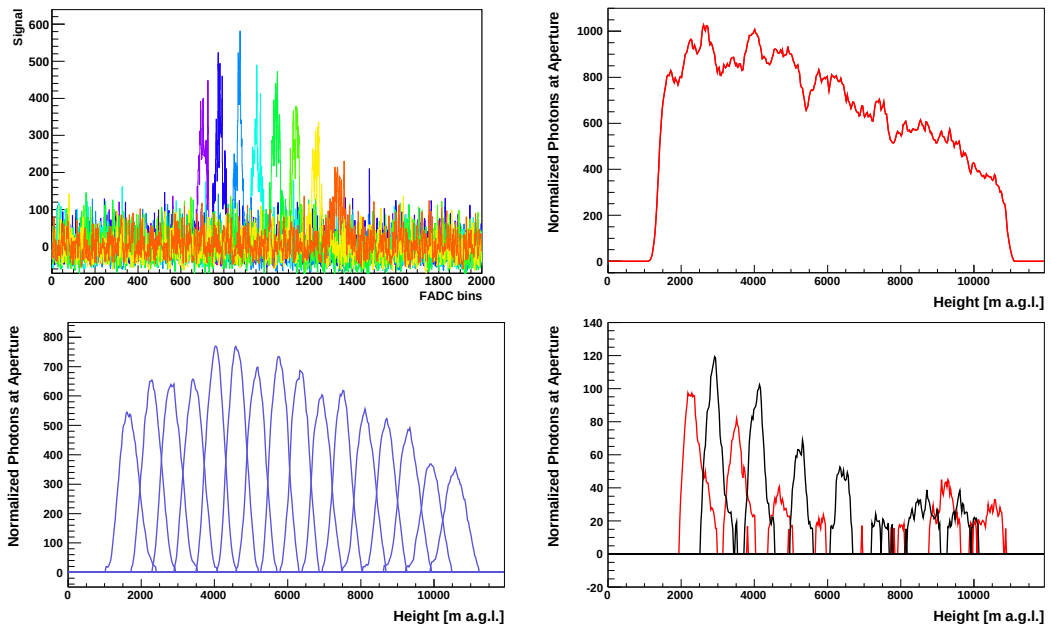

Figure 8.19: Top left: Traces from every other PMT in the central column of the AMT, starting with pixel 23, for one laser shot on January 7, 2011 at 6:01:06 UTC. Top right: Averaged measured profile on January 7, 2011 between 6 and 7 UTC. The fine structure of the light profile can be explained by the camera structure. Bottom left: Averaged signal of each PMT of the center column (23–38) pixels. Bottom right: Averaged signal of each off-center pixel drawn in red (pixels 1–16) and black (pixels 45–60).

two cloud-affected profiles are shown. It should be noted, that the clear profile (b) and the profile where the laser hit a small cloud (c) are only separated by one hour, further demonstrating the high variability of the aerosol conditions and the need for hourly aerosol profiles.

The minimum cloud height is shown in Fig. 8.21. In the left panel, the binned height of the lowest cloud that is found in the aerosol data is displayed. If no cloud is found, the minimum cloud height is set to the top of the profile at about 12.1 km. The red area of the histogram contains only profiles where an actual cloud was found. The mean height of actual clouds is 6.5 km a.g.l. In the middle panel of Fig. 8.21, the cloud height is shown versus time. In the right panel, the AMT cloud heights are compared with the cloud height determined from the Raman data. The agreement is good, only a few profiles are not marked with a cloud by the Raman LIDAR where very low clouds are found in the AMT data and vice versa. The Raman LIDAR can only detect clouds directly above the laser facility, while the AMT is also affected by clouds in the path between the laser and the detector.

All available τ_{aer} profiles are evaluated at 3, 4.5 and 6 km above ground and plotted versus time in the left column of Fig. 8.22. Profiles symbolized by red triangles are rejected as bad periods. Even though they seem to fit nicely with the rest of the data, it was decided to disregard these data due to the questionable calibration. At all heights a seasonal trend is visible, with clearer nights in the boreal

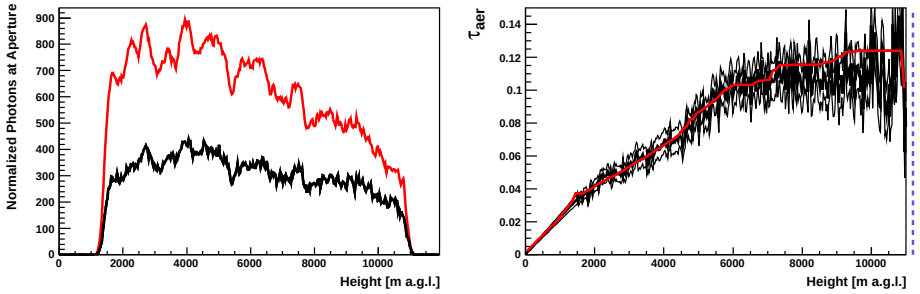

(a) November 11, 2010, 10–11 UTC: Hazy conditions.

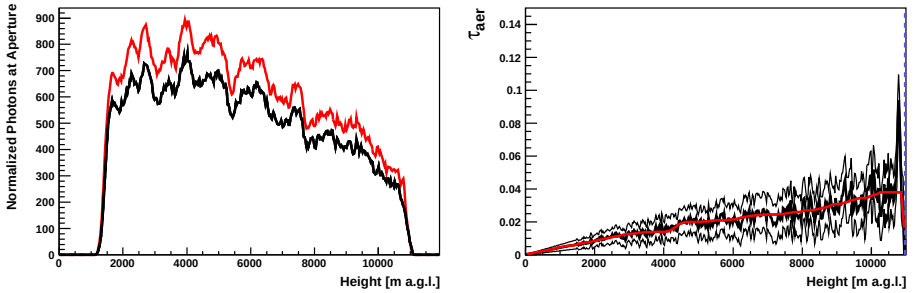

(b) December 1, 2010, 4–5 UTC: Clear conditions.

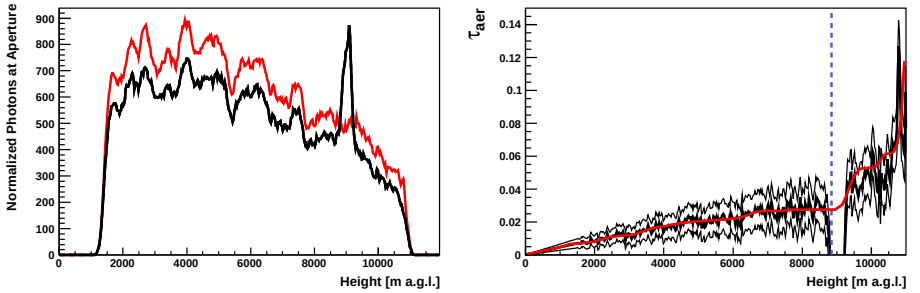

(c) December 1, 2010, 5–6 UTC: Laser hit small cloud around 8800 m a.g.l.

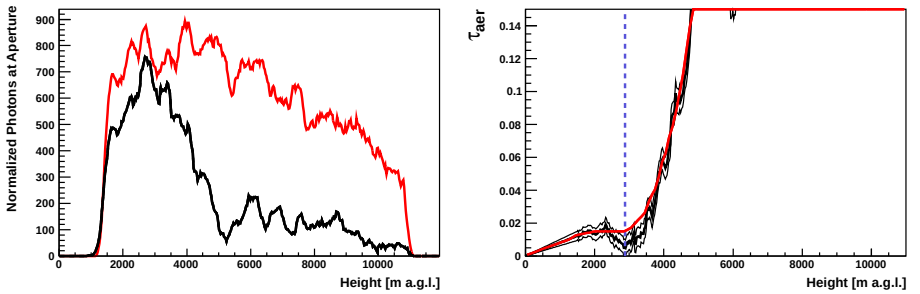

(d) December 7, 2010, 4–5 UTC: Cloud obstructing the light above 2800 m a.g.l.

Figure 8.20: Left: Light profiles as measured with the AMT in black, reference clear nights in red. Right: Measured τ_{aer} in black with uncertainties, fit τ_{aer} in red. The reconstructed minimum cloud height is marked with a blue dashed line.

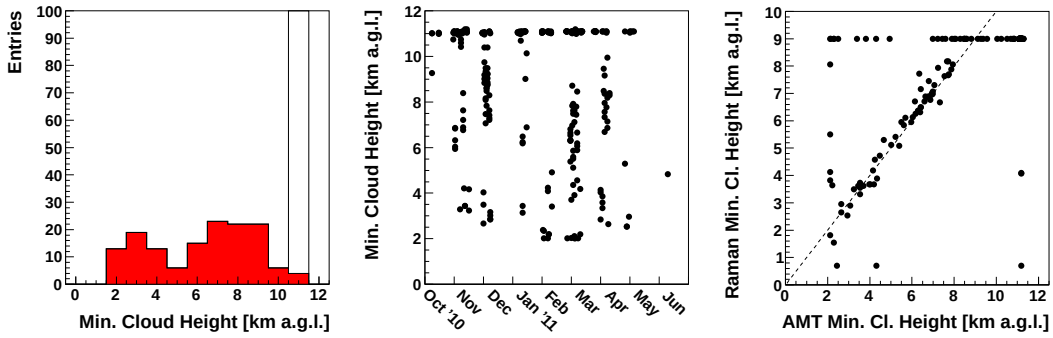

Figure 8.21: The minimum cloud height as determined from AMT data. On the left, the actual clouds are included in the red histogram, the cloud-free profiles are marked with a cloud height at the top of the field of view around 12.1 km. The last bin contains 184 entries. In the middle, the cloud height is shown versus time. In the right panel, the cloud heights of the AMT and the Raman are compared.

winter and hazier conditions in spring and early summer. In the right column of Fig. 8.22, the same information is shown as histograms. As expected, both the mean τ_{aer} and the spread increases with height. The mean τ_{aer} for 3 km is 0.032 with an RMS of 0.024, at 4.5 km the mean is 0.041 with an RMS of 0.029, and at 6 km a mean τ_{aer} of 0.049 with an RMS of 0.033 is found.

8.5 Comparisons between AMT and Raman Data

For the first time, the side-scatter method to obtain vertical aerosol depth profiles can be directly compared with a Raman LIDAR. The Raman data were analyzed by colleagues from the University of L'Aquila. In the following, the differences of τ_{aer} measurements for hours when both systems recorded data are presented at 3, 4.5 and 6 km above ground. The bottom of the AMT field of view of the laser is about 1.5 km a.g.l., so comparisons around that height are not reasonable. While LIDAR analyses in general have problems to produce good results close to the laser, the data are should be good between 0.5 to about 6 km [130].

An example of τ_{aer} profiles measured in the same hour by both instruments is shown in the left panel of Fig. 8.23. The average difference of 202 profiles without low clouds measured by both instruments are shown in the right panel. Low clouds would distort the comparison at lower altitudes. Below 4 km a.g.l., the Raman measured τ_{aer} is systematically higher than the AMT measurement. Between 4 and 6 km, the agreement is perfect, above 6 km the Raman results are not reliable anymore. A maximum difference of about -0.015 is found around 2 km above the ground.

The difference between the τ_{aer} measurements of the AMT and of the Raman at various heights is shown in Fig. 8.24. In the left column, all data are shown versus time for 3, 4.5 and 6 km a.g.l. As in Fig. 8.22, a clear seasonal trend is visible for both data sets with hazier conditions during summer. In the right column of Fig. 8.24, the measurements of τ_{aer} at the Raman LIDAR are shown versus the AMT data for common hours. A linear function is fit to the data, shown as a red line. At 3 km, the Raman-measured τ_{aer} is systematically higher than the AMT result.

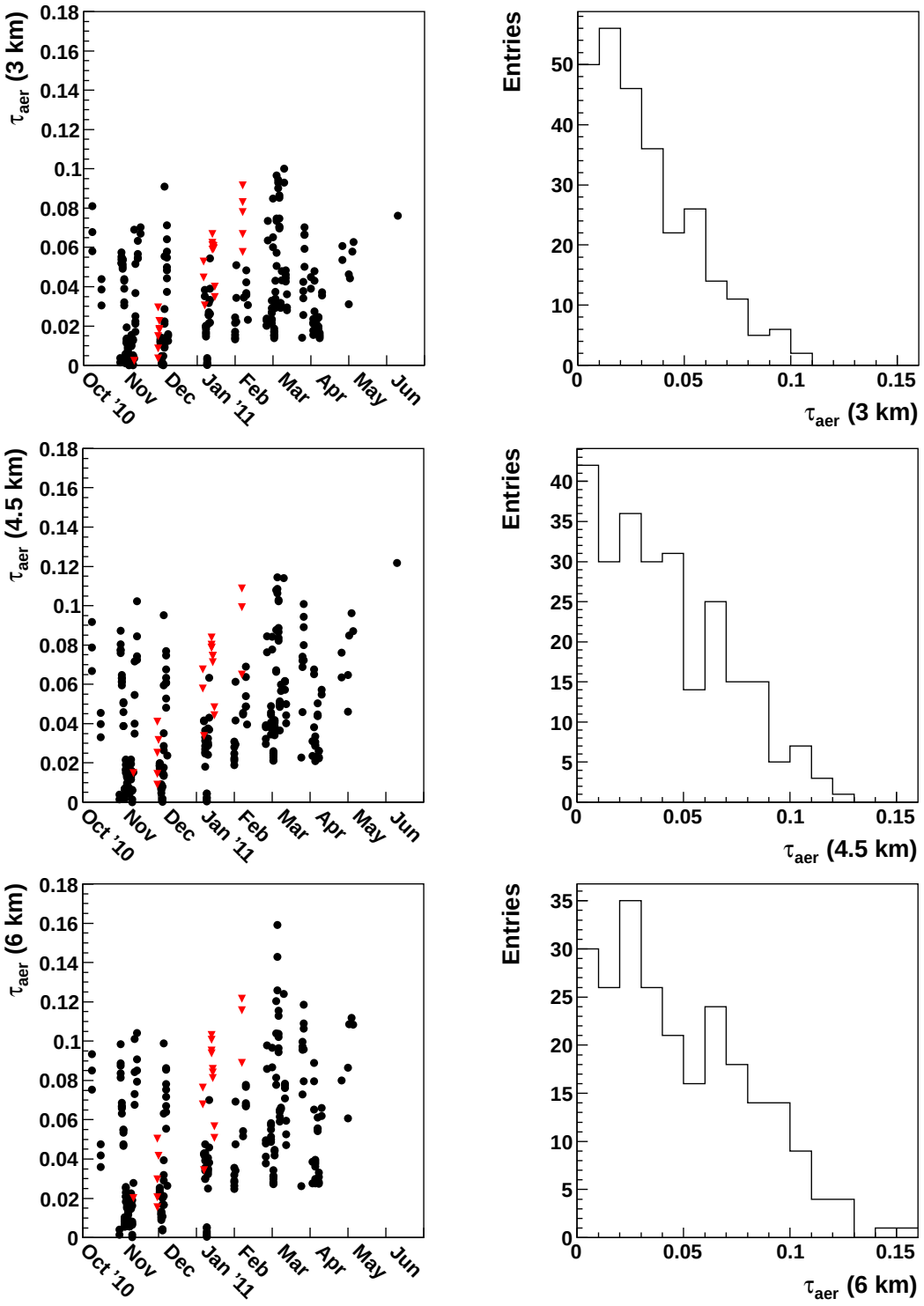

Figure 8.22: Left column: The measured τ_{aer} of the AMT versus time for altitudes of 3, 4.5 and 6 km a.g.l. Hours during bad periods are marked with red triangles. Right column: Mean τ_{aer} at 3, 4.5 and 6 km a.g.l.

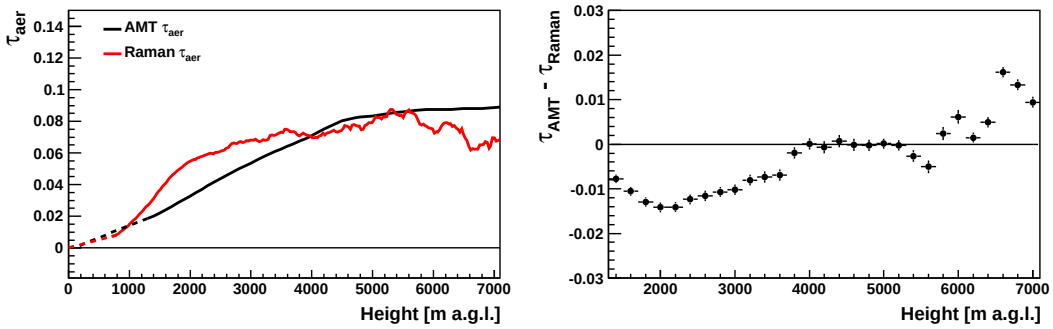

Figure 8.23: On the left, an example of τ_{aer} as measured with the AMT (black) and the Raman (red) on October 31, 2010, between the hours of 6 and 7 UTC. On the right, average difference of τ_{aer} profiles measured by the AMT and the Raman LIDAR. Dashed segments are outside the field of view of the AMT or below the valid range of the Raman.

Both systems agree very well at 4.5 km and at 6 km, a trend towards higher AMT τ_{aer} measurement is noticeable.

On the left of Fig. 8.25, the binned differences in τ_{aer} between the two analyses are shown for 3, 4.5 and 6 km. At 3 km, a mean difference of -0.010 with an RMS of 0.013 is found. At 4.5 km, the difference is 0.001 with an RMS of 0.014, the two analysis agree almost perfectly, only a few outliers are found where a higher τ_{aer} is reconstructed with the AMT data. At 6 km, the average difference is 0.004 with an RMS of 0.014.

To analyze these systematics, the τ_{aer} difference relative to the mean τ_{aer} was plotted versus time, see right column of Fig. 8.25. This relative difference in τ_{aer} has no physical meaning, since the absolute difference in τ_{aer} is the meaningful quantity when dealing with transmission factors. The normalization was done here to highlight the systematics in the data and account for larger τ_{aer} values and fluctuations at greater heights. It seems the two analyses do not agree well at 3 km in all seasons, the τ_{aer} measured by the Raman is generally higher than the one measured at the AMT, and a trend towards even larger differences is visible in boreal spring. At 4.5 km, both analysis agree very well in winter, when τ_{aer} is generally low. It also seems like a trend towards a higher Raman τ_{aer} measurement in summer is present, but it is less pronounced. At 6 km, the agreement is generally good. For conditions of medium haziness found in late winter (days 100 to 150), the analyses seem to agree better than for low aerosol concentration in late fall (before day 50), where the agreement depends on the height. For very hazy conditions in spring (after day 150), the AMT measures higher τ_{aer} as the Raman.

The average difference of the 202 AMT and Raman profiles shown in Fig. 8.23 are further analyzed by separating them into months. In Fig. 8.26, the average difference is shown for 67 profiles from October and November in black dots, January and February (55 profiles) in red triangles, and March and April (77 profiles) in blue squares. The Raman system did not record data in December, and in May and June, not enough coincidental hourly profiles were measured to make meaningful comparisons. The differences below 4 km a.g.l. increase from fall throughout the winter and are highest in spring. Between 4 and 6 km, the average τ_{aer} of the AMT

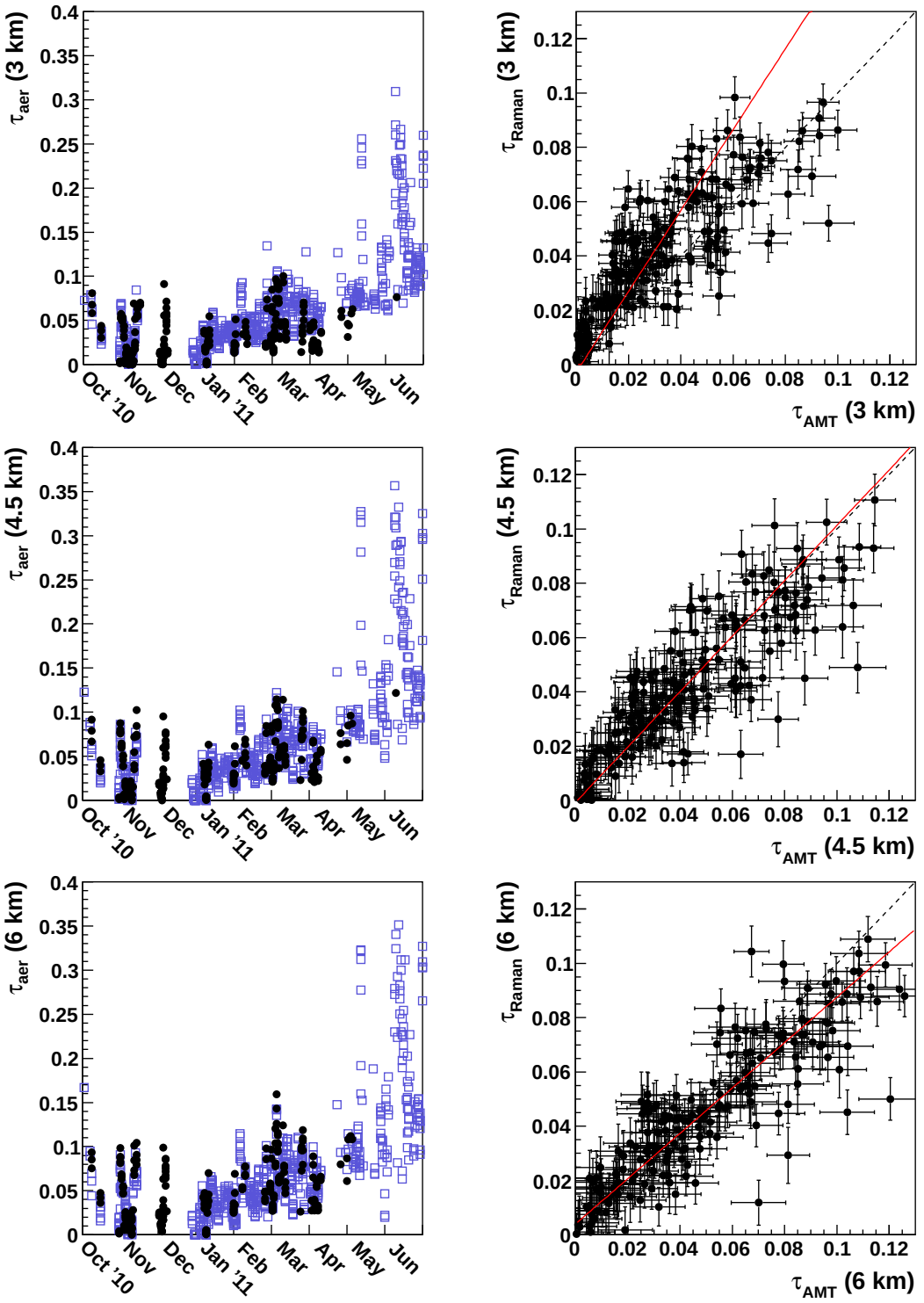

Figure 8.24: Left column: All τ_{aer} data versus time as measured with the AMT (black dots) and the Raman LIDAR (blue squares) at 3, 4.5 and 6 km a.g.l. The AMT data are the same as shown in Fig. 8.22. Right column: τ_{aer} measured with the AMT versus Raman LIDAR for hours observed with both instruments. The diagonal is shown in black, a fit to the black dots in red.

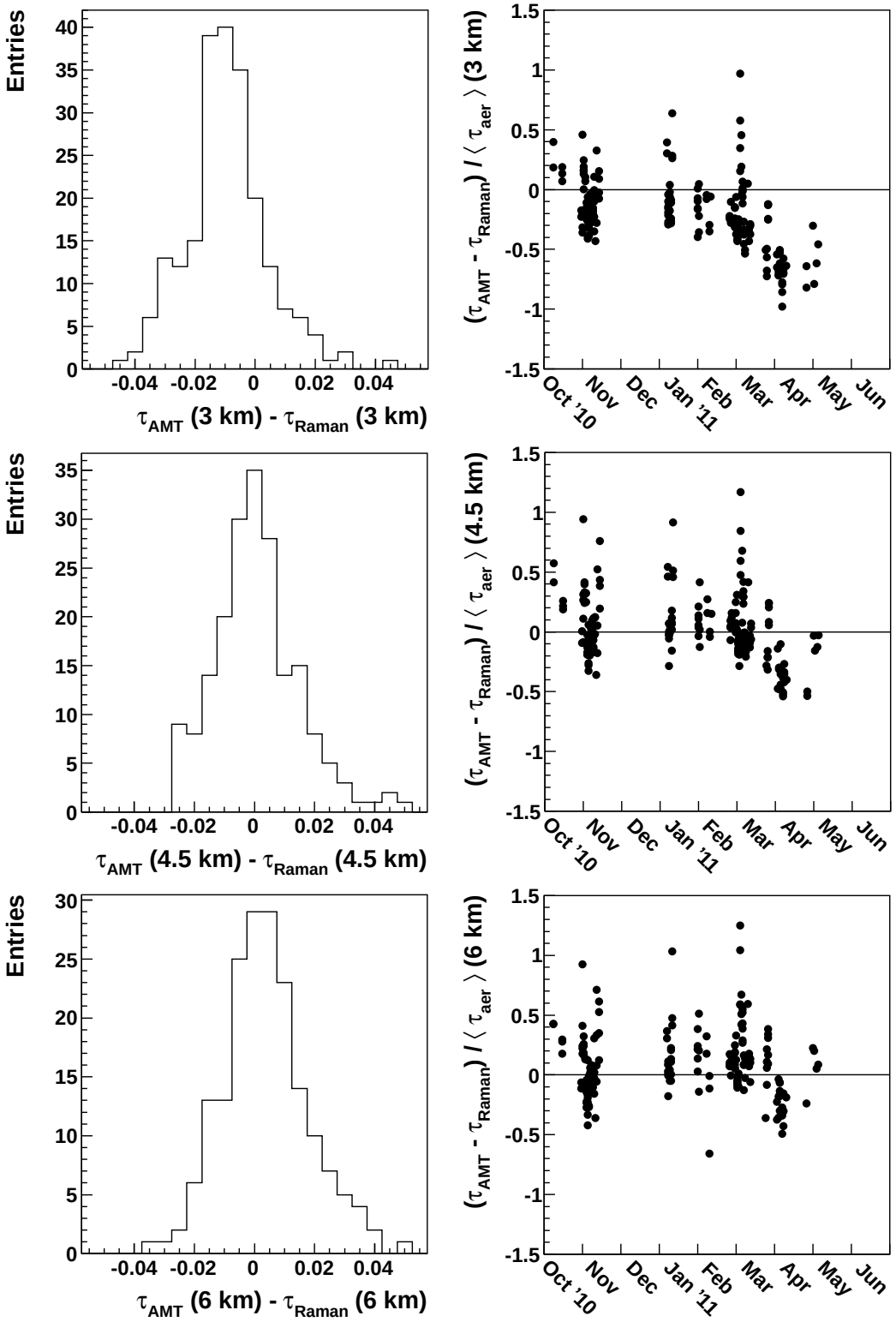

Figure 8.25: Left column: Differences between τ_{aer} measured with the AMT and the Raman LIDAR at 3, 4.5 and 6 km a.g.l. Right column: The same difference, normalized to the mean τ_{aer} of the both systems at that height, versus time.

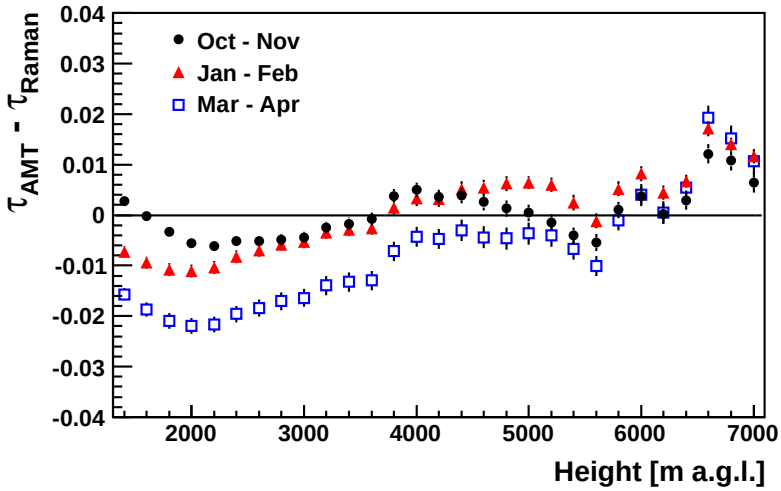

Figure 8.26: Average difference of τ_{aer} profiles measured by the AMT and the Raman LIDAR shown in Fig. 8.23, divided into months. On top left, October and November drawn in black dots, on the top right, January and February drawn in red triangles, on the bottom left, March and April drawn in blue squares. On the bottom right, all three averages are superimposed, the error bars are divided by the number of profiles in each average.

is larger than the Raman measurement in fall and winter, but smaller in spring. Similar conclusions can be drawn from the comparisons in Fig. 8.27, in which the scatter plots shown in Fig. 8.24 for 3 and 4.5 km a.g.l. are also separated into the same periods as above. A clear systematic difference is seen at 3 km in spring, as is the good overall agreement at 4.5 km.

In the comparison between AMT and Raman τ_{aer} profiles, a systematic difference in the lower part of the atmosphere is found. Above 4 km from the ground, both instruments agree well, although a seasonal effect is still visible. It is not clear what the cause for this difference is. The AMT data might have been affected by the extreme cold in the winter, if the calibration LED is not constant as expected, the AMT measurements would be mis-calibrated. The jump in high voltage seen in the monitoring data, see Fig. 8.13, was on February 14, 2010. It seems that in the months after, the data of the AMT are systematically lower than the Raman data. However, it is unclear how a drop in high voltage could result in a change in measurements, unless there is an underlying reason for this change. Unfortunately, there are almost no data in May in June when the Raman system measured a largely increasing τ_{aer} compared to the previous months, so comparisons in summer are not available. The difference at lower altitudes could also be an effect of the choice of the reference clear night in the Data Normalized method to analyze the data. If the profile is modified in some way, the estimations of the aerosol profiles would be affected. However, no modifications of the reference night in the lower part is seen compared to other reference night candidates.

As mentioned above, the Raman raw signal was not corrected for optical or detector effects. This affects the data below 1 km, but it can indirectly influence the calculations at higher altitudes. The treatment of the raw data with two different algorithms can have a significant effect on the resulting τ_{aer} profiles [125].

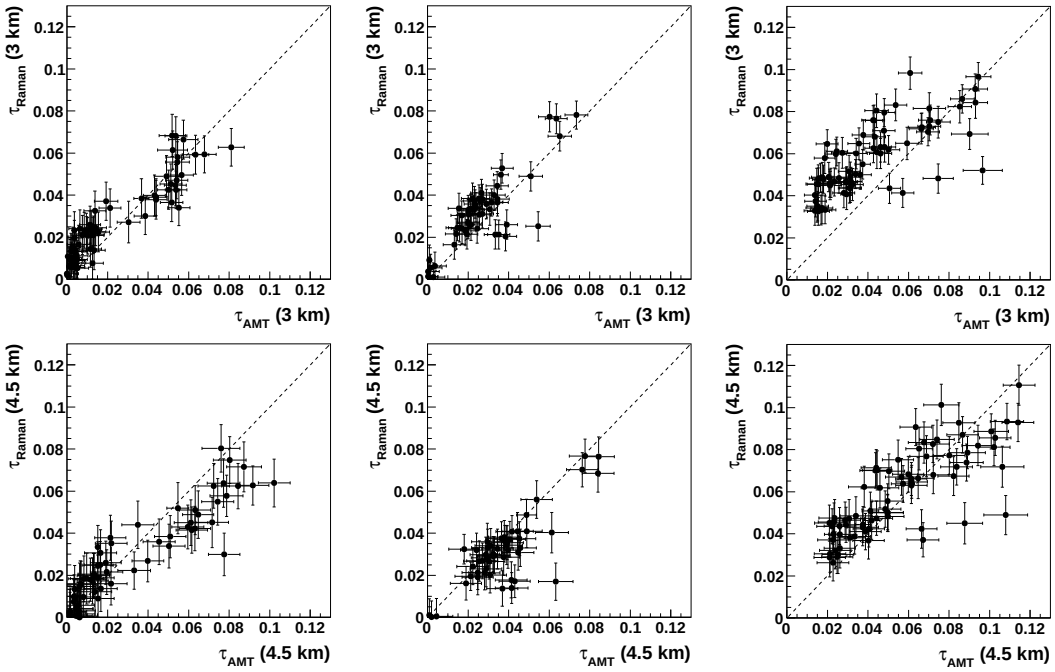

Figure 8.27: Comparison of τ_{aer} measured by the AMT and the Raman at a height of 3 km (top) and 4.5 km a.g.l. (bottom), divided into time periods of two months. On the left, October and November, in the middle January and February, and on the right March and April.

Furthermore, monthly averages were used to estimate the molecular part of the atmosphere instead of 3-hourly GDAS data, which can introduce seasonal effects. The Rayleigh scattering was only estimated in a rough calculation, but comparisons of the Raman τ_{aer} measurements with temperature and humidity measurements show no correlation that would indicate a wrong treatment of the Rayleigh scattering. The analysis of the Raman data is under investigation and will be further improved by the experts.

The measurements agree better in the upper part of the atmosphere, where the amount of aerosols typically does not increase any further. It is possible that both systems measure the integrated τ_{aer} correctly but differ in the vertical distribution of the aerosols. The DRLF is located close to the city of Lamar at a major highway with truck traffic and is surrounded by rangeland, the AMT overlooks planted fields and is far away from both the highway and any kind of civilization. This might cause a difference in the aerosol type and concentration between the AMT and Raman sites. The AMT measurements are dominated by the transmission, not the scattering out of the laser. The difference in surroundings could explain part of the difference at lower altitudes and could also be a source of seasonal variations.

The differences in measurement of τ_{aer} at the Pierre Auger Observatory are presented in Sec. 7.5 and Appendix B. Two different laser sources and four FD sites are compared. The largest differences found at various altitudes due to the non-uniformity of the aerosol concentration is of the order of 0.005, in some cases due

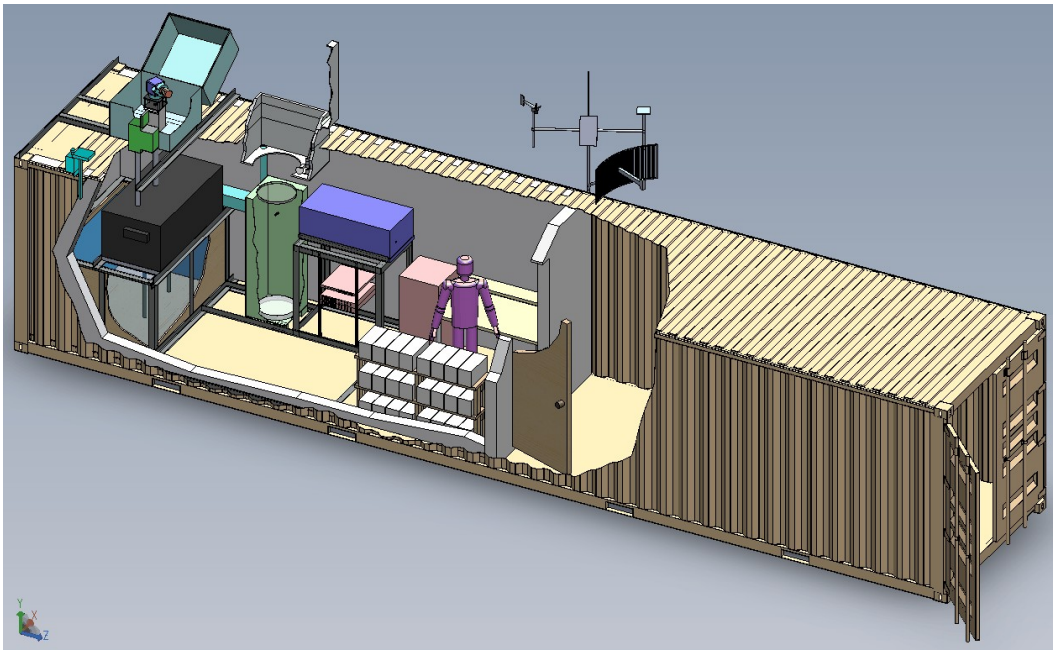

Figure 8.28: A preliminary schematic of the planned setup of the Central Raman Laser Facility of the Pierre Auger Observatory [120]. The optical table is mounted on the left with two hatches overhead, one for the vertical beam and one for the steered beam. The Raman receiver mirror is mounted on one of the side walls with the PMT assembly and the DAQ next to it and a separate hatch above it.

to poor reference nights up to 0.01. The differences found at low heights between the Raman LIDAR and the AMT measurements are larger than 0.01, up to 0.02 in boreal spring and even 0.03 in some cases. Even though in these cases two entirely different and independent measurement techniques are compared, the differences are too large to attribute them solely to changes in the atmosphere.

The comparisons of the τ_{aer} measurements of the two independent systems is promising, but needs to be studied further to draw final conclusions. More data is needed and will be provided in the coming months and years. It was shown, that a combined laser facility for both measurements can perform extremely well and safely, and that the side-scatter method is a viable technique across large baselines. Using both methods can provide a unique set of measurements that can be used to enhance the performance of both systems and ultimately further improve the quality of reconstructed air shower data at ground-based cosmic rays observatories.

8.6 Application for Current and Future Ground-based Cosmic Ray Observatories

The Colorado Atmospheric R&D was a success, but further testing and systematic checks are required. While the Raman data are still being reanalyzed, plans are advancing to move the Raman LIDAR to the Pierre Auger Observatory in Argentina [119]. Currently, the Raman is assembled with a laser setup in a 40 ft

container at the Colorado School of Mines for shipping, for a schematic of the interior design see Fig. 8.28. The laser will be the same as was used in Colorado, an automatic calibration system similar to the XLF system will be added. Some improvements were made after the operations in Colorado, the hatch on the roof of the container is improved and will not be as susceptible to high winds. After being relocated to Argentina, the container will replace the CLF. This new Central Raman Laser Facility (CRLF) will then continue taking data with the side-scatter method and the Raman LIDAR to further study the differences, this time with a proven and well-calibrated fluorescence detector, and provide the data reconstruction of the Pierre Auger Observatory with another excellent source of atmospheric data.

The AMT is still functioning and mounted at its original place. A new Raman LIDAR will be shipped to Colorado and installed in the DRLF, also collecting more data for comparisons of both analyses and checking possible sources of systematic differences like the AMT calibration or the Raman signal treatment and the use of GDAS data. An important improvement of the system will be the mechanical and operational stabilization of the AMT. After these improvements, this system is ready for exploring other locations of a possible new giant ground arrays.

Chapter 9

Summary and Outlook

The balloon program of the Pierre Auger Observatory was very successful. Almost eight years of balloon data are an invaluable source of information about the status of the atmosphere above the site in Argentina. However, as part of the rapid atmospheric monitoring system, the program was very cost-intensive and required a lot of manpower. For a long data taking period of up to 20 years, this is a major drawback. For corrections due to the state variables of the atmosphere, data from the Global Data Assimilation System (GDAS) are currently the best available data set for the Pierre Auger Observatory in Argentina. The temporal resolution of these data of three hours are superior to the resolution of the balloon measurements, which were launched several days apart. The GDAS data were compared to local measurements of weather balloons and data of ground-based weather stations and the agreement was found to be more than sufficient for the use of the data in air shower analysis. For the reconstruction of air showers, an interface was created between the GDAS data and the reconstruction framework of the Pierre Auger Observatory, where the GDAS data are now the default description of atmospheric state variables.

Using GDAS data, the validity period of balloon launches was investigated. As part of the rapid monitoring system, a launch was triggered by a high quality, high energy event. The validity of the balloon data, determined using weather stations, was about 200 minutes per balloon. Oftentimes the validity was not extended until the time of the triggering event, less than half of the 62 events were covered by a balloon launch. With GDAS data, the validity could be re-evaluated by comparing the entire measured profile, not just the ground value, of GDAS profiles before and after the launch. An average validity of 7.7 hours was found. One launch was extended in validity to a total period of 72 hours, while for some launches no valid GDAS profile was found. Still, only 40 triggering events are within the validity period of a balloon launch.

It could be shown, that the systematic uncertainties introduced by the choice of atmospheric description in the reconstruction of the energy of the air shower are significantly reduced. For the determination of the shower maximum, the uncertainty is reduced by a factor of two, from $4\,\mathrm{g\,cm^{-2}}$ at low energies and $6.5\,\mathrm{g\,cm^{-2}}$ at high energies down to 2 and $3.5\,\mathrm{g\,cm^{-2}}$, respectively. The GDAS data were also used to introduce new monthly models of the atmosphere above the Pierre Auger Observatory into the air shower simulation package CORSIKA, replacing old seasonal models that were based on only a small number of weather balloon launches. The new models work seamlessly in the simulation and reconstruction of air showers and

are currently the fall-back description of the atmosphere, in case 3-hourly GDAS data are not available.

The side-scatter method to measure the aerosol concentration was upgraded as part of this thesis. A streamlined version of the analysis program is now used to calculate aerosol corrections for the air shower data measured at the Pierre Auger Observatory. This includes a significant improvement in processing speed, but also potential sources of statistical fluctuations and uncertainties were eliminated. A set of time-dependent calibration constants from these measurements and the monthly calibrations were implemented in the analysis of the laser data. An additional set of measurements of the aerosol optical depth is provided by the analysis of a second central laser facility, the eXtreme Laser Facility. For the first time, meaningful aerosol profiles could be reconstructed for the FD site Loma Amarilla in the north of the array, which is too far from the Central Laser Facility for unbiased measurements. A cross-check between both laser stations revealed an agreement between both data sets, with only smaller systematic differences in τ_{aer} of less than 0.005. The analysis of the aerosol data at the Pierre Auger Observatory is an ongoing process. Effort is put into reducing systematics, and combining this method of analyzing the data with a second independent analysis.

The side-scatter method to estimate the aerosol optical depth can function across large baselines of 40 km and it is a viable option for future ground-based cosmic rays observatories. A combined facility of a laser for side-scatter measurements and a Raman LIDAR was assembled in south-east Colorado. A small fluorescence detector, the Atmospheric Monitoring Telescope (AMT), was deployed almost 40 km away to measure the side-scattered light. The automatization and remote control for the Raman system and the AMT were designed, implemented and tested. The electronics, computers, monitoring tools and the software performed very well under an impressive workload. Nightly measurements could be carried out without major problems, monitored from remote locations on several continents. The automatization would start all systems and check for safe operating conditions, run the relative calibration system for the AMT to correct for fluctuations in the hardware, and shut everything down properly at the end of data taking. Proven analysis methods of aerosol data from the Pierre Auger Observatory could be used to process the data. In total, 320 hours of data were collected by the AMT between October 2010 and June 2011, 937 hours by the Raman LIDAR, including 251 hours of combined data. The Raman LIDAR will be moved to the Pierre Auger Observatory and the lessons learned at the Colorado R&D site will be incorporated in the new facility.

Preliminary comparisons of the aerosol data from the side-scatter with data from the Raman LIDAR are promising, but systematic differences in τ_{aer} of about 0.02 due to a seasonal effect in the lower part of the atmosphere were seen. Due to their magnitude, these differences are not negligible. The agreement is very good above 4 km above ground level. A better preprocessing of the Raman data is needed as this could introduce a seasonal effect, and efforts to improve the Raman analysis are underway. The side-scatter system and the AMT will continue to measure in south-east Colorado. Seasonal effects and possible systematics due to the calibration system of the telescope will be studied in more detail.

A balloon program was performed in conjunction with the aerosol measurements in Colorado. Using a mobile ground station, several balloons were launched to measure profiles of atmospheric state variables in different seasons. Comparing the

measurements with GDAS data, it could be shown that the agreement is of the same order as found at the site of the Pierre Auger Observatory. A difference of less than 1.5°C in temperature, less than 0.6 hPa in pressure and vapor pressure, and less than 0.5 g cm^{-2} in atmospheric depth is seen at all altitudes. Balloon measurements performed at nearby airports are not suited as a description of the atmospheric conditions due to their limited availability and large distance to the detector site.

Future cosmic ray detectors will most likely be located in remote places where the availability of atmospheric data is sparse, so GDAS will undoubtedly be a invaluable source of data instead of a costly and very time consuming balloon program. Depending on the site, other models with even better temporal and spatial resolution might be available. A mobile ground station for weather balloon launches, like the one used in Colorado, can still serve a function to check the model data against measured profiles and make sure the models describe the local conditions to a satisfying degree.

Cosmic ray research has entered an era where systematics dominate statistical uncertainties most of the time and percentage effects become relevant. The treatment of the atmosphere and atmospheric influences on air shower development is a large part of this error budget, and reducing it further will continue to be an important task for the near future.

Acknowledgment

First and foremost I would like to thank Prof. Johannes Blümer for giving me the opportunity to continue my work in Karlsruhe and making it possible for me to live and work in Colorado as part of this work. Prof. Lawrence Wiencke from the Colorado School of Mines was gracious enough to let me join his research group and also act as advisor and co-referee for this work. The work environment at CSM was a major reason why I enjoyed my time in Colorado.

For her continued role as advisor I would like to thank Bianca Keilhauer. Her door (or email inbox) was always open for me and our fruitful discussions always helped me to advance my work. Her literary insights were very helpful in several publications and proceedings and also very much in the writing of this thesis. I thank Ralph Engel for his guidance as leader of the Pierre Auger group and Hans Klages for his many ideas and comments, his help in getting the first balloon in Colorado off the ground and converting cubic meters into cubic feet, which apparently is not as easy as it sounds.

The assembling and operation of the Atmospheric Monitoring Telescope and the Distant Raman Laser Facility would not have been possible without the tireless efforts of all Senior Design students involved: C. Allan, Adam Botts, Michael Calhoun, Bryce Carande, John Claus, Lucas Emmert, Samara Esquibel, Levi Hamilton, T. J. Heid, Blake Knoll, Sarah Morgan, Levi Patterson, Shay Robinson, and John Sherman. David Starbuck, master of troubleshooting, was instrumental in getting everything to run and keep it going, the AMT would not have worked without him. Michael Coco mostly did analysis for the Raman LIDAR, but his work on the slow control system and the automatization was essential. Special thanks to Orlen Wolf to always lend a helping hand when we needed it. The Raman LIDAR was provided by the University of L'Aquila, but especially Vincenzo Rizi and Aurelio Grillo deserve most of the thanks. The DAQ system of the AMT was provided by the Institut für Prozessdatenverarbeitung und Elektronik of the KIT. I am very indebted to Sasha Menshikov for showing me how to work with the system and providing help when something did not work. It was also he, Matthias Kleifges and his team who repaired the SLT and replaced the FLTs when they were fried in July 2010. Last but definitely not least, I want to thank Hermann-Josef Mathes for setting up and tweaking the AMT run control program he salvaged from old code from the very beginning of the Pierre Auger Observatory data taking.

I would like to thank my colleagues in Karlsruhe for the good atmosphere and my colleagues in Golden for their hospitality. I really enjoyed my time at both places. From the CSM group I have to especially thank David Schuster for showing me around in the beginning and taking the time to show the new guy how it's done. He also took me to several home games of the Colorado Rapids soccer club where

we had a lot of fun and beers and celebrated their victory in the 2010 MLS cup. Go Rapids!

From the Karlsruhe group, I have to mention several people: Marianne Ludwig, Felix Werner and Dorit Epperlein proofread parts of this document and gave me several valuable comments; Sabine Bucher made my life so much easier in the past four years; Radomir, Julia, Ben, Marianne, Daniel, Felix, Colin, Frank, Katrin, Jan and Steffen in no particular order I thank for the good time at home and away at conferences all around the world.

There are several more people to thank in Golden who made my time in Colorado unforgettable. Eric Mayotte and John Claus introduced me to the nightlife in and around Golden, showed me the fine quality of the Colorado beer and are primarily responsible for my Cribbage skills. Several epic days and nights were spent at the Golden City Brewery and the Blue Canyon with Lauren Zemp, Michael Greco, Tony Actis and so many others. I would like to thank Beverly and Craig Reeves who provided me with a home during my time in Colorado.

Zuletzt möchte ich mich bei meinen Eltern und meiner Schwester sowie bei meinen Freunden für ihre Unterstützung in den letzten Jahren bedanken.

Appendix A

GDAS Monthly Models – Parameters of Atmospheric Depth for the site of the Pierre Auger Observatory

Range [km]	a [g cm^{-2}]	b [g cm^{-2}]	c [cm]
0 – 9.4	-136.72575606	1174.8298334	982815.95248
9.4 – 15.3	-31.636643044	1204.8233453	754029.87759
15.3 – 31.6	1.8890234035	1637.7703583	594416.83822
31.6 – 100	$3.92018679839 \cdot 10^{-4}$	735.96095023	733974.36972

Table A.1: Fit parameters for January.

Range [km]	a [g cm^{-2}]	b [g cm^{-2}]	c [cm]
0 – 9.2	-137.25655862	1176.0907565	981369.6125
9.2 – 15.4	-31.793978896	1197.8951104	756657.65383
15.4 – 31	2.0616227547	1646.4616955	592969.89671
31 – 100	$4.12430622892 \cdot 10^{-4}$	755.18728657	731345.88332

Table A.2: Fit parameters for February.

Range [km]	a [g cm^{-2}]	b [g cm^{-2}]	c [cm]
0 – 9.6	-132.36885162	1172.6227784	972654.0563
9.6 – 15.2	-29.077046629	1215.3964677	742769.2171
15.2 – 30.7	2.090501509	1617.0099282	595342.19851
30.7 – 100	$4.35343379252 \cdot 10^{-4}$	769.51991638	728921.61954

Table A.3: Fit parameters for March.

Range [km]	a [g cm^{-2}]	b [g cm^{-2}]	c [cm]
0 – 10	-129.9930412	1172.3291878	962396.5521
10 – 14.9	-21.847248438	1250.2922774	711452.06673
14.9 – 32.6	1.5211136484	1542.6248413	603480.61835
32.6 – 100	$3.95590551213 \cdot 10^{-4}$	713.1008285	735460.83741

Table A.4: Fit parameters for April.

Range [km]	a [g cm^{-2}]	b [g cm^{-2}]	c [cm]
0 – 10.2	-125.11468467	1169.9511302	947742.88769
10.2 – 15.1	-14.591235621	1277.6768488	685089.57509
15.1 – 35.9	0.93641128677	1493.5303781	609640.01932
35.9 – 100	$3.24755909854 \cdot 10^{-4}$	617.9660747	747555.95526

Table A.5: Fit parameters for May.

Range [km]	a [g cm^{-2}]	b [g cm^{-2}]	c [cm]
0 – 10.1	-126.17178851	1171.0916276	940102.98842
10.1 – 16	-7.7289852811	1295.3516434	661697.57543
16 – 36.7	0.81676828638	1455.3009344	612702.0632
36.7 – 100	$3.19476768915 \cdot 10^{-4}$	595.11713507	749976.26832

Table A.6: Fit parameters for June.

Range [km]	a [g cm^{-2}]	b [g cm^{-2}]	c [cm]
0 – 9.6	-126.17216789	1172.7340688	934649.58886
9.6 – 16.5	-8.6182537514	1258.9180079	672975.82513
16.5 – 37.4	0.74177836911	1450.0537141	614888.52458
37.4 – 100	$2.93507020973 \cdot 10^{-4}$	583.07727715	752631.28536

Table A.7: Fit parameters for July.

Range [km]	a [g cm^{-2}]	b [g cm^{-2}]	c [cm]
0 – 9.6	-123.27936204	1169.763036	931569.97625
9.6 – 15.9	-10.051493041	1251.0219808	678861.75136
15.9 – 36.3	0.84187346153	1436.6499372	617363.34491
36.3 – 100	$3.24225467594 \cdot 10^{-4}$	627.42169844	746739.16141

Table A.8: Fit parameters for August.

Range [km]	a [g cm^{-2}]	b [g cm^{-2}]	c [cm]
0 – 9.5	-126.94494665	1174.8676453	936953.91919
9.5 – 16.2	-9.5556536981	1251.5588529	678906.60516
16.2 – 37.2	0.74939405052	1440.8257549	618132.60561
37.2 – 100	$2.98231169610 \cdot 10^{-4}$	606.31473165	750154.67709

Table A.9: Fit parameters for September.

Range [km]	a [g cm^{-2}]	b [g cm^{-2}]	c [cm]
0 – 9.5	-133.13151125	1176.9833473	954151.404
9.5 – 15.5	-13.973209265	1244.234531	692708.89816
15.5 – 36.5	0.8378263431	1464.0120855	615439.43936
36.5 – 100	$3.11174217600 \cdot 10^{-4}$	622.11207419	747969.08133

Table A.10: Fit parameters for October.

Range [km]	a [g cm^{-2}]	b [g cm^{-2}]	c [cm]
0 – 9.6	-134.72208165	1175.7737972	964877.07766
9.6 – 15.3	-18.172382908	1238.9538504	706199.57502
15.3 – 34.6	1.1159806845	1505.1614366	610242.24564
34.6 – 100	$3.52170255153 \cdot 10^{-4}$	670.64752105	741412.74548

Table A.11: Fit parameters for November.

Range [km]	a [g cm^{-2}]	b [g cm^{-2}]	c [cm]
0 – 9.6	-135.40825209	1174.644971	973884.44361
9.6 – 15.6	-22.830409026	1227.2753683	723759.74682
15.6 – 33.3	1.4223453493	1585.7130562	600308.13983
33.3 – 100	$3.75129217743 \cdot 10^{-4}$	691.23389637	738390.20525

Table A.12: Fit parameters for December.

Appendix B

Comparisons of Vertical Optical Depth Measurements at the Pierre Auger Observatory

In this appendix, the τ_{aer} profiles calculated with the Data Normalized method are compared for 2010 and 2011. Data measured in the same hour from both the CLF and the XLF laser stations were used. The profiles of the CLF are compared to the profiles of the XLF as measured by Los Morados and Coihueco. Furthermore, the measurements of the XLF are compared for different FD sites, similar comparisons are shown for the sites observing the CLF.

In the top row of every figure, the individual τ_{aer} measurements for 1.5, 3 and 4.5 km above ground are shown for both sites. The designations Site 1 and Site 2 are used for the two compared sites, specified in the caption of the figure. Site 1 is shown in red, the black dashed histogram is for Site 2. In the second row, the correlation between the data from both sites is shown for common hours. In the third row, the difference of the comparison is shown. In the bottom row, the average difference for each height is shown, alongside a table containing the means and RMS values of the histograms.

Same FD site, different laser source:

Different FD sites, XLF:

Different FD sites, CLF:

Figure B.1: **Site 1: CLF LM 2010, Site 2: XLF LM 2010**

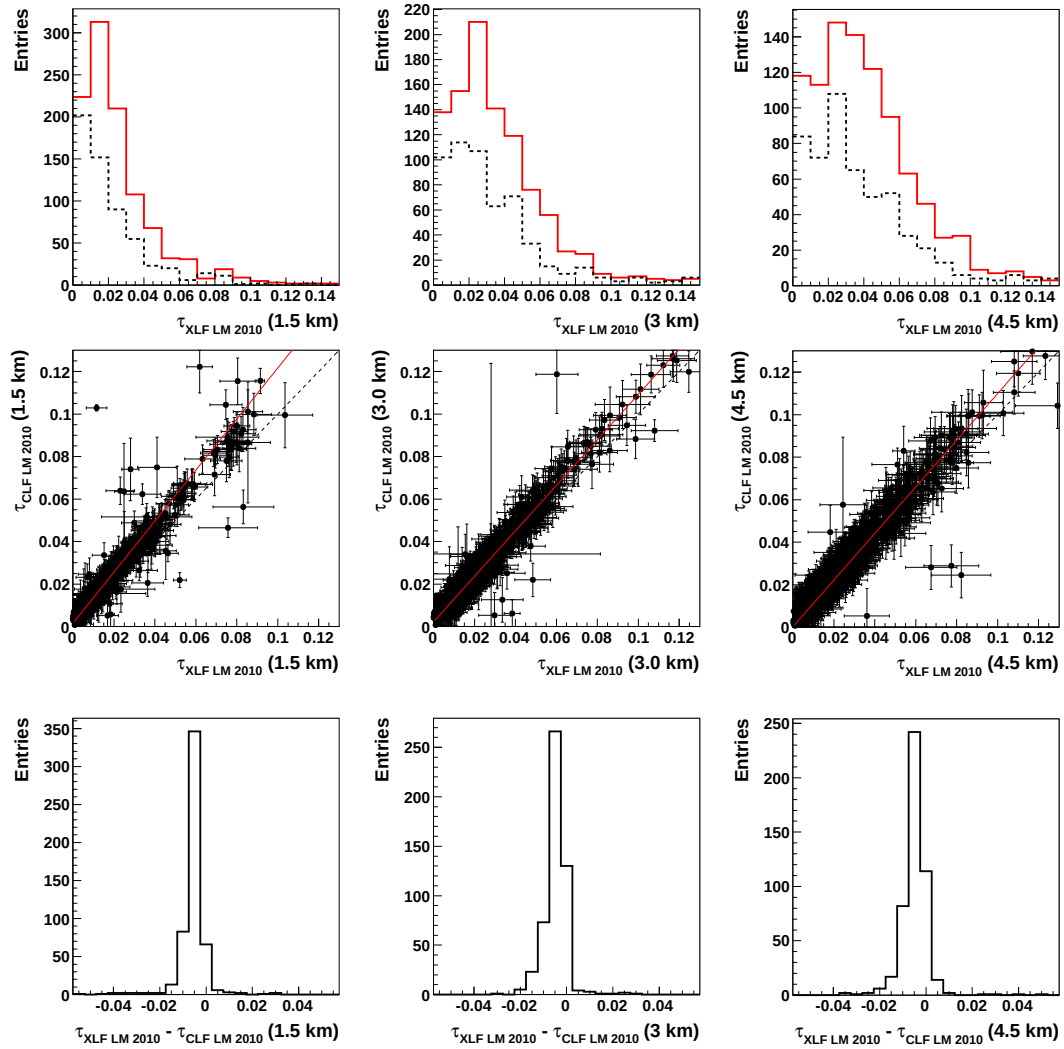

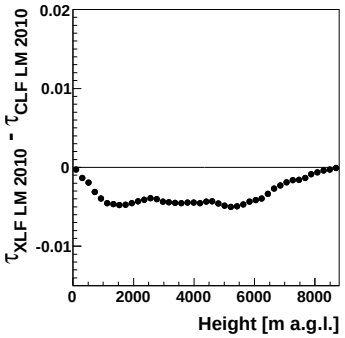

542 common hours	Mean	RMS
$\tau_{\mathrm{aer},1}$ (1.5 km)	0.026	0.022
$\tau_{\mathrm{aer},2}$ (1.5 km)	0.021	0.021
$\tau_{\mathrm{aer},1}$ (3.0 km)	0.035	0.026
$\tau_{\mathrm{aer},2}$ (3.0 km)	0.032	0.028
$\tau_{\mathrm{aer},1}$ (4.5 km)	0.041	0.028
$\tau_{\mathrm{aer},2}$ (4.5 km)	0.037	0.029
$\tau_{\mathrm{aer},2} - \tau_{\mathrm{aer},1}$ (1.5 km)	−0.005	0.006
$\tau_{\mathrm{aer},2} - \tau_{\mathrm{aer},1}$ (3.0 km)	−0.005	0.005
$\tau_{\mathrm{aer},2} - \tau_{\mathrm{aer},1}$ (4.5 km)	−0.005	0.006

Figure B.2: **Site 1: CLF LM 2011, Site 2: XLF LM 2011**

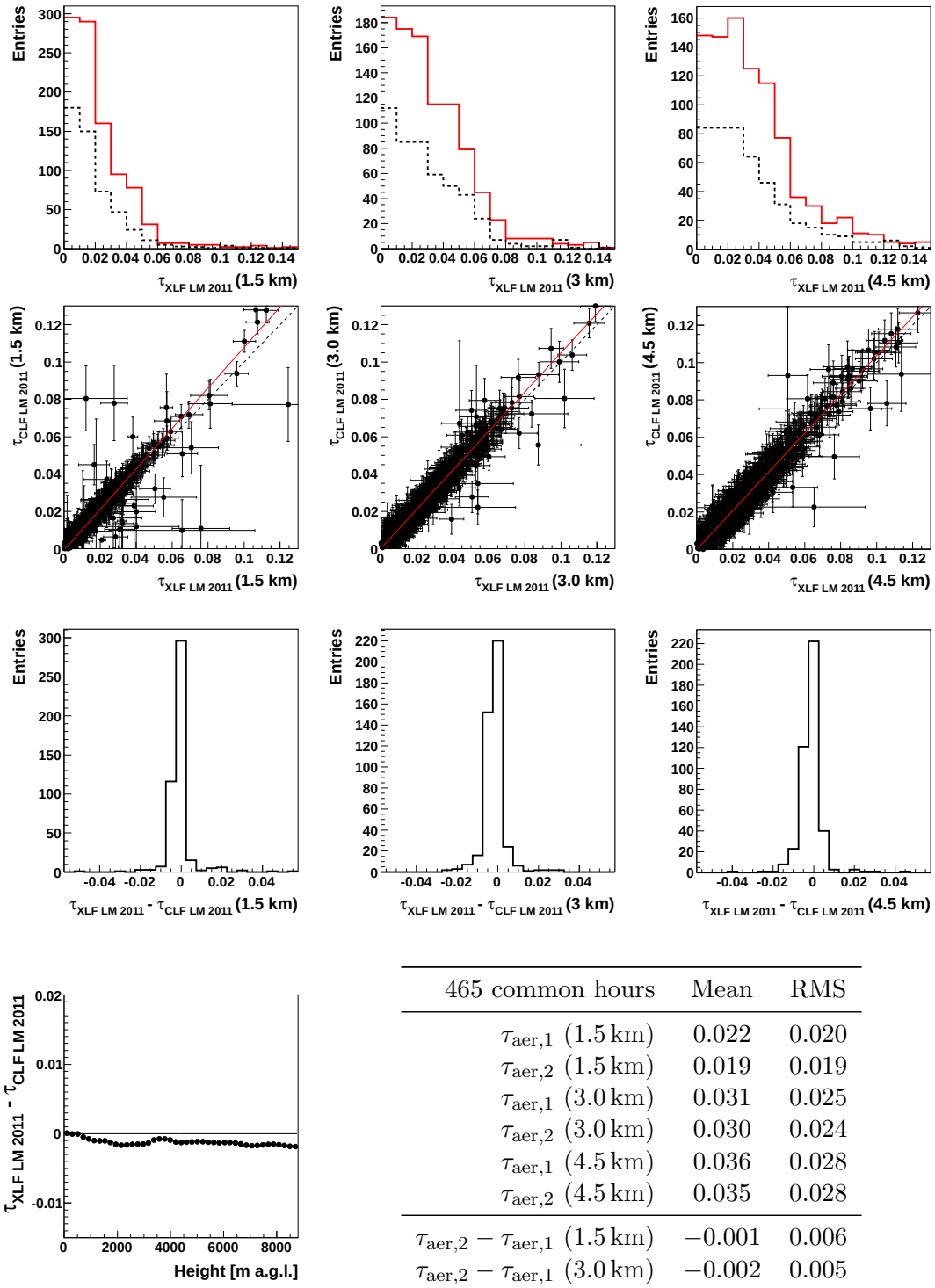

465 common hours	Mean	RMS
$\tau_{\mathrm{aer},1}$ (1.5 km)	0.022	0.020
$\tau_{\mathrm{aer},2}$ (1.5 km)	0.019	0.019
$\tau_{\mathrm{aer},1}$ (3.0 km)	0.031	0.025
$\tau_{\mathrm{aer},2}$ (3.0 km)	0.030	0.024
$\tau_{\mathrm{aer},1}$ (4.5 km)	0.036	0.028
$\tau_{\mathrm{aer},2}$ (4.5 km)	0.035	0.028
$\tau_{\mathrm{aer},2} - \tau_{\mathrm{aer},1}$ (1.5 km)	−0.001	0.006
$\tau_{\mathrm{aer},2} - \tau_{\mathrm{aer},1}$ (3.0 km)	−0.002	0.005
$\tau_{\mathrm{aer},2} - \tau_{\mathrm{aer},1}$ (4.5 km)	−0.001	0.006

Figure B.3: **Site 1: CLF CO 2010, Site 2: XLF CO 2010**

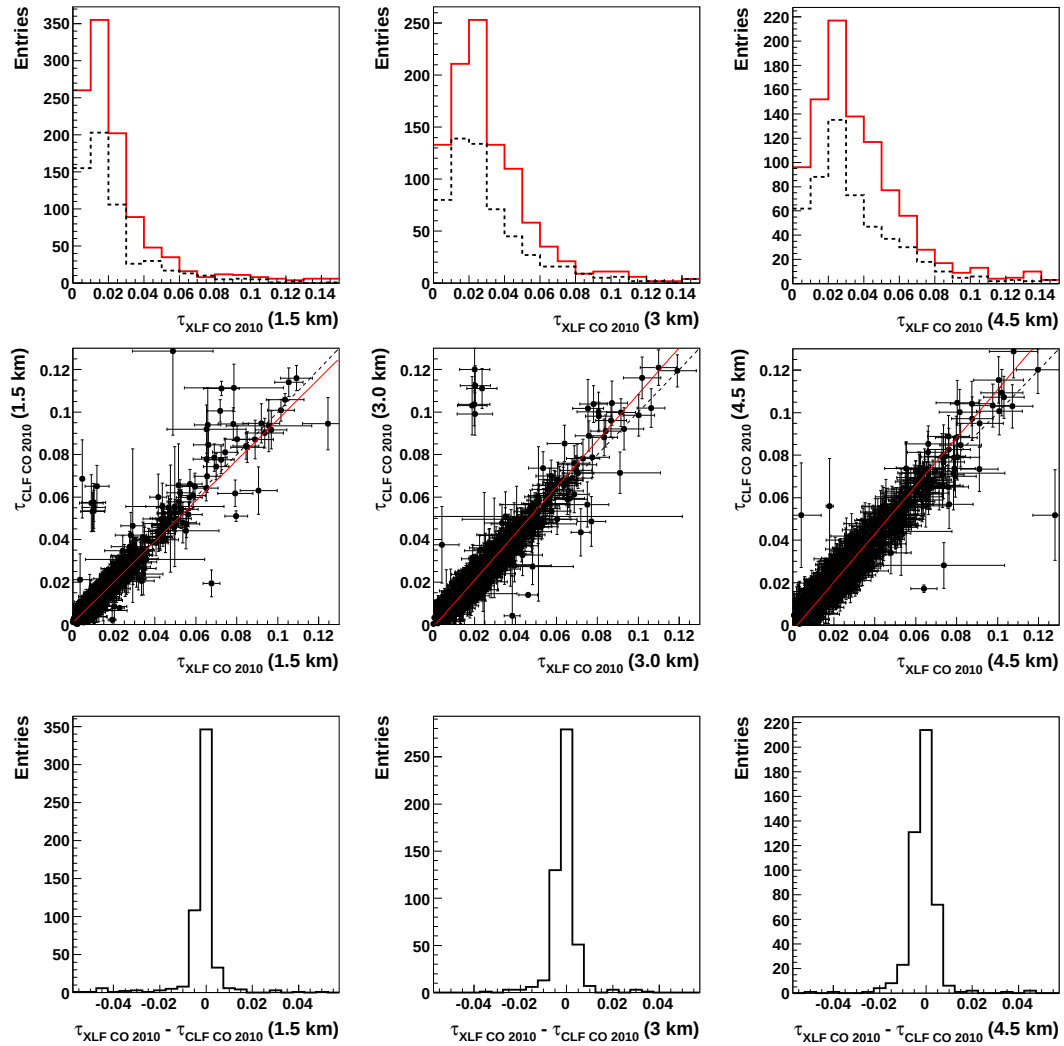

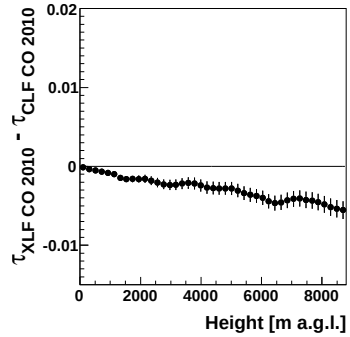

545 common hours	Mean	RMS
$\tau_{\mathrm{aer},1}$ (1.5 km)	0.025	0.025
$\tau_{\mathrm{aer},2}$ (1.5 km)	0.023	0.022
$\tau_{\mathrm{aer},1}$ (3.0 km)	0.031	0.024
$\tau_{\mathrm{aer},2}$ (3.0 km)	0.031	0.024
$\tau_{\mathrm{aer},1}$ (4.5 km)	0.037	0.026
$\tau_{\mathrm{aer},2}$ (4.5 km)	0.035	0.026
$\tau_{\mathrm{aer},2} - \tau_{\mathrm{aer},1}$ (1.5 km)	−0.002	0.008
$\tau_{\mathrm{aer},2} - \tau_{\mathrm{aer},1}$ (3.0 km)	−0.001	0.006
$\tau_{\mathrm{aer},2} - \tau_{\mathrm{aer},1}$ (4.5 km)	−0.001	0.007

Figure B.4: **Site 1: CLF CO 2011, Site 2: XLF CO 2011**

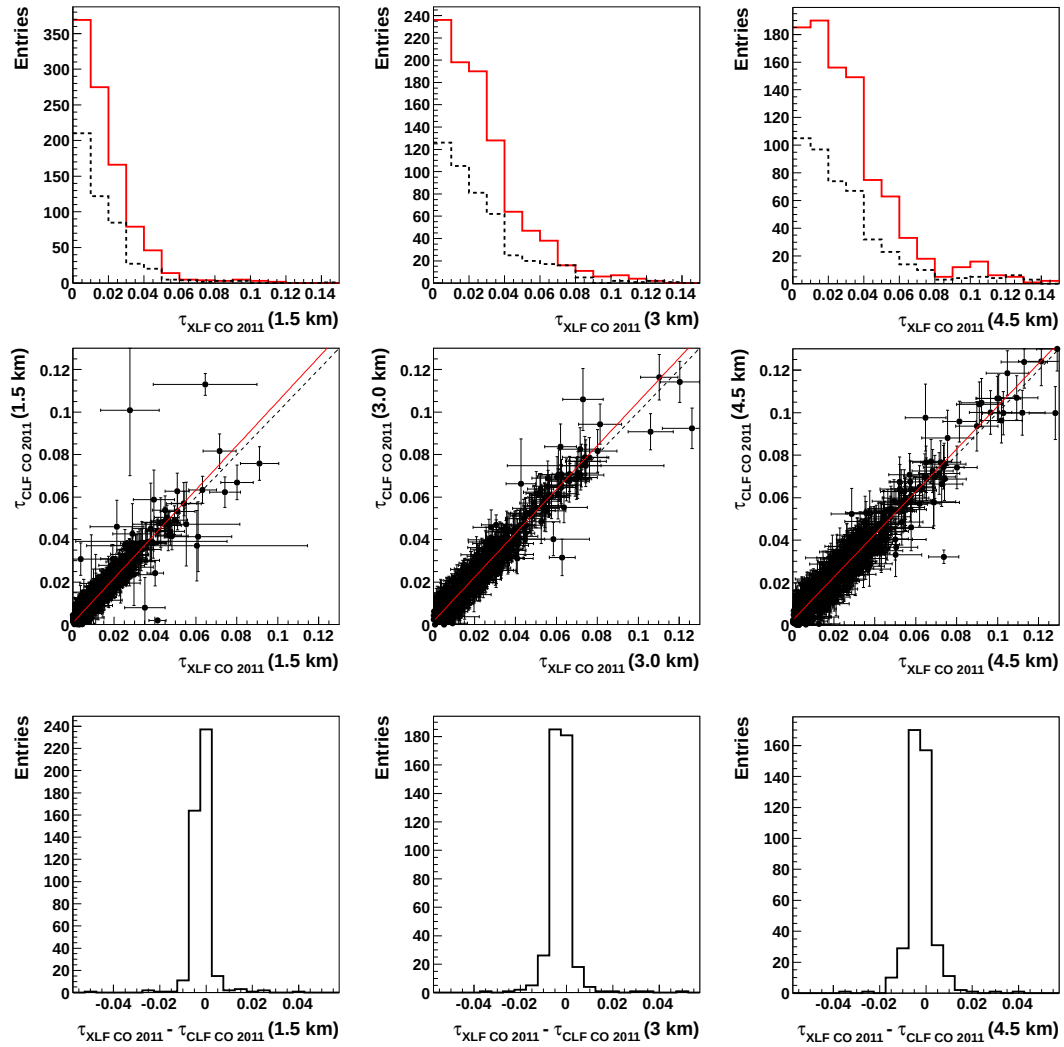

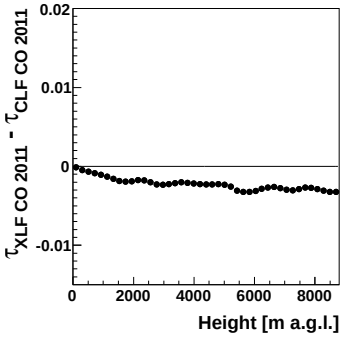

453 common hours	Mean	RMS
$\tau_{\mathrm{aer},1}$ (1.5 km)	0.018	0.016
$\tau_{\mathrm{aer},2}$ (1.5 km)	0.016	0.017
$\tau_{\mathrm{aer},1}$ (3.0 km)	0.018	0.022
$\tau_{\mathrm{aer},2}$ (3.0 km)	0.026	0.022
$\tau_{\mathrm{aer},1}$ (4.5 km)	0.031	0.025
$\tau_{\mathrm{aer},2}$ (4.5 km)	0.030	0.027
$\tau_{\mathrm{aer},2} - \tau_{\mathrm{aer},1}$ (1.5 km)	−0.002	0.005
$\tau_{\mathrm{aer},2} - \tau_{\mathrm{aer},1}$ (3.0 km)	−0.002	0.006
$\tau_{\mathrm{aer},2} - \tau_{\mathrm{aer},1}$ (4.5 km)	−0.002	0.006

Figure B.5: **Site 1: XLF LM 2010, Site 2: XLF CO 2010**

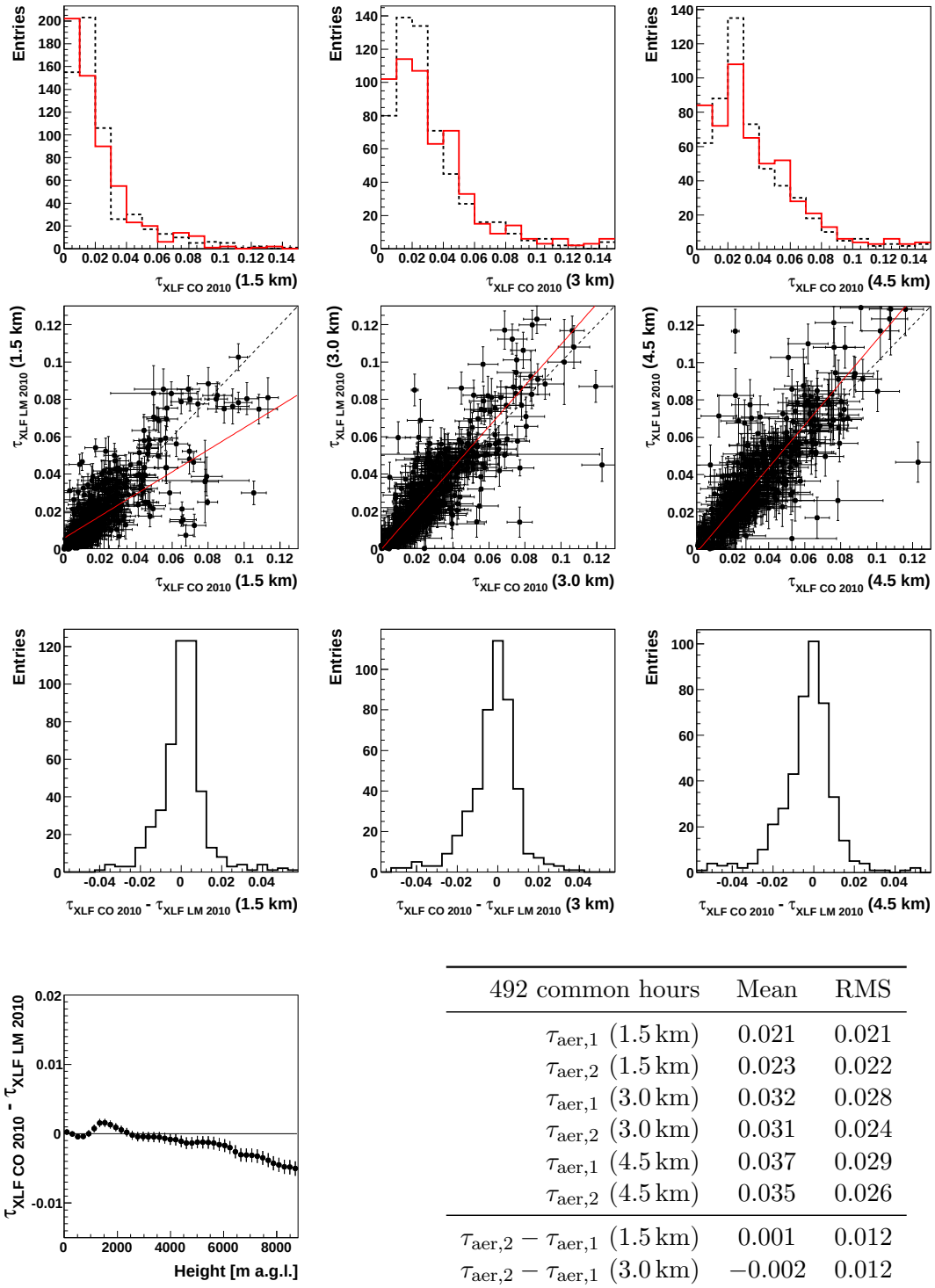

492 common hours	Mean	RMS
$\tau_{\mathrm{aer},1}$ (1.5 km)	0.021	0.021
$\tau_{\mathrm{aer},2}$ (1.5 km)	0.023	0.022
$\tau_{\mathrm{aer},1}$ (3.0 km)	0.032	0.028
$\tau_{\mathrm{aer},2}$ (3.0 km)	0.031	0.024
$\tau_{\mathrm{aer},1}$ (4.5 km)	0.037	0.029
$\tau_{\mathrm{aer},2}$ (4.5 km)	0.035	0.026
$\tau_{\mathrm{aer},2} - \tau_{\mathrm{aer},1}$ (1.5 km)	0.001	0.012
$\tau_{\mathrm{aer},2} - \tau_{\mathrm{aer},1}$ (3.0 km)	−0.002	0.012
$\tau_{\mathrm{aer},2} - \tau_{\mathrm{aer},1}$ (4.5 km)	−0.003	0.013

Figure B.6: **Site 1: XLF LM 2011, Site 2: XLF CO 2011**

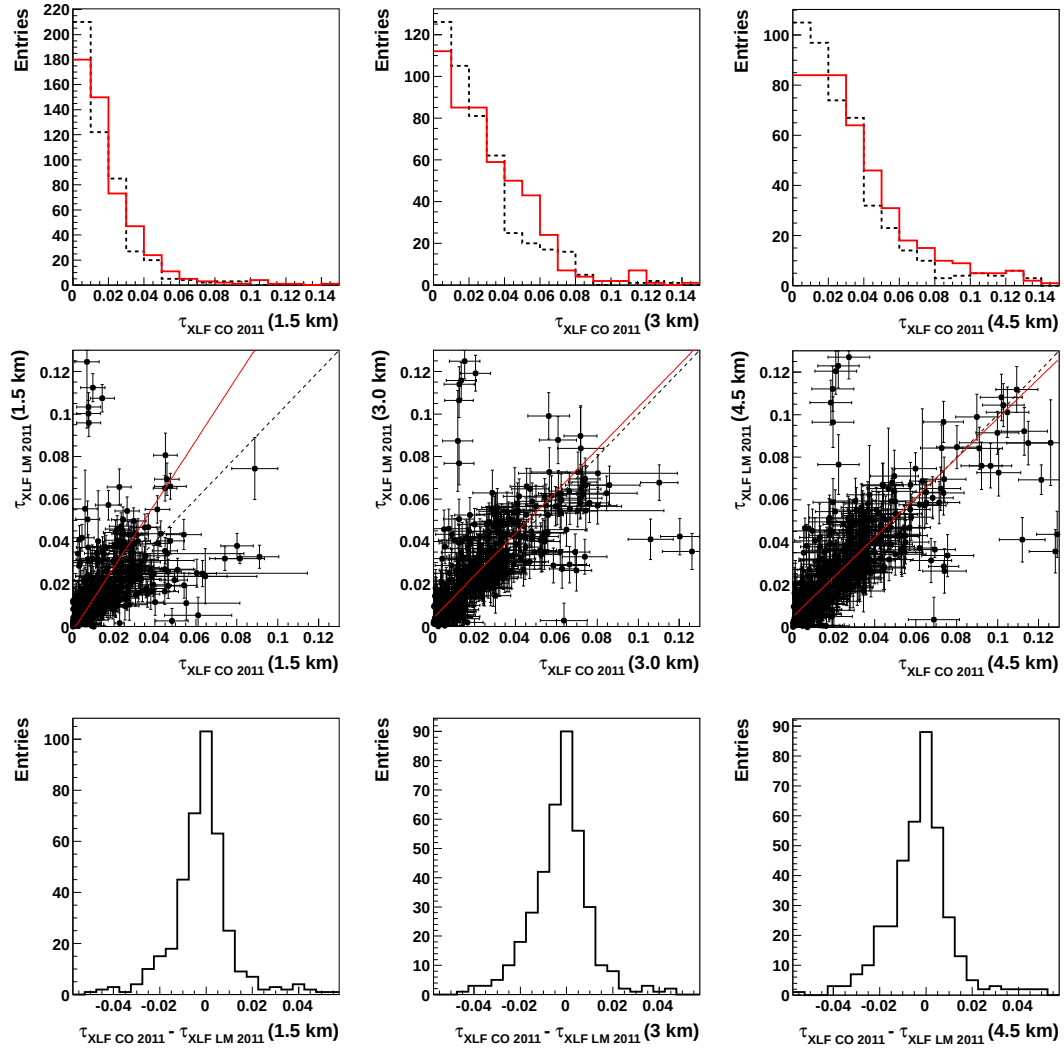

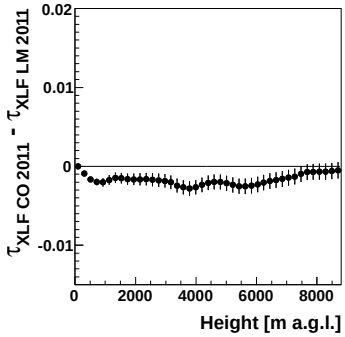

415 common hours	Mean	RMS
$\tau_{\mathrm{aer},1}$ (1.5 km)	0.019	0.019
$\tau_{\mathrm{aer},2}$ (1.5 km)	0.016	0.017
$\tau_{\mathrm{aer},1}$ (3.0 km)	0.030	0.024
$\tau_{\mathrm{aer},2}$ (3.0 km)	0.026	0.022
$\tau_{\mathrm{aer},1}$ (4.5 km)	0.035	0.028
$\tau_{\mathrm{aer},2}$ (4.5 km)	0.030	0.027
$\tau_{\mathrm{aer},2} - \tau_{\mathrm{aer},1}$ (1.5 km)	−0.001	0.013
$\tau_{\mathrm{aer},2} - \tau_{\mathrm{aer},1}$ (3.0 km)	−0.003	0.012
$\tau_{\mathrm{aer},2} - \tau_{\mathrm{aer},1}$ (4.5 km)	−0.003	0.013

Figure B.7: **Site 1: XLF LM 2010, Site 2: XLF LA 2010**

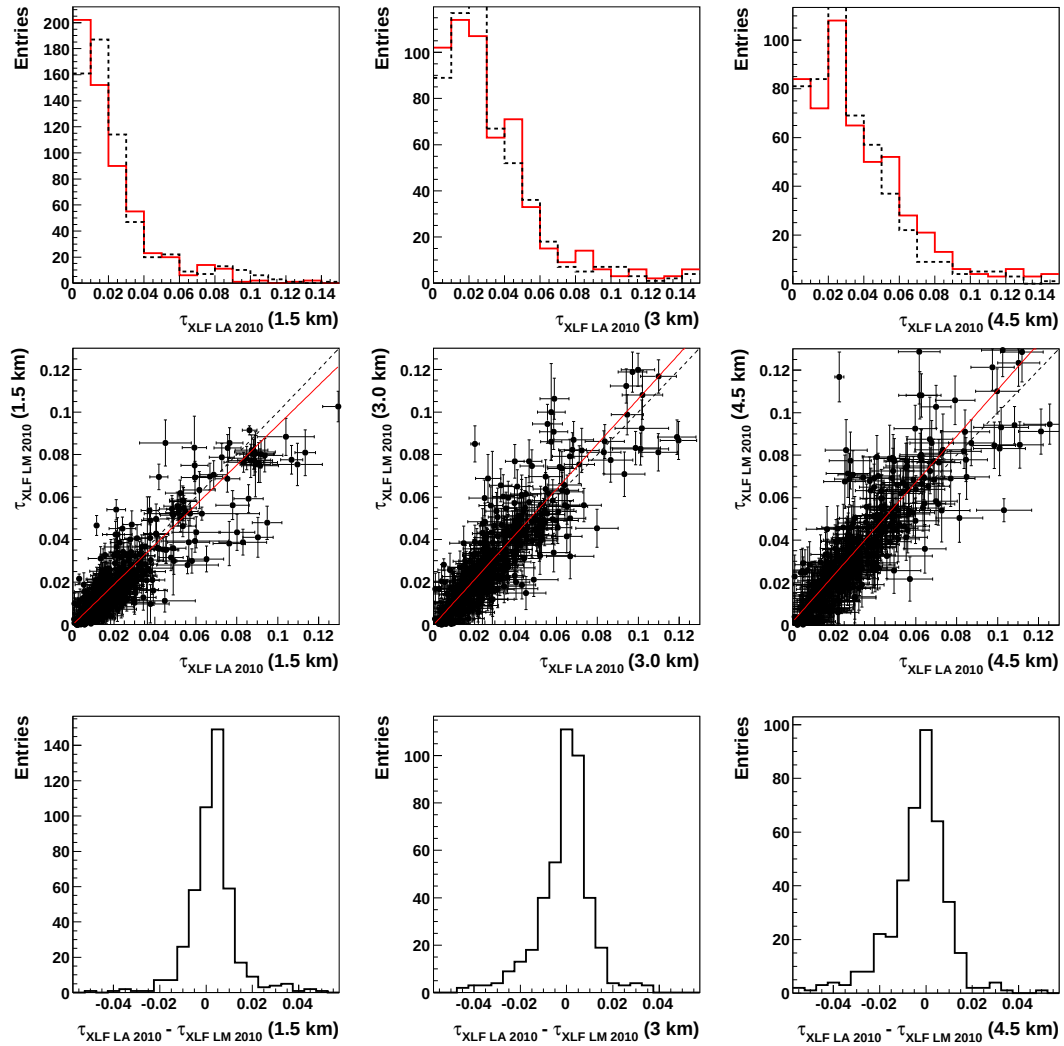

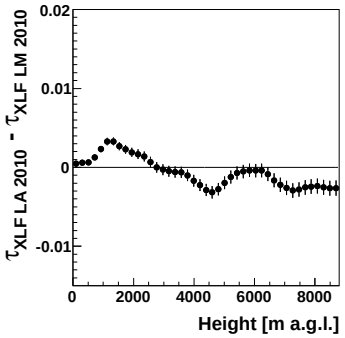

464 common hours	Mean	RMS
$\tau_{\mathrm{aer},1}$ (1.5 km)	0.021	0.021
$\tau_{\mathrm{aer},2}$ (1.5 km)	0.024	0.024
$\tau_{\mathrm{aer},1}$ (3.0 km)	0.032	0.028
$\tau_{\mathrm{aer},2}$ (3.0 km)	0.031	0.025
$\tau_{\mathrm{aer},1}$ (4.5 km)	0.037	0.029
$\tau_{\mathrm{aer},2}$ (4.5 km)	0.033	0.024
$\tau_{\mathrm{aer},2} - \tau_{\mathrm{aer},1}$ (1.5 km)	0.003	0.010
$\tau_{\mathrm{aer},2} - \tau_{\mathrm{aer},1}$ (3.0 km)	−0.001	0.011
$\tau_{\mathrm{aer},2} - \tau_{\mathrm{aer},1}$ (4.5 km)	−0.003	0.013

Figure B.8: **Site 1: XLF LM 2011, Site 2: XLF LA 2011**

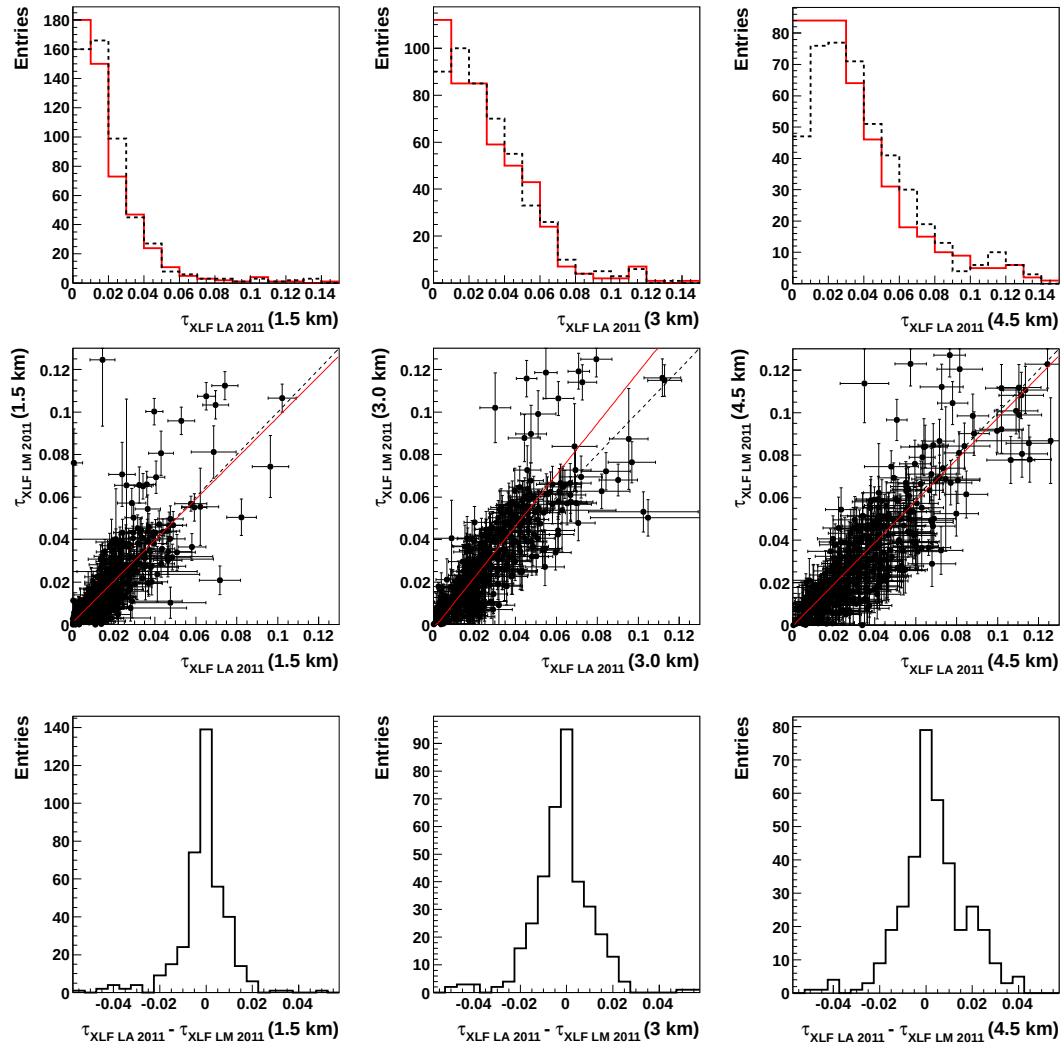

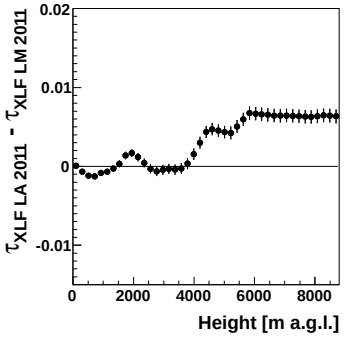

405 common hours	Mean	RMS
$\tau_{\mathrm{aer},1}$ (1.5 km)	0.019	0.019
$\tau_{\mathrm{aer},2}$ (1.5 km)	0.021	0.020
$\tau_{\mathrm{aer},1}$ (3.0 km)	0.030	0.024
$\tau_{\mathrm{aer},2}$ (3.0 km)	0.031	0.024
$\tau_{\mathrm{aer},1}$ (4.5 km)	0.035	0.028
$\tau_{\mathrm{aer},2}$ (4.5 km)	0.040	0.028
$\tau_{\mathrm{aer},2} - \tau_{\mathrm{aer},1}$ (1.5 km)	−0.001	0.011
$\tau_{\mathrm{aer},2} - \tau_{\mathrm{aer},1}$ (3.0 km)	−0.002	0.013
$\tau_{\mathrm{aer},2} - \tau_{\mathrm{aer},1}$ (4.5 km)	0.003	0.014

Figure B.9: **Site 1: XLF CO 2010, Site 2: XLF LA 2010**

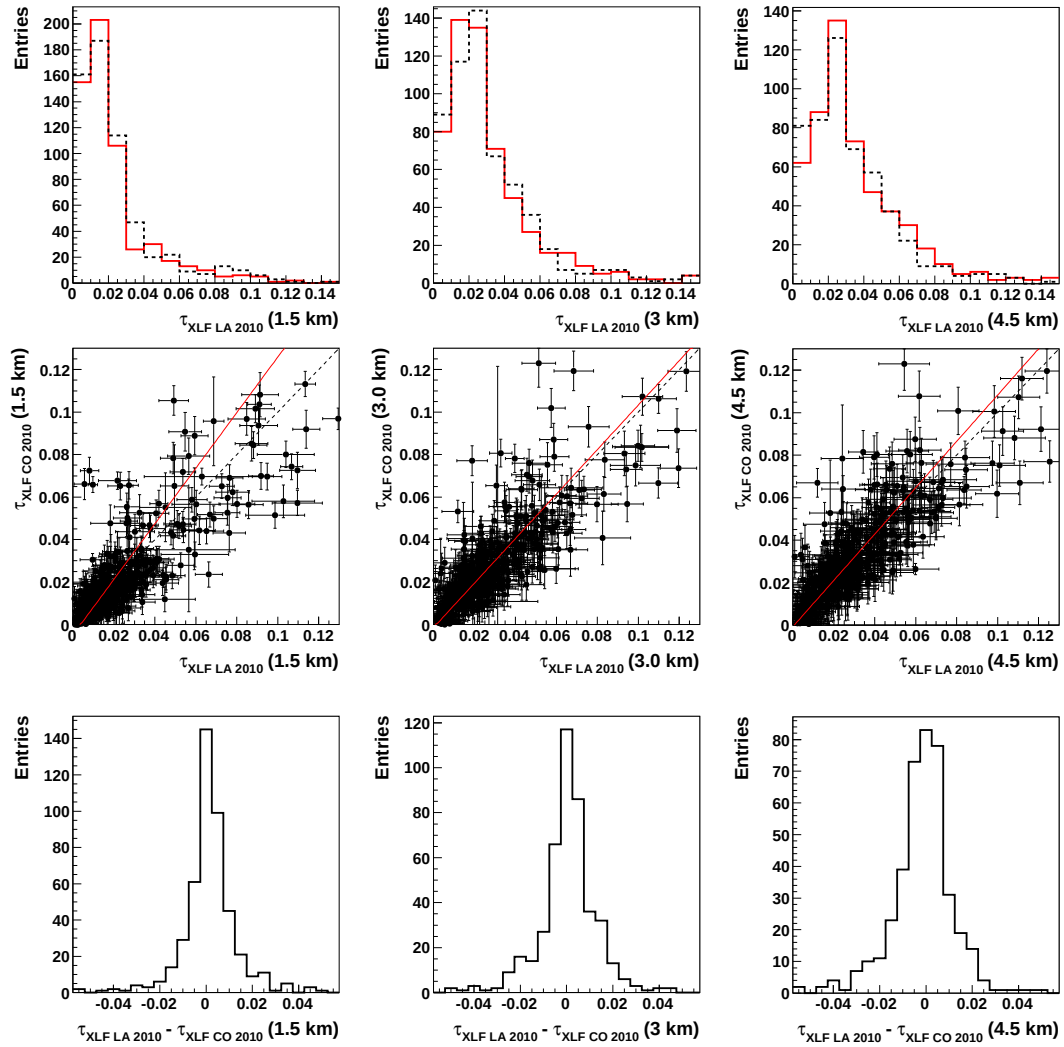

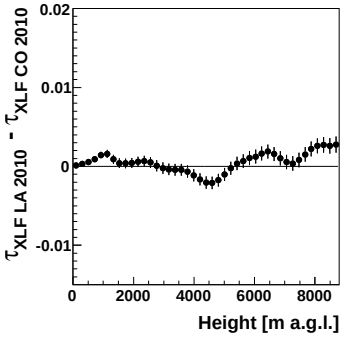

478 common hours	Mean	RMS
$\tau_{\mathrm{aer},1}$ (1.5 km)	0.023	0.022
$\tau_{\mathrm{aer},2}$ (1.5 km)	0.024	0.024
$\tau_{\mathrm{aer},1}$ (3.0 km)	0.031	0.024
$\tau_{\mathrm{aer},2}$ (3.0 km)	0.031	0.025
$\tau_{\mathrm{aer},1}$ (4.5 km)	0.035	0.026
$\tau_{\mathrm{aer},2}$ (4.5 km)	0.033	0.024
$\tau_{\mathrm{aer},2} - \tau_{\mathrm{aer},1}$ (1.5 km)	0.002	0.012
$\tau_{\mathrm{aer},2} - \tau_{\mathrm{aer},1}$ (3.0 km)	0.001	0.012
$\tau_{\mathrm{aer},2} - \tau_{\mathrm{aer},1}$ (4.5 km)	−0.002	0.013

Figure B.10: **Site 1: XLF CO 2011, Site 2: XLF LA 2011**

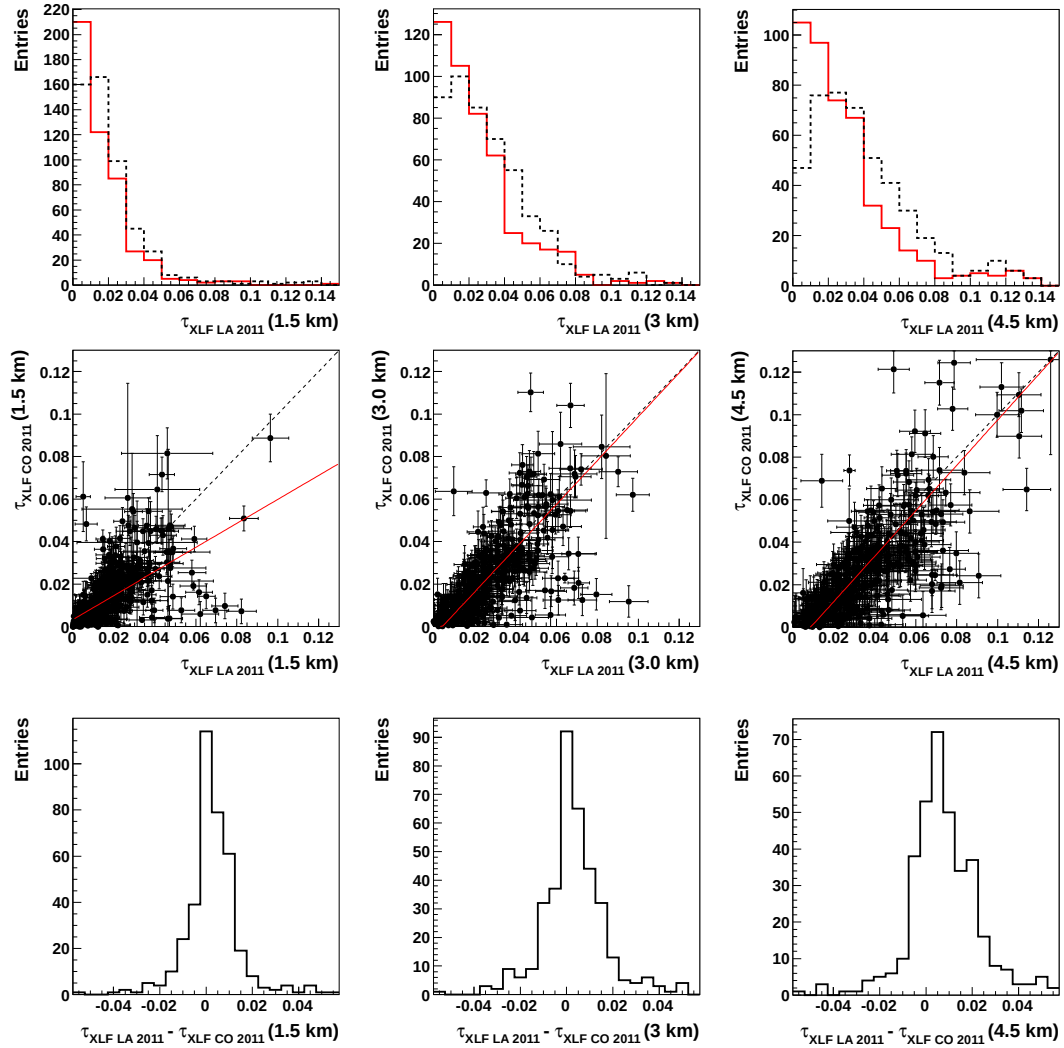

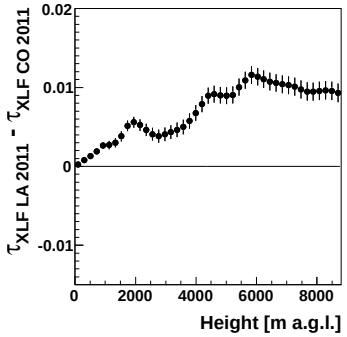

397 common hours	Mean	RMS
$\tau_{\mathrm{aer},1}$ (1.5 km)	0.016	0.017
$\tau_{\mathrm{aer},2}$ (1.5 km)	0.021	0.020
$\tau_{\mathrm{aer},1}$ (3.0 km)	0.026	0.022
$\tau_{\mathrm{aer},2}$ (3.0 km)	0.031	0.024
$\tau_{\mathrm{aer},1}$ (4.5 km)	0.030	0.027
$\tau_{\mathrm{aer},2}$ (4.5 km)	0.040	0.028
$\tau_{\mathrm{aer},2} - \tau_{\mathrm{aer},1}$ (1.5 km)	0.003	0.012
$\tau_{\mathrm{aer},2} - \tau_{\mathrm{aer},1}$ (3.0 km)	0.003	0.014
$\tau_{\mathrm{aer},2} - \tau_{\mathrm{aer},1}$ (4.5 km)	0.008	0.015

Figure B.11: **Site 1: CLF LM 2010, Site 2: CLF CO 2010**

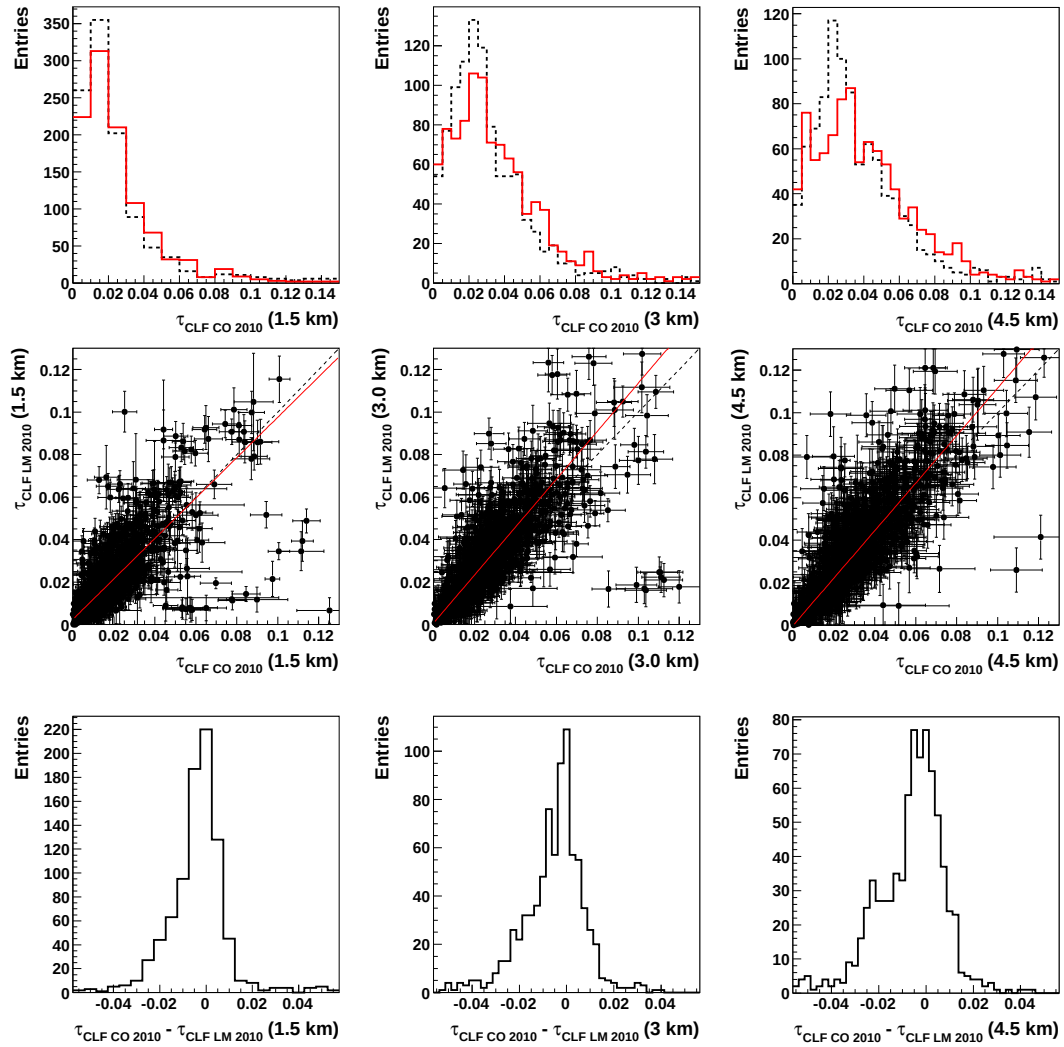

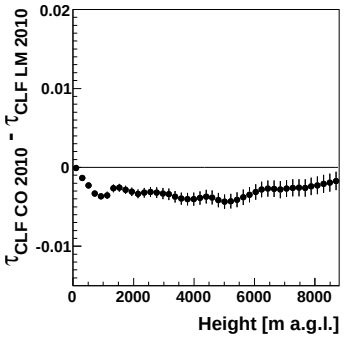

907 common hours	Mean	RMS
$\tau_{\mathrm{aer},1}$ (1.5 km)	0.026	0.022
$\tau_{\mathrm{aer},2}$ (1.5 km)	0.025	0.025
$\tau_{\mathrm{aer},1}$ (3.0 km)	0.035	0.026
$\tau_{\mathrm{aer},2}$ (3.0 km)	0.032	0.024
$\tau_{\mathrm{aer},1}$ (4.5 km)	0.041	0.028
$\tau_{\mathrm{aer},2}$ (4.5 km)	0.037	0.026
$\tau_{\mathrm{aer},2} - \tau_{\mathrm{aer},1}$ (1.5 km)	−0.004	0.013
$\tau_{\mathrm{aer},2} - \tau_{\mathrm{aer},1}$ (3.0 km)	−0.005	0.013
$\tau_{\mathrm{aer},2} - \tau_{\mathrm{aer},1}$ (4.5 km)	−0.006	0.014

Figure B.12: **Site 1: CLF LM 2011, Site 2: CLF CO 2011**

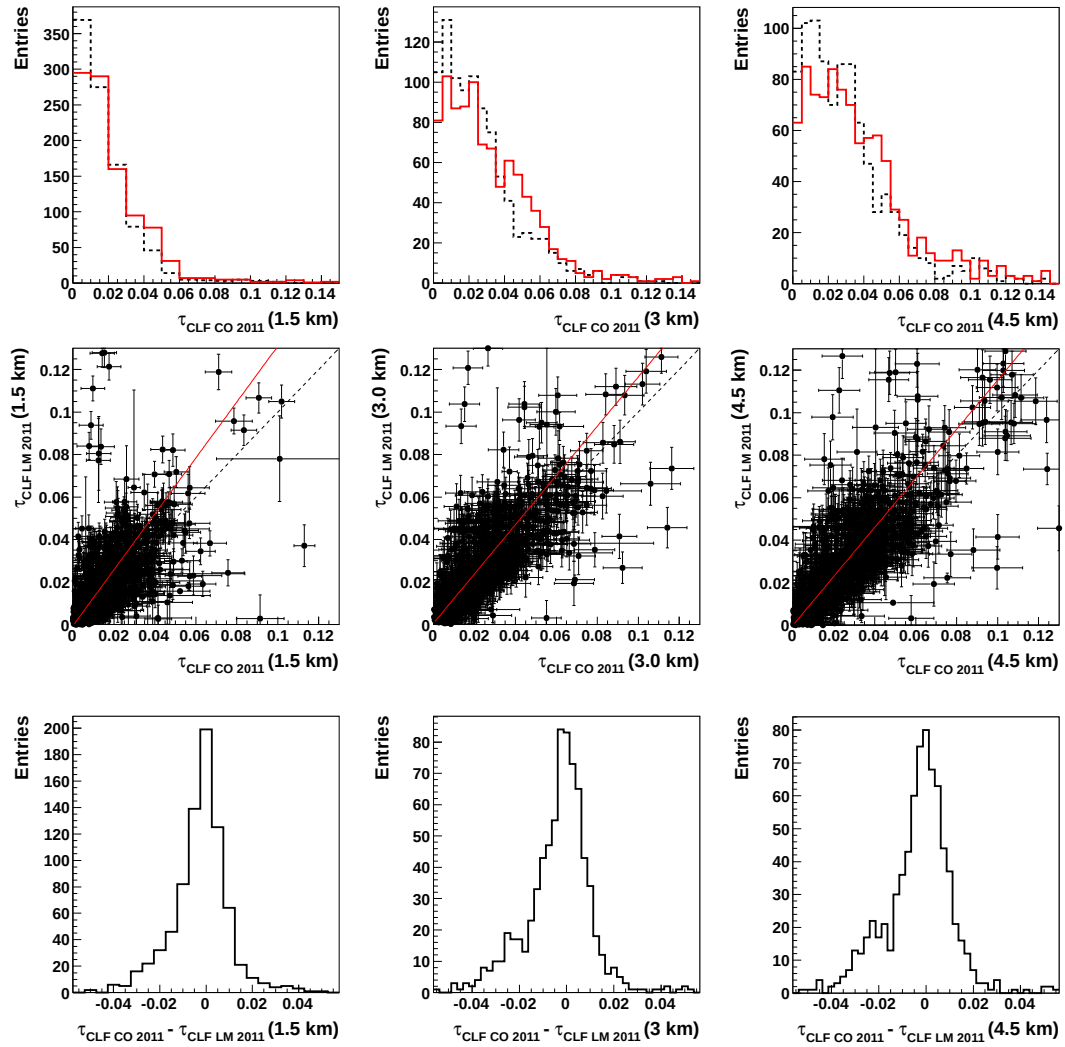

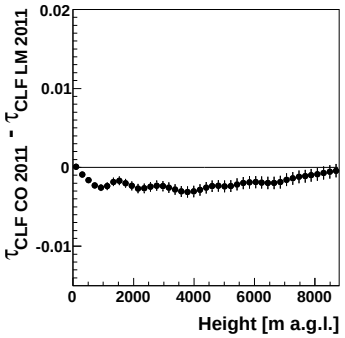

822 common hours	Mean	RMS
$\tau_{\mathrm{aer},1}$ (1.5 km)	0.022	0.020
$\tau_{\mathrm{aer},2}$ (1.5 km)	0.018	0.016
$\tau_{\mathrm{aer},1}$ (3.0 km)	0.031	0.025
$\tau_{\mathrm{aer},2}$ (3.0 km)	0.027	0.022
$\tau_{\mathrm{aer},1}$ (4.5 km)	0.036	0.028
$\tau_{\mathrm{aer},2}$ (4.5 km)	0.031	0.025
$\tau_{\mathrm{aer},2} - \tau_{\mathrm{aer},1}$ (1.5 km)	−0.002	0.012
$\tau_{\mathrm{aer},2} - \tau_{\mathrm{aer},1}$ (3.0 km)	−0.003	0.014
$\tau_{\mathrm{aer},2} - \tau_{\mathrm{aer},1}$ (4.5 km)	−0.003	0.014

Figure B.13: **Site 1: CLF LM 2010, Site 2: CLF LL 2010**

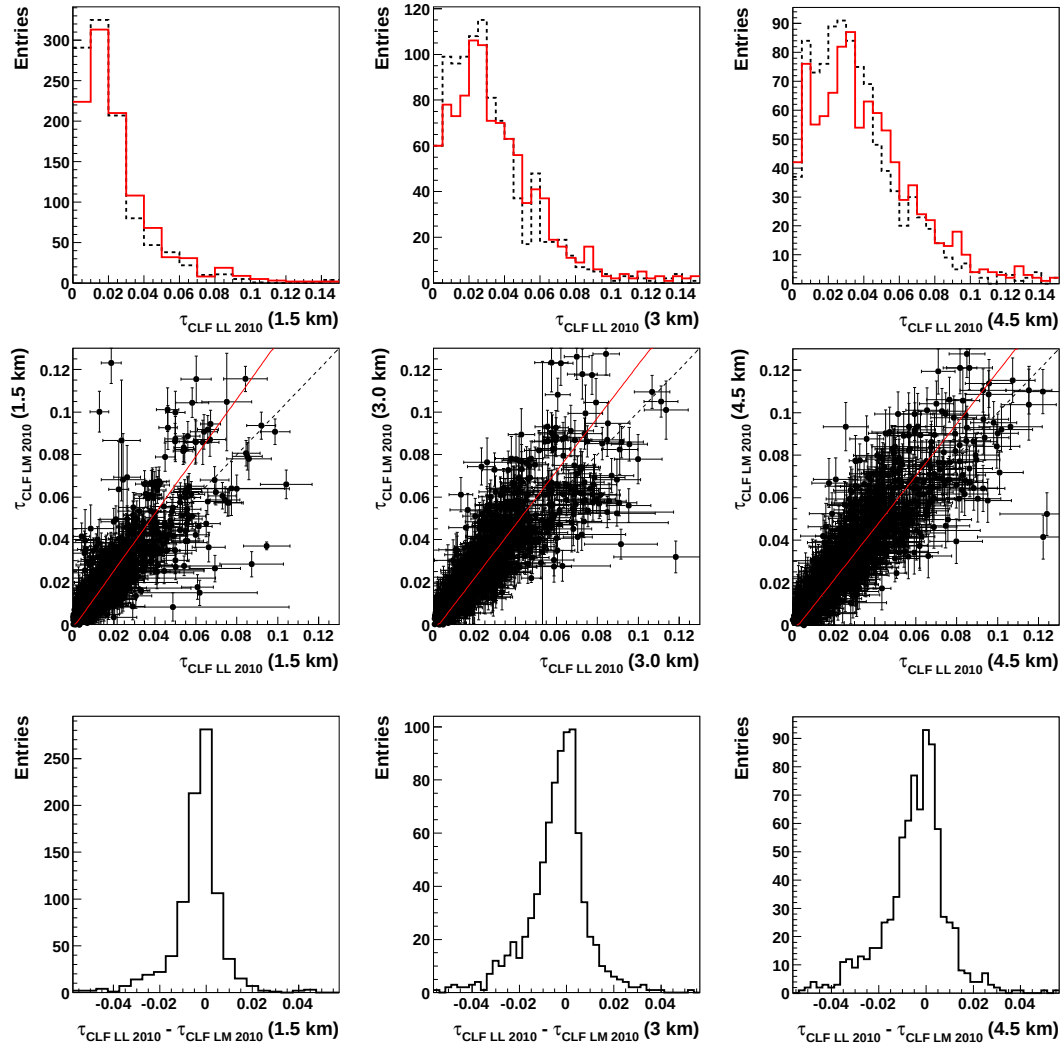

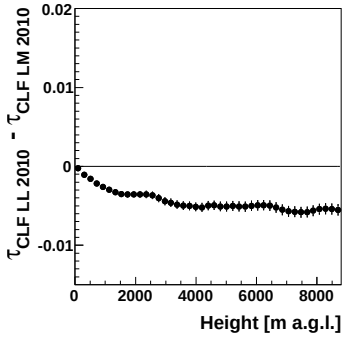

889 common hours	Mean	RMS
$\tau_{\mathrm{aer},1}$ (1.5 km)	0.026	0.022
$\tau_{\mathrm{aer},2}$ (1.5 km)	0.022	0.020
$\tau_{\mathrm{aer},1}$ (3.0 km)	0.035	0.026
$\tau_{\mathrm{aer},2}$ (3.0 km)	0.031	0.023
$\tau_{\mathrm{aer},1}$ (4.5 km)	0.041	0.028
$\tau_{\mathrm{aer},2}$ (4.5 km)	0.036	0.025
$\tau_{\mathrm{aer},2} - \tau_{\mathrm{aer},1}$ (1.5 km)	−0.004	0.011
$\tau_{\mathrm{aer},2} - \tau_{\mathrm{aer},1}$ (3.0 km)	−0.004	0.013
$\tau_{\mathrm{aer},2} - \tau_{\mathrm{aer},1}$ (4.5 km)	−0.005	0.014

Figure B.14: **Site 1: CLF LM 2011, Site 2: CLF LL 2011**

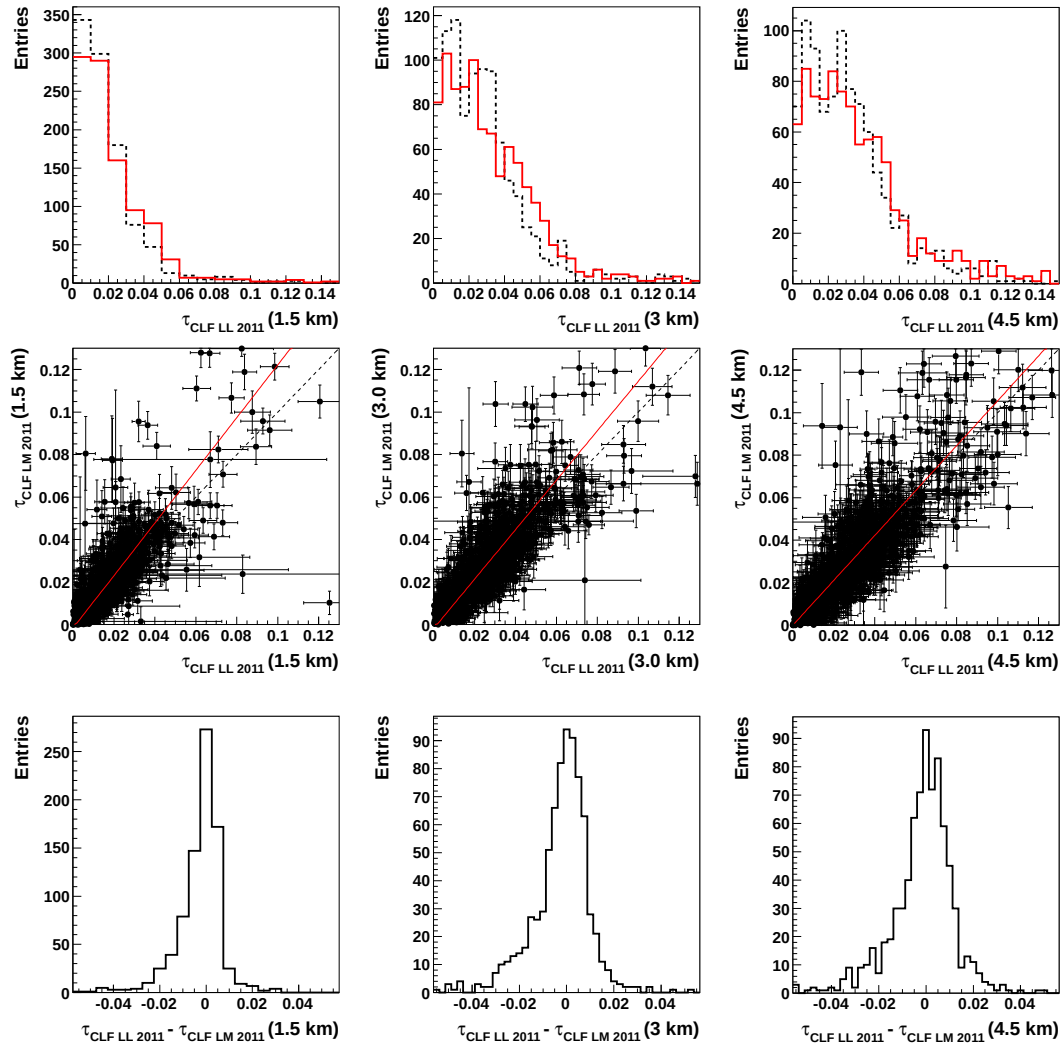

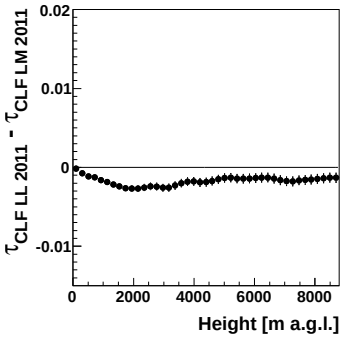

833 common hours	Mean	RMS
$\tau_{\mathrm{aer},1}$ (1.5 km)	0.022	0.020
$\tau_{\mathrm{aer},2}$ (1.5 km)	0.019	0.017
$\tau_{\mathrm{aer},1}$ (3.0 km)	0.031	0.025
$\tau_{\mathrm{aer},2}$ (3.0 km)	0.028	0.024
$\tau_{\mathrm{aer},1}$ (4.5 km)	0.036	0.028
$\tau_{\mathrm{aer},2}$ (4.5 km)	0.032	0.025
$\tau_{\mathrm{aer},2} - \tau_{\mathrm{aer},1}$ (1.5 km)	−0.003	0.010
$\tau_{\mathrm{aer},2} - \tau_{\mathrm{aer},1}$ (3.0 km)	−0.002	0.012
$\tau_{\mathrm{aer},2} - \tau_{\mathrm{aer},1}$ (4.5 km)	−0.001	0.013

Figure B.15: **Site 1: CLF CO 2011, Site 2: CLF LL 2011**

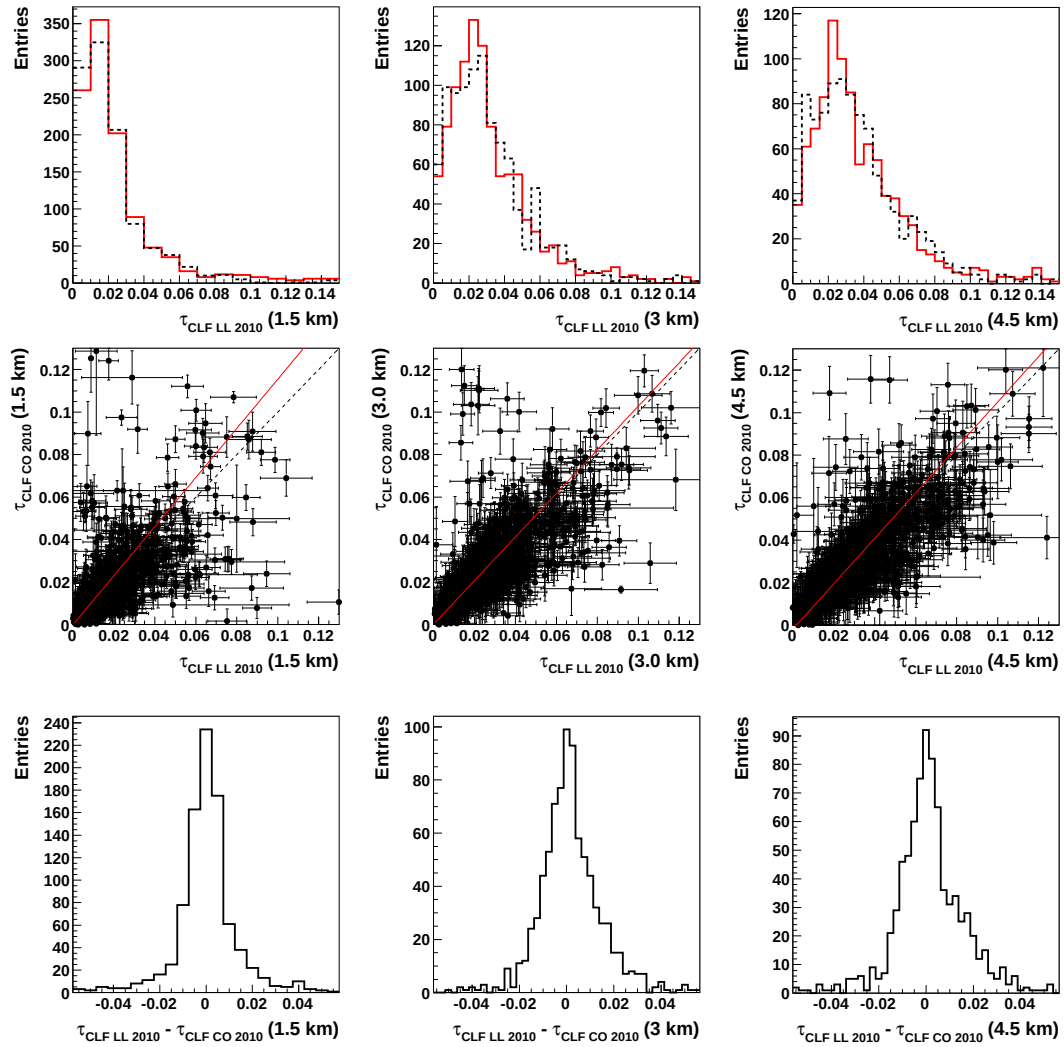

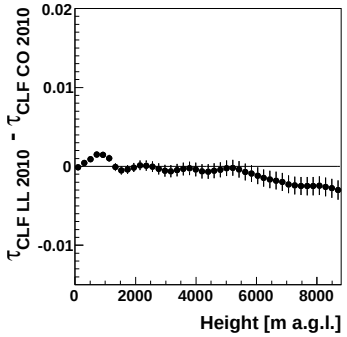

925 common hours	Mean	RMS
$\tau_{\mathrm{aer},1}$ (1.5 km)	0.025	0.025
$\tau_{\mathrm{aer},2}$ (1.5 km)	0.022	0.020
$\tau_{\mathrm{aer},1}$ (3.0 km)	0.031	0.024
$\tau_{\mathrm{aer},2}$ (3.0 km)	0.031	0.023
$\tau_{\mathrm{aer},1}$ (4.5 km)	0.037	0.026
$\tau_{\mathrm{aer},2}$ (4.5 km)	0.036	0.025
$\tau_{\mathrm{aer},2} - \tau_{\mathrm{aer},1}$ (1.5 km)	0.000	0.013
$\tau_{\mathrm{aer},2} - \tau_{\mathrm{aer},1}$ (3.0 km)	0.002	0.013
$\tau_{\mathrm{aer},2} - \tau_{\mathrm{aer},1}$ (4.5 km)	0.002	0.014

Figure B.16: **Site 1: CLF CO 2011, Site 2: CLF LL 2011**

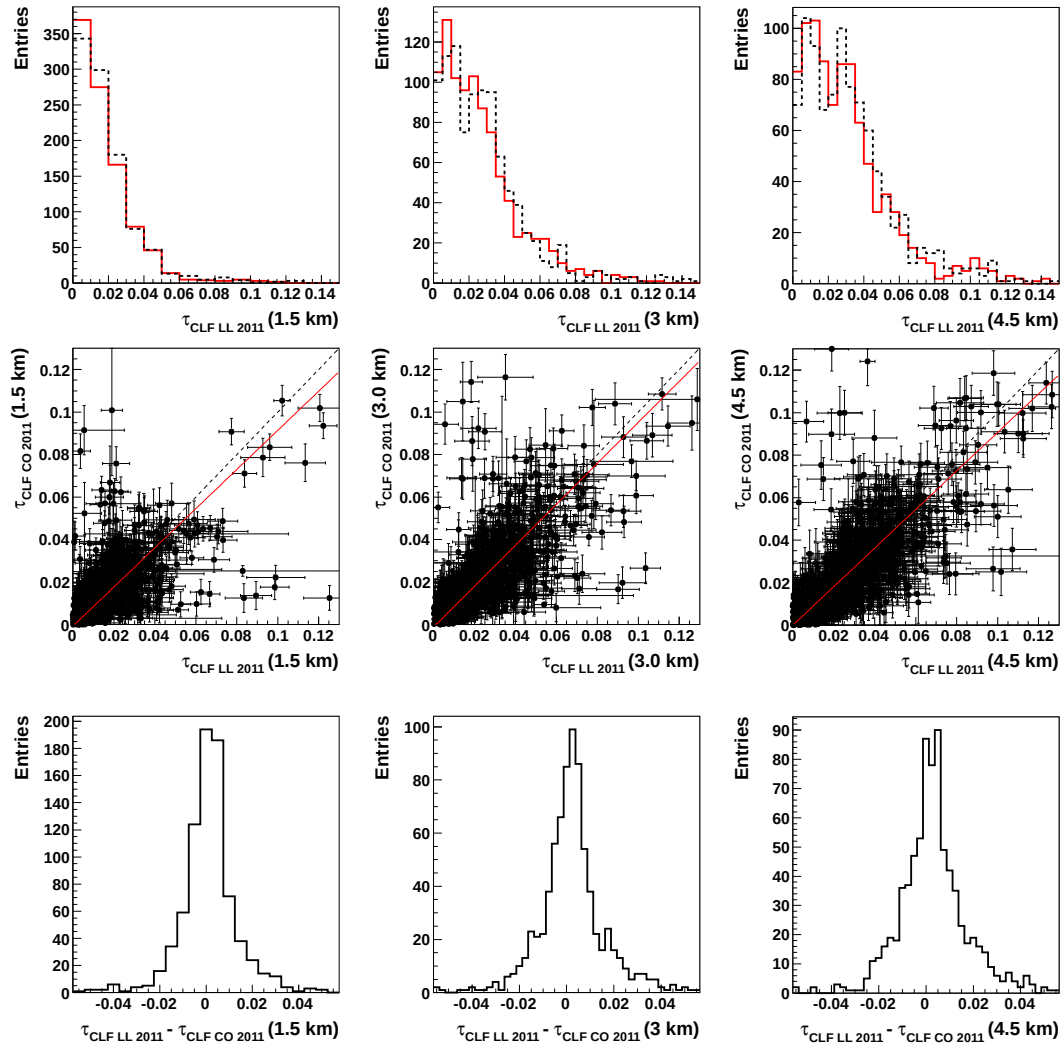

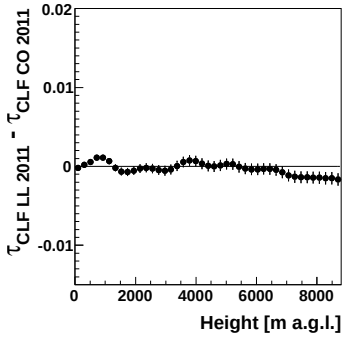

972 common hours	Mean	RMS
$\tau_{\mathrm{aer},1}$ (1.5 km)	0.018	0.016
$\tau_{\mathrm{aer},2}$ (1.5 km)	0.019	0.017
$\tau_{\mathrm{aer},1}$ (3.0 km)	0.027	0.022
$\tau_{\mathrm{aer},2}$ (3.0 km)	0.028	0.024
$\tau_{\mathrm{aer},1}$ (4.5 km)	0.031	0.025
$\tau_{\mathrm{aer},2}$ (4.5 km)	0.032	0.025
$\tau_{\mathrm{aer},2} - \tau_{\mathrm{aer},1}$ (1.5 km)	0.001	0.012
$\tau_{\mathrm{aer},2} - \tau_{\mathrm{aer},1}$ (3.0 km)	0.002	0.014
$\tau_{\mathrm{aer},2} - \tau_{\mathrm{aer},1}$ (4.5 km)	0.003	0.014

Bibliography

[1] J. Blümer, R. Engel, J. Hörandel, Cosmic Rays from the Knee to the Highest Energies, Prog. Part. Nucl. Phys 63 (2009) 293–338. arXiv:0904.0725.

[2] W.-M. Yao, et al., Review of Particle Physics, J. Phys. G33 (2006) 1. URL http://pdg.lbl.gov

[3] R. Ulrich, Measurement of the proton-air cross section using hybrid data of the Pierre Auger Observatory, Ph.D. thesis, Universität Karlsruhe (TH), Germany (2007).

[4] W. Heitler, The Quantum Theory of Radiation, 2nd Edition, Oxford University Press, 1944.

[5] P. Auger, et al., Extensive Cosmic-Ray Showers, Rev. Mod. Phys. 11 (1939) 288–291.

[6] J. Linsley, L. Scarsi, B. Rossi, Extremely energetic cosmic-ray event, Phys. Rev. Lett 6 (1961) 485–487.

[7] T. Egorov, et al., The Yakutsk EAS complex array, in: Proc. 12th ICRC, Hobart, Australia, 1971.

[8] G. Navarra, et al., The KASCADE-Grande Collaboration, KASCADE-Grande: a large acceptance, high-resolution cosmic-ray detector up to 10^{18} eV, Nucl. Instr. Meth. A518 (2004) 207–209.

[9] N. Chiba, et al., The AGASA Collaboration, Akeno Giant Air Shower Array (AGASA) covering 100 km^2 area, Nucl. Instr. Meth. A311 (1992) 338–349.

[10] J. Matthews, et al., for the Telescope Array Collaboration, The Telescope Array Experiment, in: Proc. 32nd ICRC, Vol. 2, Beijing, China, 2011, pp. 273–276.

[11] H. R. Allan, et al., The Distribution of Energy in Extensive Air Showers and the Shower Size Spectrum, Proc. Phys. Soc. 79 (1962) 1170–1182.

[12] J. Abraham, et al., The Pierre Auger Collaboration, Properties and performance of the prototype instrument for the Pierre Auger Observatory, Nucl. Instr. Meth. A523 (2004) 50–95.

[13] H. E. Bergeson, et al., Measurement of Light Emission from Remote Cosmic-Ray Air Showers, Phys. Rev. Lett. 39 (1977) 847–849.

[14] P. Sokolsky, G. B. Thomson, Highest energy cosmic rays and results from the HiRes experiment, J. Phys. G34 (2007) R401. arXiv:0706.1248.

[15] H. Falcke, et al., Detection and imaging of atmospheric radio flashes from cosmic ray air showers, Nature 435 (2005) 313–316. arXiv:astro-ph/0505383.

[16] B. Revenu, et al., for the Pierre Auger Collaboration, Autonomous detection and analysis of radio emission from air showers detected at the Pierre Auger Observatory, in: Proc. 32nd ICRC, Vol. 3, Beijing, China, 2011, pp. 172–175. arXiv:1107.4807.

[17] J. Kelley, et al., for the Pierre Auger Collaboration, AERA: the Auger Engineering Radio Array, in: Proc. 32nd ICRC, Vol. 3, Beijing, China, 2011, pp. 112–115. arXiv:1107.4807.

[18] P. W. Gorham, Observations of Microwave Continuum Emission from Air Shower Plasmas, Phys. Rev. D78 (2008) 032007.

[19] M. Monasor, et al., The Microwave Air Yield Beam Experiment (MAYBE): measurement of GHz radiation for Ultra-High Energy Cosmic Rays detection, in: Proc. 32nd ICRC, Vol. 3, Beijing, China, 2011, pp. 192–195. arXiv:1108.6321.

[20] V. Verzi, et al., The Air Microwave Yield (AMY) experiment to measure the GHz emission from air shower plasmas, in: International Symposium on Future Directions in UHECR Physics, CERN, 2012.

[21] R. Šmída, et al., First results of the CROME experiment, in: Proc. 32nd ICRC, Vol. 3, Beijing, China, 2011, pp. 17–20. arXiv:1108.0588.

[22] R. Šmída, et al., Microwave Emission from Extensive Air Showers as seen by CROME, in: International Symposium on Future Directions in UHECR Physics, CERN, 2012.

[23] P. Allison, et al., for the Pierre Auger Collaboration, Microwave detection of cosmic ray showers at the Pierre Auger Observatory, in: Proc. 32nd ICRC, Vol. 3, Beijing, China, 2011, pp. 137–140. arXiv:1107.4807.

[24] V. F. Hess, Über die Beobachtung der durchdringenden Strahlung bei sieben Freiballonfahrten, Phys. Zeitschr. 13 (1912) 1084–1091.

[25] P. Bhattacharjee, G. Sigl, Origin and Propagation of Extremely High Energy Cosmic Rays, Phys. Rept. 327 (2000) 109–247. arXiv:astro-ph/9811011.

[26] E. Fermi, On the origin of cosmic radiation, Phys. Rev. 75 (1949) 1169–1174.

[27] A. M. Hillas, The Origin of Ultra-High-Energy Cosmic Rays, Ann. Rev. Astron. Astrophys. 22 (1984) 425–444.

[28] P. O. Lagage, C. J. Cesarsky, The maximum energy of cosmic rays accelerated by supernova shocks, Astron. Astrophys. 125 (1983) 249–257.

[29] N. E. Yanasak, Measurement of the Secondary Radionuclides ^{10}Be, ^{26}Al, ^{36}Cl, ^{54}Mn, and ^{14}C and Implications for the Galactic Cosmic-Ray Age, Astrophys. J. 563 (2001) 768–792.

[30] D. F. Torres, L. A. Anchordoqui, Astrophysical Origins of Ultrahigh Energy Cosmic Rays, Rept. Prog. Phys. 67 (2004) 1663–1730. arXiv:astro-ph/0402371.

[31] K. Greisen, End to the Cosmic-Ray Spectrum?, Phys. Rev. Lett. 16 (17) (1966) 748–750.

[32] G. T. Zatsepin, V. A. Kuz'min, Upper Limit of the Spectrum of Cosmic Rays, JETP Lett. 4 (1966) 78–80.

[33] T. Antoni, et al., The KASCADE Collaboration, KASCADE measurements of energy spectra for elemental groups of cosmic rays: Results and open problems, Astropart. Phys. 24 (2005) 1–25. arXiv:astro-ph/0505413.

[34] W. D. Apel, et al., The KASCADE-Grande Collaboration, Kneelike Structure in the Spectrum of the Heavy Component of Cosmic Rays Observed with KASCADE-Grande, Phys. Rev. Lett. 107 (2011) 171104. arXiv:1107.5885.

[35] F. Salamida, for the Pierre Auger Collaboration, Update on the measurement of the CR energy spectrum above 10^{18} eV made using the Pierre Auger Observatory, in: Proc. 32nd ICRC, Vol. 2, Beijing, China, 2011, pp. 145–148. arXiv:1107.4809.

[36] D. Ikeda, et al., for the Telescope Array Collaboration, Ultra-high energy cosmic-ray spectra measured by the Telescope Array experiment from hybrid observations, in: Proc. 32nd ICRC, Vol. 2, Beijing, China, 2011, pp. 238–241.

[37] J. Abraham, et al., The Pierre Auger Collaboration, Measurement of the Energy Spectrum of Cosmic Rays above 10^{18} eV using the Pierre Auger Observatory, Phys. Lett. B685 (2010) 239–246. arXiv:1002.1975.

[38] T. Wibig, A. W. Wolfendale, At what particle energy do extragalactic cosmic rays start to predominate?, J. Phys. G31 (2005) 255–264.

[39] V. Berezinsky, A. Z. Gazizov, S. I. Grigorieva, Dip in UHECR spectrum as signature of proton interaction with CMB, J. Phys. G31 (2005) 255–264.

[40] R. U. Abbasi, et al., The High Resolution Fly's Eye Collaboration (HiRes), First Observation of the Greisen-Zatsepin-Kuzmin Suppression, Phys. Rev. Lett. 100 (2008) 101101.

[41] J. Abraham, et al., The Pierre Auger Collaboration, Observation of the suppression of the flux of cosmic rays above 4×10^{19} eV, Phys. Rev. Lett. 101 (2008) 061101. arXiv:0806.4302.

[42] D. Allard, et al., Implications of the cosmic ray spectrum for the mass composition at the highest energies, JCAP 10 (2008) 033. arXiv:0805.4779.

[43] P. Abreu, et al., The Pierre Auger Collaboration, Update on the correlation of the highest energy cosmic rays with nearby extragalactic matter, Astropart. Phys. 34 (2011) 314–326. arXiv:1009.1855.

[44] I. Tkachev, et al., for the Telescope Array Collaboration, Anisotropy and Point Sources Searches in the Telescope Array Data, in: Proc. 32nd ICRC, Vol. 2, Beijing, China, 2011, pp. 281–284.

[45] P. Abreu, et al., Search for First Harmonic Modulation in the Right Ascension Distribution of Cosmic Rays Detected at the Pierre Auger Observatory, Astropart. Phys. 34 (2011) 627–639. arXiv:1103.2721.

[46] P. Facal, for the Pierre Auger Collaboration, The distribution of shower maxima of UHECR air showers, in: Proc. 32nd ICRC, Vol. 2, Beijing, China, 2011, pp. 105–108. arXiv:1107.4804.

[47] R. U. Abbasi, et al., Indications of Proton-Dominated Cosmic Ray Composition above 1.6 EeV, Phys. Rev. Lett. 104 (2010) 161101. arXiv:0910.4184.

[48] Y. Guardincerri, for the Pierre Auger Collaboration, The Pierre Auger Observatory and UHE neutrinos: upper limits to the diffuse flux and from point-like sources, in: Proc. 32nd ICRC, Vol. 4, Beijing, China, 2011, pp. 201–204. arXiv:1107.4805.

[49] G. I. Rubtsov, et al., for the Telescope Array Collaboration, Search for Ultra-high Energy Photons and Neutrinos Using Telescope Array Surface Detector, in: Proc. 32nd ICRC, Vol. 2, Beijing, China, 2011, pp. 242–245.

[50] M. Settimo, for the Pierre Auger Collaboration, An update on the search for ultra-high energy photons using the Pierre Auger Observatory, in: Proc. 32nd ICRC, Vol. 2, Beijing, China, 2011, pp. 55–58. arXiv:1107.4805.

[51] I. Allekotte, et al., The Pierre Auger Collaboration, The Surface Detector System of the Pierre Auger Observatory, Nucl. Instr. Meth. A586 (2008) 409–420. arXiv:0712.2832.

[52] T. Suomijärvi, The Pierre Auger Collaboration, Performance and operation of the Surface Detector of the Pierre Auger Observatory, in: Proc. 31st ICRC, Łódź, Poland, 2009. arXiv:0906.2354.

[53] R. Pesce, for the Pierre Auger Collaboration, Energy calibration of data recorded with the surface detectors of the Pierre Auger Observatory: an update, in: Proc. 32nd ICRC, Vol. 2, Beijing, China, 2011, pp. 214–217. arXiv:1107.4809.

[54] F. Sanchez, et al., for the Pierre Auger Collaboration, The AMIGA detector of the Pierre Auger Observatory: overview, in: Proc. 32nd ICRC, Vol. 3, Beijing, China, 2011, pp. 145–148. arXiv:1107.4809.

[55] J. Abraham, et al., The Pierre Auger Collaboration, The Fluorescence Detector of the Pierre Auger Observatory, Nucl. Instr. Meth. A620 (2010) 227–251. arXiv:0907.4282.

[56] H. J. Mathes, et al., for the Pierre Auger Collaboration, The HEAT telescopes of the Pierre Auger Observatory: status and first data, in: Proc. 32nd ICRC, Vol. 3, Beijing, China, 2011, pp. 149–152. arXiv:1107.4807.

[57] P. Abreu, et al., The Pierre Auger Collaboration, The exposure of the hybrid detector of the Pierre Auger Observatory, Astropart. Phys. 34 (2011) 368–381. arXiv:1010.6162.

[58] M. Mostafá, The Pierre Auger Collaboration, Hybrid Activities of the Pierre Auger Observatory, Nucl. Phys. Proc. Suppl. 165 (2007) 50–58. arXiv:astro-ph/0608670.

[59] F. Arqueros, J. R. Hörandel, B. Keilhauer, Air fluorescence relevant for cosmic-ray detection - Summary of the 5th fluorescence workshop, El Escorial 2007, Nucl. Instr. Meth. A597 (2008) 1–22. arXiv:0807.3760.

[60] M. Unger, B. R. Dawson, R. Engel, F. Schüssler, R. Ulrich, Reconstruction of Longitudinal Profiles of Ultra-High Energy Cosmic Ray Showers from Fluorescence and Cherenkov Light Measurements, Nucl. Instr. Meth A588 (2008) 433–441. arXiv:0801.4309.

[61] J. Abraham, et al., The Pierre Auger Collaboration, Measurement of the Depth of Maximum of Extensive Air Showers above 10^{18} eV, Phys. Rev. Lett. 104 (2010) 091101. arXiv:1002.0699.

[62] Interdisciplinary Science at Auger Observatory (IS@AO) (April 2011). URL http://www.auger.org/ISatAO/

[63] A. S. Tonachini, for the Pierre Auger Collaboration, Observation of Elves with the Fluorescence Detectors of the Pierre Auger Observatory, in: Proc. 32nd ICRC, Vol. 11, Beijing, China, 2011, pp. 400–403. arXiv:1107.4806.

[64] P. Abreu, et al., The Pierre Auger Collaboration, The Pierre Auger Observatory scaler mode for the study of solar activity modulation of galactic cosmic rays, JINST 6 (2011) P01003.

[65] M. Jelinek, et al., The bright optical flash from GRB 060117, Astron. Astrophys. 454 (2006) L119. arXiv:0606004.

[66] B. A. Bodhaine, et al., On rayleigh optical depth calculations, J. Atmos. Ocean. Tech. 16 (1999) 1854–1861.

[67] F. Herbert, Data for the basic structure of the atmosphere, in: G. Fischer (Ed.), Landolt-Börnstein, New Series, Group V, Vol. 4a, Springer, 1987.

[68] M. Ave, et al., The AIRFLY Collaboration, Temperature and humidity dependence of air fluorescence yield measured by AIRFLY, Nucl. Instr. Meth. A597 (2008) 50–54.

[69] M. Boháčová, for the AIRFLY Collaboration, Temperature and Humidity Dependence of Air Fluorescence Yield, in: 6th Air Fluorescence Workshop, L'Aquila, Italy, 2009.

[70] M. Nagano, et al., New measurement on photon yields from air and the application to the energy estimation of primary cosmic rays, Astropart. Phys. 22 (2004) 235–248.

[71] J. C. Owens, et al., Optical Refractive Index of Air: Dependence on Pressure, Temperature and Composition, Appl. Opt. 6 (1967) 51–59.

[72] P. E. Ciddor, et al., Refractive index of air: 3. The roles of CO_2, H_2O, and refractivity virials, Appl. Opt. 41 (2002) 2292–2298.

[73] K. P. Birch, M. J. Downs, An Updated Edlén Equation for the Refractive Index of Air, Metrologia 30 (1993) 155–162.

[74] C. Tomasi, et al., Improved algorithm for calculations of Rayleigh-scattering optical depth in standard atmospheres, Appl. Opt. 44 (2005) 3320–3341.

[75] A. Bucholtz, Rayleigh scattering calculations for the terrestrial atmosphere, Appl. Opt. 34 (1995) 2765–2773.

[76] E. S. Fishburne, M. E. Neer, G. Sandri, Voice Communication via Scattered Ultraviolet Radiation, Aeronautical Research Associates of Princeton, Inc., NJ, Report 274 (1976) 1–83.

[77] F. Riewe, A. E. S. Green, Ultraviolet aureole around a source at a finite distance, Appl. Opt. 17 (1978) 1923–1929.

[78] L. G. Henyey, J. L. Greenstein, Diffuse radiation in the galaxy, Astrophys. J. 93 (1941) 70–83.

[79] J. Abraham, et al., The Pierre Auger Collaboration, A Study of the Effect of Molecular and Aerosol Conditions in the Atmosphere on Air Fluorescence Measurements at the Pierre Auger Observatory, Astropart. Phys. 33 (2010) 108–129. arXiv:1002.0366.

[80] GRAW Radiosondes GmbH & Co. KG.
URL http://www.graw.de

[81] P. Abreu, et al., The Pierre Auger Collaboration, Data from the Global Data Assimilation System (GDAS) for the Pierre Auger Observatory, Astropart. Phys. 35 (2012) 591–607. arXiv:1201.2276.

[82] M. Will, Influence of Humidity on the Development and Reconstruction of Extensive Air Showers at the Pierre Auger Observatory, Diploma thesis, Universität Karlsruhe (TH), Germany (2009).

[83] NCAS British Atmospheric Data Centre.
URL http://badc.nerc.ac.uk/

[84] The Tornado History Project (2011).
URL http://www.tornadohistoryproject.com/

[85] B. Keilhauer, M. Unger, Fluorescence emission induced by extensive air showers in dependence on atmospheric conditions, in: Proc. 31st ICRC, Łódź, Poland, 2009. arXiv:0906.5487.

[86] B. Keilhauer, for the Pierre Auger Collaboration, Rapid atmospheric monitoring after the detection of high-energy showers at the Pierre Auger Observatory, in: Proc. 31st ICRC, Łódź, Poland, 2009. arXiv:0906.2358.

[87] P. Abreu, et al., The Pierre Auger Collaboration, The Rapid Monitoring System of the Pierre Auger Observatory, subm. to JINST.

[88] S. Argirò, et al., The Offline Software Framework of the Pierre Auger Observatory, Nucl. Instr. Meth. A580 (2007) 1485–1496. arXiv:0707.1652.

[89] B. Wilczyńska, et al., Variation of Atmospheric Depth Profile on Different Time Scales, Astropart. Phys. 25 (2006) 106–117. arXiv:astro-ph/0603088.

[90] B. Keilhauer, for the Pierre Auger Collaboration, The Balloon-the-Shower programme of the Pierre Auger Observatory, in: Proc. 22nd Europ. Cosmic Ray Symp.; Astrophys. Space Sci. Trans., Vol. 6, Turku, Finland, 2010, pp. 27–30.

[91] M. Will, for the Pierre Auger Collaboration, Implementation of meteorological model data in the air shower reconstruction of the Pierre Auger Observatory, in: Proc. 32nd ICRC, Vol. 2, Beijing, China, 2011, pp. 51–54. arXiv:1107.4806.

[92] L. F. Richardson, Weather Prediction by Numerical Process, Cambridge University Press, 1922.

[93] J. Charney, R. Fjørtoft, J. von Neumann, Numerical Integration of the Barotropic Vorticity Equation, Tellus 2 (2050) 237–254.

[94] P. Müller, H. von Storch, Computer modeling in atmospheric and oceanic sciences, Springer Verlag (2004).

[95] W. Wergen, Datenassimilation – ein Überblick, promet 27 (3/4) (2002) 142–149.

[96] NOAA Air Resources Laboratory (ARL), Global Data Assimilation System (GDAS1) Archive Information, Tech. rep. (2004).
URL http://ready.arl.noaa.gov/gdas1.php

[97] National Aeronautics and Space Administration (NASA), U.S. Standard Atmosphere 1976, NASA-TM-X-74335 (1976).

[98] National Centers for Environmental Prediction (NCEP), GFS/GDAS Changes Since 1991, Tech. rep. (2010).
URL http://www.emc.ncep.noaa.gov/gmb/STATS/html/model_changes.html

[99] B. Stunder, NOAA Air Resources Laboratory, private communication (November 2011).

[100] M. J. Mahoney, A Discussion of Various Measures of Altitude, Tech. rep. (2008).
URL http://mtp.jpl.nasa.gov/notes/altitude/altitude.html

[101] K. Louedec, for the Pierre Auger Collaboration, Origin of atmospheric aerosols at the Pierre Auger Observatory using backward trajectory of air masses, in: Proc. 23rd ECRS (accepted), Moscow, Russia, 2012.

K. Louedec, M. Urban, Where do aerosols come from ? – Study done with HYSPLIT, Auger Technical Note GAP-2011-058 (2011).
URL `http://www.auger.org/admin/GAP_Notes/GAP2011/GAP2011_058.pdf`

[102] M. Ave, et al., The AIRFLY Collaboration, Measurement of the pressure dependence of air fluorescence emission induced by electrons, Astropart. Phys. 28 (2007) 41–57.

[103] B. Keilhauer, J. Blümer, R. Engel, H. O. Klages, Altitude dependence of fluorescence light emission by extensive air showers, Nucl. Instr. Meth. A597 (2008) 99–104. `arXiv:0801.4200`.

[104] T. Bergmann, et al., One-dimensional hybrid approach to extensive air shower simulation, Astropart. Phys. 26 (2007) 420–432.

[105] S. Ostapchenko, QGSJET-II: towards reliable description of very high energy hadronic interactions, Nucl. Phys. Proc. Suppl. 151 (2006) 143–146.

[106] D. Heck, et al., CORSIKA: A Monte Carlo Code to Simulate Extensive Air Showers, Forschungszentrum Karlsruhe Report 6019 (1998) 1–98.

[107] B. Keilhauer, Investigation of Atmospheric Effects on the Development of Extensive Air Showers and their Detection with the Pierre Auger Observatory, Ph.D. thesis, Universität Karlsruhe (TH), Germany (2003).

[108] M. I. Micheletti, et al., Elemental analysis of aerosols collected at the Pierre Auger South Observatory of cosmic rays, subm. to Nucl. Instr. Meth. B.

[109] D. Oku, et al., for the Telescope Array Collaboration, LIDAR system in Central Laser Facility of Telescope Array Experiment, in: Proc. 32nd ICRC, Vol. 3, Beijing, China, 2011, pp. 321–324.

[110] T. Tomida, et al., for the Telescope Array Collaboration, Atmospheric Calibrations for Air Fluorescence Observations in the Telescope Array Experiment by LIDAR system, in: Proc. 32nd ICRC, Vol. 3, Beijing, China, 2011, pp. 325–328.

[111] R. U. Abbasi, et al., The High Resolution Fly's Eye Collaboration (HiRes), Techniques for measuring atmospheric aerosols at the High Resolution Fly's Eye experiment, Astropart. Phys. 25 (2006) 74–83. `arXiv:astro-ph/0512423`.

[112] S. BenZvi, et al., The Lidar system of the Pierre Auger Observatory, Nucl. Instr. Meth. A574 (2007) 171–184.

[113] M. Winnick, Cloud Cameras at the Pierre Auger Observatory, Ph.D. thesis, University of Adelaide, Australia (2010).

[114] S. Y. BenZvi, et al., Measurement of the aerosol phase function at the Pierre Auger Observatory, Astropart. Phys. 28 (2007) 312–320. `arXiv:0704.0303`.

[115] K. Louedec, Atmospheric aerosols at the Pierre Auger Observatory: characterization and effect on the energy estimation for ultra-high energy cosmic rays, Ph.D. thesis, Université Paris Sud XI, France (2011).

[116] M. Prouza, et al., FRAM - The Robotic Telescope for the Monitoring of the Wavelength Dependence of the Extinction: Description of Hardware, Data Analysis, and Results, Adv. Astron. 2010 (2010) 849382.

[117] B. Fick, et al., The Central Laser Facility at the Pierre Auger Observatory, JINST 1 (2006) 11003.

[118] L. Wiencke, et al., Calibrating laser test-beams for cosmic-ray observatories, in: Proc. 31st ICRC, Łódź, Poland, 2009. arXiv:1105.4016.

[119] L. Wiencke, et al., for the Pierre Auger Collaboration, Atmospheric "Super Test Beam" for the Pierre Auger Observatory, in: Proc. 32nd ICRC, Vol. 3, Beijing, China, 2011, pp. 141–144. arXiv:1107.4806.

[120] L. Wiencke, Colorado School of Mines, Golden, private communication (March 2012).

[121] P. Abreu, et al., The Pierre Auger Collaboration, Techniques for Measuring Aerosols using the Central Laser Facility at the Pierre Auger Observatory, subm. to JINST.

[122] L. Valore, Atmospheric Aerosol Determination using Vertical Laser Tracks in the Pierre Auger Experiment, Ph.D. thesis, Università degli Studi di Napoli, Italy (2007).

[123] L. Valore, Università di Napoli and Sezione INFN, private communication (April 2012).

[124] D. J. Starbuck, Measuring the Vertical Aerosol Optical Depth Using an Automated Cosmic Ray Fluorescence Detector and Elastic Side Scattering, and Comparing to Raman Lidar Measurements, Master's thesis, Colorado School of Mines, United States (2011).

[125] M. Coco, A Comparison of Raman Lidar Signal Estimation and Smoothing Methods and Correlation Between the Pierre Auger Side Scattering Method for Determining the Aerosol Content in the Troposphere, Master's thesis, Colorado School of Mines, United States (2012).

[126] F. Sarazin, et al., for the Pierre Auger Collaboration, New technologies for the Pierre Auger Observatory: research and development in southeastern Colorado, in: Proc. 32nd ICRC, Vol. 3, Beijing, China, 2011, pp. 196–199. arXiv:1107.4807.

[127] V. Rizi, et al., for the Pierre Auger Collaboration, UV Raman Lidar and Side Scattering Detector for the Monitoring of Aerosol Optical Transmission at the Pierre Auger Observatory, in: Proc. 26th ILRC, Porto Heli, Greece, 2012.

[128] L. Wiencke, et al., The High Resolution Fly's Eye Collaboration (HiRes), Radio-controlled Xenon Flashers for Atmospheric Monitoring at the HiRes Cosmic Ray Observatory, Nucl. Instr. Meth. A428 (1999) 593–607.

[129] Vaisala.
URL `http://www.vaisala.com`

[130] V. Rizi, CETEMPS and Dipartimento di Fisica, Università Degli Studi dell'Aquila, private communication (April 2012).